EXPERIMENTAL CHARACTERIZATION OF THE TEMPERATURE

DEPENDENCE OF THE PIEZORESISTIVE

COEFFICIENTS OF SILICON

Except where reference is made to the work of others, the work described in this dissertation is my own or was done in collaboration with my advisory committee. This dissertation does not include proprietary or classified information.

_____
Chun Hyung Cho

Certificate of Approval:

_____   _____
Richard C. Jaeger, Co-Chair   Jeffrey C. Suhling, Co-Chair
Distinguished University Professor   Quina Distinguished Professor
Electrical and Computer Engineering Mechanical Engineering

_____   _____
Bogdan Wilamowski   Greg Harris
Professor   Associate Professor
Electrical and Computer Engineering Mathematics and Statistics

_____
Joe F. Pittman
Interim Dean
Graduate School

EXPERIMENTAL CHARACTERIZATION OF THE TEMPERATURE

DEPENDENCE OF THE PIEZORESISTIVE

COEFFICIENTS OF SILICON

Chun Hyung Cho

A Dissertation

Submitted to

the Graduate Faculty of

Auburn University

in Partial Fulfillment of the

Requirement for the

Degree of

Doctor of Philosophy

Auburn, Alabama
August 04, 2007

EXPERIMENTAL CHARACTERIZATION OF THE TEMPERATURE

DEPENDENCE OF THE PIEZORESISTIVE

COEFFICIENTS OF SILICON

Chun Hyung Cho

_____

Signature of Author

_____

Date of Graduation

VITA

Chun Hyung Cho, son of Nam Jin Cho and Sung Dong Hong, was born on October 27, 1970 in Daejeon, Korea. He graduated from North Daejeon High School, Daejeon, Korea in 1989, and from Seoul National University, Seoul, Korea in 1997 with the degree of Bachelor of Science in Electrical Engineering. He started his M.S. Program in the Electrical Engineering Department, Auburn University, Alabama, in 1998. He received his M.S. in Electrical Engineering in 2001. He continued his Ph.D. program in Auburn University from 2001. He married Eun Ok Jeong on December 29, 2001. On September 30, 2002, their first son, Sung Am Cho, was born and on September 12, 2004, their second son, Sung Mok Cho was born.

DISSERTATION ABSTRACT

EXPERIMENTAL CHARACTERIZATION OF THE TEMPERATURE

DEPENDENCE OF THE PIEZORESISTIVE

COEFFICIENTS OF SILICON

Chun Hyung Cho

Doctor of philosophy, August 04, 2007
(Master of Science, Auburn University, 2001)
(B.S. Electrical Engineering, Seoul National University, South Korea, 1997)

321 Typed Pages

Directed by Richard C. Jaeger and Jeffrey C. Suhling

In this work, the dependence of the silicon piezoresistive coefficients π_{11}, π_{12}, and π_{44} on temperature is investigated. Experimental calibration results for the piezoresistive coefficients of silicon as a function of temperature are presented and compared and contrasted with existing values from the literature.

Stress-sensing test chips are widely used to investigate die stresses occurring to assembly and packaging operations. They incorporate resistor- or transistor-sensing elements that are able to measure stresses through the observation of the changes in their

resistivity/mobility. The piezoresistive behavior of such sensors can be completely characterized through the use of three piezoresistive (pi) coefficients, which are electro-mechanical material constants. In most prior investigations, calibration of the piezoresistive coefficients has been performed at room temperature. Such restriction limits the accuracy of test chip stress measurements made at other temperatures. In this work, we have performed an extensive experimental study on temperature dependence of the piezoresistive behavior of silicon. Calibration has been performed using four-point bending of chip-on-beam specimens. A special four-point bending apparatus has been constructed and integrated into an environmental chamber capable of temperatures from -185 to 300°C. Finite element analysis has been used to calculate the stress states applied to the calibration samples. Our test results show that the piezoresistive coefficients for p- and n-type silicon decrease monotonically when temperature is increased from -150 to 125°C.

Our goals in this work are to enable packaging stress measurements over a wide range of temperature, to obtain a comprehensive set of piezoresistive coefficients over a broad range of temperature, to resolve sign issues and demonstrate proper methods for relating coefficients at different temperatures, and to obtain consistent formulation of $R(\sigma, T)$ valid over wide temperature range.

Style manual or journal used <u>Guide to Preparation and Submission of Theses and</u>

<u>Dissertations</u>

Computer software used <u>Microsoft Word 2002 and Microsoft Excel 2002</u>

TABLE OF CONTENTS

LIST OF TABLES

CHAPTER 1

INTRODUCTION

As VLSI chips have become highly integrated with advances in semiconductors

and microelectronics, their feature sizes have become smaller and smaller. Too, VLSI die

sizes have become larger and larger. Hence the effects of mechanical stresses on the

structural reliability of electronic packages have become an important issue. These

stresses are caused during both the fabrication and operation of an electronic package

from mechanical loads and from uneven expansions and contractions of the various

package materials.

Because of thermal and mechanical loadings, stresses in electronic packages

may cause not only premature mechanical failures but also alteration of the function of

the semiconductor devices. Thus stress related problems such as fracture of the die, die

bond failure, solder fatigue, severing of connections, and encapsulant cracking are

prevalent in semiconductor manufacturing. Especially, thermally induced stresses are

created during packaging procedures such as encapsulation and die attachment, as well as

during the application of the package in a thermally changing environment. Typical IC

packages are comprised of a variety of materials which expand and contract at different

rates and have different elastic moduli. Under heating and cooling of such assemblies of

materials, the coefficient of thermal expansion mismatches lead to mechanical stresses. In

addition, heat dissipated by high power density devices during operation produces thermally induced stresses.

As the electronic industry continues to develop, the ratio of package size to chip size becomes an issue for higher I/Os. Thus the stress distribution may change rapidly over small scales.

Piezoresistive stress sensors are a powerful tool for experimental structural analysis of electronic packages. Figure 1.1 illustrates the basic application concepts. The structures of interest are semiconductor chips which are incorporated in electronic packages. The sensors are an integral part of the structure to be analyzed. The stresses in the chip induce resistance change in the sensors because of the piezoresistive effect and may be easily measured. Thus the sensors are capable of providing non-intrusive measurements of surface stress states on a chip even within encapsulated packages.
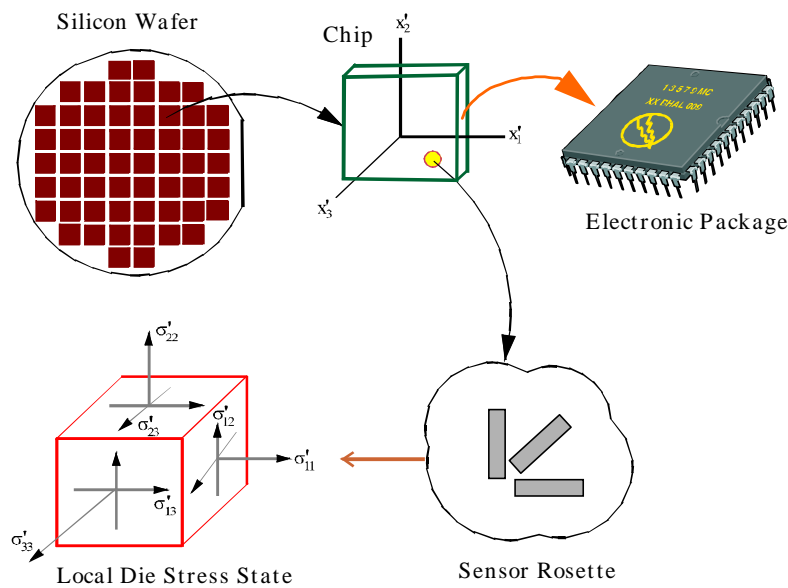
Fig. 1.1 - Basic concept of piezoresistive sensor

If the piezoresistive sensors are calibrated over a wide temperature range, thermally induced stresses may be measured. A full-field mapping of the stress distribution over the surface of a die can be obtained using specially designed test chips which incorporate an array of sensor rosettes (or resistors). In addition to being applied to packaging stress measurements, piezoresistive sensors have widespread applications as sensing elements in various transducers.

Accurate values of the piezoresistive coefficients of the sensing resistors, as well as recognition of the many potential sources of error that may be present during calibration and measurement, are required for the successful application of piezoresistive stress sensors. Therefore, it is very important to search for the optimal wafer orientation in order to minimize the associated calibration errors for (001) silicon wafer. Misalignment with respect to the true crystallographic axes of the semiconductor crystals, such as the tilt of wafer plane, affects the calibration values of piezoresistive coefficient. Errors in misalignment with the given crystallographic axes are described and analyzed because precise determination of the crystallographic orientation in (001) silicon wafers is found to be essential for accurate determination of piezoresistive coefficients of silicon. On the other hand, for (111) silicon wafers, errors associated with misalignment have no effect on the calculation of piezoresistive coefficients of silicon due to the isotropic characteristics of (111) silicon.

Enhanced calibration techniques are needed for accurate determination of piezoresistive coefficients prior to application of piezoresistive sensors within packages. For experimental techniques and methods, a four-point bending fixture system and a hydrostatic pressure vessel system have been constructed. In order to extract a complete

set of pi-coefficients (π_{11}, π_{12}, and π_{44}) for both p- and n-type sensors, hydrostatic tests are needed for (111) silicon. On the other hand, the hydrostatic tests are not required for stress sensors on (001) silicon. In order to determine a complete set of pi-coefficients, (001) silicon wafers are cut along two directions (e.g., the [100] axis and the [110] axis). Associated beam rotational errors in piezoresistive coefficients induced by the rotational misalignment of the strip on the supports with respect to the ideal longitudinal axis of the strip are explained.

In the chip-on-board (or strip-on-beam) method, a die (or strip) is adhered to a board which is subjected to pure bending. The general equation for an off-axis (0, 90, +45, and -45) resistor oriented at some arbitrary angle is discussed. The fabrication and calibration of the (001) or (111) silicon test chips for p- and n-type materials are explained. Finite element analysis has been presented to calculate the stress states applied to the calibration samples. In addition, several issues related to the regular four-point bending calibration procedure have been described.

The hydrostatic pressure calibration technique has been reviewed for sensors fabricated on the (111) silicon. In the case of hydrostatic calibration, a high capacity pressure vessel is used to subject a single die to triaxial compression. The temperature effects must be removed from hydrostatic calibration data before evaluating the pressure coefficients, and accurate determination of the TCR (temperature coefficients of resistance) of a sensor must be done prior to pressure coefficient measurement. Finally, a combination of four-point bending and hydrostatic calibration tests has been shown to be suitable for obtaining a comprehensive set of piezoresistive coefficients.

4

Stress analyses of electronic packages and their components have been performed using experimental, numerical, and analytical methods. Experimental approaches have included the use of test chips incorporating piezoresistive stress sensors, whereas numerical studies have typically considered finite element solutions for sophisticated package geometries. Analytical investigations have been concerned primarily with finding closed-form elasticity solutions for layered structures.

In the current microelectronics industry, it is most common for silicon devices to be fabricated using the (001) silicon wafers. The other customarily utilized wafer orientation is (111). In this work, the general piezoresistivity theories at fixed and variable temperatures are presented, and the general equations for sensors fabricated on the (001) and the (111) silicon wafers along with the basic sensor rosette configurations are reviewed and expanded. Further, the general expressions for the resistance changes experienced by in-plane resistors fabricated on these two types of silicon wafers have been reviewed. In particular, for each wafer type the normalized resistance change for an in-plane resistor has been expressed as a function of the resistor orientation and a set of linearly independent combined piezoresistive coefficients.

The directionally dependent nature of silicon crystals will be explained to help with the understanding of physical properties of semiconductor materials and the linear elastic silicon stress-strain relations have been presented in tensor notation. The appropriate selection of stress-strain relations has been discussed.

Over the years, the VDP (Van der Pauw) structures have been used to measure resistivity or sheet resistance of materials. Sheet resistivity of a flat conductive structure can be calculated using the resistivity value measured using VDP structure. It is

noteworthy that dimensional changes of VDP structures during loading have not been considered in prior investigations.

In this work, however, the dimensional changes of VDP structures and resistor during loading will be discussed. Furthermore, strain-effects of VDP structures and resistor sensors on piezoresistive coefficients and sensitivity magnifications will be discussed and compared to the cases in which strain-effects are not considered. Simultaneously, the VDP stress sensitivities will be compared with analogous resistor sensors on the same wafer and with the same doping concentration.

CHAPTER 2

LITERATURE REVIEW

In 1932, Bridgman [1-3] observed that applied transverse and longitudinal stresses in certain crystals changed their electrical resistance. Bridgman, credited with making the first piezoresistance measurements, initially observed piezoresistive behavior in metals. He subjected metals to tension and hydrostatic pressure. Experimental observations of the piezoresistive effect in semiconductors (silicon and germanium) were first made by Taylor [4], Bridgman [5], Smith [6], and Paul and Pearson [7].

Smith [6] described the piezoresistance effect that is a major sensing principle in micro-mechanical sensors. In 1961, Pfann and Thurston [8] derived longitudinal and transverse piezoresistance coefficients for various directions in cubic crystals of silicon. These formulations were later clarified and formulized using tensor analysis techniques by Mason and Thurston [9], Thurston [10], and Smith [11]. Since then, many researchers have studied the piezoresistance coefficients of silicon both analytically and experimentally, as a function of doping concentration mostly at room temperature. An extensive derivation of the piezoresistive theory was given by Bittle, et al. [12-13]. A detailed theory for silicon piezoresistive sensors was derived by Bittle et al. [14], and Kang [15] explored piezoresistive theory for silicon on various wafer planes.

In the early work, stress was often applied by hanging a weight on a string fixed to

the end of the silicon cantilever. Only the largest coefficients, π_{44} for p-type silicon and π_{11} for n-type material, are easily measured. The effects of crystallographic misalignment and temperature errors were generally ignored. A design tool for precise determination of the crystallographic orientation in the (001) silicon wafer using anisotropic wet etching was introduced by Vangbo [16]. Jaeger and Suhling [17] showed that temperature variations and measurement errors play a pivotal role in determining accuracy of the results obtained during both calibration and application of piezoresistive stress sensors. They demonstrated the significance of thermally induced errors in the calibration and application of silicon piezoresistive stress sensors in [17]. Furthermore, Cordes, et al. [18] presented optimal temperature compensated piezoresistive stress sensor rosettes.

Matsuda [19] measured the nonlinear piezoresistance effect in silicon and presented the theoretical and experimental values of piezoresistive coefficients. Kanda [20] offered a graphical representation of the piezoresistance coefficients in silicon, based on the literature values of piezoresistive coefficients by Smith. He plotted the theoretical longitudinal and transverse piezoresistance coefficients at room temperature as a function of the crystal directions for orientations in the (100), (110), and (211) crystallographic planes. Richter et al. [21] presented experimentally obtained results for the piezoresistive effect in p-type silicon. They measured the longitudinal (π_L) and transverse (π_T) components for the [110] direction of the (001) silicon. Vladimir [22] produced numerical simulations of the piezoresistance effect in silicon using a relaxation time formation. The results in these publications were for fixed temperature

The temperature dependence of the piezoresistance of high-purity silicon and

8

germanium was described by Morin [23]. The temperature dependence of the large

coefficients (π_{44} for p-type silicon and π_{11} for n-type silicon) has been measured by Tufte

and Stelzer [24-25] as a function of impurity concentration. Suhling, et al. [26-27] used

piezoresistive sensors to measure and investigate thermally-induced stresses. Lenkkeri

[28] presented experimental values of the piezoresistance coefficients at 77K and 300K.

Jaeger et al. [29] presented experimental results for the piezoresistive coefficients of

silicon, π_{44} and π_D, as a function of temperature (25°C~140°C), and Lund [30] measured

the piezoresistance coefficients in p-type silicon, using the 22.5° off-axis direction of

silicon, over the temperature range 5°C to 140°C. Gniazdowski [31] measured the

longitudinal (π_L) and transverse (π_T) components of the piezoresistance coefficient in p-

type [110] silicon over the temperature range 25°C to 105°C. Toriyama [32] derived an

approximate piezoresistance equation for p-type silicon as a function of impurity

concentration and temperature (-100°C~100°C) taking into account spin-orbit interaction.

Kozlovskiy [33] calculated the piezoresistance coefficients, π_{44} in p-type silicon and π_{11}

in n-type silicon as a function of temperature for different impurity concentrations.

Yamada, et al. [34] described the nonlinearity of the piezoresistive effect.

The results of all these efforts indicate relatively good agreement in magnitude for

the large (and hence easily measured) coefficients as well as a small relative temperature

dependency. However, π_{11} and π_{12} in p-type material are much less well defined

with large discrepancies in magnitude and even sign among researchers. The overall

goal of this work is to try to resolve these discrepancies and produce a set of coefficients

for use in packaging measurements over 77K - 450K.

For experimental structural analysis of electronic packages, piezoresistive sensors are a highly useful tool. The piezoresistive sensors are usually resistors that are conveniently fabricated into the surface of the die using current microelectronic technology, and are capable of providing non-intrusive measurements of surface stress state on a chip even within encapsulated packages [35-40].

Stress sensors based on piezoresistive field effect transistors (PIFET's) were proposed and designed [41-48] using the relations between the MOS drain current change and applied mechanical stress. In addition, Mian, et al. studied the sensitivity of the resistance of Van der Pauw structures to applied stress [49-50].

A four-point bending calibration procedure was discussed and utilized by Bittle, et al. [12-13], Suhling, et al. [26-27], Beaty, et al. [51], Jaeger, et al. [17, 29, 52], and Van Gestal [53]. A wafer-level procedure and calibration for piezoresistive stress sensors was developed and utilized by Cordes [54], and Suhling, et al. [55-57]. This technique for wafer-level calibration of stress sensing test chips was successfully applied to different test chip designs by Cordes [54]. The errors associated with the design and calibration of piezoresistive stress sensors in (100) silicon was analyzed by Jaeger, et al. [58-59]. Many researchers have performed experimental studies using test chips with piezoresistive stress sensors in the literature [60-66]. A hydrostatic calibration method for (111) silicon test chips was developed and applied by Kang [15], and Suhling, et al. [67-68]. Finite element simulations provide useful insight into the stress distributions produced in plastic packages during die attachment, encapsulation, and reliability tests. Various package processes and reliability tests can be investigated by means of finite element methods

[69-72].

Test chips with resistor sensors have been used to measure die stresses in various packages [13, 73-77]. However, resistor sensors are typically made using serpentine conduction paths to increase the unstressed resistance values (they have large numbers of conductive squares and thus have a relatively large resistance values) in order to reduce the measurement errors. In addition, resistor sensors have several drawbacks such as the large sensor sizes and less sensitivities.

Van der Pauw (VDP) structures used as stress sensors have the potential to solve the deficiencies of resistor based sensor. The VDP structure requires only one square of material, and its characteristics are also size independent. Thus such sensors can be made small enough to capture stress variation in a small area without any loss of sensitivity. VDP structures have been used as piezoresistive stress sensors [50]. The van der Pauw method is a widely used technique for measuring resistivity of arbitrary shaped samples of constant thickness In addition, VDP structures have been used for Hall mobility measurements. The techniques are based on the theoretical developments of van der Pauw [78-79]. Since then, many researchers have extended the originally proposed ideas to develop a variety of approaches for evaluating the resistivities of both isotropic and anisotropic materials using VDP-type structures [80-87].

An extensive review of results from the literature are presented and compared in this Chapter as discussed below:

The composite data for π_{11}, π_{12}, and π_{44} collected from the literature for p-type silicon at room temperature are displayed in Table 2.1, where the letter "C" represents calculated (theoretical) values from the literature and the letter "E" represents experimental results.

Table 2.1 - Composite data for π_{11}, π_{12}, and π_{44} collected from the literature for p-type silicon at room temperature $(TPa)^{-1}$

Author	Doping C.	π_{11}	π_{12}	π_{44}
Lund [30]	8.0E+17	170	-120	1040
(E, 99)	8.2E+18	30	-210	930
Tufte [98]	3.0E+18			1100
	9.0E+18			975
(E, 62)	5.0E+19			785
	3.0E+20			600
	5.0E+20			465
	2.0E+21			335
Toriyama [32]	1.0E+17			1100
(C, 02)	1.0E+18			975
	2.0E+18			980
	4.0E+18			960
Matsuda [19]	1.0E+17	0	20	1190
(E, 93)	5.0E+17	-60	10	1120
	8.0E+18	-40	30	970
Jaeger et al. [29] (E, 93)	1.5E+18	5.2	26	870
N/A [50](E, 00)	N/A			1107
Zou [77] (E, 98)	1.8E+18	-255	109	1160
Kozlovskiy [33] (C, 04)	9.0E+18	-39	19	1190
Mian [50] (E, 00)	N/A			871
Pikus [100] (C, 74)	N/A	115	-58	631
Smith [6] (E, 53)	lightly doped	66	-11	1381
Vladimir [22] (C, 00)	Low doped	72	-23	1175
Rahim [99] (E, 05)	JSE FC	-615	263	1269

Author	Doping C.	π_{44}
Lenkkeri [28]	1.0E+18	780
impurity	3.0E+18	750
scattering	9.0E+18	690
(C, 86)	5.0E+19	730
	1.0E+20	480
	3.0E+20	270
Lenkkeri [28]	1.0E+18	1150
optical pho-	3.0E+18	1120
non scattering	9.0E+18	1040
(C, 86)	5.0E+19	730
	1.0E+20	560
	3.0E+20	270
Sugiyama [101]	1.0E+18	1200
(E, 94)	4.0E+18	1050
	2.0E+19	900
Jaeger et al. [102] (E, 99)	Sandia ATC-04	796
Jaeger et al. [102] (E, 99)	Auburn-AAA2	1107
Lenkkeri [28] (E, 86)	6.0E+19	466
Lenkkeri [28] (E, 86) at 77K	6.0E+19	696

Literature data for π_{44}, π_{11}, and π_{12} for p-type material as a function of impurity concentration at room temperature appear in Figs. 2.1 through 2.3, respectively. The results indicate that π_{44}, a relatively large coefficient, versus impurity concentration is

relatively well defined in magnitude and sign as shown in Fig. 2.1. On the other hand, π_{11} and π_{12} in p-type material are much less defined with large discrepancies in magnitude and sign among researchers, as shown in Figs. 2.2 and 2.3.
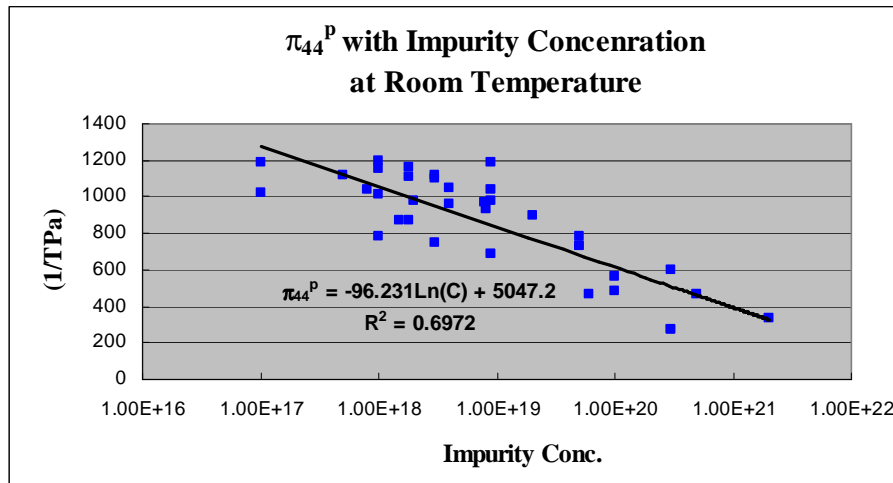
Fig. 2.1 - Composite π_{44} data collected from the literature for p-type silicon as a function of impurity concentration at room temperature
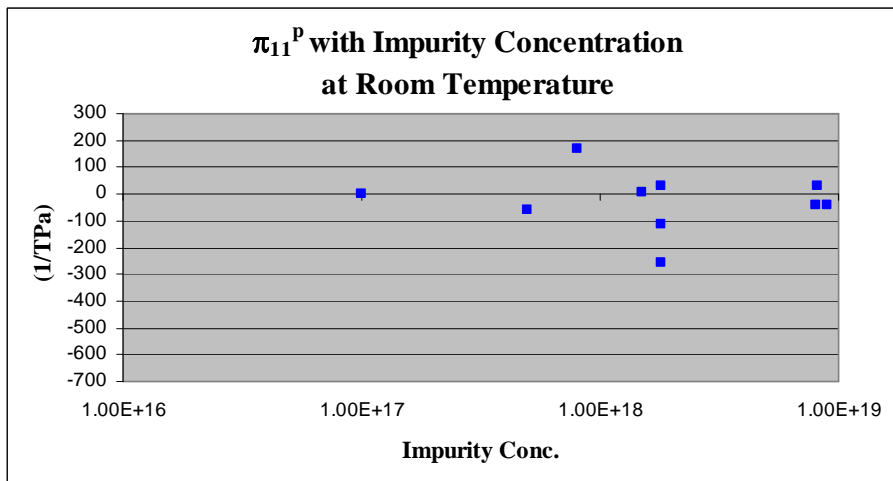
Fig. 2.2 - Literature data for π_{11} versus concentration for p-type silicon at room temperature
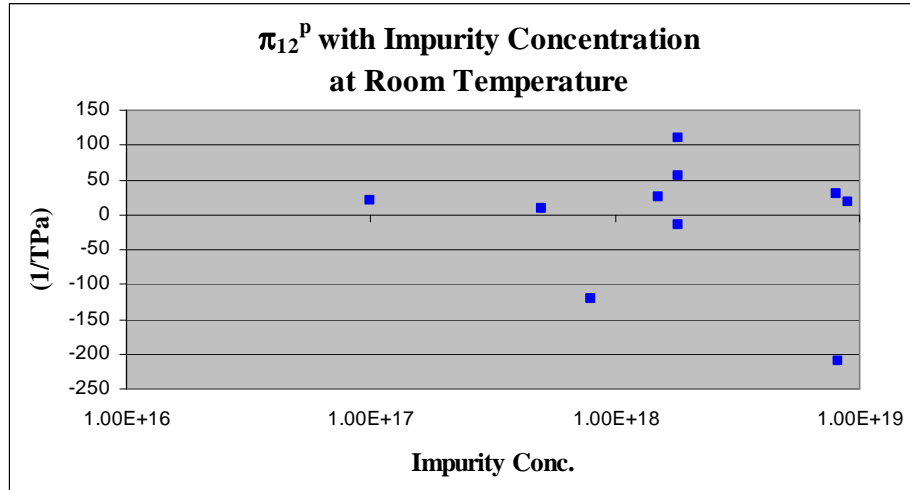
Fig. 2.3 - Literature data for π_{12} versus concentration for p-type silicon at room temperature

Similarly, for n-type material, π_{11}, π_{12}, and π_{44} from the literature are presented as a function of impurity concentration at room temperature in Tables 2.2 and 2.3. Note that the underlined values in Table 2.3 are generated by assuming the approximation $\pi_{11} \cong -2\pi_{12}$ [23]. In those cases, π_S is originally given instead of π_{11} and π_{12}. The largest coefficient π_{11} for n-type material is relatively well defined versus impurity concentration as displayed in Fig. 2.4. Unlike p-type material, the smaller coefficients (π_{12} and π_{44} in n-type material) are also well defined with impurity concentration despite the limited amount of data, as shown in Fig. 2.5.

14

Table 2.2 - Literature data for π_{11} versus concentration for n-type silicon at room temperature $(TPa)^{-1}$		
Author	Doping C.	π_{11}
Tufte [98] (E, 62)	1.80E+18	-870
Tufte [98] (E, 62)	8.80E+18	-635
Tufte [98] (E, 62)	5.20E+19	-575
Tufte [98] (E, 62)	9.00E+19	-435
Tufte [98] (E, 62)	2.10E+20	-360
Tufte [24] (E, 63)	1.30E+16	-1100
Tufte [24] (E, 63)	4.60E+16	-1050
Tufte [24] (E, 63)	9.40E+16	-1000
Tufte [24] (E, 63)	9.40E+17	-880
Tufte [24] (E, 63)	9.00E+18	-710
Tufte [24] (E, 63)	2.00E+19	-600
Tufte [24] (E, 63)	5.00E+19	-490
Tufte [24] (E, 63)	1.00E+20	-380
Tufte [24] (E, 63)	1.50E+20	-330

Table 2.3 - Composite data for π_{11}, π_{12}, and π_{44} collected from the literature for n-type silicon as a function of impurity concentration at room temperature $(TPa)^{-1}$				
Author	Doping C.	π_{11}	π_{12}	π_{44}
Matsuda [19] (E, 93)	4.00E+16	-840	430	-200
Matsuda [19] (E, 93)	1.00E+17	-770	390	-140
Matsuda [19] (E, 93)	2.00E+18	-650	330	-120
Zou [77] (E, 98)	1.80E+18	-686	359	-133
N/A [50] (E, 00)	1.80E+18	-700	350	-139
Kozlovskiy [33] (C, 04)	1.30E+16	-1156	578	
Smith [6] (E, 53)	lightly doped	-1022	534	-136
Herring [23] (C, 56)		-770	386	
Tufte [24] (E, 63)		-1070	530	
Mian [50] (E, 00)		-618	309	-95
Rahim [99] (E, 05)		-800	358	144
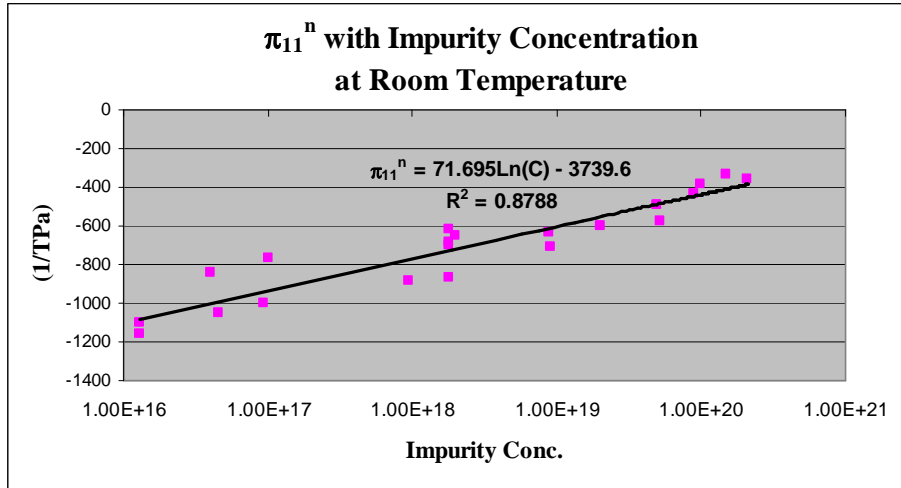
Fig. 2.4 - Literature data for π_{11} versus concentration for n-type silicon at room temperature
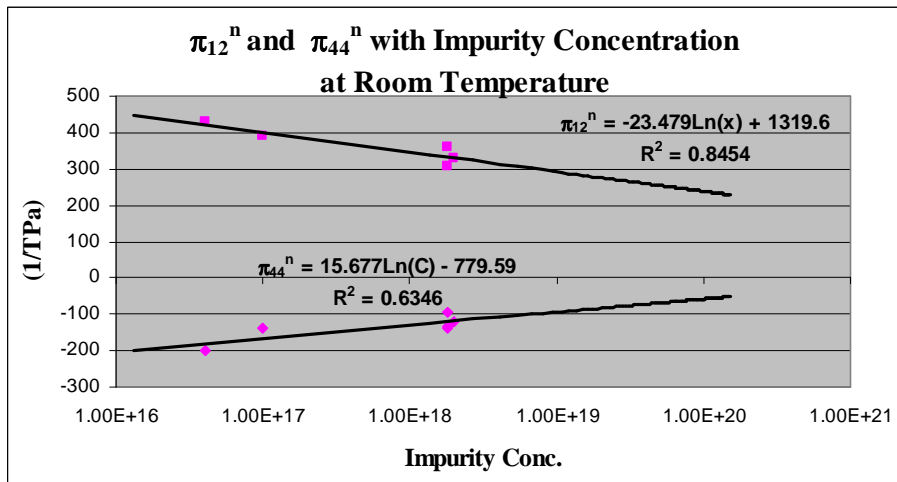
Fig. 2.5 - Literature data for π_{12} and π_{44} versus concentration for n-type silicon at room temperature

- Piezoresistive values with varying temperatures

Values of π_{44} collected from the literature for p-type silicon versus temperature are displayed in Table 2.4, whose plots are shown in Figs. 2.6 and 2.7. Also, π_{11} in n-type material versus temperature is shown in Table 2.5, whose plot is displayed in Fig. 2.8. These literature data show that the piezoresistive coefficients π_{44} in p-type material and π_{11} in n-type material decrease monotonically with rising temperature. This is in agreement with the predictions [23] that the piezoresistance is linear in T^{-1} over most of the temperature range. Note that few values of the small pi-coefficients, π_{11} and π_{12} for p-type silicon and π_{12} and π_{44} for n-type silicon, versus temperature can be found in the literature data.

Table 2.4 - Composite data for π_{44} collected from the literature for p-type silicon versus temperature with different doping concentration $(TPa)^{-1}$

Author	Toriyama [32] (C, 02)	Lund [30] (E, 99)	Toriyama [32] (C, 02)	Tufte [98] (E, 62)	Lund [30] (E, 99)	Tufte [98] (E, 62)	Toriyama [32] (C, 02)	Tufte [98] (E, 62)	Toriyama [32] (C, 02)	Gniazdowski [31] (E,98)
T (C)	1.0E+17	8.0E+17	1.0E+18	3.0E+18	8.2E+18	9.0E+18	1.0E+19	5.0E+19	1.0E+20	NA
-100	1320		1275	1625		1450	1030	1230	710	
-50	1160		1130	1500		1330	985	1020	710	
0	1070		1035	1300		1125	935	860	710	
25	1020	1040	1010	1220	930	1050	920	800	705	1237
50	990	1000	975	1170	935	990	905	760	705	1170
75	950	980	945	1100	880	920	890	730	700	1114
100	930	940	910	1030	850	900	875	700	700	1064
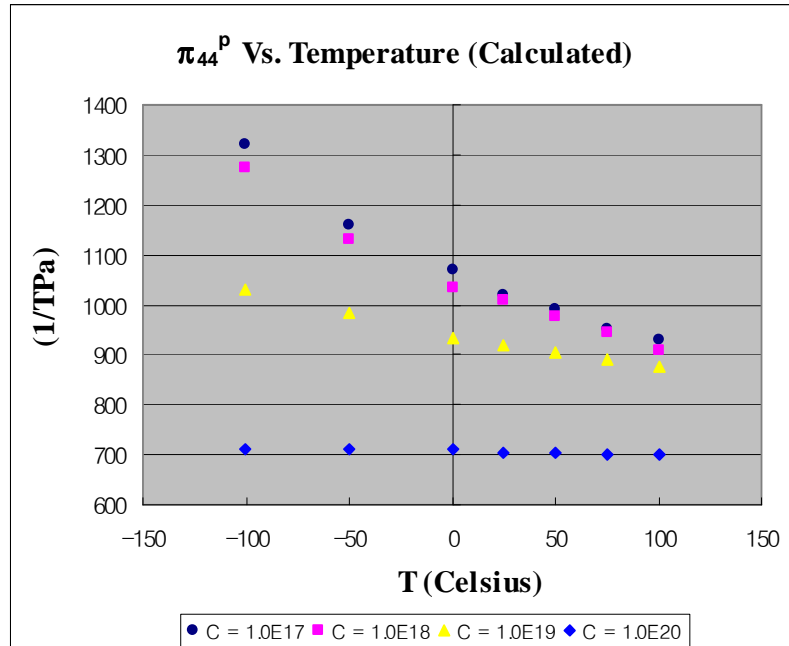
Fig. 2.6 - Calculated literature data for π_{44} versus temperature with different doping concentration for p-type silicon
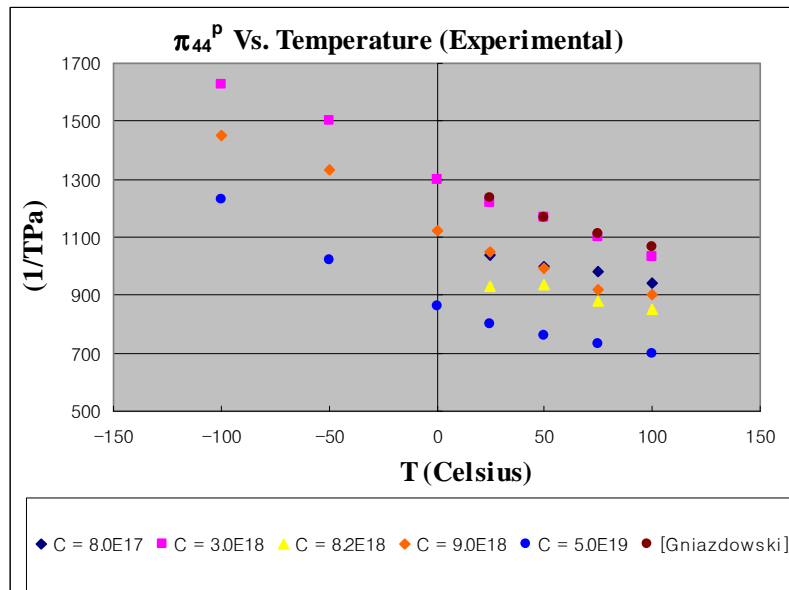
Fig. 2.7 - Experimental literature data for π_{44} versus temperature with different doping concentration for p-type silicon

Table 2.5 - Composite data for π_{11} collected from the literature for n-type silicon versus temperature with different doping concentration $(TPa)^{-1}$

Author	Tufte [24] (E, 63)	Tufte [98] (E, 62)	Tufte [98] (E, 62)	Tufte [98] (E, 62)	Tufte [22] (E, 63)	Tufte [98] (E, 62)	Tufte [98] (E, 62)
T (C)	1.3E+16	1.8E+18	8.8E+18	5.2E+19	5.0E+19	9.0E+19	2.1E+20
-200	-3200				-590	-500	-300
-150	-2200				-585	-510	-360
-100	-1800		-1100		-570	-500	-360
-50	-1400	-1020	-780	-675	-530	-490	-360
0	-1300	-925	-690	-600	-500	-450	-360
25	-1156	-870	-635	-575	-490	-435	-360
50	-1000	-790	-590	-520	-480	-420	-360
75	-800	-710	-555	-500	-470	-415	-360
100		-660	-540	-475			
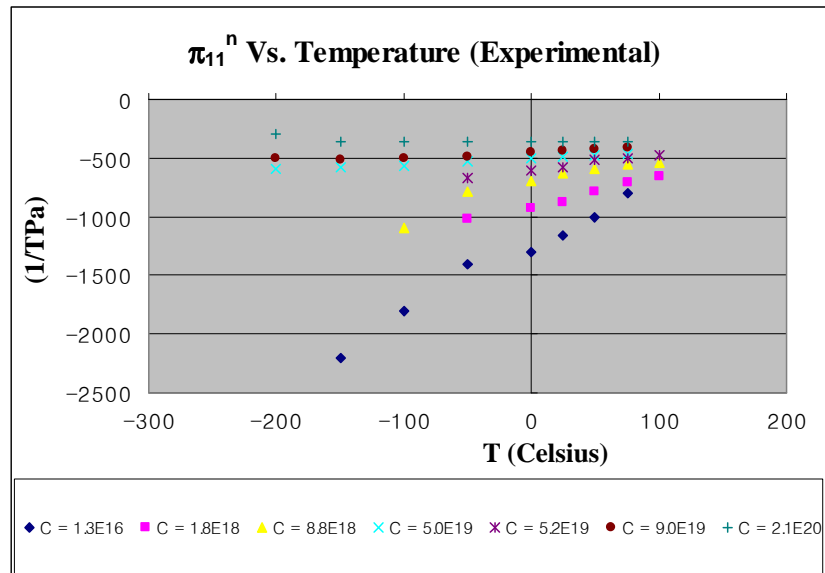
Fig. 2.8 - Experimental literature data for π_{11} versus temperature with different doping concentration for n-type silicon

CHAPTER 3

REVIEW OF PIEZORESISTIVITY THEORY

A filamentary silicon conductor arbitrarily oriented in a crystallographic coordinate system is shown in Fig. 3.1.
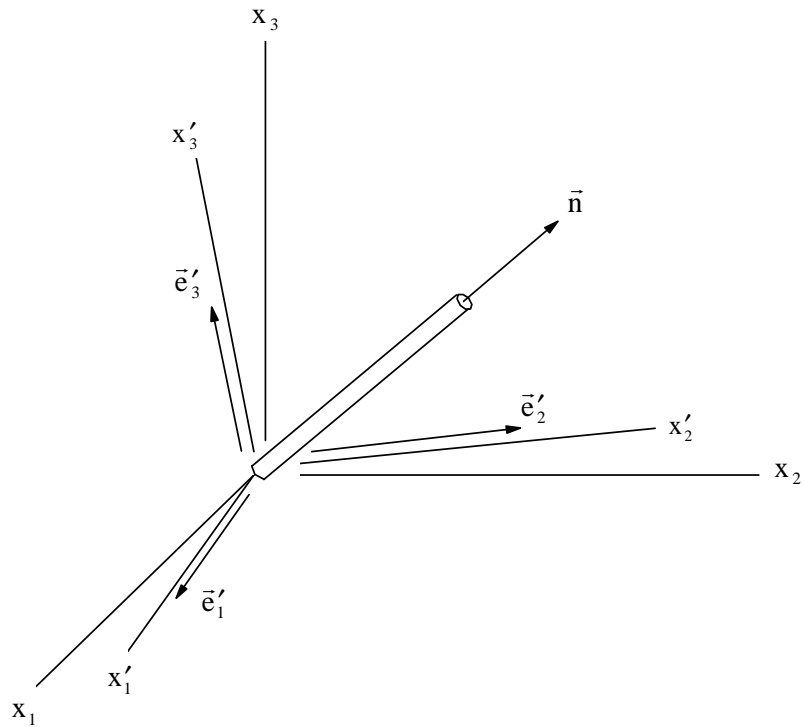
Fig. 3.1 - An arbitrary oriented, filamentary conductor

The unprimed axes $x_1 = [100]$, $x_2 = [010]$, and $x_3 = [001]$ are the principal crystallographic directions of the cubic silicon crystal. The primed coordinate system is arbitrarily rotated

20

with respect to this unprimed crystallographic system. For this conductor, the general

expression for the resistance change of a filamentary piezoresistive sensor in the plane of

the wafer may be obtained as follows [12, 15, 50, 99, 105]:

$$\frac{\Delta R}{R} = (\pi'_{1\alpha}\sigma'_{\alpha})l'^2 + (\pi'_{2\alpha}\sigma'_{\alpha})m'^2 + (\pi'_{3\alpha}\sigma'_{\alpha})n'^2$$

$$+ 2(\pi'_{4\alpha}\sigma'_{\alpha})l'n' + 2(\pi'_{5\alpha}\sigma'_{\alpha})m'n' + 2(\pi'_{6\alpha}\sigma'_{\alpha})l'm' \qquad \text{Eq. (3.1)}$$

$$+ [\alpha_1\Delta T + \alpha_2\Delta T^2 + ...]$$

where $\pi'_{\alpha\beta}$ $(\alpha, \beta = 1, 2,..., 6)$ are the off-axis temperature dependent piezoresistive

coefficients. α_1, α_2, … are the temperature coefficients of resistance, and $\Delta T = T_m - T_{ref}$

is the difference between the measurement temperature and reference temperature, and l',

m', and n' are the direction cosines of the conductor orientation with respect to the x'_1,

x'_2, and x'_3 axes, respectively. Equation (3.1) assumes that geometric changes are neglected.

When the primed axes are aligned with the unprimed (crystallographic) axes, Eq.

(3.1) reduces to

$$\frac{\Delta R}{R} = [\pi_{11}\sigma_{11} + \pi_{12}(\sigma_{22} + \sigma_{33})]\cos^2\phi + [\pi_{11}\sigma_{22} + \pi_{12}(\sigma_{11} + \sigma_{33})]\sin^2\phi$$

$$\text{Eq. (3.2)}$$

$$+ \pi_{44}\sigma_{12}\ \sin 2\phi + [\alpha_1\Delta T + \alpha_2\Delta T^2 + ...]$$

where ϕ is the angle between the x_1-axis and resistor orientation.

For an arbitrarily oriented in-plane resistor, the resistance change equation can be

obtained by using Eq. (3.1).

21

3.1 Resistance Change Equations for the (001) Silicon Wafer Planes

A general (001) silicon wafer is shown in Fig. 3.2.
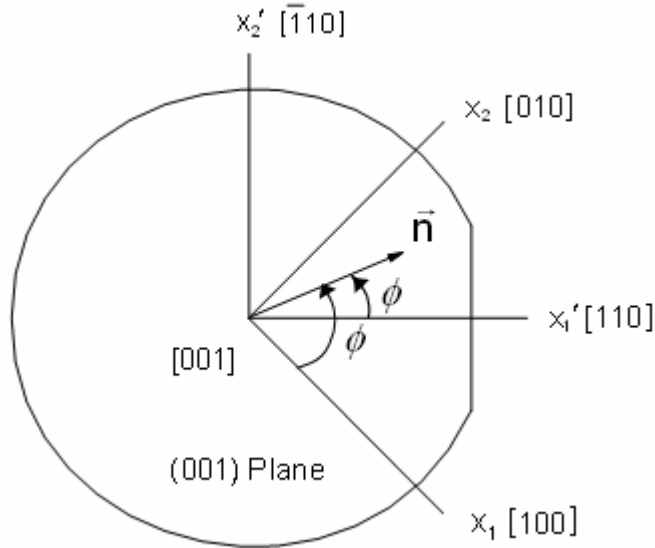
Fig. 3.2 - General (001) silicon wafer

A convenient wafer coordinate system may be used where the primed axes $x_1^{'}$, $x_2^{'}$ are chosen to be parallel and perpendicular to the primary wafer flat. The $x_3^{'}$-axis is then be perpendicular to the wafer plane--that is, $x_1^{'} = [110]$, $x_2^{'} = [\bar{1}10]$, and $x_3^{'} = [001]$. For the unprimed and primed coordinate systems shown in Fig. 3.2, the appropriate direction cosines for the primed axes are shown as follows:

$$[a_{ij}] = \begin{bmatrix} \dfrac{1}{\sqrt{2}} & \dfrac{1}{\sqrt{2}} & 0 \\[2mm] -\dfrac{1}{\sqrt{2}} & \dfrac{1}{\sqrt{2}} & 0 \\[2mm] 0 & 0 & 1 \end{bmatrix} \qquad \text{Eq. (3.1.1)}$$

Substitution of the off-axis piezoresistive coefficients into Eq. (3.1) yields the general expression for the resistance of a resistor which is oriented at an angle ϕ with respect to the $x_1' = [110]$ axis on the (001) surface of a silicon wafer as follows [12-13, 15, 17, 27, 29, 35, 39, 49-50, 72, 92, 99, 105]:

$$\frac{\Delta R}{R} = \left[\left(\frac{\pi_{11} + \pi_{12} + \pi_{44}}{2} \right) \sigma_{11}' + \left(\frac{\pi_{11} + \pi_{12} - \pi_{44}}{2} \right) \sigma_{22}' \right] \cos^2 \phi$$

$$+ \left[\left(\frac{\pi_{11} + \pi_{12} - \pi_{44}}{2} \right) \sigma_{11}' + \left(\frac{\pi_{11} + \pi_{12} + \pi_{44}}{2} \right) \sigma_{22}' \right] \sin^2 \phi \qquad \text{Eq. (3.1.2)}$$

$$+ \ \pi_{12}\sigma_{33} + (\pi_{11} - \pi_{12})\sigma_{12}' \ \sin 2\phi + + [\alpha_1 \Delta T + \alpha_2 \Delta T^2 + ...]$$

where

$$l' = \cos\phi, \quad m' = \sin\phi, \ \text{and} \ n' = 0 \qquad \text{Eq. (3.1.3)}$$

has been introduced. Equation (3.1.2) indicates that the out-of-plane shear stresses σ_{13}' and σ_{23}' do not influence the resistances of stress sensors fabricated on (001) wafers. This means that a sensor rosette on (001) silicon may at best measure four of the six unique components of the stress tensor. All three of the unique piezoresistive coefficients for silicon (π_{11}, π_{12}, and π_{44}) appear in Eq. (3.1.2).

3.2   Resistance Change Equations for the (111) Silicon Wafer Planes

The other common silicon crystal orientation used in semiconductor fabrication is the (111) surface. A general (111) silicon wafer is shown in Fig. 3.3.
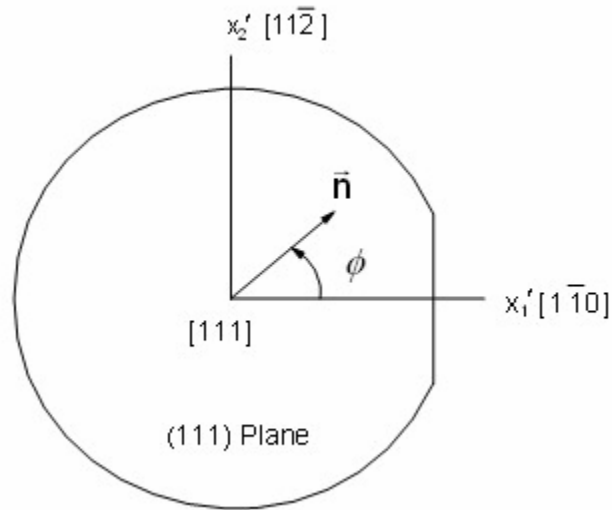
Fig. 3.3 - General (111) silicon wafer

The surface of the wafer is a (111) plane--that is, the [111] direction is normal to the wafer plane. Since the principal crystallographic axes $x_1 = [100]$, $x_2 = [010]$, and $x_3 = [001]$ do not lie in the wafer plane, they have not been indicated. As mentioned previously, it is convenient to work in an off-axis primed wafer coordinate system where the axes $x_1^{'}$ and $x_2^{'}$ are parallel and perpendicular to the primary wafer flat. If Eq. (3.1) is used, the resistance change of an arbitrarily oriented in-plane sensor may be expressed in terms of the stress components derived in this natural wafer coordinate system. For the primed

24

coordinate system indicated in Fig. 3.3, the appropriate direction cosines for the primed axes are as follows:

$$[a_{ij}] = \begin{bmatrix} -\dfrac{1}{\sqrt{2}} & \dfrac{1}{\sqrt{2}} & 0 \\ -\dfrac{1}{\sqrt{6}} & -\dfrac{1}{\sqrt{6}} & \dfrac{2}{\sqrt{6}} \\ \dfrac{1}{\sqrt{3}} & \dfrac{1}{\sqrt{3}} & \dfrac{1}{\sqrt{3}} \end{bmatrix} \qquad \text{Eq. (3.2.1)}$$

The general expression for the normalized change in resistance of a resistor that is oriented at an angle of ϕ with respect to the $x_1^{'} = [1\bar{1}0]$ axis on the (111) surface of a silicon wafer is given by [15, 35, 49-50, 72, 92, 99, 105]:

$$\frac{\Delta R}{R} = [B_1\sigma_{11}^{'} + B_2\sigma_{22}^{'} + B_3\sigma_{33}^{'} - 2\sqrt{2}(B_2 - B_3)\sigma_{23}^{'}]\cos^2\phi$$
$$+ [B_2\sigma_{11}^{'} + B_1\sigma_{22}^{'} + B_3\sigma_{33}^{'} + 2\sqrt{2}(B_2 - B_3)\sigma_{23}^{'}]\sin^2\phi \qquad \text{Eq. (3.2.2)}$$
$$+ [2\sqrt{2}(B_3 - B_2)\sigma_{13}^{'} + (B_1 - B_2)\sigma_{12}^{'}]\sin 2\phi + [\alpha_1\Delta T + \alpha_2\Delta T^2 + \ldots]$$

where ϕ is again the angle between the $x_1^{'}$-axis and the resistor orientation. The coefficients

$$B_1 = \frac{\pi_{11} + \pi_{12} + \pi_{44}}{2}, \quad B_2 = \frac{\pi_{11} + 5\pi_{12} - \pi_{44}}{6}, \quad B_3 = \frac{\pi_{11} + 2\pi_{12} - \pi_{44}}{3}$$

are a set of linearly independent temperature-dependent combined piezoresistive parameters. These parameters must be calibrated before stress component values may be extracted from resistance change measurements. It is noteworthy that the general resistance change expression in Eq. (3.2.2) is dependent on all six of the unique stress components.

Therefore, the potential exists for developing a sensor rosette which may measure the complete three-dimensional states of stress at points on the surface of a die.

Theoretical analysis has established that properly designed sensor rosettes on the (111) silicon wafer plane have several advantages relative to sensors fabricated using the standard (001) silicon. In particular, optimized sensors on the (111) silicon may be used to measure the complete state of stress (six stress components) at a point on the top surface of the die, while optimized rosettes on the (001) silicon measure, at most, four stress components [26]. The additional stress components that may be measured are the out-of-plane (interfacial) shear stresses. Knowledge of these shear stresses may be important for determining the integrity of die interfaces or for the detection of interface delamination [99]. Further, optimized sensors on the (111) silicon offer the unique capability of measuring four temperature compensated combined stress components, whereas those on the (001) silicon may only be used to measure two temperature compensated quantities. In our discussion, "temperature-compensated" refers to the ability to extract the stress components directly from the resistance change measurements (without the need to know the temperature change ΔT). This is a particularly important attribute, given the large thermally induced errors that often may be found in stress sensor data. The four stress components that may be measured in a temperature compensated manner using the (111) silicon sensors are the three shear stress components and the difference of the in-plane normal stress components.

CHAPTER 4

CALIBRATION OF SENSORS ON THE (111) SURFACE

In this work, the (001) and (111) silicon test chips containing an array of optimized piezoresistive stress sensor rosettes have been successfully applied. Calibrated and characterized stress test chips are assembled into chip-on-beam specimens. The resistances of the sensors are then recorded. The stresses on the die surface are calculated using the measured resistance changes and the appropriate theoretical equations. For comparison purpose, two-dimensional linear finite element simulations are also performed.

Three sets of test chip experiments are performed in this work. In the first set of experiments, 200 x 200 mil JSE WB100C test chips fabricated on the (111) silicon [99, 105] are utilized to characterize the tensile die stresses on chip-on-beam specimens. These test chips will be described in more detail later. The JSE WB 100C chip contains wire bonding pads on the perimeter of the die. With this design, the wire-bonding is used to provide electrical connection between the chip and PC board. In addition, soldering is used for electrical connection between the outer pads on the board and external instrumentation through wires. In the second set of experiments, test strips fabricated on the (001) silicon are used to measure die stresses.

4.1   Experimental Setup

The general procedures of resistance measurements with the JSE-WB100C test chips are now discussed.

The equipment we utilized in the experimental procedure included:

- Semiconductor Parametric Analyzer 4155C

The 4155C is an electronic instrument for measuring and analyzing the characteristics of semiconductor devices. This instrument has four highly accurate source/monitor units (SMUs), two voltage source units (VSUs). It has high resolution enough for voltage/current measurement. In this work, sweeping voltage and measurement of voltage/current through the resistor sensors is performed by using this instrument. When measuring the sensor resistances on the test chip, the 4155C is used to provide bias in the circuit, and to provide voltage to the measured resistors. In this work, the voltage across the resistor is swept from 0.6V to 1.0V in 20mV steps. For an n-substrate and p-well, the voltage is set to be 1V and -1V, respectively. This is for electrical isolation between the doped surface resistor and the bulk of the chip by using proper reverse biasing of the resistor and substrate regions. Measurement results are saved to a 3.5 inch diskette.

- Environmental Test Chamber (Delta Design 2850)

This environmental chamber is capable of temperatures from -155 to +300$^{\mathrm{o}}$C with a 0.1$^{\mathrm{o}}$C resolution. The temperature in the experiments reported here is typically swept over a large range from a low temperature (as low as -150 $^{\mathrm{o}}$C) to a high temperature (as high as 100 $^{\mathrm{o}}$C). For low temperatures, a liquid-nitrogen (LN$_2$) tank is hooked up with this chamber. A special four-point bending apparatus was constructed and integrated into

28

this environmental chamber. The increment of the temperature between sensor readings is usually set to be 25 or 50 ^{o}C, and the temperature at each step is maintained for at least 10 minutes before measurements are taken to ensure a uniform temperature distribution on the silicon chip.

- Digital Panel Mount Meter (DPM-3)

The DPM-3 panel instrument is a versatile, cost effective solution to a wide variety of monitoring and control application. This instrument is easily set to produce an accurate display of weight or load. Digital calibration of all ranges eliminates drift associated with potentiometers found in non-microcomputer-based meters. In addition, the fast read rate provides an accurate display of input and quick response in applications. During loading in a four-point bending fixture, the precise reading of applied load is essential. This instrument is used to determine the exact load on the chip-on-beam specimens.

- Four-Point Bending Apparatus

A special four-point bending (4PB) apparatus has been constructed and integrated into the Delta Design environmental chamber. Details will be discussed in a later section.

- Accessories

For TCR measurements and hydrostatic tests, a pair of edge connectors are used to contact to the outer pads on the board. Those are needed to provide electrical connections between the chip and external instrumentation.

4.1.1 Four-Point Bending Apparatus

In the four-point bending method, a rectangular strip containing a row of chips is cut from a wafer and is loaded in a four-point bending fixture to generate a uniaxial stress state. A general four-point bending loading fixture is shown in Fig. 4.1. Using the free diagram and its corresponding 3 equations ($\sum F_x = 0, \sum F_y = 0,$ and $\sum M = 0$), the normal stress σ_{11} induced at points on the top surface of the strip that are between the bottom supports is given by

$$\sigma = \frac{3F(L-D)}{bh^2}$$
Eq. (4.1.1)

where

$b \equiv$ width of beam

$h \equiv$ thickness of beam

$L \equiv$ distance between two top supports

$D \equiv$ distance between two bottom supports
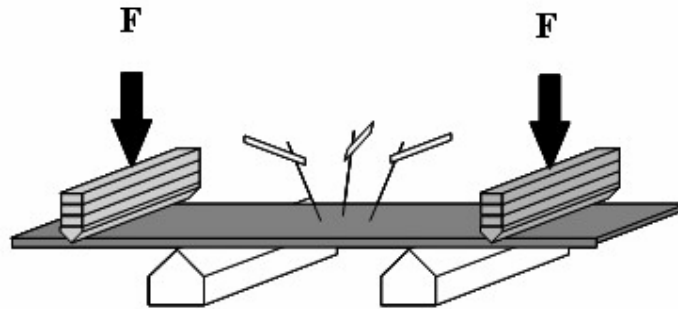
Fig. 4.1 - Four-point bending loading fixture

The details about parts of four-point bending fixture are given in Fig. 4.2. The silicon strip is loaded on bottom supports. By controlling the micrometer, uniaxial stress

can be generated. F can be calculated from the output of the load-cell. A special four-point bending apparatus is constructed and integrated into the environmental chamber as shown in Fig. 4.3. Through a ceramic rod penetrating the bottom side of the oven, force generated by a vertical translation stage is applied to the strip in the four-point bending fixture inside the chamber (see Fig. 4.4).
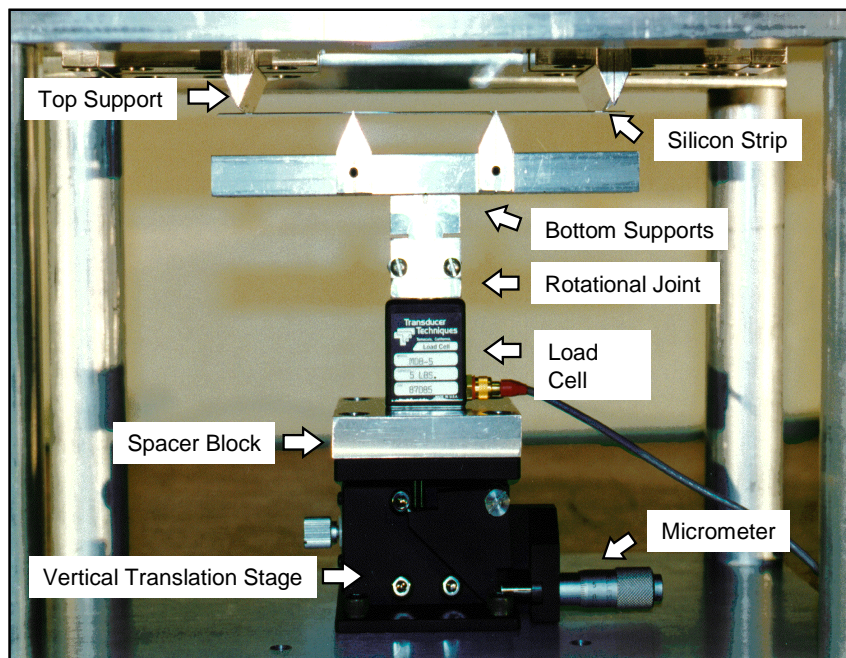
Fig. 4.2 - The details about the parts of the four-point bending fixture
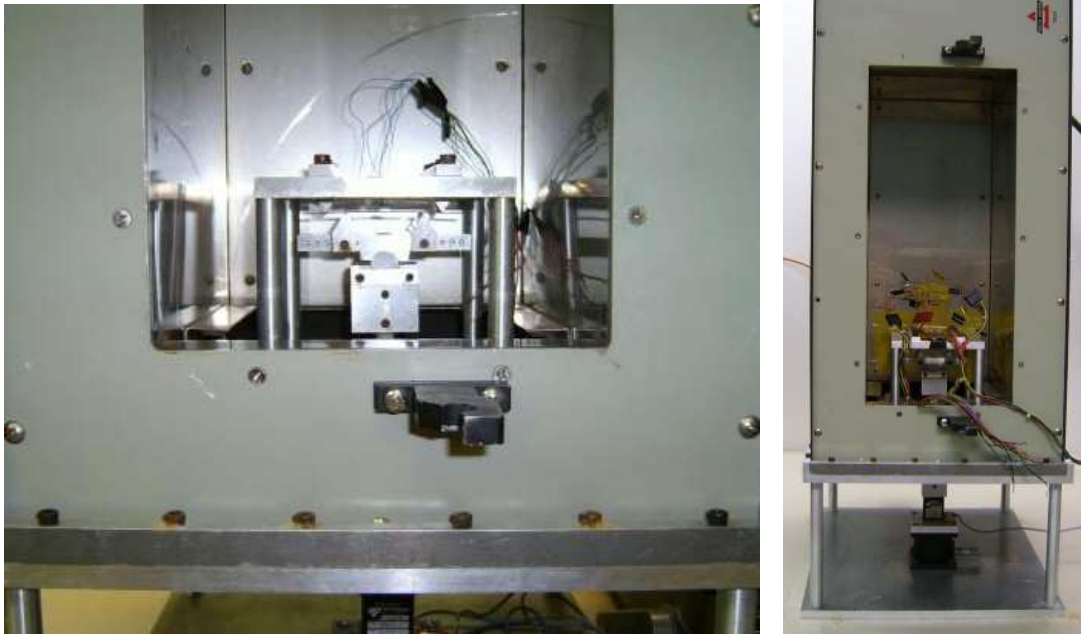
Fig. 4.3 – A four-point bending fixture mounted inside the oven
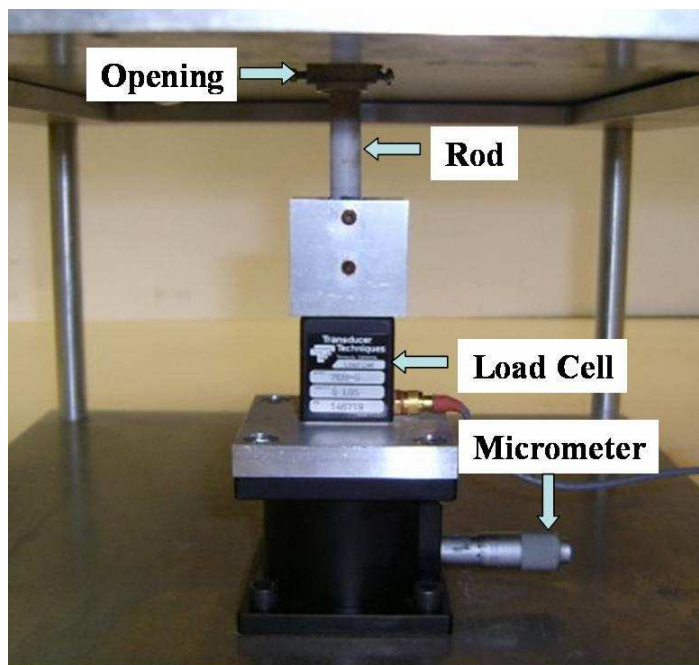
Fig. 4.4 - A four-point bending fixture: Exterior of the oven

Four-point bending calibration produces a well-defined uniaxial stress state. Like any other calibration techniques, the four-point bending method has its limitations. For example, it necessitates cutting the wafer containing the fabricated test chips into strips. Each of these strips must then be individually loaded, making the calibration process tedious. Also, only sensor rosettes in the middle of each strip can typically be calibrated. If a wafer strip along the x_1' direction is subjected to four point bending and a known uniaxial stress $\sigma_{11}' = \sigma$ is applied in the x_1'-direction, the 0° and 90° oriented sensors yield the following resistance changes:

- (001) plane: with respect to the unprimed axes

$$\frac{\Delta R}{R} = [\pi_{11}\sigma_{11} + \pi_{12}(\sigma_{22} + \sigma_{33})]\cos^2 \phi + [\pi_{11}\sigma_{22} + \pi_{12}(\sigma_{11} + \sigma_{33})]\sin^2 \phi$$

Eq. (4.1.2)

$$+ \pi_{44}\sigma_{12} \sin 2\phi + [\alpha_1 \Delta T + \alpha_2 \Delta T^2 + ...]$$

where ϕ is the angle between the x_1' axis and the resistor orientation. For the 0-90° oriented sensors,

$$\frac{\Delta R_0}{R_0} = \pi_{11}\sigma_{11} \quad \text{and} \quad \frac{\Delta R_{90}}{R_{90}} = \pi_{12}\sigma_{11} \qquad \text{Eq. (4.1.3)}$$

- (001) plane: with respect to the primed axes

$$\frac{\Delta R}{R} = \left[\left(\frac{\pi_{11} + \pi_{12} + \pi_{44}}{2} \right) \sigma_{11}' + \left(\frac{\pi_{11} + \pi_{12} - \pi_{44}}{2} \right) \sigma_{22}' \right] \cos^2 \phi$$

$$+ \left[\left(\frac{\pi_{11} + \pi_{12} - \pi_{44}}{2} \right) \sigma_{11}' + \left(\frac{\pi_{11} + \pi_{12} + \pi_{44}}{2} \right) \sigma_{22}' \right] \sin^2 \phi \qquad \text{Eq. (4.1.4)}$$

$$+ \pi_{12} \sigma_{33}' + (\pi_{11} - \pi_{12}) \sigma_{12}' \sin 2\phi + [\alpha_1 \Delta T + \alpha_2 \Delta T^2 + ...]$$

For the 0° and 90° oriented sensors,

$$\frac{\Delta R_0}{R_0} = (\frac{\pi_{11} + \pi_{12} + \pi_{44}}{2}) \sigma_{11}' \qquad \text{Eq. (4.1.5)}$$

$$\frac{\Delta R_{90}}{R_{90}} = (\frac{\pi_{11} + \pi_{12} - \pi_{44}}{2}) \sigma_{11}' \qquad \text{Eq. (4.1.6)}$$

- (111) plane: the primed axes

$$\frac{\Delta R}{R} = [B_1 \sigma_{11}' + B_2 \sigma_{22}' + B_3 \sigma_{33}' - 2\sqrt{2}(B_2 - B_3)\sigma_{23}'] \cos^2 \phi$$

$$+ [B_2 \sigma_{11}' + B_1 \sigma_{22}' + B_3 \sigma_{33}' + 2\sqrt{2}(B_2 - B_3)\sigma_{23}'] \sin^2 \phi \qquad \text{Eq. (4.1.7)}$$

$$+ [2\sqrt{2}(B_3 - B_2)\sigma_{13}' + (B_1 - B_2)\sigma_{12}'] \sin 2\phi + [\alpha_1 \Delta T + \alpha_2 \Delta T^2 + \ldots]$$

For the 0° and 90° oriented sensors,

$$\frac{\Delta R_0}{R_0} = B_1 \sigma_{11}' \quad \text{and} \quad \frac{\Delta R_{90}}{R_{90}} = B_2 \sigma_{11}' \qquad \text{Eq. (4.1.8)}$$

4.1.2 The (111) Silicon Test Chips

When piezoresistive sensors are used in experimental stress analysis studies of microelectronic packages, special test chips are typically designed and fabricated. The test chip contains an array of the optimized eight-element dual polarity measurement rosettes. Due to the piezoresistive effect, the stresses in the chip yield measurable changes in the sensor resistance. The doped active region of a piezoresistive sensor is a serpentine pattern in order to achieve acceptable resistance for measurement. Figure 4.5(a) shows the basic die image of JSE-WB100C resistor test chip on the (111) silicon plane. In the chip-on-beam case, the sensors are located in the top surface of the die, a free surface, and the sensor elements used here are the horizontal and vertical (0 and 90°) sensor elements from the eight-element rosette. A microphotograph of an eight-element sensor rosette is shown in Fig. 4.5(b) [92].

The die then is attached to the specially designed printed wiring board (PWB) with die-attached material (ME525). For the test, an FR-406 PWB is designed using Lavenir software as shown in Fig. 4.6. The (111) silicon test chip (JSE WB100C) is attached to the center of the PWB.
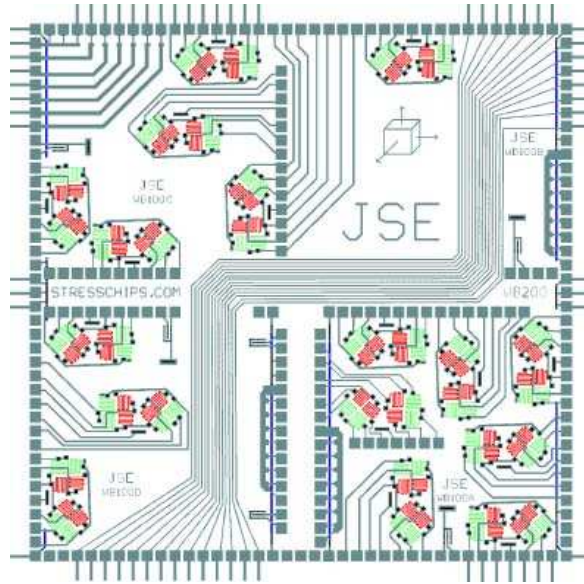
Fig. 4.5(a) - The (111) silicon test chip (JSE-WB100C)
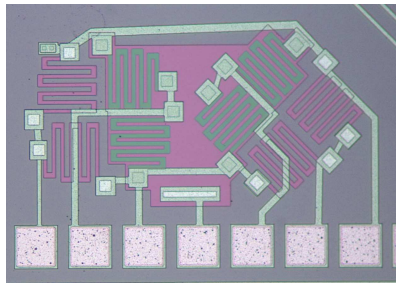
Fig. 4.5(b) - Microphotograph of eight-element sensor rosette
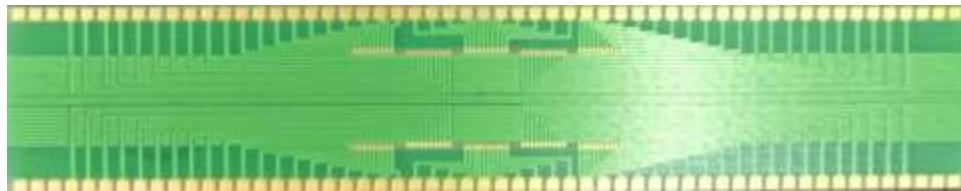
Fig. 4.6 - A specially designed printed wiring board

36

During the experiments, a chip-on-beam is placed on the bottom supports of the four-point bending fixture. For electrical connection between chip and board, wire-bonding is made between the inner pads on the board and the pads on the silicon chip as shown in Fig. 4.7, where only the central part of a chip-on-beam structure is shown and enlarged. The inner and outer pads on the boards are electrically connected and protected by a solder mask. In addition, the outer pads on the board are electrically connected to external instruments through wires by soldering. The picture of a wire-bonded chip-on-beam structure is shown in Fig.4.8.
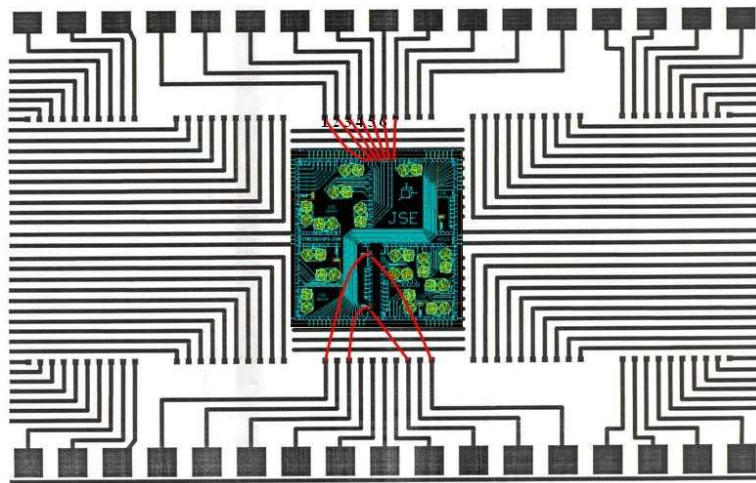
Fig. 4.7- A wire-bonded chip-on-beam structure (central part)
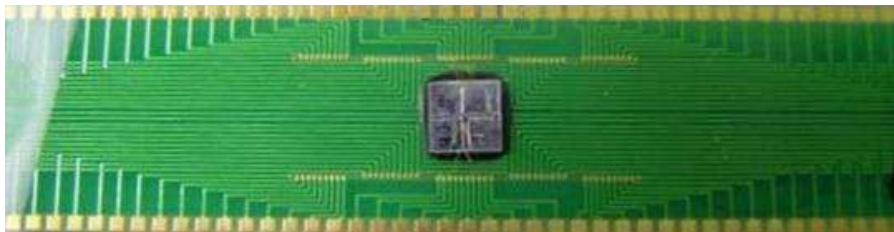
Fig. 4.8 - A wire-bonded chip-on-beam structure

The dimensions of the board material (FR-406), (111) silicon chip, and adhesive material (ME525) are measured with a resolution of 0.05mil. In Table 4.1 the dimensions of composite materials of chip-on-beam samples are presented. Following are the average values of 10 specimens:

Table 4.1 - Dimensions of composite materials (Unit: mil)			
	board material	(111) silicon	adhesive material
length (l)	3400	200	200
width(b)	650	200	200
thickness(h)	22.67	25	1.60

4.2   Sensor Calibration for the (111) Silicon Test Chips

The eight sensors are configured as a parallel connection of four two-element half-bridges in order to simplify the measurements. The n-substrate is maintained as 1 V, and a bias of -1 V is applied to the p-well for electrical isolation between the bulk of the chip and the doped surface resistor whose voltage is swept from 0.6 V to 1.0 V during measurements.

The Four-point bending apparatus is used to generate the required stress. Since the cross section of the chip-on-beam structure is three-dimensional at the die site, two-dimensional states of stress are induced. Thus Eq. (4.1.1) for the calculation of uniaxial stress is not applicable to this case. Hence, all the calibrations are performed with respect to applied F. The following expression is for the stress-induced resistance changes for the (111) silicon:

38

$$\frac{\Delta R}{R} = [B_1\sigma'_{11} + B_2\sigma'_{22} + B_3\sigma'_{33} - 2\sqrt{2}\,(B_2\text{-}B_3)\sigma'_{23}]\cos^2\phi$$

$$+[B_2\sigma'_{11} + B_1\sigma'_{22} + B_3\sigma'_{33} + 2\sqrt{2}(B_2\text{-}B_3)\sigma'_{23}]\sin^2\phi$$

$$\text{Eq. (4.2.1)}$$

$$+[2\sqrt{2}(B_3\text{-}B_2)\sigma'_{13} + (B_1\text{-}B_2)\sigma'_{12}]\sin 2\phi$$

$$+[\alpha_1\Delta T + \alpha_2\Delta T^2 + ...]$$

In the process, we consider two-dimensional states of stress (σ'_{11} and σ'_{22}) and defined temperature terms $[\alpha_1\,\Delta T + \alpha_2\,\Delta T^2 + ...]$ as $f\,(\Delta T)$ in Eq. (4.2.1). The result is that Eq. (4.2.1) simplifies to

$$\frac{\Delta R_0}{R_0} = B_1\sigma'_{11} + B_2\sigma'_{22} + f(\Delta T) \qquad\qquad \text{Eq. (4.2.2)}$$

$$\frac{\Delta R_{90}}{R_{90}} = B_2\sigma'_{11} + B_1\sigma'_{22} + f(\Delta T) \qquad\qquad \text{Eq. (4.2.3)}$$

We also adopt the following notations:

$$\sigma'_{11} \equiv \sigma'_{11F}F, \quad \sigma'_{22} \equiv \sigma'_{22F}F$$

$$S_\phi \equiv \frac{d}{dF}(\frac{\Delta R_\phi}{R_\phi}) \qquad\qquad \text{Eq. (4.2.4)}$$

Assuming $f(\Delta T) = 0$ in Eqs. (4.2.2) and Eq. (4.2.3) and using the notations above yield the following results:

$$S_0 = B_1\sigma'_{11F} + B_2\sigma'_{22F} \qquad\qquad \text{Eq. (4.2.5)}$$

$$S_{90} = B_2\sigma'_{11F} + B_1\sigma'_{22F} \qquad\qquad \text{Eq. (4.2.6)}$$

Solving for B_1 and B_2 in Eqs. (4.2.5) and (4.2.6) yield the results below:

$$B_1 = \frac{\sigma'_{22F}S_{90} - \sigma'_{11F}S_0}{(\sigma'_{22F})^2 - (\sigma'_{11F})^2} \qquad \text{Eq. (4.2.7)}$$

$$B_2 = \frac{\sigma'_{22F}S_0 - \sigma'_{11F}S_{90}}{(\sigma'_{22F})^2 - (\sigma'_{11F})^2} \qquad \text{Eq. (4.2.8)}$$

Measurements of S_0 and S_{90} of the (111) silicon are performed over varying temperatures. Typical results of S_0 and S_{90} of the (111) silicon for each temperature are displayed in Appendix A. The average values for each temperature are presented in Table 4.2 which reflects the average values of 10 specimens.

Table 4.2 - S_0 and S_{90} versus temperature (Unit: N^{-1})				
T(Celsius)	S_0^p	S_{90}^p	S_0^n	S_{90}^n
-133.4	-2.46E-03	5.00E-03	1.34E-03	-1.52E-03
-93.2	-2.23E-03	4.55E-03	1.29E-03	-1.46E-03
-48.2	-2.05E-03	3.83E-03	1.17E-03	-1.42E-03
-23.6	-1.96E-03	3.63E-03	1.11E-03	-1.36E-03
0.6	-1.87E-03	3.43E-03	1.06E-03	-1.31E-03
25.1	-1.77E-03	3.20E-03	1.04E-03	-1.26E-03
49.9	-1.58E-03	2.83E-03	9.50E-04	-1.12E-03
75.1	-1.40E-03	2.51E-03	8.79E-04	-1.03E-03
100.6	-1.32E-03	2.30E-03	8.13E-04	-9.66E-04

Subtraction of Eq. (4.2.6) from Eq. (4.2.5) leads to

$$S_0 - S_{90} = (B_2 - B_1)(\sigma'_{22F} - \sigma'_{11F}) \qquad \text{Eq. (4.2.9)}$$

We analyze $\dfrac{R_{90}}{R_0}$ in terms of F. In the process, we define A as the slope of $\dfrac{R_{90}}{R_0}$

with respect to F, $\dfrac{R_{90}}{R_0}$ can be expressed as

$$\frac{R_{90}(\sigma,\Delta T)}{R_0(\sigma,\Delta T)} = AF + \frac{R_{90}(0,0)}{R_0(0,0)} \qquad \text{Eq. (4.2.10)}$$

Assuming $f(\Delta T) = 0$ leads to

$$\frac{R_{90}(0,0)}{R_0(0,0)}\left[\frac{1+B_2\sigma_{11}'+B_1\sigma_{22}'}{1+B_1\sigma_{11}'+B_2\sigma_{22}'}\right] = AF + \frac{R_{90}(0,0)}{R_0(0,0)} \qquad \text{Eq. (4.2.11)}$$

Then we let $\dfrac{R_{90}(0,0)}{R_0(0,0)} \equiv C$ with the following result:

$$C\left[\frac{1+B_2\sigma_{11}'+B_1\sigma_{22}'}{1+B_1\sigma_{11}'+B_2\sigma_{22}'}\right] = AF + C \qquad \text{Eq. (4.2.12)}$$

Assuming $B_1\sigma \ll 1$ and $B_2\sigma \ll 1$, the result becomes:

$$C(1-B_1\sigma_{11}'-B_2\sigma_{22}'+B_2\sigma_{11}'+B_1\sigma_{22}') = AF + C$$

$$\text{Eq. (4.2.13)}$$

$$(B_1-B_2)(\sigma_{22}'-\sigma_{11}') = \frac{AF}{C}$$

$C \cong 1$ for both p- and n-type yields

$$(B_1-B_2)(\sigma_{22}'-\sigma_{11}') \cong AF \qquad \text{Eq. (4.2.14)}$$

Re-using the notation, $\sigma_{11}' \equiv \sigma_{11F}'F$ and $\sigma_{22}' \equiv \sigma_{22F}'F,$ we arrive at the result below:

$$A \cong (B_1-B_2)(\sigma_{22F}'-\sigma_{11F}') \qquad \text{Eq. (4.2.15)}$$

Comparing Eq. (4.2.9) and Eq. (4.2.15) yields

$$S_0(F)-S_{90}(F) \cong -A \qquad \text{Eq. (4.2.16)}$$

41

By performing extensive measurements over temperatures, we determined the validity of Eq. (4.2.16) as shown in Table 4.3.

T(Celsius)	$S_0^p - S_{90}^p$	A(slope_p)	$S_0^n - S_{90}^n$	A(slope_n)
-133.4	-7.45E-03	7.54E-03	2.85E-03	-2.57E-03
-93.2	-6.78E-03	6.75E-03	2.74E-03	-2.53E-03
-48.2	-5.88E-03	6.07E-03	2.59E-03	-2.45E-03
-23.6	-5.59E-03	5.71E-03	2.47E-03	-2.41E-03
0.6	-5.31E-03	5.23E-03	2.37E-03	-2.35E-03
25.1	-4.97E-03	4.76E-03	2.30E-03	-2.26E-03
49.9	-4.42E-03	4.32E-03	2.07E-03	-2.11E-04
75.1	-3.91E-03	3.93E-03	1.91E-03	-2.01E-03
100.6	-3.61E-03	3.63E-03	1.78E-03	-1.98E-03

Table 4.3 - Comparison between S_0-S_{90} and A (= slope of R_{90}/R_0 versus F) by measurements

By Table 4.3, it can be summarized that Eq. (4.2.16) is valid over the temperature range of -150 to 100 ^{o}C.

4.3   Simulation Results for the (111) Silicon Test Chips

Finite element simulations are used to determine the actual states of stress in the silicon chip. The finite element model predictions are used to approximate trends of the various stress component distributions, so that the experimental data could be better understood. In our simulations, σ'_{11} and σ'_{22} at the site of sensor are obtained when F = 1N is applied to both sides. Mesh plots of chip-on-beam are shown in Fig. 4.9.

In the finite element models, the materials are modeled as linear elastic. Temperature dependent elastic modulus E is displayed in Table 4.4. Poisson's ratio ν of ME525, (111) silicon and FR-406 are assumed to be 0.3, 0.262, and 0.117, respectively [97]. Solder is neglected to simplify the analysis in the finite element models.

Table 4.4 - Elastic modulus of composite materials versus temperature (Unit: GPa)			
T (Celsius)	ME525	(111) silicon	FR-406
-151.0	19.81	173.5	28.82
-133.4	18.46	172.9	27.41
-93.2	15.99	172.3	25.57
-48.2	13.70	170.9	25.12
-23.6	12.85	170.2	24.80
0.6	12.00	169.5	24.68
25.1	10.43	169.1	23.73
49.9	9.85	168.5	22.05
75.1	8.75	167.9	20.26
100.6	7.72	167.0	18.55
125.9	4.98	166.6	16.37
151.5	0.98	165.5	14.87

The silicon chip is meshed into 24 x 24 x 3 elements as shown in Fig. 4.10. The relative size and location of the sensors are presented in Fig. 4.11. The location of the sensor corresponds to the node (#49788). It also should be mentioned that the size of 4 combined resistor sensors is 1.2 times larger than that of one element on the mesh plot. In order to load a uniform force on the line in chip-on-beam structure (see Fig. 4.9), the width between two nodes is kept constant. From Table 4.1, the ratio of silicon chip to board is 200:650 in width. Hence the board should be 78-element width.
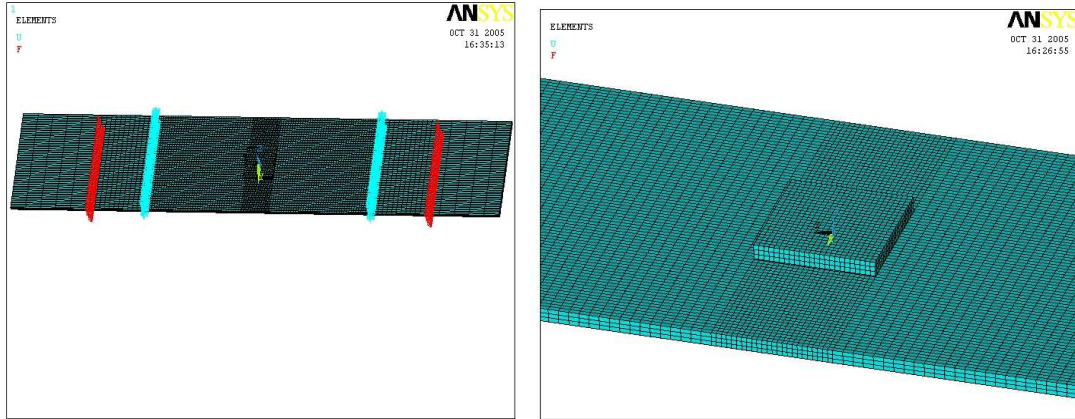
Fig. 4.9 - Mesh plot of chip-on-beam structure
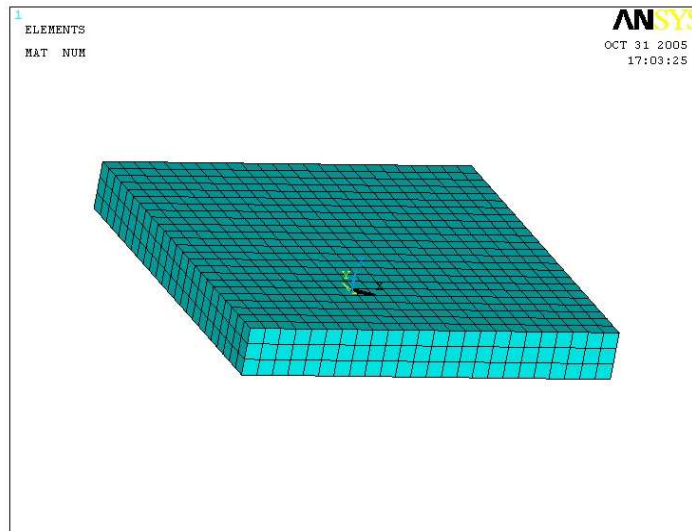
Fig. 4.10 - Mesh plot of silicon chip

Fig. 4.11 - The relative size and location of the sensor on the mesh plot

In Fig. 4.12 and Fig. 4.13, the contour plots of σ'_{11} and σ'_{22} in the silicon chip are presented. The colors of contour represent the stress value at the rosette site.
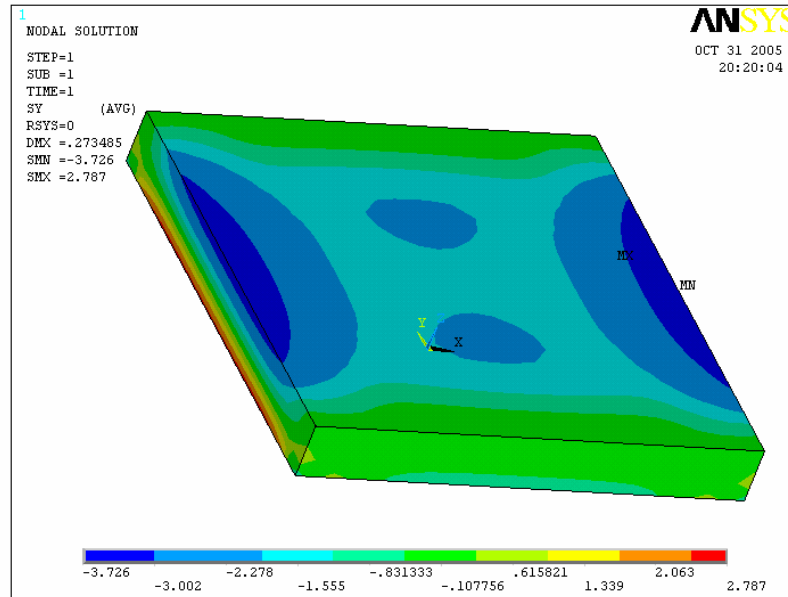
Fig. 4.12 - Contour plot of σ'_{11} at 25°C
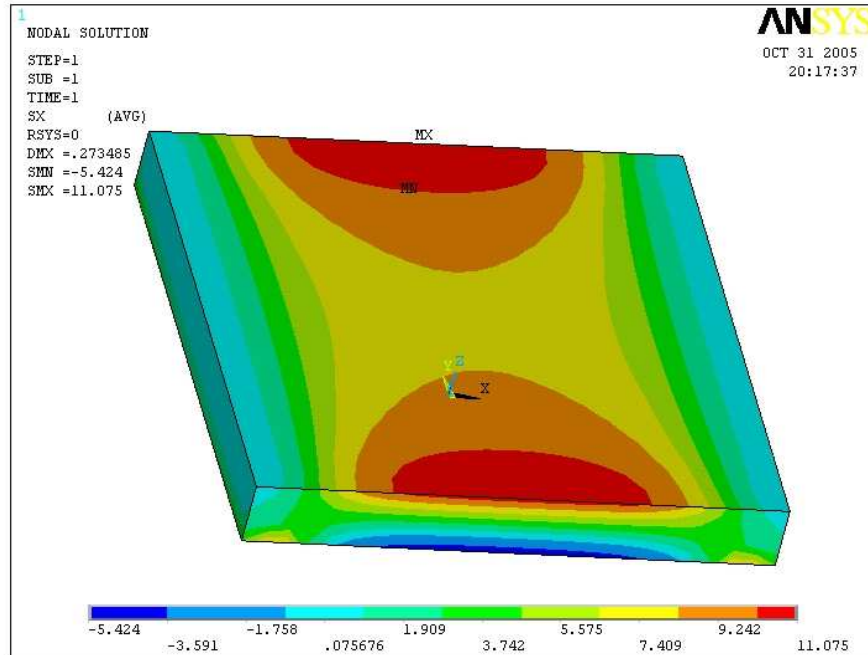
Fig. 4.13 - Contour plot of σ'_{22} at $25^{o}C$

It is to be emphasized that the direction of σ'_{22} is parallel to the direction of the beam in our case. At room temperature, σ'_{11} and σ'_{22} at the sensor location appear in Table 4.5 where the other 8 nodes surrounding node #49788 are presented as well. The comparison of the average of 9 nodes (node #49788 and 8 surrounding nodes) with the value at node #49788 proved the two to be very close, as expected. For further measurements, the value at node #49788 is chosen.

Similar tests are also performed on the same resistor sensors over the temperature range of -150 ^{o}C to 100 ^{o}C. It is observed that σ'_{11} and σ'_{22} at sensor location increases in magnitude with increasing temperatures even though contour plots for different temperature looks similar. This phenomenon is due to the uneven change in mechanical property such as E with temperature among silicon, die attachment adhesive (ME 525),

46

and PCB material (FR-406). In Table 4.6, σ'_{11} and σ'_{22} at sensor location (assuming node #49788) appear.

In our simulations, Poisson's ration ν of ME 525, (111) silicon and FR-406 are assumed to be 0.3, 0.262 and 0.117, respectively [97].

Table 4.5 - Simulation results of stresses around the sensor location at 25 $^{\mathrm{o}}$C (Unit: MPa)						
node #	σ'_{22}	σ'_{11}	σ'_{33}	σ'_{12}	σ'_{23}	σ'_{13}
49787	7.976	-1.866	-6.131E-03	-6.015E-02	7.003E-03	1.711E-02
49788	**8.051**	**-1.883**	**-5.649E-03**	**-1.211E-01**	**1.474E-02**	**1.727E-02**
49789	8.1792	-1.907	-4.433E-03	-1.832E-01	2.437E-02	1.758E-02
49798	7.843	-1.848	-8.494E-03	-8.816E-02	6.940E-03	2.963E-02
49799	7.916	-1.868	-8.080E-03	-1.777E-01	1.461E-02	2.991E-02
49800	8.041	-1.883	-6.997E-03	-2.694E-01	2.417E-02	3.045E-02
49776	8.052	-1.879	-5.195E-03	-3.048E-02	7.028E-03	7.942E-03
49777	8.129	-1.898	-4.670E-03	-6.129E-02	1.479E-02	8.015E-03
49778	8.259	-1.926	-3.373E-03	-9.261E-02	2.443E-02	8.150E-03
Average	**8.050**	**-1.884**	**-5.891E-03**	**-1.205E-01**	**1.534E-02**	**1.845E-02**
170:center	8.052	-1.877	-5.099E-03	1.111E-10	2.243E-11	5.142E-11

Table 4.6 - σ'_{11} and σ'_{22} at the sensor location versus temperature (Unit: MPa)			
T (Celsius)	σ'_{22}	σ'_{11}	σ'_{22}-σ'_{11}
-151.0	7.608	-1.749	9.357
-133.4	7.690	-1.772	9.462
-93.2	7.795	-1.809	9.604
-48.2	7.886	-1.824	9.709
-23.6	7.937	-1.846	9.783
0.6	7.993	-1.869	9.863
25.1	8.051	-1.883	9.934
49.9	8.262	-1.945	10.207
75.1	8.515	-2.020	10.535
100.6	8.735	-2.089	10.824
125.9	8.932	-2.128	11.060

Assuming that the chip-on-beam structure is made of one material, finite element simulations have given σ'_{11} and σ'_{22} at sensor location at 25 °C (assuming node #49788) as shown in Table 4.7.

Table 4.7 - σ'_{11} and σ'_{22} at the sensor location at 25°C (Unit: MPa)			
Composite material	σ'_{22}	σ'_{11}	σ'_{22}-σ'_{11}
Silicon	4.538	-1.424	5.962
FR-406	4.442	-1.087	5.529

As the table shows, σ'_{11} and σ'_{22} at sensor location is about half compared with the real case. If we consider a strip without a silicon chip and adhesive material, only uniaxial stress is induced as reflected in the following:

$$\sigma = \frac{3F(L-D)}{bh^2}$$

Eq. (4.3.1)

where F = 1N, (L-D) = 2 x 10^{-2} m, b = 650 mil (1.651 x 10^{-2} m), and h = 22.67 mil (5.758 x 10^{-4} m). Substitution of these dimensions into the equation above yields σ'_{22} = 10.961 MPa.

4.4   Extraction of Piezoresistive Coefficients, B_1 and B_2

For a given fixed temperature, the piezoresistive coefficients can thus be evaluated by performing controlled experiments where the resistance changes of the resistor sensors are monitored as a function of applied force. Large errors can be induced in the measured resistance changes, and thus in the values of the extracted piezoresistive coefficients, if the temperature varies between measurements during experiments. Hence, much attention has

been given to minimize the errors in the resistance change by keeping a given fixed temperature for sufficient time duration. As seen in Section.4.2, using an individual-temperature reference, B_1 and B_2 are given by

$$B_1 = \frac{\sigma'_{22F}S_{90} - \sigma'_{11F}S_0}{(\sigma'_{22F})^2 - (\sigma'_{11F})^2}, \quad B_2 = \frac{\sigma'_{22F}S_0 - \sigma'_{11F}S_{90}}{(\sigma'_{22F})^2 - (\sigma'_{11F})^2} \qquad \text{Eq. (4.4.1)}$$

where S_0 and S_{90} of (111) silicon are determined by experiments performed over temperature, and σ'_{11F} and σ'_{22F} at sensor location are obtained by computer simulations. It is obvious that σ'_{11F} and σ'_{22F} for a 1-N force are σ'_{11} and σ'_{22}, respectively. Hence the piezoresistive coefficients B_1 and B_2 can be extracted. Using Table 4.2 and Table 4.6, B_1 and B_2 with temperatures are presented in Table 4.8 and their corresponding plots are shown in Fig. 4.14.

Table 4.8 - Extracted B_1 and B_2 with temperature (Unit: TPa^{-1})				
T($^{\circ}$C)	B_1^p	B_2^p	B_1^n	B_2^n
-133.4	608.2	-179.6	-166.2	135.3
-93.2	542.1	-157.3	-155.4	127.3
-48.2	447.3	-154.9	-152.7	112.7
-23.6	422.8	-148.6	-146.8	105.7
0.6	398.7	-142.6	-141.0	101.0
25.1	366.2	-133.9	-133.7	97.4
49.9	315.3	-117.3	-114.5	88.1
75.1	271.0	-100.1	-102.5	78.9
100.6	239.6	-92.4	-93.2	70.2
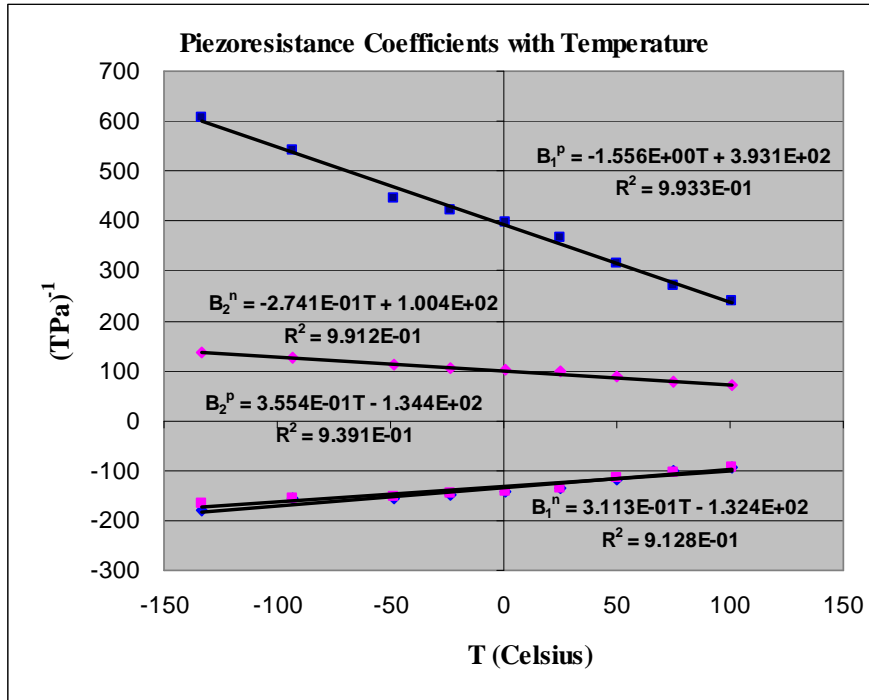
Fig. 4.14 - Extracted B_1 and B_2 with temperature

Test results show that all coefficients decrease monotonically with increasing temperature in magnitude.

4.5 Relationship between Piezoresistive Coefficients with Different Temperatures

In this section, the relationship between piezoresistive coefficients with different temperatures will be explained. Also, determination of the values of β's will be described. In order to extract a complete set of pi-coefficients (π_{11}, π_{12}, and π_{44}) for both p- and n-type sensors, B_3 (as well as B_1 and B_2) is needed. To be discussed later is the requirement of hydrostatic tests for the extraction of B_3.

50

4.5.1. General Resistance Change Equations at a fixed Temperature Reference

In most prior investigations, calibration of the piezoresistive coefficients has been performed at room temperature. Such restriction limits the accuracy of test chip stress measurements made at other temperatures. In this work, we have performed an extensive experimental study on temperature dependence of the piezoresistive behavior of silicon. From Chapter 3, the general resistance change equations are described. For convenience of discussion, those equations are repeated here:

- (001) plane: with respect to the unprimed axes

$$\frac{\Delta R}{R} = [\pi_{11}\sigma_{11} + \pi_{12}(\sigma_{22} + \sigma_{33})]\cos^2\phi + [\pi_{11}\sigma_{22} + \pi_{12}(\sigma_{11} + \sigma_{33})]\sin^2\phi$$

Eq. (4.5.1)

$$+ \pi_{44}\sigma_{12} \ \sin 2\phi + [\alpha_1\Delta T + \alpha_2 \Delta T^2 + ...]$$

- (001) plane: with respect to the primed axes

$$\frac{\Delta R}{R} = \left[\left(\frac{\pi_{11} + \pi_{12} + \pi_{44}}{2}\right)\sigma_{11}' + \left(\frac{\pi_{11} + \pi_{12} - \pi_{44}}{2}\right)\sigma_{22}'\right]\cos^2\phi$$

$$+ \left[\left(\frac{\pi_{11} + \pi_{12} - \pi_{44}}{2}\right)\sigma_{11}' + \left(\frac{\pi_{11} + \pi_{12} + \pi_{44}}{2}\right)\sigma_{22}'\right]\sin^2\phi \quad \text{Eq. (4.5.2)}$$

$$+ \ \pi_{12}\sigma_{33}' + (\pi_{11}\text{-}\pi_{12})\sigma_{12}' \ \sin 2\phi \ + [\alpha_1\Delta T + \alpha_2\Delta T^2 + ...]$$

- (111) plane: with respect to the primed axes

$$\frac{\Delta R}{R} = [B_1\sigma_{11}' + B_2\sigma_{22}' + B_3\sigma_{33}' - 2\sqrt{2}(B_2\text{-}B_3)\sigma_{23}']\cos^2\phi$$

$$+ [B_2\sigma_{11}' + B_1\sigma_{22}' + B_3\sigma_{33}' + 2\sqrt{2}(B_2\text{-}B_3)\sigma_{23}']\sin^2\phi$$

Eq.(4.5.3)

$$+ [2\sqrt{2}(B_3\text{-}B_2)\sigma_{13}' + (B_1\text{-}B_2)\sigma_{12}']\sin 2\phi$$

$$+ [\alpha_1\Delta T + \alpha_2\Delta T^2 + ...]$$

Simply, the general expression of resistance is expressed as follows:

$$R(\sigma, \Delta T) = R(0,0)\{1 + f(\Delta T) + [\Pi + \beta(\Delta T)]\sigma\}$$ Eq. (4.5.4)

where $[\Pi + \beta(\Delta T)]\sigma$ is the summation of combined stress terms and

$$f(\Delta T) = \alpha_1\Delta T + 2\alpha_2\Delta T^2 + ...$$ Eq. (4.5.5)

: $\alpha_1, \alpha_2 \ldots$ temperature coefficients of resistance

$$\beta(\Delta T) = \beta^{(1)}\Delta T + 2\beta^{(2)}\Delta T^2 + ...$$ Eq. (4.5.6)

: $\beta^{(1)}, \beta^{(2)} \ldots$ temperature coefficients of piezoresistance

in which $\Delta T = T_m\text{-}T_{ref}$ is the difference between the measurement temperature and the reference temperature at which the reference resistance $R(0,0)$ is measured. From Eq. (4.5.4), the normalized change in resistance is given as follows:

$$\frac{\Delta R}{R} = \frac{R(\sigma, \Delta T) - R(0,0)}{R(0,0)}$$

$$= f(\Delta T) + [\Pi + \beta(\Delta T)]\sigma$$

Eq. (4.5.7)

in which we let $R_{T_{ref}}(\sigma, \Delta T)$ be the resistance with the change in stress σ and the change in temperature ΔT with respect to the reference temperature.

Much attention has to be given in order to reduce the error induced by measurement of temperature for the calculation of Π. To minimize the discrepancy from the set point, maintaining temperature of the oven at the set point for a long period of time is necessary. Mathematical calculations based on the many-valley model predict a decrease of the piezoresistance effect with increasing temperature [23, 96]. Based on the quantum physics, the doping concentration can be calculated and the piezoresistance coefficients decrease with increasing impurity concentration. For p-type, when the temperature is into the range where most of the carriers are freezing out onto donors and acceptors, a similar tendency is observed.

In our case, two-dimensional states of stress are induced. For a 0-degree resistor sensor on the (111) silicon surface, the term $[\Pi + \beta(\Delta T)]\sigma$ in Eq. (4.5.7) is given by

$$[B_1 + \beta_{B_1}(\Delta T)]\sigma'_{11} + [B_2 + \beta_{B_2}(\Delta T)]\sigma'_{22} \qquad \text{Eq. (4.5.8)}$$

Similarly, for a 90-degree resistor sensor on the (111) silicon surface, the term $[\Pi + \beta(\Delta T)]\sigma$ in Eq. (4.5.7) is given by

$$[B_1 + \beta_{B_1}(\Delta T)]\sigma'_{22} + [B_2 + \beta_{B_2}(\Delta T)]\sigma'_{11} \qquad \text{Eq. (4.5.9)}$$

In Eqs. (4.5.8) and (4.5.9), $\beta_{B_1}(\Delta T)$ and $\beta_{B_1 2}(\Delta T)$ are given by

$$\beta_{B_1}(\Delta T) = \frac{1}{2}[\sum_{N=1}^{n}(\beta_{11}^{(N)} + \beta_{12}^{(N)} + \beta_{44}^{(N)})(\Delta T)^N]$$

$$\beta_{B_2}(\Delta T) = \frac{1}{6}[\sum_{N=1}^{n}(\beta_{11}^{(N)} + 5\beta_{12}^{(N)} - \beta_{44}^{(N)})(\Delta T)^N]$$

$$\text{Eq. (4.5.10)}$$

4.5.2 General Resistance Change Equations with Varying Temperatures

Now, consider two reference temperatures, A and B. Typical responses of resistance subjected to the change in temperature and applied force are shown in Fig. 4.15 where resistance changes with varying temperatures and applied force (or stress). The equation of relationship between piezoresistive coefficients with different temperatures is derived below.
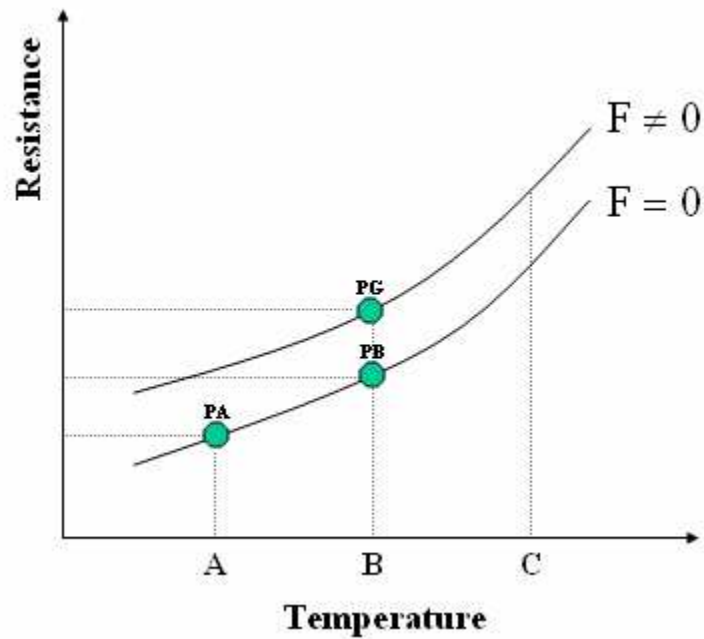
Fig. 4.15 - The plot of resistance with temperature and stress

From PA to PG in Fig. 4.15, the resistance equation becomes:

$$R_A(\sigma, \Delta T) = R_A(0,0)\{1 + f(\Delta T) + [\Pi_A + \beta_A(\Delta T)]\sigma\}$$
$$= R_A(0,0)[1 + f(\Delta T)] + R_A(0,0)[\Pi_A + \beta_A(\Delta T)]\sigma \qquad \text{Eq. (4.5.11)}$$

Similarly, from PB to PG, the resistance equation may be expressed as

$$R_B(\sigma, 0) = R_B(0,0)\{1 + \Pi_B\sigma\}$$
$$= R_B(0,0) + R_B(0,0)\Pi_B\sigma \qquad \text{Eq. (4.5.12)}$$

54

in which we let $R_{T_{ref}}(\sigma, \Delta T)$ be the resistance with σ (change in stress) and ΔT (change in temperature) with respect to T_{ref}. By comparing Eq. (4.5.11) and Eq. (4.5.12), it is apparent that

$$R_A(\sigma, \Delta T) = R_B(\sigma, 0), \quad R_A(0,0)[1 + f(\Delta T)] = R_B(0,0) \qquad \text{Eq. (4.5.13)}$$

in which $\Delta T = T_{mea} - T_{ref} = B - A$. Subtracting Eq. (4.5.12) from Eq. (4.5.11) leads to

$$R_A(0,0)[\Pi_A + \beta_A(\Delta T)]\sigma = R_B(0,0)\Pi_B\sigma \qquad \text{Eq. (4.5.14)}$$

To get the same σ in the equation as in Eq. (4.5.14)

$$\Pi_B = \frac{R_A(0,0)[\Pi_A + \beta_A(\Delta T)]}{R_B(0,0)} \qquad \text{Eq. (4.5.15)}$$

Hence

$$[\Pi_A + \beta_A(\Delta T)] = \frac{R_B(0,0)}{R_A(0,0)}\Pi_B = [1 + f(\Delta T)]\Pi_B \qquad \text{Eq. (4.5.16)}$$

Substitution of $\Delta T = B - A$ into Eq. (4.5.16) yields

$$[\Pi_A + \beta_A(\Delta T)] = [1 + f(\Delta T)]\Pi_{A+\Delta T} \qquad \text{Eq. (4.5.17)}$$

Hence

$$\beta_A(\Delta T) = [1 + f(\Delta T)]\Pi_{A+\Delta T} - \Pi_A \qquad \text{Eq. (4.5.18)}$$

From Eq. (4.5.7),

$$\beta_A(\Delta T) = \frac{1}{\sigma}[\frac{\Delta R}{R} - f(\Delta T)] - \Pi_A \qquad \text{Eq. (4.5.19)}$$

Substitution of the equation above into Eq. (4.5.17) yields

$$\Pi_{A+\Delta T} = \frac{1}{1 + f(\Delta T)}\frac{1}{\sigma}[\frac{\Delta R}{R} - f(\Delta T)] \qquad \text{Eq. (4.5.20)}$$

In addition, substitution of Eq. (4.5.17) into Eq. (4.5.7) yields

55

$$\frac{\Delta R}{R} = \frac{R_A(\sigma, \Delta T) - R_A(0,\ 0)}{R_A(0,\ 0)} = f(\Delta T) + [\Pi_A + \beta_A(\Delta T)]\sigma$$

$$\frac{\Delta R}{R} = f(\Delta T) + [1 + f(\Delta T)]\Pi_{A+\Delta T}\sigma$$

Eq. (4.5.21)

In differentiating both terms of Eq. (4.5.21) with respect to σ (stress) we derive at the

following:

$$\frac{\partial}{\partial\sigma}(\frac{\Delta R}{R}) = [1 + f(\Delta T)]\Pi_{A+\Delta T}$$

Eq. (4.5.22)

Thus

$$\Pi_{A+\Delta T} = \frac{1}{1 + f(\Delta T)}\frac{\partial}{\partial\sigma}(\frac{\Delta R}{R})$$

Eq. (4.5.23)

In Section 4.2, the reference temperature for each case is varied. On the other hand, in

order to have a constant reference temperature (e.g. room temperature) for all cases, the

general equations for any ΔT are given by using Eq. (4.5.21):

$$\frac{\Delta R_0}{R_0} = f(\Delta T) + [1 + f(\Delta T)]\,(B_1\sigma_{11}' + B_2\sigma_{22}')$$

Eq. (4.5.24)

$$\frac{\Delta R_{90}}{R_{90}} = f(\Delta T) + [1 + f(\Delta T)]\,(B_2\sigma_{11}' + B_1\sigma_{22}')$$

Eq. (4.5.25)

For any small ΔT, it is obvious that $1 + f(\Delta T) \cong 1$. Hence the equations become

$$\frac{\Delta R_0}{R_0} = f(\Delta T) + (B_1\sigma_{11}' + B_2\sigma_{22}')$$

Eq. (4.5.26)

$$\frac{\Delta R_{90}}{R_{90}} = f(\Delta T) + (B_2\sigma_{11}' + B_1\sigma_{22}')$$

Eq. (4.5.27)

Re-using the notations, $\sigma'_{11} \equiv \sigma'_{11F}F$ and $\sigma'_{22} \equiv \sigma'_{22F}F$, and $S_\phi \equiv \dfrac{d}{dF}(\dfrac{\Delta R_\phi}{R_\phi})$ in Eqs.

(4.5.24) and (4.5.25) leads to

$$S_0 = [1 + f(\Delta T)][B_1\sigma'_{11F} + B_2\sigma'_{22F}] \qquad \text{Eq. (4.5.28)}$$

$$S_{90} = [1 + f(\Delta T)][B_2\sigma'_{11F} + B_1\sigma'_{22F}] \qquad \text{Eq. (4.5.29)}$$

Solving for B_1 and B_2 in Eq. (4.5.28) and Eq. (4.5.29) yields the findings below:

$$B_1 = \frac{\sigma'_{22F}\dfrac{S_{90}}{[1+f(\Delta T)]_{90}} - \sigma'_{11F}\dfrac{S_0}{[1+f(\Delta T)]_0}}{(\sigma'_{22F})^2 - (\sigma'_{11F})^2}$$

$$\text{Eq. (4.5.30)}$$

$$B_2 = \frac{\sigma'_{22F}\dfrac{S_0}{[1+f(\Delta T)]_0} - \sigma'_{11F}\dfrac{S_{90}}{[1+f(\Delta T)]_{90}}}{(\sigma'_{22F})^2 - (\sigma'_{11F})^2}$$

Assuming $1 + f(\Delta T) = [1 + f(\Delta T)]_0$ and $1 + f(\Delta T) = [1 + f(\Delta T)]_{90}$ yields

$$B_1 = \frac{1}{1+f(\Delta T)}\frac{\sigma'_{22F}S_{90} - \sigma'_{11F}S_0}{(\sigma'_{22F})^2 - (\sigma'_{11F})^2}$$

$$\text{Eq. (4.5.31)}$$

$$B_2 = \frac{1}{1+f(\Delta T)}\frac{\sigma'_{22F}S_0 - \sigma'_{11F}S_{90}}{(\sigma'_{22F})^2 - (\sigma'_{11F})^2}$$

in which B_1 and B_2 are combined piezoresistive parameters with the change in temperature ΔT. For instance, Eq. (4.5.31) reduces to Eq. (4.4.1) when $\Delta T = 0$. Accurate calibration of $f(\Delta T)$ is essential for this purpose.

57

4.6   Summary

In this chapter, finite element analysis is used to calculate the stress states applied to the calibration samples. Specially, stressing sensing test chips are used to measure the mechanical stresses on the rosette site. Stress values (σ'_{11} and σ'_{22}) monotonically increase with rising temperatures in magnitude. Relationship between piezoresistive coefficients with different temperatures is derived. It is observed that all coefficients decrease monotonically with increasing temperature in magnitude.

CHAPTER 5

HYDROSTATIC TESTS AND TCR MEASUREMENTS

5.1 Hydrostatic Tests

Calibration of (111) test chips may not be accomplished completely by using four-point bending tests. For extracting a complete set of pi-coefficients (π_{11}, π_{12}, and π_{44}) for both p- and n-type sensors, hydrostatic tests are needed. If a sensor is subjected to hydrostatic pressure ($\sigma_{11}' = \sigma_{22}' = \sigma_{33}' = -p$), the resistivity is expressed as the following [50]:

$$\frac{\Delta\rho}{\rho} = \frac{\rho(\sigma,\Delta T) - \rho(0,0)}{\rho(0,0)} = -(\pi_{11} + 2\pi_{12})p + f(\Delta T) = \pi_p p + f(\Delta T) \qquad \text{Eq. (5.1.1)}$$

In addition, π_p is called "pressure coefficient" and is given by $\pi_p = -(\pi_{11} + 2\pi_{12})$ $= -(B_1 + B_2 + B_3)$.

In Eq. (5.1.1), $\rho(\sigma, \Delta T)$ is the stressed resistivity component with temperature change ΔT, and $\rho(0,0)$ is the unstressed resistivity component. It is noteworthy that Eq. (5.1.1) is independent of the sensor orientation on both (100) and (111) wafer planes, implying that any silicon conductor remains isotropic under a hydrostatic pressure. If we neglect the dimensional changes of resistor sensor during loading, the result is

$$\frac{\Delta R}{R} \cong \frac{\Delta \rho}{\rho} = -(\pi_{11} + 2\pi_{12})p + f(\Delta T) = \pi_p p + f(\Delta T) \qquad \text{Eq. (5.1.2)}$$

where π_p may be evaluated if $\dfrac{\Delta R}{R}$, p, and $f(\Delta T)$ are known. For determining $f(\Delta T)$, further TCR (temperature coefficient of resistance) measurements are required. The expected values for the pressure coefficients are small in both p- and n-type silicon, so direct measurement of the values is quite difficult. In fact, it has been shown theoretically that $\pi_{11} \cong -2\pi_{12}$ in n-type silicon so that π_p should be zero for n-type material [23].

5.2   TCR Measurements and f(ΔT)

During the application of pressure, a change in T is inevitable. For example, it has been observed that the temperature of the hydraulic fluid changes by 0.6~0.7 $^{\circ}$C because of a change in p by 13 MPa at room temperature.   Thus temperature-compensated hydrostatic measurements are not possible. In order to evaluate π_p accurately, temperature effects must be removed from hydrostatic calibration data. For $p = 0$, Eq. (5.1.2), $f(\Delta T)$ may be extracted by measuring the normalized resistance change with respect to a temperature change of a resistor sensor in a temperature controllable chamber. The resistance value of p- and n-type silicon with varying temperatures and forces applied to the Chip-on-Board structure appear in Tables 5.1 and 5.2 for p-type and n-type resistors, respectively. Also, their corresponding plots are shown in Figs. 5.1 and 5.2. In this work, the case in which $\phi = 0$ is considered.

60

Table 5.1 - P-type resistance with varying temperatures and forces (Unit: kohm)				
T (Celsius)	F = 0	F = 0.15 N	F = 0.3 N	F = 0.45 N
-133.4	13.888	13.883	13.877	13.871
-93.2	10.365	10.362	10.358	10.356
-48.2	9.927	9.923	9.921	9.918
0.6	10.163	10.160	10.158	10.155
25.1	10.368	10.366	10.363	10.360
49.9	10.812	10.810	10.807	10.805
75.1	11.283	11.280	11.278	11.275
100.6	11.840	11.838	11.836	11.833
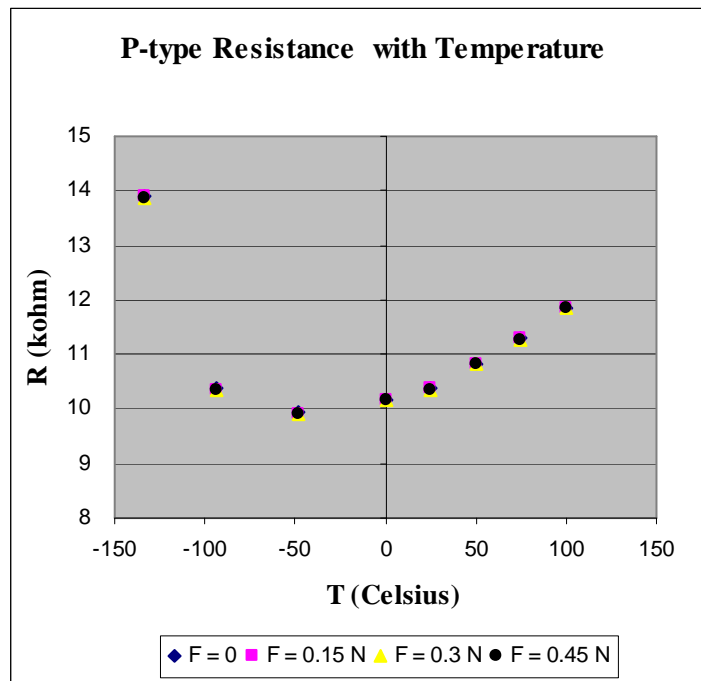
Fig. 5.1 - Plot of p-type resistance with varying temperatures and forces

Table 5.2 - N-type resistance with varying temperatures and forces (Unit: kohm)				
T (Celsius)	F = 0	F = 0.15 N	F = 0.3 N	F = 0.45 N
-133.4	1.742	1.743	1.743	1.744
-93.2	1.900	1.900	1.901	1.901
-48.2	2.049	2.049	2.050	2.050
0.6	2.218	2.218	2.219	2.219
25.1	2.309	2.309	2.310	2.310
49.9	2.421	2.422	2.422	2.422
75.1	2.518	2.518	2.519	2.519
100.6	2.619	2.619	2.619	2.620
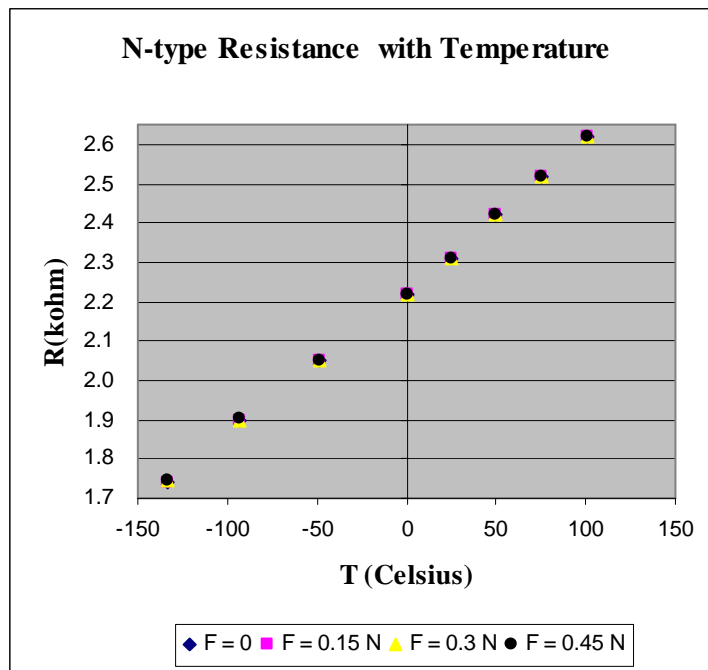
Fig. 5.2 - Plot of n-type resistance with varying temperatures and forces

As seen in Figs. 5.1 and 5.2, the change in resistance due to varying force at fixed temperature is relatively small. Resistance is measured over the temperature range of

-133 to 100 $^{\circ}$C. Freeze-out is observed for the p-type sample during low temperature operation. In the freeze-out temperature region, the concentration of electrons and holes drops significantly, which leads to an increase in resistance. Contrary to the case for p-type, the slope of resistance over the whole temperature range for the n-type samples is observed to be linear due to heavy doping. That is, freeze-out is not observed for the n-type resistor sensors.

In Tables 5.3 and 5.4, ΔR with applied force at each temperature of measurement is presented. The plots are shown in Figs. 5.3 and 5.4 for p-type and n-type resistors respectively. The reference value at each temperature of measurement is the unstressed (F = 0) resistance.

Table 5.3 - ΔR for a p-type resistor with varying temperatures and forces (Unit: kohm)				
T (Celsius)	F = 0	F = 0.15 N	F = 0.3 N	F = 0.45 N
-133.4	0	-5.660E-03	-1.139E-02	-1.709E-02
-93.2	0	-3.390E-03	-6.780E-03	-9.590E-03
-48.2	0	-3.300E-03	-5.620E-03	-8.590E-03
0.6	0	-2.780E-03	-5.350E-03	-8.170E-03
25.1	0	-2.360E-03	-5.260E-03	-7.970E-03
49.9	0	-2.450E-03	-5.210E-03	-7.850E-03
75.1	0	-2.510E-03	-5.140E-03	-7.570E-03
100.6	0	-2.090E-03	-4.250E-03	-6.445E-03
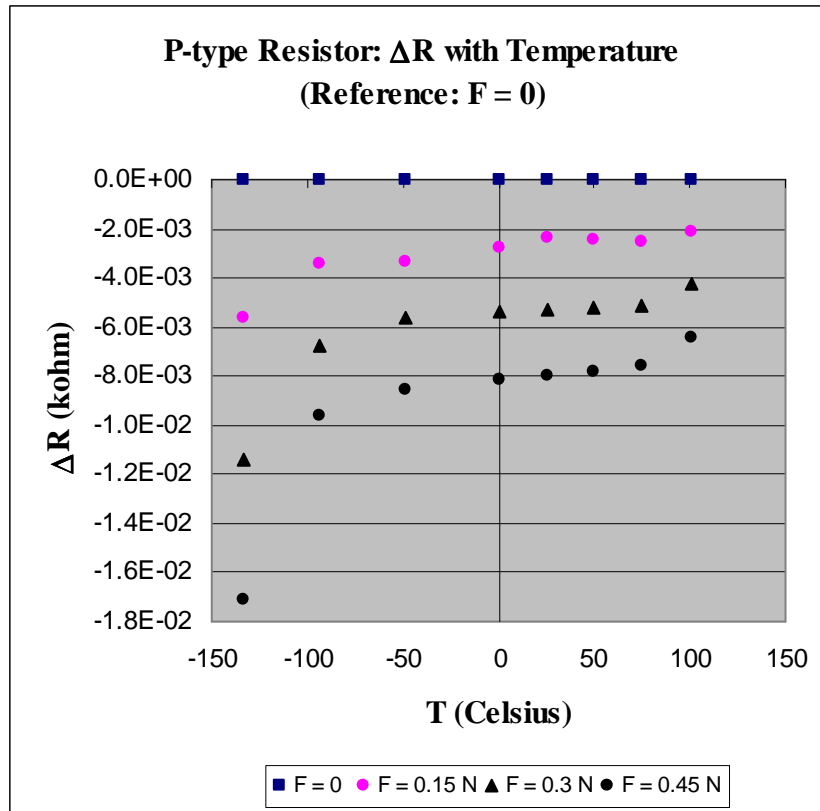
Fig. 5.3 - Plot of ΔR for a p-type resistor with varying temperatures and forces

Table 5.4 - ΔR for an n-type resistor with varying temperatures and forces (Unit: kohm)				
T (Celsius)	F = 0N	F = 0.15 N	F = 0.3 N	F = 0.45 N
-133.4	0	4.700E-04	9.400E-04	1.310E-03
-93.2	0	3.800E-04	7.400E-04	1.160E-03
-48.2	0	3.700E-04	7.500E-04	1.130E-03
0.6	0	3.500E-04	7.700E-04	1.070E-03
25.1	0	3.300E-04	6.800E-04	1.070E-03
49.9	0	3.200E-04	6.700E-04	1.003E-03
75.1	0	2.700E-04	6.300E-04	9.730E-04
100.6	0	2.500E-04	6.200E-04	9.630E-04
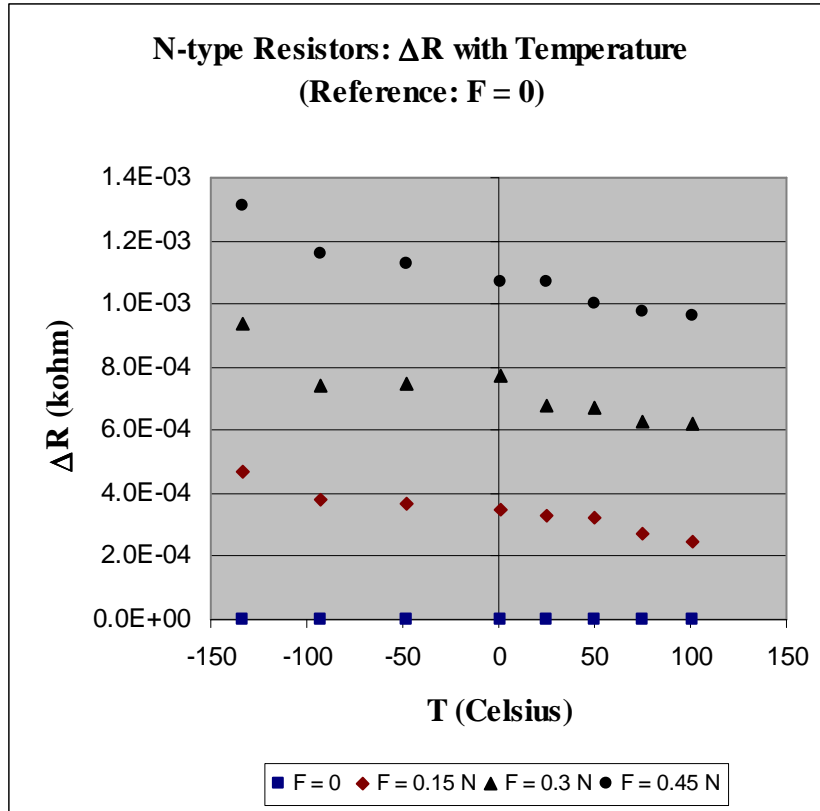
Fig. 5.4 - Plot of ΔR for an n-type resistor with varying temperatures and forces

The general expression of resistance is repeated as shown below:

$$R(\sigma, \Delta T) = R(0,0)\{1 + f(\Delta T) + [\Pi + \beta(\Delta T)]\sigma\} \qquad \text{Eq. (5.2.1)}$$

where $[\Pi + \beta(\Delta T)]\sigma$ is the summation of combined stress terms as presented in Eq. (4.5.10). The equation of normalized change in resistance is given as follows:

$$\frac{\Delta R}{R} = f(\Delta T) + [\Pi + \beta(\Delta T)]\sigma \qquad \text{Eq. (5.2.2)}$$

in which the condition $\Delta T = 0$ leads to

$$\Delta R = R\,\Pi\,\sigma \qquad \text{Eq. (5.2.3)}$$

65

For our heavily-doped n-type resistor, R is observed to increase monotonically with rising temperature, whereas Π decreases monotonically with rising temperature. Therefore, the two effects tend to cancel out for n-type, which results in a relatively small change in ΔR with varying temperatures as shown in Fig. 5.4. The same cancellation still holds for our more lightly-doped p-type samples from -50 ^{o}C up to 100 ^{o}C. On the other hand, below -50 ^{o}C, both R and Π increase with decreasing temperature resulting in a drastic increase in ΔR (see Fig. 5.3). Although the magnitude of σ'_{11} and σ'_{22} increases monotonically with rising temperature (see Table 4.6), the change in R and Π with temperature is relatively large in Eq. (5.2.3).

Typical resistance changes over the temperature range of -175 to 125 ^{o}C are presented in Table 5.5. The plots are shown in Fig. 5.5 and Fig. 5.6 for p-type and n-type resistors respectively, for the $F = 0$ case.

Table 5.5 - Resistance with varying temperatures (Unit: kohm)				
T (Celsius)	R_0^p	R_{90}^p	R_0^n	R_{90}^n
-175	20.411	21.096	1.631	1.621
-150	14.359	15.101	1.693	1.685
-125	11.642	12.121	1.758	1.751
-100	10.394	10.737	1.833	1.828
-75	9.871	10.137	1.913	1.908
-50	9.730	9.936	1.997	1.994
-25	9.826	9.987	2.084	2.083
0	10.085	10.209	2.174	2.174
25	10.476	10.566	2.269	2.271
50	10.943	10.994	2.361	2.367
75	11.465	11.496	2.452	2.500
100	12.048	12.057	2.544	2.554
125	12.615	12.661	2.639	2.648

Furthermore, the resistance of 0 and 90 degree sensors for p- and n-type silicon with varying temperatures are presented and compared in Table 5.5. Both orientations are very close to each other for p- and n-type resistors (see Figs. 5.5 and 5.6) as should be expected.
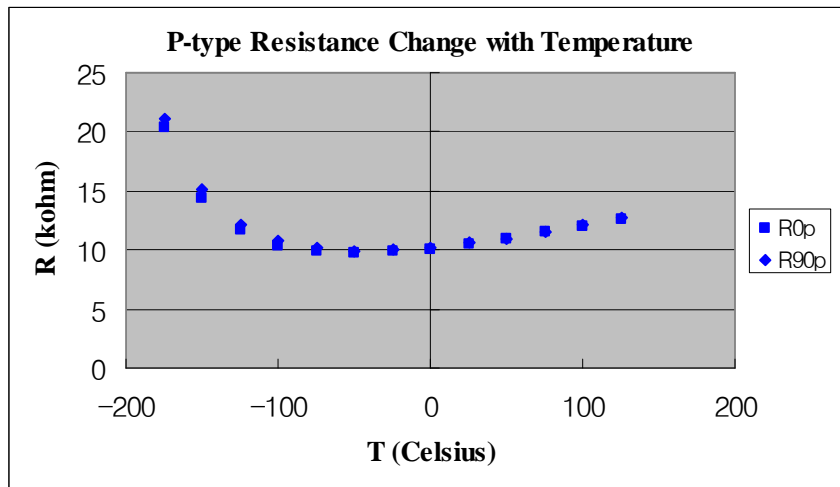
Fig. 5.5 - Resistance of p-type sensors with varying temperatures for $\phi = 0$ and $\phi = 90^\circ$
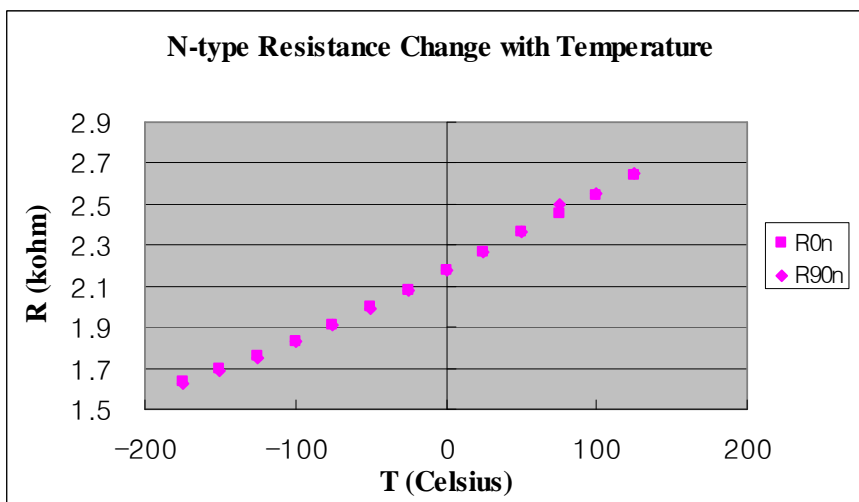
Fig. 5.6 - Resistance of n-type sensors with varying temperatures for $\phi = 0$ and $\phi = 90^\circ$

As described in Section 4.5, accurate calibration of f (ΔT) is essential to determine the pressure coefficients with temperature. To this purpose, extensive calibrations of resistance with varying temperatures are performed in a temperature controllable chamber. Typical experimental resistance change over the temperature range of -180 to 130 ^{o}C with a step size 2.5^{o}C is shown in Figs. 5.7 and 5.8.
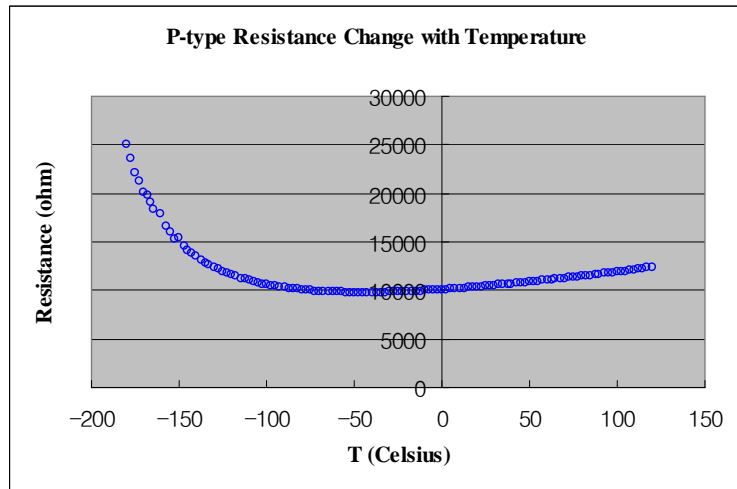
Fig. 5.7 - P-type resistance change with varying temperatures
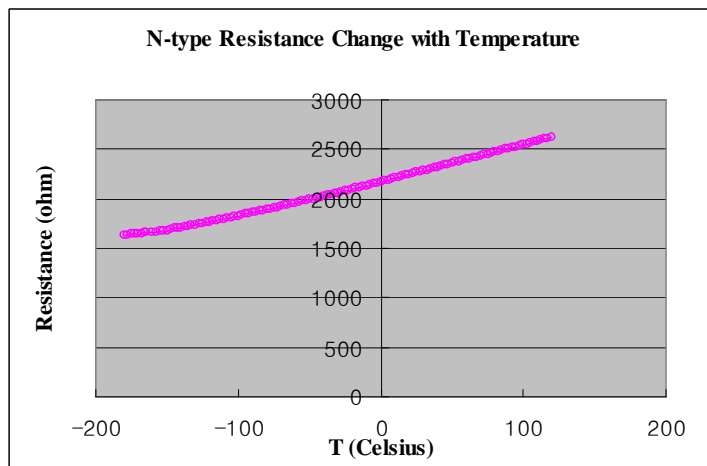
Fig. 5.8 - N-type resistance change with varying temperatures

As depicted in Fig. 5.7 and Fig. 5.8, the resistance of the p-type sensor elements increases rapidly at low temperatures as a result of carrier freeze-out in lightly doped p-type silicon material. Clearly, the temperature dependence of resistance cannot be modeled by a linear term, but requires a more general formulation for $f(\Delta T)$. On the other hand, the n-type sensor elements have a much higher doping level and are much less affected by freeze-out over the measurement range.

From Fig. 5.7 and Fig. 5.8, the normalized change in resistance induced by ΔT, defined as $f(\Delta T)$, may be evaluated assuming $\sigma = 0$:

$$\frac{\Delta R}{R} = \frac{R(0, \Delta T) - R(0,0)}{R(0,0)} = f(\Delta T) = \alpha_1 \Delta T + \alpha_2 \Delta T^2 + \alpha_3 \Delta T^3 + ... \qquad \text{Eq. (5.2.4)}$$

Through the use of Eq. (5.2.4), temperature coefficients of resistance for p- and n-type sensors may be obtained, as shown in Figs. 5.9 and 5.10, respectively. For p-type sensors, $f(\Delta T)$ may clearly not be modeled by a linear term but requires higher order terms. The n-type sensors also exhibit some curvature in $f(\Delta T)$.
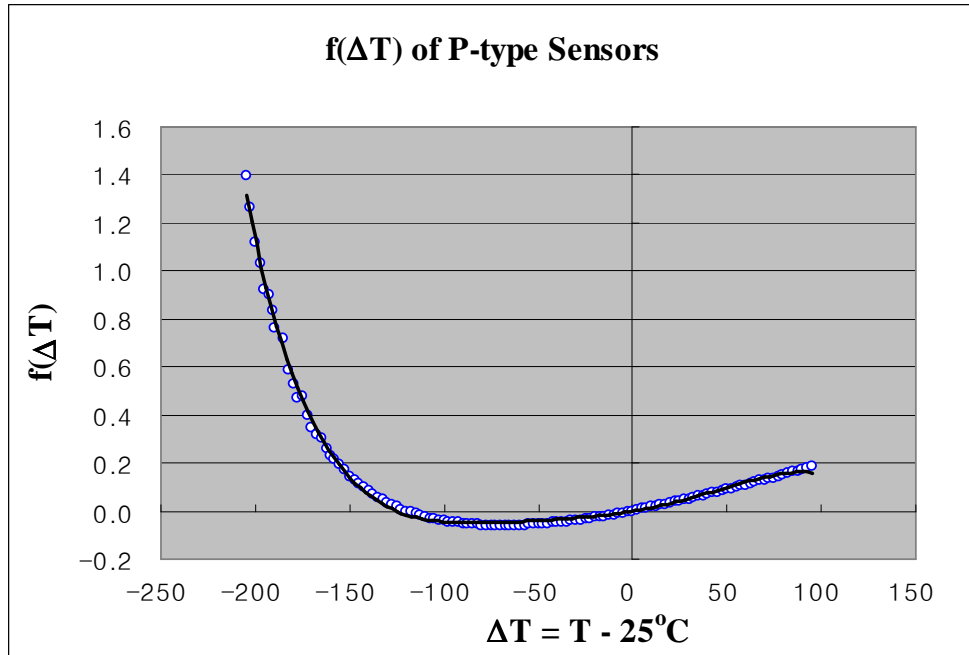
Fig. 5.9 - f (ΔT) of p-type sensors with varying temperatures
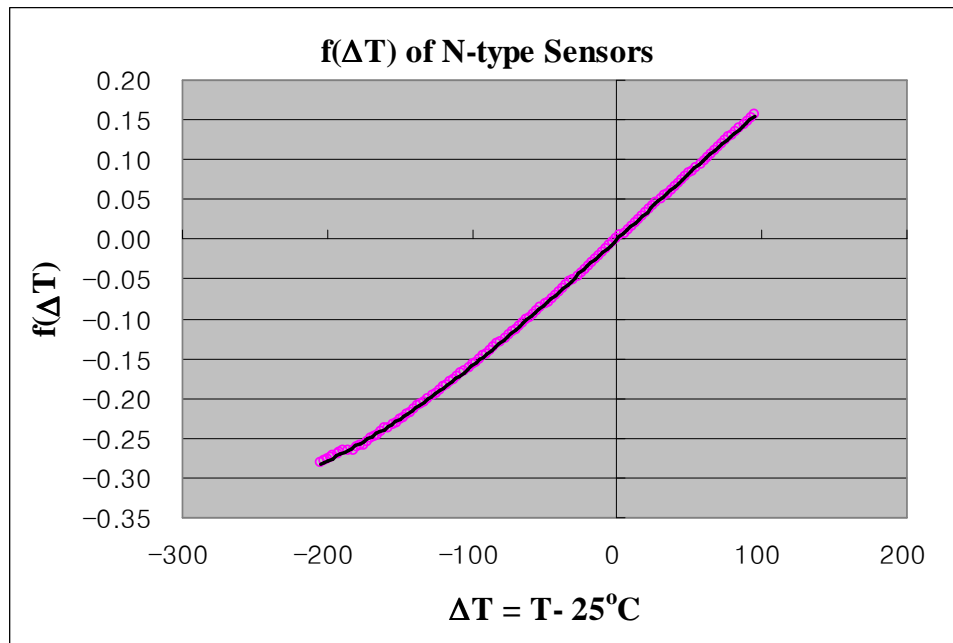
Fig. 5.10 - f (ΔT) of n-type sensors with varying temperatures

Tables 5.6 and 5.7 present the results of least square fits to the $f(\Delta T)$ data in Figs. 5.9 and 5.10, based upon 24 sensors of each type. For the p-type resistors, a 5th-order equation is used. On the other hand, for n-type, a 3rd-order equation provides a good curve fitting.

Table 5.6 - Temperature coefficients of resistance with varying temperatures (p-type resistors)

	α_1	α_2	α_3	α_4	α_5
Average	1.416E-03	9.258E-06	1.738E-08	-2.710E-10	-4.572E-12
Std. Dev	7.398E-05	1.283E-06	1.401E-08	2.559E-10	1.260E-12

Table 5.7 - Temperature coefficients of resistance with varying temperatures (n-type resistors)

	α_1	α_2	α_3
Average	1.663E-03	2.497E-07	-4.784E-09
Std. Dev	1.119E-05	7.945E-08	2.984E-10

On the other hand, at a given reference temperature, a quadratic equation is enough to fit $f(\Delta T)$ over any small range of temperature, especially for the hydrostatic tests, for both p-type and n-type samples. In Table 5.8, only α_1 of the average of 32 specimens is presented at each reference temperature. From Table 5.8, it is observed that α_1 increases with rising temperature for p-type. However, for n-type sensors, α_1 is less defined at low temperatures, but decreases with rising temperature in higher temperature regions. In Table 5.9, α_2 as well as α_1 measured at a given reference temperature for p-type sensors is displayed.

Table 5.8 - Average of α_1 of 32 specimens for p- and n-type sensors measured at a given reference temperature (Unit: $10^{-3}/^{\circ}C$)

T (Celsius)	P- type sensors	N-type sensors
-151.0	-24.5	1.81
-133.4	-12.6	1.72
-93.2	-3.42	1.74
-48.2	-0.191	1.73
0.6	1.18	1.74
25.1	1.56	1.70
49.9	1.76	1.61
75.1	1.82	1.58
100.6	1.98	1.44
125.9	2.11	1.38

Table 5.9 - Average of α_1 (Unit: $10^{-3}/^{\circ}C$) and α_2 (Unit: $10^{-3}/^{\circ}C^2$) of 32 specimens for p-type sensors measured at a given reference temperature

T (Celsius)	α_1	α_2
-151.0	-22.0	9.39E-01
-133.4	-10.7	4.04E-01
-113.4	-6.60	-7.43E-02
-93.2	-3.45	5.55E-02
-71.4	-1.16	-2.02E-02
-48.2	-0.191	1.50E-02
-23.6	0.573	-4.09E-03
0.6	1.14	-7.28E-03
25.1	1.49	9.06E-03
49.9	1.73	8.11E-04
75.1	1.76	4.90E-02
100.6	2.04	8.24E-03
125.9	2.06	1.91E-03

In Table 5.10 and Table 5.11, experimental calibration results for the piezoresistive coefficients of silicon with room-temperature reference as a function of temperature are presented and compared and contrasted with the values from individual reference temperature by using Eq. (4.5.31):

$$B_1 = \frac{1}{1+f(\Delta T)} \frac{\sigma'_{22F}S_{90} - \sigma'_{11F}S_0}{(\sigma'_{22F})^2 - (\sigma'_{11F})^2}$$

<div style="text-align:right">Eq. (5.2.5)</div>

$$B_2 = \frac{1}{1+f(\Delta T)} \frac{\sigma'_{22F}S_0 - \sigma'_{11F}S_{90}}{(\sigma'_{22F})^2 - (\sigma'_{11F})^2}$$

Table 5.10- Piezoresistive coefficients with room-temperature reference (1/TPa)				
T(Celsius)	B_1^p	B_2^p	B_1^n	B_2^n
-133.4	607.2	-164.7	-165.9	136.3
-93.2	548.7	-151.6	-155.2	127.8
-48.2	447.9	-151.5	-152.5	113.0
0.6	397.3	-141.1	-140.7	101.0
25.1	366.2	-133.9	-133.7	97.4
49.9	314.9	-118.0	-114.6	87.9
75.1	269.6	-100.7	-104.6	78.2
100.6	238.2	-93.3	-93.3	70.0

Table 5.11 - Piezoresistive coefficients with a given reference temperature (1/TPa)				
T(Celsius)	B_1^p	B_2^p	B_1^n	B_2^n
-133.4	608.1	-179.6	-166.2	135.3
-93.2	542.1	-157.3	-155.4	127.3
-48.2	447.3	-154.9	-152.7	112.7
0.6	398.7	-142.6	-141.0	101.0
25.1	366.2	-133.9	-133.7	97.4
49.9	315.3	-117.3	-114.5	88.1
75.1	271.0	-100.1	-102.5	78.9
100.6	239.6	-92.4	-93.2	70.2

As seen from Table 5.10 and Table 5.11, the piezoresistive coefficients of silicon as a function of temperature are in good agreement. Furthermore, by using $f(\Delta T)$ for a fixed reference temperature (e.g., at room temperature), we may obtain $f(\Delta T)$ for arbitrary reference temperature. From the general equation of resistance with $\sigma = 0$,

$$R(0, \Delta T) = R(0,0)[1 + f(\Delta T)] \qquad \text{Eq. (5.2.4)}$$

Assuming $T_m - T_{ref} = \Delta T = \Delta T' + \Delta T''$, where T_m is the measurement temperature, leads

to

$$\begin{aligned}R(0, \Delta T' + \Delta T'') &= R(0,0)[1 + f(\Delta T' + \Delta T'')] = R(0, \Delta T')[1 + f_{\Delta T'}(\Delta T'')] \\ &= R(0,0)[1 + f(\Delta T')][1 + f_{\Delta T'}(\Delta T'')]\end{aligned} \qquad \text{Eq. (5.2.5)}$$

In the equation, $f_{\Delta T'}(\Delta T'')$ is defined as $f(\Delta T'')$ with the reference temperature $\Delta T'$.

Combining Eq. (5.2.4) and Eq. (5.2.5) yields

$$f_{\Delta T'}(\Delta T'') = \frac{f(\Delta T) - f(\Delta T')}{1 + f(\Delta T')} = \frac{f(\Delta T' + \Delta T'') - f(\Delta T')}{1 + f(\Delta T')} \qquad \text{Eq. (5.2.6)}$$

$f(\Delta T) = \alpha_1 \Delta T + \alpha_2 \Delta T^2 + \alpha_3 \Delta T^3$ in Eq. (5.2.6) yields

$$f_{\Delta T'}(\Delta T'') = \frac{\alpha_3 (\Delta T'')^3 + (\alpha_2 + 3\alpha_3 \Delta T')(\Delta T'')^2 + [\alpha_1 + 2\alpha_2 \Delta T' + 3\alpha_3 (\Delta T')^2]\Delta T''}{1 + \alpha_1 \Delta T' + \alpha_2 (\Delta T')^2 + \alpha_3 (\Delta T')^3}$$

$$\text{Eq. (5.2.7)}$$

Therefore

$$\begin{aligned}(\alpha_1)_{\Delta T'} &= \frac{\alpha_1 + 2\alpha_2 \Delta T' + 3\alpha_3 (\Delta T')^2}{1 + f(\Delta T')} \\ (\alpha_2)_{\Delta T'} &= \frac{\alpha_2 + 3\alpha_3 \Delta T'}{1 + f(\Delta T')} \\ (\alpha_3)_{\Delta T'} &= \frac{\alpha_3}{1 + f(\Delta T')}\end{aligned} \qquad \text{Eq. (5.2.8)}$$

where $(\alpha_1)_{\Delta T'}$, $(\alpha_2)_{\Delta T'}$, and $(\alpha_3)_{\Delta T'}$ are the temperature coefficients of resistance at a

reference temperature $T_{ref} + \Delta T'$. From Eq. (5.2.8), once $f(\Delta T)$ is obtained for a fixed

reference temperature, f(ΔT) at any other reference temperature may be determined .

74

In our cases, extensive TCR measurements are performed especially around the temperature of measurement.

5.3   Analysis of Hydrostatic Tests and TCR Measurements

Once the TCR measurements are completed, the die is then ready for hydrostatic tests. In our work, hydrostatic tests are carried out on the resistor sensors of the JSE-WB100C test chip (see Fig. 5.11). The (111) silicon test chips have dimensions of 100 x 100 mil.
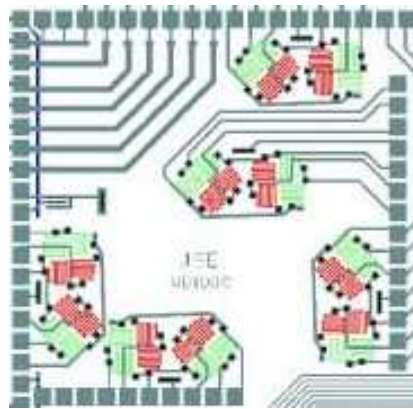
Fig. 5.11 - Quarter model of JSE-WB100C for TCR and hydrostatic tests

One corner of the die is attached to a specially designed printed circuit board (PCB) using a small amount of die attachment adhesive (ME 525). Lavenir software is used to design the PCB and its picture is shown in Fig. 5.12. The resistor sensors on the die are wire-bonded to the pads on the PCB to get the electrical access as shown in Fig. 5.13. During the TCR measurements, the Chip-on-Board is inserted into the connector inside the test fixture as shown in Fig. 5.14.
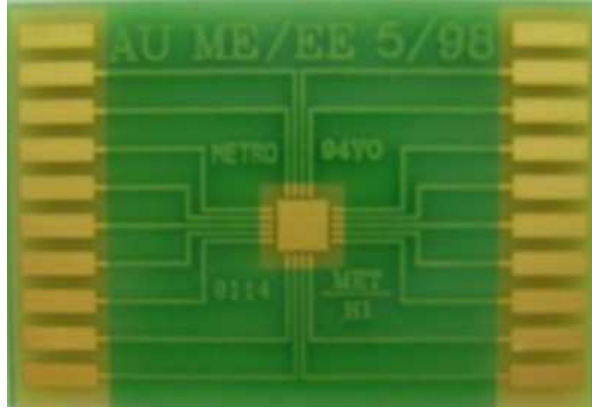
Fig. 5.12 - Specially designed PCB for TCR and hydrostatic tests
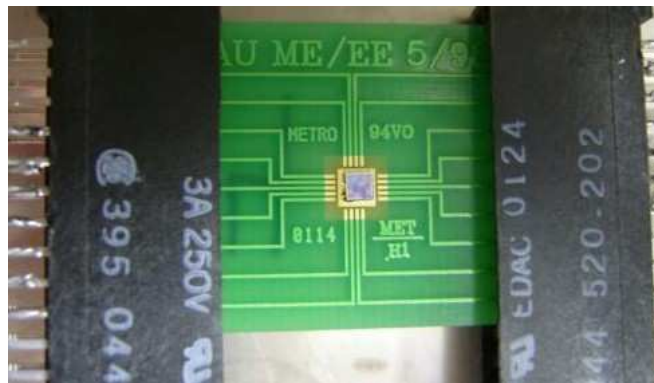
Fig. 5.13 - Wire-bonded chip on the board for TCR and hydrostatic tests

Only one corner of the die is attached to the board to satisfy the condition $\sigma'_{11} = \sigma'_{22} = \sigma'_{33} = -p$. Then, the wire-bonded die is subjected to temperature change with monitoring each resistance of the sensors through the use of computer-controlled GPIB devices. An OMEGA CN3251 temperature controller is used for controlling the temperature of calibration. However, the recording of the actual temperature is made by a thermistor inside the vessel. It is noteworthy that the temperature reading by the thermistor is very close to that of the temperature controller. The hydrostatic experiments

are performed on the test chips over the temperature range of -25 ^{o}C to100 ^{o}C. In order to increase the temperature of fluid, a resistance heater is used inside the pressure vessel. To lower the temperature of fluid, we use liquid nitrogen, which is injected into a specially designed box surrounding the pressure vessel. In addition, another microprocessor-based temperature controller CN76000 is used to monitor the temperature inside the box. The input type is a "K" thermocouple. In order to reach the equilibrium between the temperature inside the box and the fluid temperature inside the vessel, a longer duration of time is required.

Fig. 5.14 - Hydrostatic test chamber

Fig. 5.15 - Hydrostatic test setup
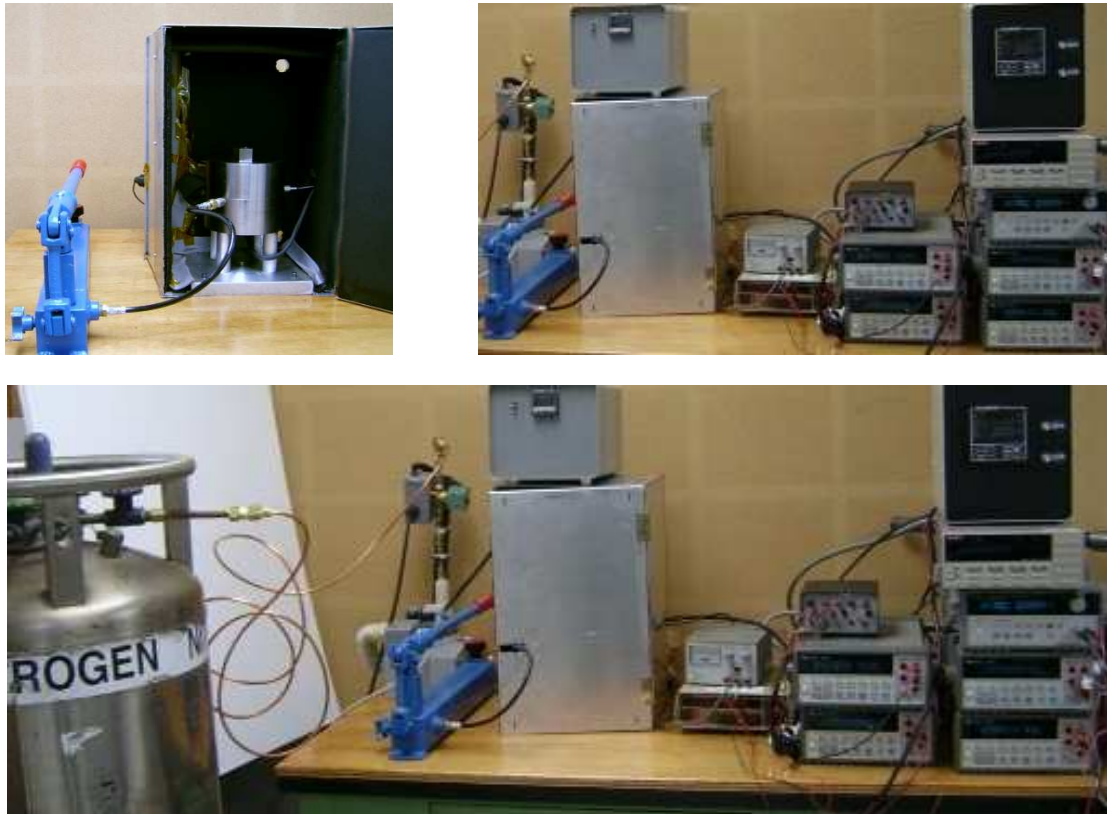
Fig. 5.16 - Expanded hydrostatic test setup for high and low temperatures

For TCR measurements, a program is used to control the oven temperature. Like hydrostatic tests, the measurements of resistances are made by computer-controlled GPIB devices. During the TCR measurements, no stress is applied. During hydrostatic tests, the die is put into the pressure vessel, whose set up is shown in Fig. 5.14. A pump connected to the vessel is used to generate pressure, as shown in Fig. 5.15. In addition, the expanded hydrostatic test setup for high and low temperatures is shown in Fig. 5.16.

Typical change in resistance with varying temperatures is shown in Fig. 5.17 for a p-type resistor in which the measured and temperature-induced normalized resistance changes are plotted together. The shape of the curve is slightly parabolic. Similar behavior is observed for n-type resistors.
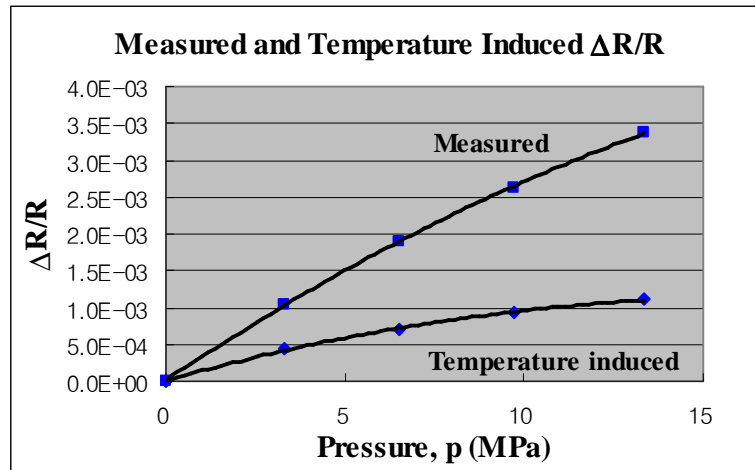
Fig. 5.17 - An example of measured and temperature induced $\Delta R/R$ for p-type resistors

Subtraction of the effect of temperature from the resistance change determines the pressure coefficient. A nonlinear change in the temperature of the hydraulic fluid for a p-

type resistor is observed during the application of pressure, as shown in Fig. 5.18. Similar behavior is observed for n-type resistors.

Temperature Change with Pressure
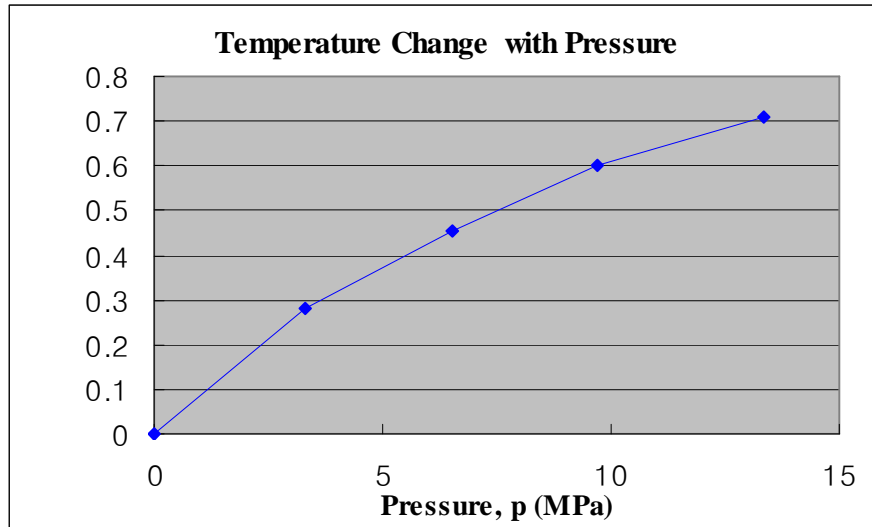
Fig. 5.18 - Fluid temperature change with pressure for p-type resistors

Adjusted resistance change appears to be linear with pressure as expected in Eq. (5.1.2), as shown in Fig. 5.19, whose slope of the curve corresponds to the piezoresistive coefficient π_p as given in the following equation:

$$\frac{\Delta R}{R} - f(\Delta T) = -(\pi_{11} + 2\pi_{12})p$$
$$= -(B_1 + B_2 + B_3)p \qquad \text{Eq. (5.3.1)}$$
$$= \pi_p p$$

Typical results of the pressure coefficient of (111) silicon for each temperature are displayed in Appendix C.
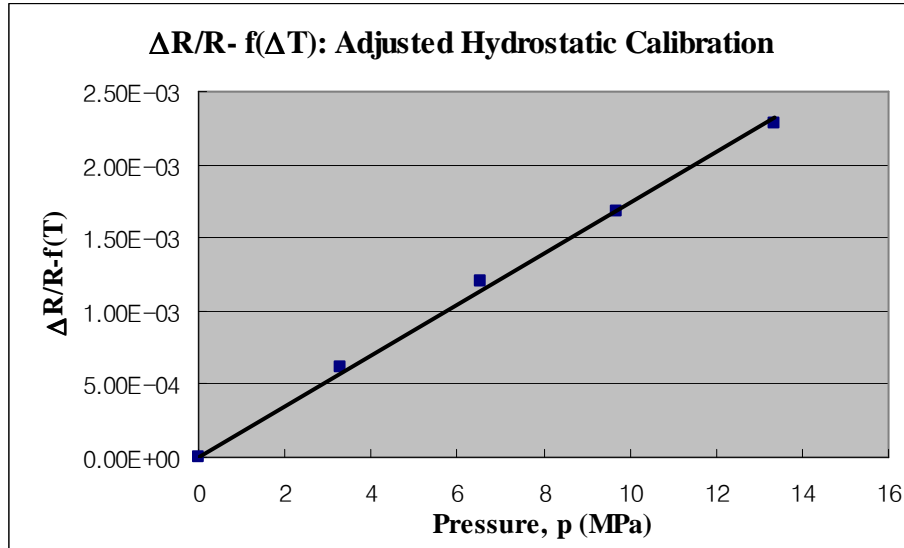
Fig. 5.19 - Adjusted hydrostatic calibration for p-type sensors

The pressure coefficient data for p-type and n-type sensors over the temperature range of -25°C to100°C are presented in Table 5.12, and graphs of the data appear in Figs. 5.20 and Fig. 5.21. It is observed that the pressure coefficient for both the p- and n-type decreases with rising temperature. Compared with p-type silicon, the pressure coefficient of n-type silicon has relatively small value. This phenomenon is in good agreement with the experimental results of the hydrostatic-pressure coefficient of n-type silicon [25], which showed that the hydrostatic-pressure coefficient is small at all concentration in n-type silicon at 300K. It may be noted that the values in Table 5.12 reflect only the counted specimens among 32. The values in Table 5.8 are used for the determination of temperature-induced normalized resistance change. It is noteworthy that the unit is 1/TPa for the pressure coefficient and all pi-coefficients throughout this dissertation.

Table 5.12 - Pressure coefficient data for p- and n-type sensors versus temperature						
T (^{o}C)	# of sensors (p-type)	Average (1/TPa)	Std. Dev. (1/TPa)	# of sensors (n-type))	Average (1/TPa)	Std. Dev. (1/TPa)
-23.6	13	165.4	20.8	11	40.0	11.9
0.6	13	153.4	30.5	10	36.3	9.9
25.1	30	145.9	34.1	22	31.0	8.1
49.9	26	135.1	29.1	15	19.2	24.5
75.1	20	119.7	35.3	10	3.8	22.1
100.6	22	108.9	33.5	16	-3.1	14.9
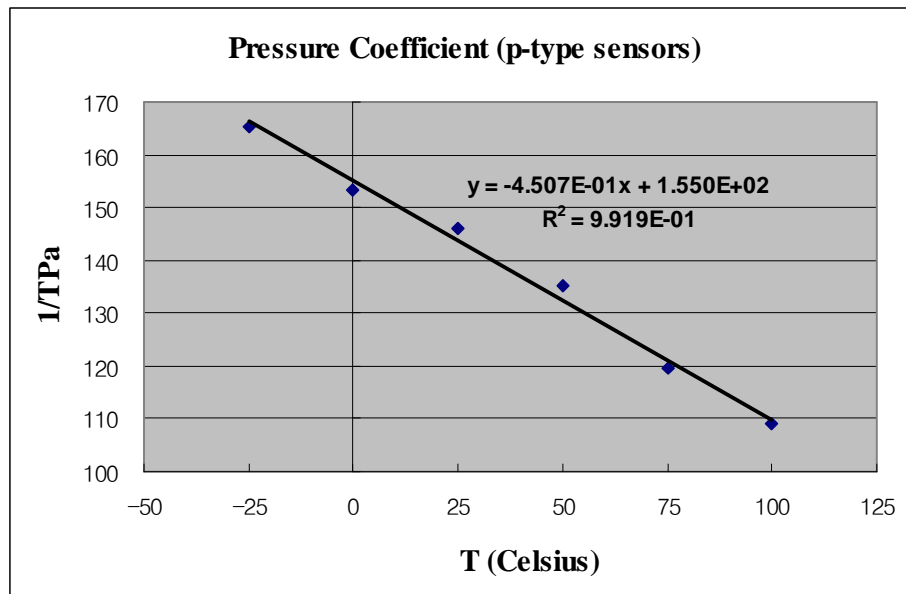
Fig. 5.20 - Pressure coefficient versus temperature for p-type sensors

As mentioned earlier, it has been argued theoretically that the pressure coefficient should be zero for n-type silicon and these results are consistent with the theory.
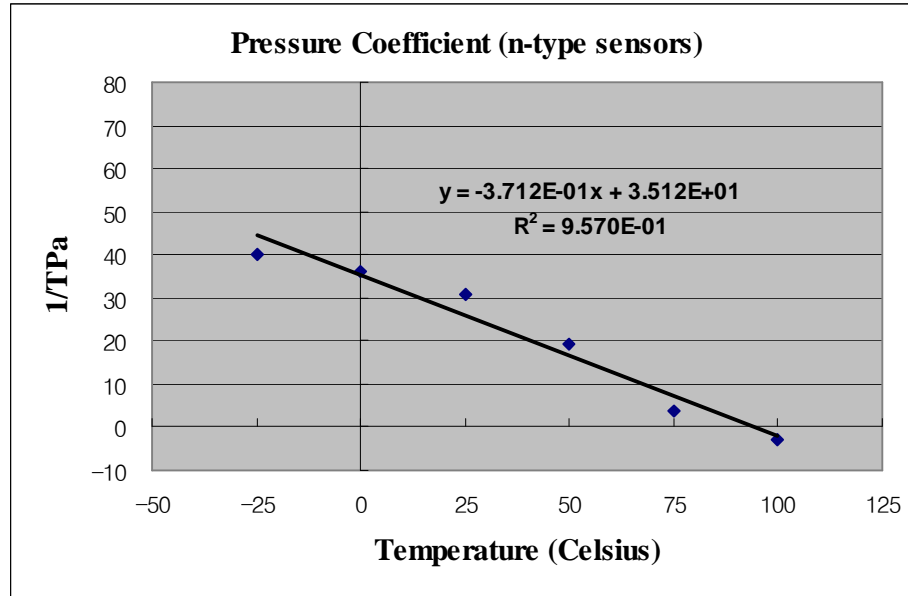
Fig. 5.21 - Pressure coefficient versus temperature for n-type sensors

As described in Chapter 4, four-point bending tests are used to measure B_1 and B_2, whereas hydrostatic tests are used to measure B_3. A complete set of pi-coefficients (π_{11}, π_{12}, and π_{44}) can be extracted by combining hydrostatic tests and four-point bending tests:

$$B_1 = \frac{\pi_{11} + \pi_{12} + \pi_{44}}{2}$$

$$B_2 = \frac{\pi_{11} + 5\pi_{12} - \pi_{44}}{6} \qquad \text{Eq. (5.3.2)}$$

$$B_3 = \frac{\pi_{11} + 2\pi_{12} - \pi_{44}}{3}$$

$$\pi_{11} = B_1 - 3B_2 + 3B_3$$

$$\pi_{12} = 2B_2 - B_3 \qquad \text{Eq. (5.3.3)}$$

$$\pi_{44} = B_1 + B_2 - 2B_3$$

- Pi-coefficients with neglect of γ ($\gamma = 1$)

In this work, γ is defined as the ratio of axial portion to the sum of axial and transverse portion of a resistor. More details about γ will be discussed in Chapter 7. Pi-coefficients of p-type silicon versus temperature with neglect of γ are presented in Table 5.13, whose graphs of the data appear in Figs. 5.22 and Fig. 5.23. As reflected in Table 5.13, all the coefficients in p-type material decrease monotonically with increasing temperature over the temperature range of -25°C to 100°C.

Table 5.13 - Pi-coefficients of p-type silicon versus temperature with neglect of γ

T(Celsius)	B_1^p	B_2^p	B_3^p	π_{11}^p	π_{12}^p	π_{44}^p	π_p
-23.6	422.8	-148.6	-439.6	-450.2	142.4	1153.4	165.4
0.6	398.7	-142.6	-409.5	-402.0	124.3	1075.1	153.4
25.1	366.2	-133.9	-378.2	-366.7	110.4	988.7	145.9
49.9	315.3	-117.3	-333.1	-332.1	98.5	864.2	135.1
75.1	271.0	-100.1	-290.6	-300.5	90.4	752.1	119.7
100.6	239.6	-92.4	-256.1	-251.5	71.3	659.4	108.9
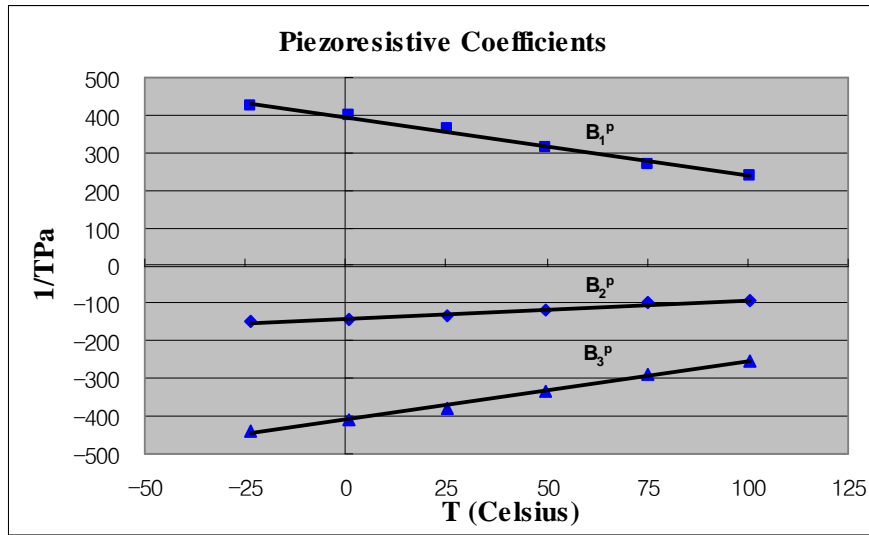
Fig. 5.22 - Combined pi-coefficients for p-type silicon versus temperature with neglect of γ

The smallest coefficients π_{11} and π_{12} exhibit discrepancies in sign with the data from the literature [6].
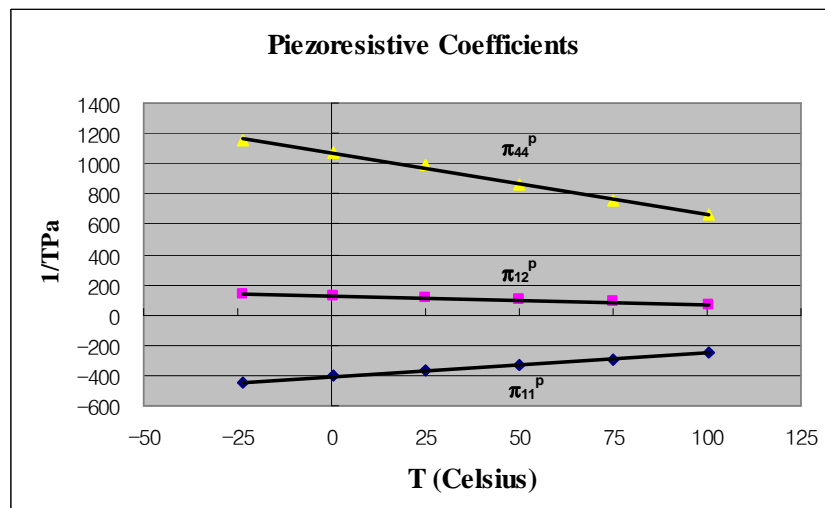
Fig. 5.23 - Pi-coefficients for p-type silicon versus temperature with neglect of γ

Likewise, pi-coefficients of n-type silicon versus temperature with neglect of γ are presented in Table 5.14, whose graphs of the data appear in Figs. 5.24 and 5.25. The data in Table 5.14 indicate that B_3 and π_{44} in n-type material exhibit an opposite tendency in magnitude. It may be noted that they are the smallest coefficients in n-type material. The other coefficients are well defined.

Table 5.14 - Pi-coefficients for n-type silicon versus temperature with neglect of γ							
T(Celsius)	B_1^n	B_2^n	B_3^n	π_{11}^n	π_{12}^n	π_{44}^n	π_p
-23.6	-146.8	105.7	1.1	-460.6	210.3	-43.3	40.0
0.6	-141.0	101.0	3.7	-432.9	198.3	-47.4	36.3
25.1	-133.7	97.4	5.3	-410.0	189.5	-46.9	31.0
49.9	-114.5	88.1	7.2	-357.2	169.0	-40.8	19.2
75.1	-102.5	78.9	19.8	-279.8	138.0	-63.2	3.8
100.6	-93.2	70.2	26.1	-225.5	114.3	-75.2	-3.1
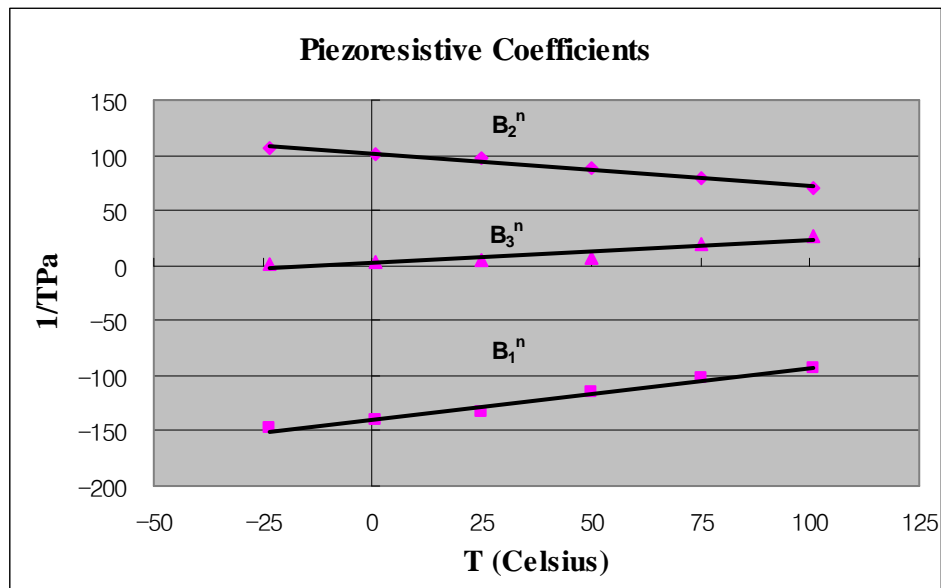
Fig. 5.24 - Combined pi-coefficients for n-type silicon versus temperature
with neglect of γ
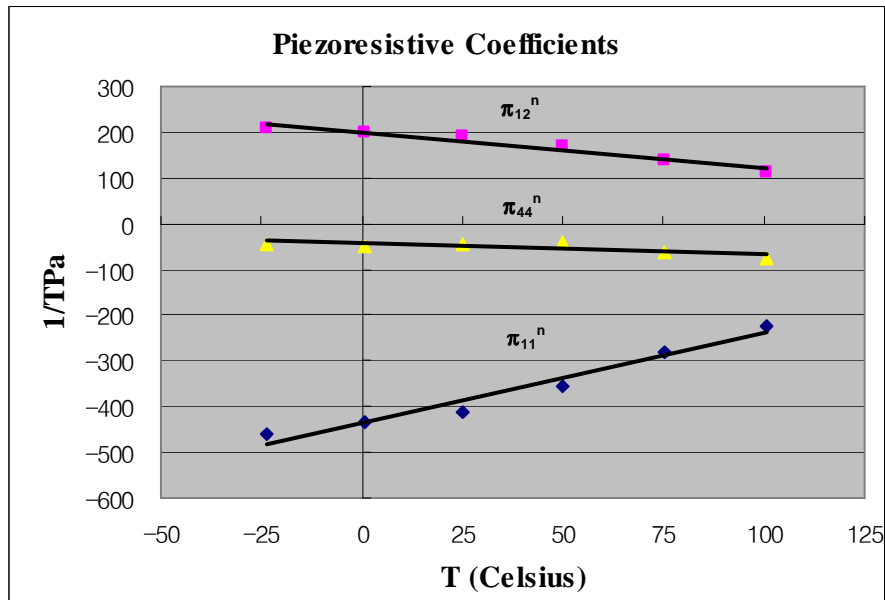
Fig. 5.25 - Pi-coefficients for n-type silicon versus temperature with neglect of γ

- Pi-coefficients with consideration of γ

For effective and realistic pi-coefficients, consideration of γ is necessary. As will be discussed in Chapter 7, $B_1 + B_2$ is constant, regardless of γ. Thus B_3 in Eq. (5.3.2) and π_{44} in Eq. (5.3.3) are independent of γ. The pi-coefficients of p-type silicon versus temperature with consideration of γ are presented in Table 5.15, whose graphs of the data also appear in Figs. 5.26 and 5.27. As observed in the cases $\gamma = 1$, the smallest coefficients π_{11} and π_{12} also exhibit discrepancies in sign with the data from the literature [6]. However, the consideration of γ significantly reduces π_{11} and π_{12} in magnitude.

Table 5.15- Pi-coefficients for p-type silicon versus temperature with consideration of γ							
T(Celsius)	B_1^p	B_2^p	B_3^p	π_{11}^p	π_{12}^p	π_{44}^p	π_p
-23.6	491.2	-217.0	-439.6	-176.6	5.6	1153.4	165.4
0.6	463.5	-207.4	-409.5	-142.8	-5.3	1075.1	153.4
25.1	426.1	-193.8	-378.2	-127.1	-9.4	988.7	145.9
49.9	367.1	-169.1	-333.1	-124.9	-5.1	864.2	135.1
75.1	315.4	-144.5	-290.6	-122.9	1.6	752.1	119.7
100.6	279.4	-132.2	-256.1	-92.3	-8.3	659.4	108.9
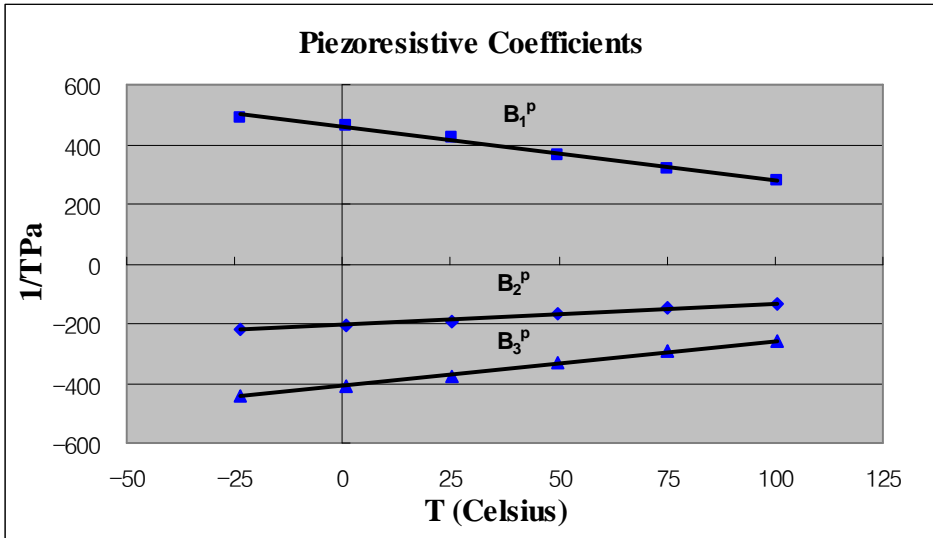
Fig. 5.26 - Combined pi-coefficients for p-type silicon versus temperature with consideration of γ

88
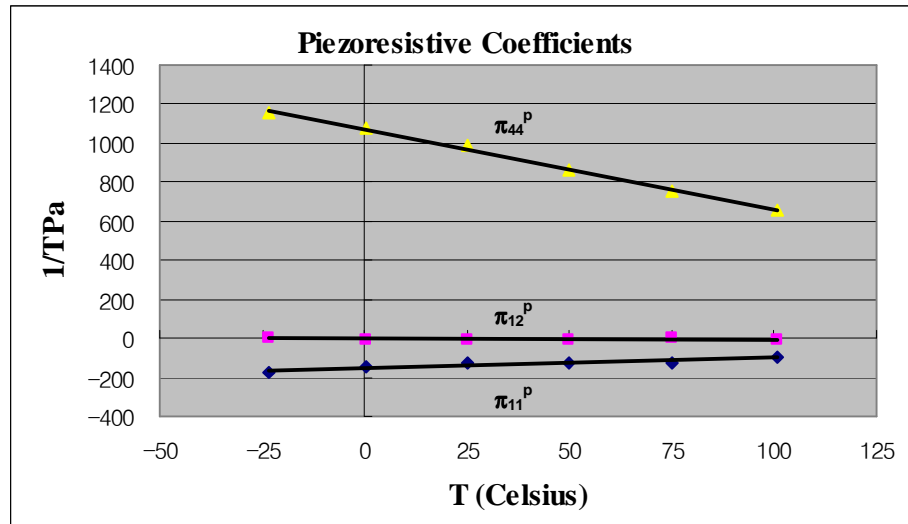
Fig. 5.27 - Pi-coefficients for p-type silicon versus temperature with consideration of γ

Likewise, pi-coefficients of n-type silicon versus temperature with consideration of γ are presented in Table 5.16, whose graphs of the data are also shown in Figs. 5.28 and 5.29. The data in Table 5.16 indicate that B_3 and π_{44} in n-type material exhibit an opposite tendency in magnitude. It may be noted that they are the smallest coefficients in n-type material. The other coefficients are well defined.

Table 5.16 - Pi-coefficients for n-type silicon versus temperature with consideration of γ							
T(Celsius)	B_1^n	B_2^n	B_3^n	π_{11}^n	π_{12}^n	π_{44}^n	π_p
-23.6	-177.0	135.9	1.1	-581.4	270.7	-43.3	40.0
0.6	-170.0	130.0	3.7	-548.8	256.3	-47.4	36.3
25.1	-161.4	125.1	5.3	-520.8	244.9	-46.9	31.0
49.9	-138.8	112.4	7.2	-454.4	217.6	-40.8	19.2
75.1	-124.2	100.6	19.8	-366.6	181.4	-63.2	3.8
100.6	-112.8	89.8	26.1	-303.9	153.5	-75.2	-3.1
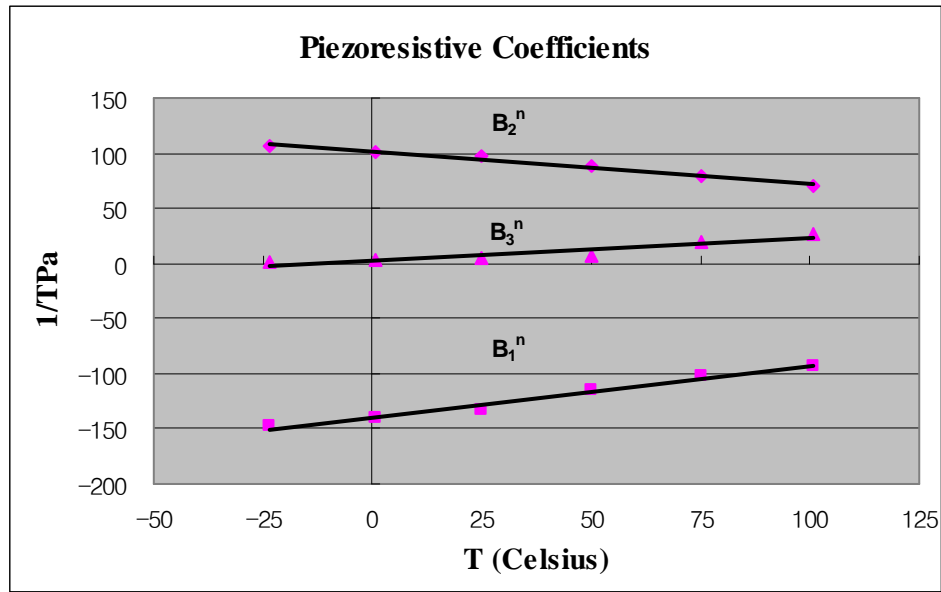
Fig. 5.28 - Combined pi-coefficients for n-type silicon versus temperature with consideration of γ
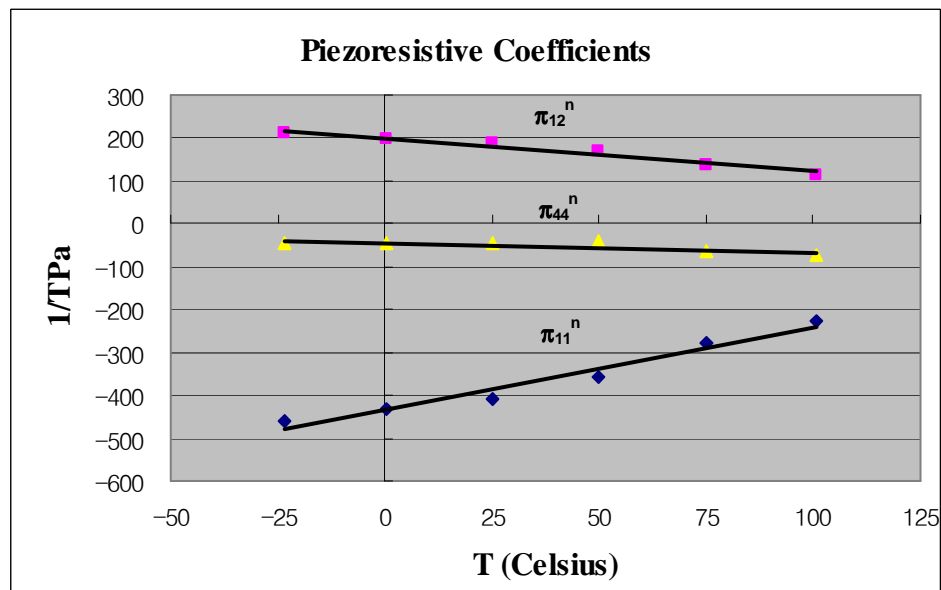
Fig. 5.29 - Pi-coefficients for n-type silicon versus temperature with consideration of γ

5.4   Summary

In this chapter, TCR measurements and hydrostatic tests have been described. The pressure coefficient π_p may be determined by combining TCR measurements and hydrostatic tests. It may be stressed that the pressure coefficient π_p, for the (111) silicon test chips, is orientation independent because the conductor remains isotropic under hydrostatic pressure. In order to determine π_p, the data of adjusted resistance versus pressure are essential. By subtraction of temperature-induced resistance change from the total resistance change at each data point, adjusted resistance versus pressure data may be obtained. For n-type, π_p is very small in each data point, as expected from the approximation $\pi_{11} \cong -2\pi_{12}$ [23]. On the other hand, for p-type, π_p obviously decreases in magnitude with rising temperature. In this chapter, a complete set of pi-coefficients (π_{11}, π_{12}, and π_{44}) may be extracted by performing hydrostatic tests.

91

CHAPTER 6

SILICON STRESS-STRAIN RELATIONS AND MEASUREMENT OF YOUNG'S

MODULUS OF SILICON

6.1   Silicon Stress-Strain Relations

Silicon exhibits linear elastic material behavior and the generalized Hooke's Law, the

most general formula of linear elastic stress-strain relations, is given by [15]:

$$\sigma_{ij} = C_{ijkl}\varepsilon_{kl} \qquad\qquad \text{Eq. (6.1.1)}$$

where σ_{ij} and ε_{kl} are the stress and strain components, and C_{ijkl} are the components of

the stiffness tensor. Inverting Eq. (6.1.1) gives

$$\varepsilon_{ij} = S_{ijkl}\sigma_{kl} \qquad\qquad \text{Eq. (6.1.2)}$$

where S_{ijkl} are the compliance components. Also, the transformation relations for the

reduced index stress and strain components can be expressed as indicated below [15]:

$$\sigma_\alpha = T_{\alpha\beta}^{-1}\sigma_\beta^{'} \qquad\qquad \text{Eq. (6.1.3)}$$

$$\varepsilon_\alpha = T_{\alpha\beta}^{t}\varepsilon_\beta^{'} \qquad\qquad \text{Eq. (6.1.4)}$$

where the coefficients $T_{\alpha\beta}$ are elements of a six by six transformation matrix related to

the direction cosines for the unprimed and primed coordinate systems. Also, note that σ_α

and ε_α are the stress and strain tensor components in the unprimed system, respectively, whereas σ'_β and ε'_β are those components in a rotated primed coordinate system. Inverting Eq. (6.1.4) leads to

$$\varepsilon' = (T^t)^{-1}\varepsilon \qquad \qquad \text{Eq. (6.1.5)}$$

If Eq. (6.1.2) is plugged into Eq. (6.1.5), the result is

$$\varepsilon' = (T^t)^{-1}S\sigma \qquad \qquad \text{Eq. (6.1.6)}$$

Finally, substitution Eq. (6.1.3) into Eq. (6.1.6) yields the relations between stress and strain in a rotated primed coordinate system as follows:

$$\varepsilon' = (T^t)^{-1}S\,T^{-1}\sigma' \qquad \qquad \text{Eq. (6.1.7)}$$

If an unprimed coordinate system is assumed, $(T^t)^{-1}$ and T^{-1} in Eq. (6.1.7) simplify to unit matrices. Thus Eq. (6.1.7) reduces down to Eq. (6.1.2).

6.2 Elastic Constants of Silicon by Equations

Very few tests have been performed on silicon. However, the three independent elastic constants, stiffness coefficients, of silicon were measured by several researchers. The relationships for the piezoresistive effect based on the strain components, and the expressions relating the piezoresistive coefficients and the elastoresistive coefficients using the elastic coefficients for cubic crystals were given in [9-10]. For instance, McSkimin [88-89] obtained those constants by using ultrasonic measurement techniques in which ultrasonic waves were transmitted into a specimen and measurement of the reflections within specimen yielded values for the velocities of wave propagation and the elastic constants. Using this technique, second-order elastic constants of single crystals

93

were experimentally measured. The first row in Table 6.1 presents the summary of literature values for the stiffness coefficients of silicon by Wortman [90]. The three compliance coefficients can be evaluated by using Eq. (6.1.6). The results are $s_{11}=7.68$ x 10^{-12} Pa^{-1}, $s_{12}=-2.14$ x 10^{-12} Pa^{-1} and $s_{44}=1.26$ x 10^{-11} Pa^{-1} as presented in the second row in Table 6.1.

Table 6.1 - Literature values for the stiffness coefficients of silicon [90]		
c_{11}	c_{12}	c_{44}
165.7 GPa	63.9 GPa	79.6 GPa
s_{11}	s_{12}	s_{44}
7.68 x 10^{-12} Pa^{-1}	-2.14 x 10^{-12} Pa^{-1}	1.26 x 10^{-11} Pa^{-1}

Another method is the use of the three compliance coefficients (s_{11}, s_{22}, and s_{44}). Based on the values in Table 6.1, the elastic modulus and Poisson's ratio can be evaluated. The cubic nature of silicon lattice leads to orthotropic properties. Hence, Young's Modulus E and Poisson's ratio ν are dependent on direction. Generally, simple isotropic values for the elastic properties are commonly used. However, in some situations, greater accuracy may be needed and achieved by employing the directional nature of these properties. Equation (6.1.7) allows direct calculation of Young's modulus. In Eq. (6.1.7),

$$
\begin{pmatrix} \sigma_1' \\ \sigma_2' \\ \sigma_3' \\ \sigma_4' \\ \sigma_5' \\ \sigma_6' \end{pmatrix} = \begin{pmatrix} \sigma_{11}' \\ \sigma_{22}' \\ \sigma_{33}' \\ \sigma_{13}' \\ \sigma_{23}' \\ \sigma_{12}' \end{pmatrix} \quad \text{and} \quad \begin{pmatrix} \varepsilon_1' \\ \varepsilon_2' \\ \varepsilon_3' \\ \varepsilon_4' \\ \varepsilon_5' \\ \varepsilon_6' \end{pmatrix} = \begin{pmatrix} \varepsilon_{11}' \\ \varepsilon_{22}' \\ \varepsilon_{33}' \\ 2\varepsilon_{13}' \\ 2\varepsilon_{23}' \\ 2\varepsilon_{12}' \end{pmatrix} = \begin{pmatrix} \varepsilon_{11}' \\ \varepsilon_{22}' \\ \varepsilon_{33}' \\ \gamma_{13}' \\ \gamma_{23}' \\ \gamma_{12}' \end{pmatrix} \qquad \text{Eq. (6.2.1)}
$$

To obtain Young's modulus in one direction (e.g., x_1), setting all other stresses to zero and solving for $\dfrac{\sigma_1'}{\varepsilon_1'}$ allows direct calculation of E_1. Similarly, setting all other stresses to zero and solving for $-\dfrac{\varepsilon_2'}{\varepsilon_1'}$ gives Poisson's ratio ν_1.

The direction cosines l_i, m_i, and n_i are required in order to determine $(T^t)^{-1}$ and T^{-1} in Eq. (6.1.7). If the conductor orientation is rotated counter-clockwise by ϕ from the specified axis (e.g., x_1' axis [110]), l_i, m_i, and n_i are determined by solving 3 simultaneous equations as follows. For instance, $i =1$

- Plane Equation: The conductor is on (001) plane.

$$
0(l_1) + 0(m_1) + 1(n_1) = 0 \;\rightarrow\; n_1 = 0 \qquad \text{Eq. (6.2.2)}
$$

- Inner Product: Note that the angle between the x_1' axis and the resistor orientation is ϕ.

$$
l_1\left(\frac{1}{\sqrt{2}}\right) + m_1\left(\frac{1}{\sqrt{2}}\right) + n_1(0) = \cos\phi \;\rightarrow\; l_1 + m_1 = \sqrt{2}\cos\phi \qquad \text{Eq. (6.2.3)}
$$

- Unit Vector: The magnitude of the unit vector is unity.

$$
\sqrt{(l_1^2 + m_1^2 + n_1^2)} = 1 \qquad \text{Eq. (6.2.4)}
$$

There are two roots in these simultaneous equations. It may be noted that one of two corresponds to the root for the clockwise rotation.

For the following discussion, the geometry for silicon wafers of interest here is given in Fig. 6.1. Miller indices are introduced to describe directions and planes in crystal. The rules for selecting the crystallographic axes are presented in [93].
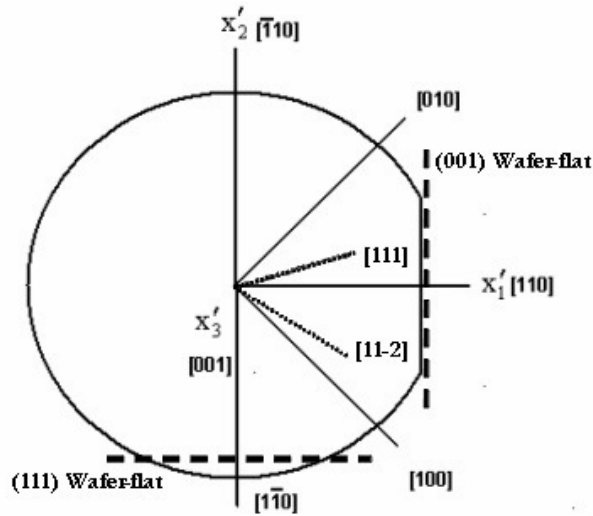
Fig. 6.1 - Silicon wafer geometry

For the (001) plane, the direction cosines are

$$
\begin{bmatrix} l_1 & m_1 & n_1 \\ l_2 & m_2 & n_2 \\ l_3 & m_3 & n_3 \end{bmatrix} = \begin{bmatrix} \cos(\phi + \frac{\pi}{4}) & \sin(\phi + \frac{\pi}{4}) & 0 \\ \cos(\phi + \frac{\pi}{4} + \frac{\pi}{2}) & \sin(\phi + \frac{\pi}{4} + \frac{\pi}{2}) & 0 \\ 0 & 0 & 1 \end{bmatrix}
$$

$$
= \begin{bmatrix} \cos(\phi + \frac{\pi}{4}) & \sin(\phi + \frac{\pi}{4}) & 0 \\ -\sin(\phi + \frac{\pi}{4}) & \cos(\phi + \frac{\pi}{4}) & 0 \\ 0 & 0 & 1 \end{bmatrix}
$$

Eq. (6.2.5)

where ϕ is the angle of counter-clockwise rotation from the $x_1^{'}$ axis [110]. By Eq. (6.1.7), E and ν are expressed as

$$E = \frac{4}{2[1 + \sin^2(2\phi)s_{11} + 2\cos^2(2\phi)s_{12} + \cos^2(2\phi)s_{44}]} \qquad \text{Eq. (6.2.6)}$$

$$\nu_{12} = -\frac{\varepsilon_2^{'}}{\varepsilon_1^{'}} = -\frac{2\cos^2(2\phi)s_{11} + 2[1 + \sin^2(2\phi)]s_{12} - \cos^2(2\phi)s_{44}}{2[1 + \sin^2(2\phi)]s_{11} + 2\cos^2(2\phi)s_{12} + \cos^2(2\phi)s_{44}} \qquad \text{Eq. (6.2.7)}$$

In Eqs. (6.2.6) and (6.2.7), the periods of E and ν on the (001) silicon plane are $\frac{\pi}{2}$ respectively (see Figs. 6.2-6.5). The maximum and the minimum values of E are 169.1 GPa and 130.1 GPa respectively. For ν, the maximum and the minimum values are 0.278 and 0.062 respectively. E and ν show anisotropic characteristics on the (001) silicon plane. Note that three compliance coefficients s_{11}, s_{22}, and s_{44} are based on the literature value of stiffness coefficients c_{11}, c_{22}, and c_{44} from Wortman [90].
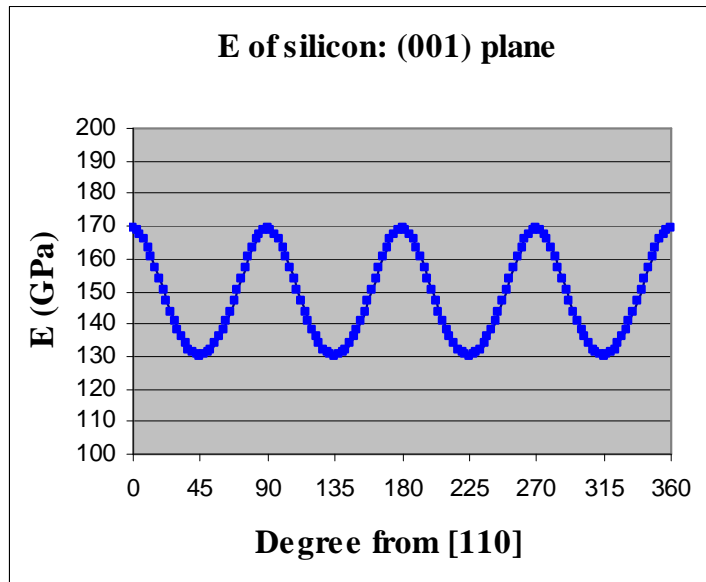
Fig. 6.2 - E on the (001) silicon
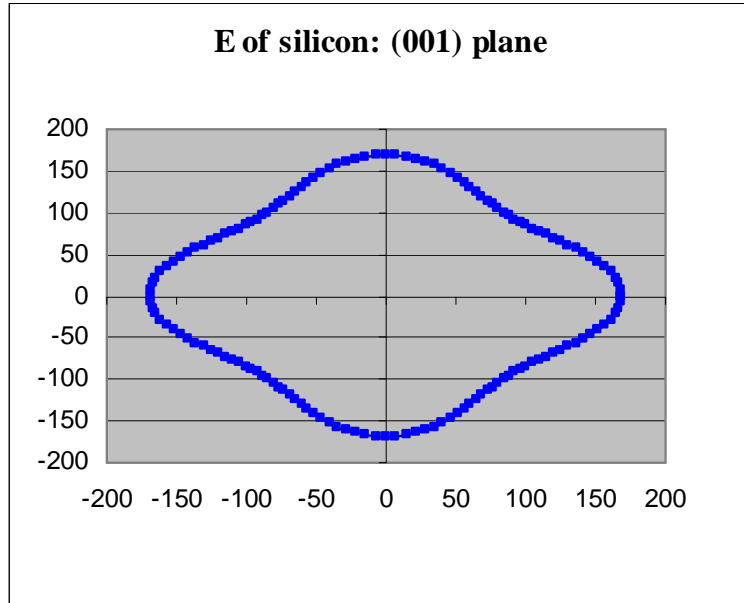
Fig. 6.3 - E on the (001) silicon
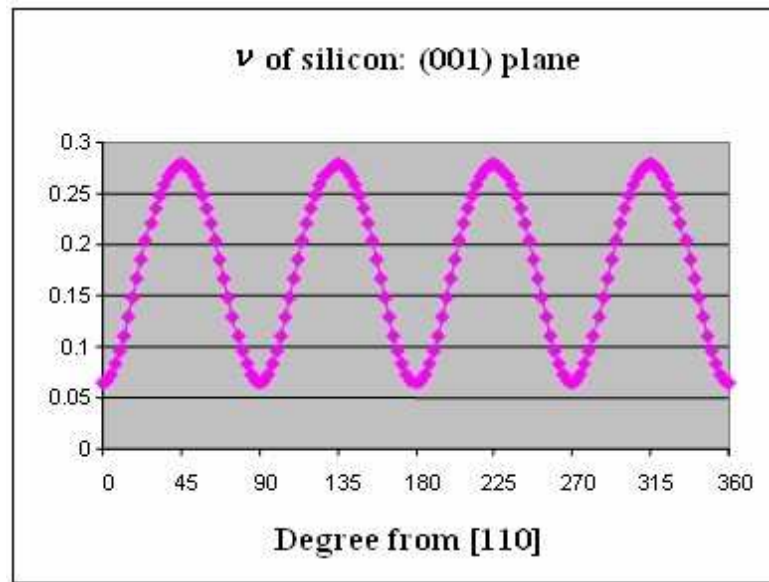
Fig. 6.4 - ν on the (001) silicon
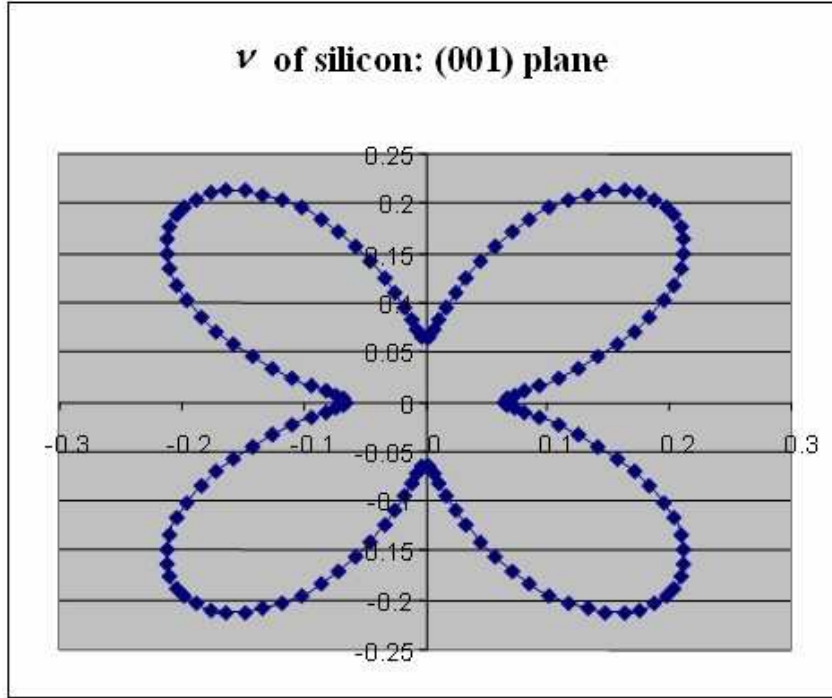
Fig. 6.5 - ν on the (001) silicon

E and ν of the (001) silicon at varying angular locations with respect to [110] axis are

plotted in Figs. 6.2 through 6.5. For example, the positive x-axis is the [110] direction

and 45° represents the [010] direction. Similarly, -45° is the [100] direction.

On the (111) silicon plane, the direction cosines are

$$
\begin{bmatrix} l_1 & m_1 & n_1 \\ l_2 & m_2 & n_2 \\ l_3 & m_3 & n_3 \end{bmatrix} = \begin{bmatrix} \dfrac{\sin\phi}{\sqrt{6}} + \dfrac{\cos\phi}{\sqrt{2}} & \dfrac{\sin\phi}{\sqrt{6}} - \dfrac{\cos\phi}{\sqrt{2}} & \dfrac{-2\sin\phi}{\sqrt{6}} \\ -\dfrac{\sin\phi}{\sqrt{2}} + \dfrac{\cos\phi}{\sqrt{6}} & \dfrac{\sin\phi}{\sqrt{2}} + \dfrac{\cos\phi}{\sqrt{6}} & \dfrac{-2\cos\phi}{\sqrt{6}} \\ 1 & 1 & 1 \end{bmatrix} \qquad \text{Eq. (6.2.8)}
$$

where ϕ is the angle of counter-clockwise rotation from the x'_1 axis $[1\bar{1}0]$. By Eq. (6.1.7),

E and ν are given by

$$E = \frac{4}{2s_{11} + 2s_{12} + s_{44}} \qquad\qquad \text{Eq. (6.2.9)}$$

$$\nu_{12} = -\frac{\varepsilon_2'}{\varepsilon_1'} = -\frac{2s_{11} + 10s_{12} - s_{44}}{6s_{11} + 6s_{12} + 3s_{44}} \qquad\qquad \text{Eq. (6.2.10)}$$

In Eqs. (6.2.9) and (6.2.10), the periods of E and ν are infinity. That is, E and ν are constant with ϕ as shown in Figs. 6.6 through 6.9, where E and ν exhibits an isotropic characteristic on the (111) silicon plane where the elastic properties (E and ν) are independent of direction (E = 169.1 GPa, ν = 0.262).
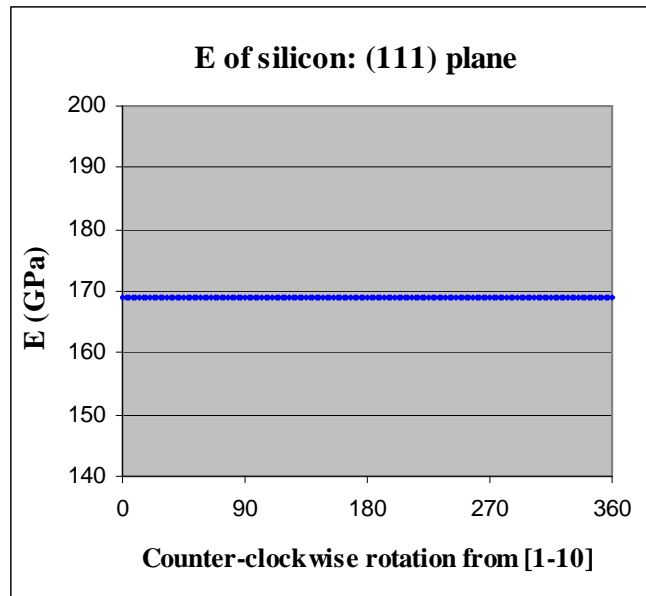
Fig. 6.6 - E on the (111) silicon
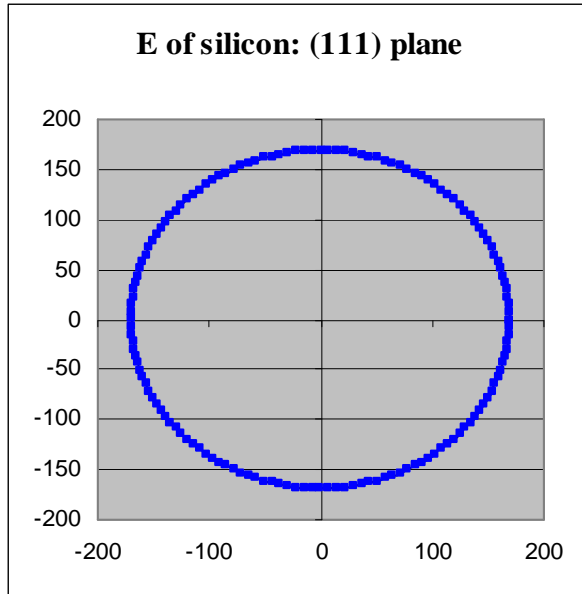
Fig. 6.7 - E on the (111) silicon

Fig. 6.8 - ν on the (111) silicon

101
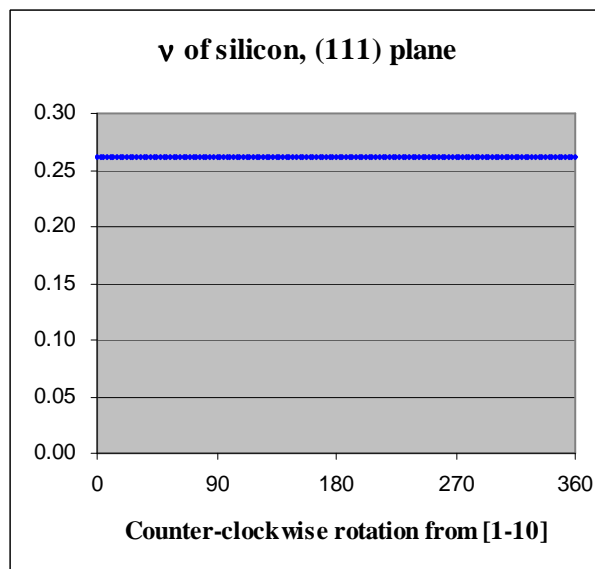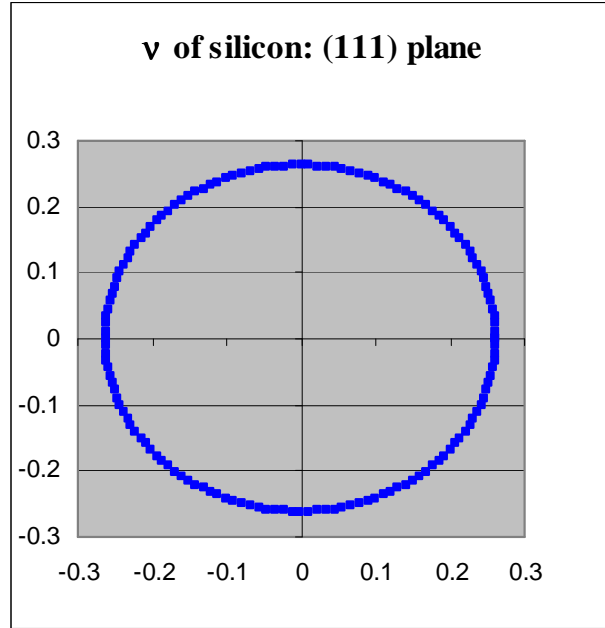
Fig. 6.9 - ν on the (111) silicon

For the $(1\bar{1}0)$ plane, if we assume that ϕ is the angle of clockwise rotation from the axis [111], the direction cosines are

$$\begin{bmatrix} l_1 & m_1 & n_1 \\ l_2 & m_2 & n_2 \\ l_3 & m_3 & n_3 \end{bmatrix} = \begin{bmatrix} \dfrac{\sin\phi}{\sqrt{6}} + \dfrac{\cos\phi}{\sqrt{3}} & \dfrac{\sin\phi}{\sqrt{6}} + \dfrac{\cos\phi}{\sqrt{3}} & \dfrac{-2\sin\phi}{\sqrt{6}} + \dfrac{\cos\phi}{\sqrt{3}} \\ \dfrac{-\sin\phi}{\sqrt{3}} + \dfrac{\cos\phi}{\sqrt{6}} & \dfrac{-\sin\phi}{\sqrt{3}} + \dfrac{\cos\phi}{\sqrt{6}} & \dfrac{-\sin\phi}{\sqrt{3}} - \dfrac{2\cos\phi}{\sqrt{6}} \\ \dfrac{1}{\sqrt{2}} & -\dfrac{1}{\sqrt{2}} & 0 \end{bmatrix}$$ Eq. (6.2.11)

If $\phi = 0$,

$$\begin{bmatrix} l_1 & m_1 & n_1 \\ l_2 & m_2 & n_2 \\ l_3 & m_3 & n_3 \end{bmatrix} = \begin{bmatrix} \dfrac{1}{\sqrt{3}} & \dfrac{1}{\sqrt{3}} & \dfrac{1}{\sqrt{3}} \\ \dfrac{1}{\sqrt{6}} & \dfrac{1}{\sqrt{6}} & \dfrac{2}{\sqrt{6}} \\ \dfrac{1}{\sqrt{2}} & -\dfrac{1}{\sqrt{2}} & 0 \end{bmatrix} \qquad \text{Eq. (6.2.12)}$$

By Eq. (6.1.7), E and ν on the $(1\bar{1}0)$ silicon plane are given by

$$E = \frac{1}{s_{11} - 36(2s_{11} - 2s_{12} - s_{44})[(1+\cos^2\phi)^2 + 8 + 6\sqrt{2}\sin2\phi \dfrac{(\sin^2\phi - 5\sqrt{2}\sin2\phi)}{12}]} \qquad \text{Eq. (6.2.13)}$$

$$\nu_{12} = -\frac{\varepsilon_2'}{\varepsilon_1'} = -\frac{s_{12} + (s_{11} - s_{12} - \dfrac{s_{44}}{2})(12 - \dfrac{21}{2}\sin^2 2\phi - 3\sqrt{2}\sin4\phi)}{s_{11} - 36(2s_{11} - 2s_{12} - s_{44})[(1+\cos^2\phi)^2 + 8 + 6\sqrt{2}\sin2\phi \dfrac{(\sin^2\phi - 5\sqrt{2}\sin2\phi)}{12}]} \qquad \text{Eq. (6.2.14)}$$

Similarly, the periods of E and ν on the $(1\bar{1}0)$ silicon plane are π, respectively, as shown in Figs. 6.10 and 6.11. The maximum and minimum values of E are 187.9 GPa and 130.1 GPa respectively. For ν, the maximum and minimum values are 0.35 and 0.15 respectively. E and ν are dependent on the direction on the $(1\bar{1}0)$ silicon plane. For example, E and ν of [111] direction are 187.9 GPa and 0.180 respectively.
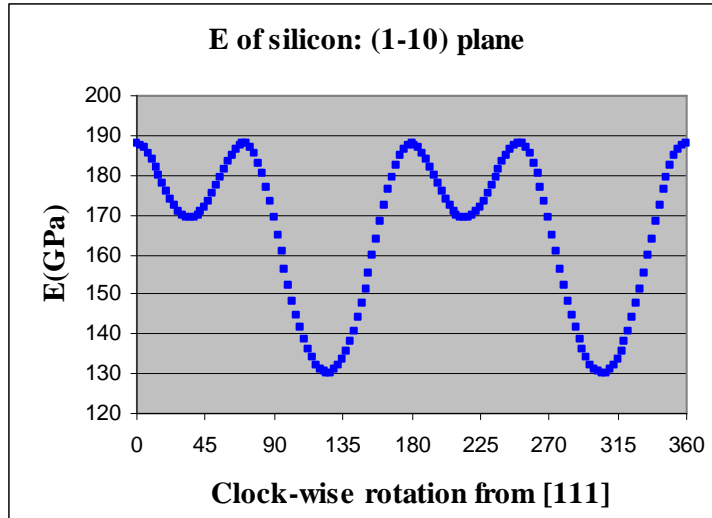
Fig. 6.10 - E on the $(1\bar{1}0)$ silicon

Fig. 6.11 - ν on the $(1\bar{1}0)$ silicon

104
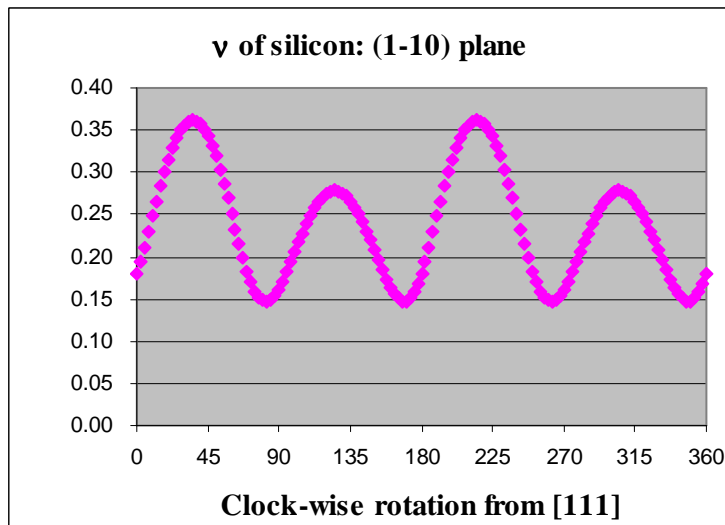
In summary:

- For any crystallographic direction of silicon, E and ν may be expressed in terms of compliance coefficients (s_{11}, s_{12}, and s_{44}).

- E and ν are dependent on the direction of the silicon.

It should be noted that E and ν are based on the literature values of stiffness coefficients, c_{11}, c_{12}, and c_{44} from Wortman [90]. Further, using other literature values of stiffness coefficients from different authors, E values are presented and compared in Table 6.2.

Table 6.2 - E values for different directions and different authors (Unit: GPa)							
Author\Direction	[100]	[010]	[001]	[110]	[1-10]	[11-2]	[111]
Mcskimi	130.80	130.80	130.80	169.71	169.71	169.71	188.38
Wortman	130.13	130.13	130.13	169.10	169.10	169.10	187.85
Hall	130.02	130.02	130.02	168.96	168.96	168.96	187.68

6.3   Measurement of the Elastic Constants by Deflection of Beams

Kang [15] used a strain gauge technique to measure E of silicon using a four-point bending fixture in which strain gauges are mounted on the surface of specimen strips. Usually, a micro-tester has been used to measure E. However, due to some limitations of a micro-tester for measuring E of stiff materials such as silicon, the *"Deflection of Beams"* theorem [91] with a four-point bending fixture is introduced, as presented in Fig. 6.12, in our analysis.
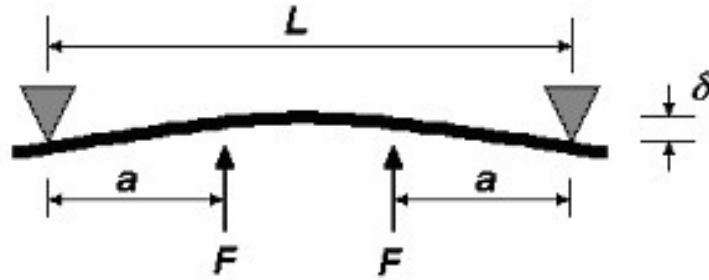
Fig. 6.12 - Deflection of a beam in a four-point bending fixture

In Fig. 6.12, L is the distance between two supports and the deflection at distance "a" from the adjacent support is

$$\delta = \frac{Fa^2(3L-4a)}{6EI} \qquad \text{Eq. (6.3.1)}$$

In Eq. (6.3.1), the new notation F' is defined as

$$F' \equiv \frac{Fa^2(3L-4a)}{6I} \qquad \text{Eq. (6.3.2)}$$

where the moment of inertia I is defined as $\frac{bh^3}{12}$ for the rectangular of beam in which b is the width and h is the thickness of the beam. Deflection δ may be measured by reading a micro-positioner. The applied force F is measured by a load-cell. In our case, the sensitivity shows 8.58 x 10^{-3} mV/gram. Combining Eq. (6.3.1) and Eq. (6.3.2) yields $F' = \delta E$ where E is easily obtained by evaluating the slope of δ with respect to F'. An Example is presented in Table 6.3.

δ (μm)	load cell (mV)	W (gram)	F (N)	F'
0	55.691	0.00	0.0000	0.00E+00
50	55.901	24.5	0.1199	6.35E+12
100	56.117	49.7	0.2433	1.29E+13
150	56.333	74.8	0.3666	1.94E+13
200	56.554	100.6	0.4929	2.61E+13
250	56.772	126.0	0.6174	3.27E+13

Table 6.3 - Example: Measurement of E using deflection of beams

In these measurements, L = 6.05 cm, a = 1.20 cm, b = 1.016 cm (= 400 mil), and h = 6.35 x 10^{-2} cm (= 25 mil), respectively. In order to obtain E, F' in Eq. (6.3.3) is plotted with respect to δ as shown in Fig. 6.13.

E calculation by deflection: $E_{[100]}$

y = 1.302E+11x
R^2 = 9.999E-01
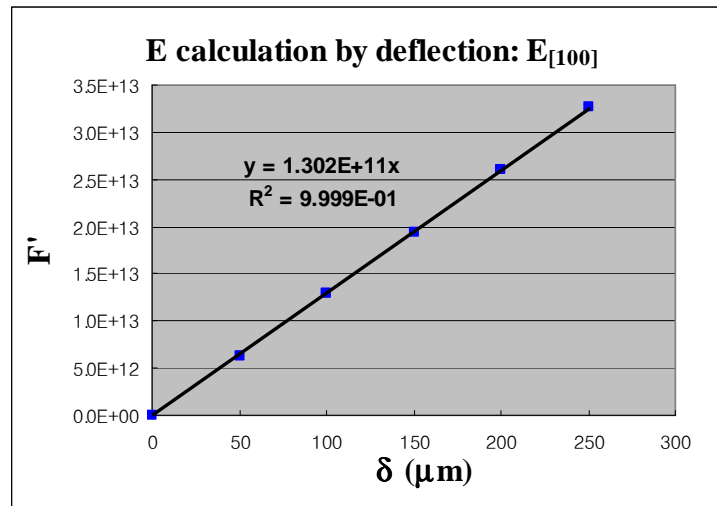
Fig. 6.13 - Plot of F' with respect to δ

Further, extensive measurements are performed for several directions of silicon. For each direction, 10 specimens are measured. Comparing the measured values in Table 6.4 with the literature values in Table 6.2, one finds a good agreement. In Table 6.4, E for the

[100] direction is 130.0 GPa, but E for the [110], [$\bar{1}$10], [1$\bar{1}$0], and [11$\bar{2}$] directions are about 169 GPa. It may be noted that $E_{[100]}$ = 132.8 GPa and $E_{[110]}$ = 170.3 GPa from the literature [15].

Table 6.4 - Measurement of E for several directions of silicon (Unit: GPa)				
#\Direction	$E_{[100]}$	$E_{[110]}$	$E_{[-110]}$	$E_{[1-10]}$	$E_{[11-2]}$
1	130.2	168.7	168.4	168.4	167.0
2	130.6	166.9	171.1	169.6	168.9
3	131.6	167.8	166.6	167.1	170.2
4	125.9	165.5	169.4	169.0	169.6
5	130.3	167.6	169.1	169.4	169.2
6	130.9	167.8	165.3	170.1	169.1
7	130.2	167.7	166.3	170.4	170.7
8	129.6	166.9	166.7	170.5	171.0
9	130.6	169.6	171.2	169.2	171.3
10	129.8	167.1	170.6	169.5	170.6
Avg.	130.0	167.6	168.5	169.3	169.8
Std.	1.53	1.09	2.16	1.00	1.28

In Table 6.5, the temperature dependence of E for the [11$\bar{2}$] direction is presented. For this work, a special four-point bending apparatus was constructed and integrated into an environmental chamber capable of temperatures from -185 ^{o}C to +300 ^{o}C. As expected, it is observed that E for the [11$\bar{2}$] direction decreases monotonically with increasing temperature over the temperature range -150 ^{o}C to +150 ^{o}C as plotted in Fig. 6.14.

Table 6.5 - E for the $[11\bar{2}]$ direction on the (111) silicon versus temperature (Unit: GPa)									
#\T(°C)	-133.4	-93.2	-48.2	0.6	25.1	49.9	75.1	100.6	125.9	151.5
1	173.9	172.7	171.4	168.7	168.0	167.0	166.5	165.5	164.3	164.2
2	174.1	172.2	170.6	169.8	168.2	168.0	166.7	166.0	165.6	165.5
3	173.8	172.1	172.0	169.6	168.8	169.4	169.0	167.9	166.4	165.9
4	173.6	172.2	169.2	168.5	168.9	168.8	168.0	168.2	167.7	164.2
5	172.5	172.8	170.4	169.6	169.6	169.3	168.1	166.2	167.4	164.2
6	173.4	173.3	171.4	170.0	168.2	167.5	166.9	167.8	166.0	165.0
7	171.6	172.5	171.3	169.7	170.7	169.7	168.5	166.4	168.1	167.1
8	170.5	170.1	171.4	170.3	169.6	168.7	168.6	167.0	167.0	165.6
9	170.7	171.9	171.9	170.8	170.5	168.6	168.6	166.7	167.1	166.2
10	174.5	173.4	169.6	168.2	168.5	168.0	167.7	168.0	166.6	166.7
Avg.	172.9	172.3	170.9	169.5	169.1	168.5	167.9	167.0	166.6	165.5
Std.	1.45	0.91	0.95	0.81	0.97	0.88	0.88	0.94	1.12	1.05
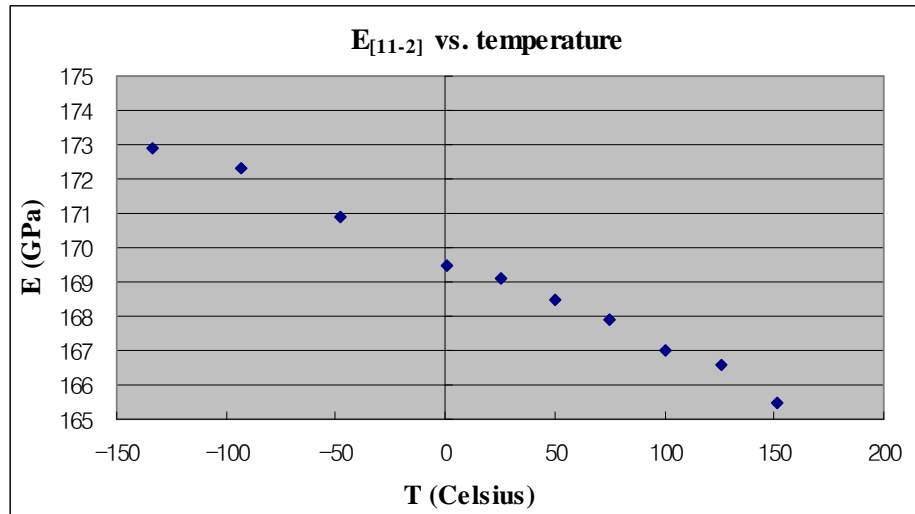
Fig. 6.14 - Plot of E for the $[11\bar{2}]$ direction on the (111) silicon versus temperature

Also, E for PCB material (FR-406) is measured over temperatures ranging from -133 °C to +151 °C as shown in Table 6.6. In this work, 10 specimens are used.

#\T(°C)	-133.4	-93.2	-48.2	0.6	25.1	49.9	75.1	100.6	125.9	151.5

Table 6.6 - E for FR-406 versus temperature (Unit: GPa)

#\T(°C)	-133.4	-93.2	-48.2	0.6	25.1	49.9	75.1	100.6	125.9	151.5
1	27.4	24.8	24.9	24.7	23.6	21.2	19.1	19.0	17.0	14.9
2	27.8	26.1	25.3	24.8	22.6	22.9	20.7	18.6	16.6	14.8
3	27.0	26.0	25.2	24.4	22.2	20.9	19.1	18.6	16.7	15.0
4	27.2	25.7	24.3	24.4	23.5	22.0	21.5	17.6	16.7	15.0
5	27.9	25.8	25.4	24.4	25.1	21.8	20.0	18.7	17.1	16.3
6	26.7	25.5	24.2	24.1	24.5	22.3	20.4	17.6	15.4	13.1
7	27.6	26.3	25.4	25.0	23.4	22.2	20.8	19.3	15.6	16.4
8	26.8	25.0	25.0	24.6	24.3	23.1	20.0	19.4	16.7	15.2
9	27.9	26.2	25.5	25.0	24.3	21.6	21.5	18.9	15.9	14.4
10	27.8	25.3	25.1	24.5	23.8	22.5	19.5	17.7	16.0	13.6
Avg.	27.4	25.7	25.0	24.6	23.7	22.1	20.3	18.6	16.4	14.9
Std.	0.46	0.52	0.46	0.29	0.87	0.70	0.88	0.68	0.59	1.02

Similarly, E for FR-406 with temperatures is plotted as shown in Fig. 6.15.
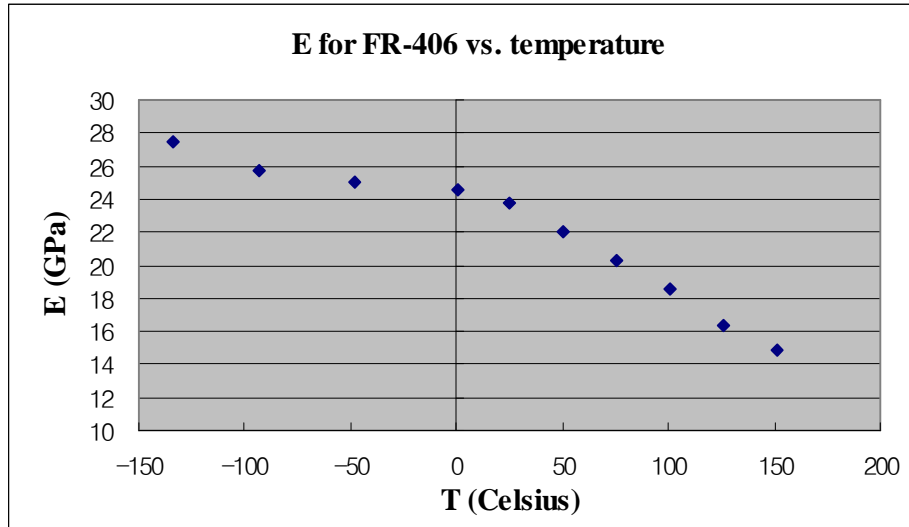
Fig. 6.15 - Plot of E for FR-406 versus temperature

Similarly, E for die attachment adhesive (ME 525) are measured over temperatures ranging from -150 °C to +150 °C as shown in Table 6.9 and its plot is shown in Fig. 6.16.

Table 6.7 - E of ME 525 versus temperature (Unit: GPa)	
T (Celsius)	ME 525
-151.0	19.81
-133.4	18.46
-93.2	15.99
-48.2	13.70
0.6	12.00
25.1	10.43
49.9	9.85
75.1	8.75
100.6	7.72
125.9	4.98
151.5	0.89
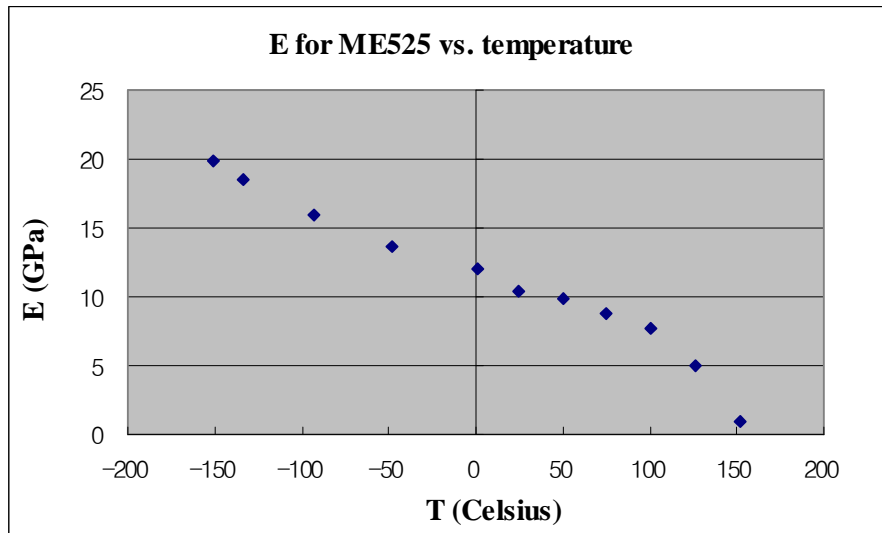
Fig. 6.16 - Plot of E for ME525 versus temperature

E for the composite materials of the chip-on-beam samples for varying temperatures are summarized in Table 6.8.

Table 6.8 - Summary: Measurement of E vs. temperature (Unit: GPa)			
T (Celsius)	ME 525	(111)silicon:$[11\overline{2}]$	FR-406
-133.4	18.46	172.9	27.41
-93.2	15.99	172.3	25.57
-48.2	13.70	170.9	25.12
0.6	12.00	169.5	24.68
25.1	10.43	169.1	23.73
49.9	9.85	168.5	22.05
75.1	8.75	167.9	20.26
100.6	7.72	167.0	18.55
125.9	4.98	166.6	16.37
151.5	0.98	165.5	14.87

In this work, E values for silicon are calculated analytically and those values are in agreement with experimental results. The expressions of E and ν for each direction are summarized in Table 6.9 in which analytic values of E are compared with experimental values.

Table 6.9 - The expressions of E and ν for each direction of silicon

Direction	E & theoretical value [GPa]		Measurement	ν & theoretical value & transverse direction	
$E_{[100]}$	$1/s_{11}$	:130.13	129.96	$-s_{12}/s_{11}$ transverse direction: [010]	:0.278
$E_{[001]}$	$1/s_{11}$	:130.13	NA	$-s_{12}/s_{11}$ transverse direction: [010]	:0.278
$E_{[010]}$	$1/s_{11}$	:130.13	NA	$-s_{12}/s_{11}$ transverse direction: [100]	:0.278
$E_{[110]}$	$4/(2s_{11}+2s_{12}+s_{44})$	:169.10	167.55	$(-2s_{11}-2s_{12}+s_{44})/(2s_{11}+2s_{12}+s_{44})$ transverse direction: [1-10]	:0.062
$E_{[1-10]}$	$4/(2s_{11}+2s_{12}+s_{44})$	:169.10	169.32	$(-2s_{11}-2s_{12}+s_{44})/(2s_{11}+2s_{12}+s_{44})$ transverse direction: [110]	:0.062
$E_{[111]}$	$3/(s_{11}+2s_{12}+s_{44})$	:187.85	NA	$(-2s_{11}-4s_{12}+s_{44})/(2s_{11}+4s_{12}+2s_{44})$ transverse direction: [11-2]	:0.180
$E_{[11-2]}$	$4/(2s_{11}+2s_{12}+s_{44})$	:169.10	169.80	$(-2s_{11}-10s_{12}+s_{44})/(6s_{11}+6s_{12}+3s_{44})$ transverse direction: [1-10]	: 0.262

6.4   Summary

In this chapter, it is observed that the cubic nature of the single crystal silicon lattice leads to orthotropic material properties--that is, E (*Young's modulus*) and ν (*Poisson's ratio*) are dependent upon the direction on the silicon surface. For any crystallographic direction of silicon, E and ν may be expressed by compliance coefficients (s_{11}, s_{12}, and s_{44}).   In this work, E of silicon has been calculated analytically, and calculations are in agreement with experimental value by using "*Deflection of Beams*" method.   In addition, E values of the other composite materials comprising the chip-on-beam specimens were obtained by this method.

CHAPTER 7

VAN DER PAUW STRUCTURE

7.1   Van der Pauw's Theorem

Van der Pauw's theorem is used to measure the specific resistivity of an arbitrary shaped sample of constant thickness without isolated holes [78-80]. A flat sample of conducting material with uniform thickness is shown in Fig. 7.1 where A, B, C, and D are contacts on the conducting material. Also, a simple structure is shown in Fig. 7.2.
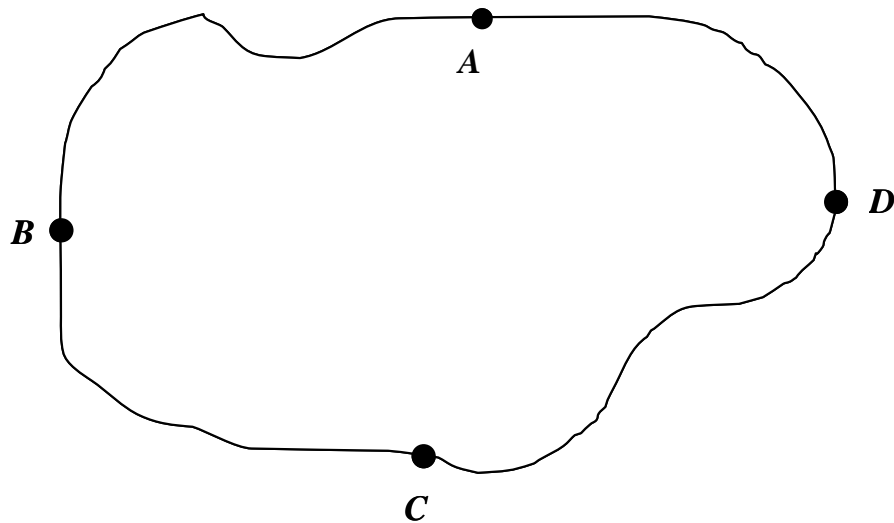
Fig. 7.1 - A flat sample of conducting material with uniform thickness
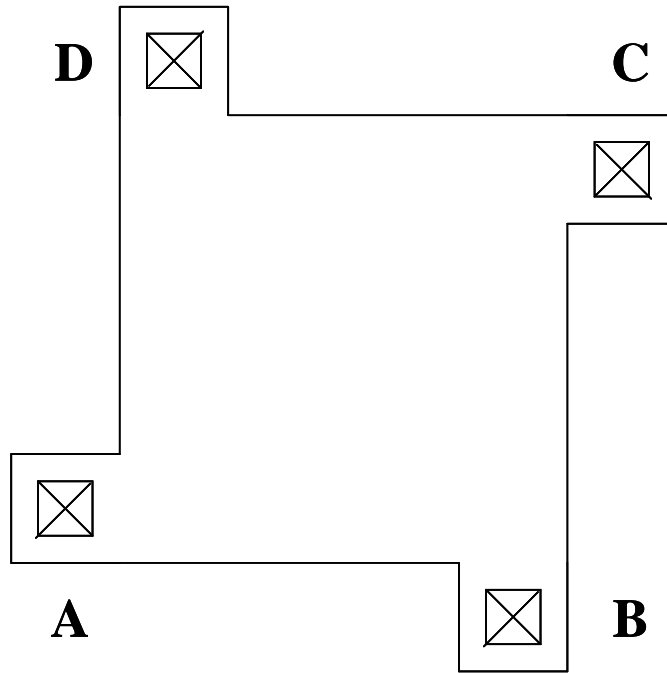
Fig. 7.2 - A simple van der Pauw test structure

A current is injected through one pair of the contacts, and the voltage is measured across another pair of contacts. $R_{AB,CD}$ is defined as the potential difference between the contacts D and C divided by the current through contacts A and B. For an isotropic conductor, Van der Pauw [78] demonstrated that two of theses measurement may be related by

$$\exp(-\frac{\pi t R_{AB,CD}}{\rho}) + \exp(-\frac{\pi t R_{BC,DA}}{\rho}) = 1 \qquad \text{Eq. (7.1.1)}$$

where t is the thickness of the sample and ρ is the isotropic resistivity. For an isotropic conductor, $R_{AB,CD} = R_{BC,DA}$. Hence, Eq. (7.1.1) can be simplified to

$$\rho = \frac{\pi t}{\ln 2} R_{AB,CD} \qquad \text{Eq. (7.1.2)}$$

The equation of the sheet resistance R_S may be calculated using Eq. (7.1.2)

$$R_S = \frac{\rho}{t} = \frac{\pi}{\ln 2} R_{AB,CD}$$

Eq. (7.1.3)

The sheet resistance R_S in Eq. (7.1.3) depends on $R_{AB,CD}$. With no information of t, the sheet resistance may be calculated. In addition, Van der Pauw [79-80] also extended Eq. (7.1.1) to the following equation for anisotropic conductors of constant thickness:

$$\exp\left(-\frac{\pi t R_{AB,CD}}{\sqrt{\rho_1 \rho_2}}\right) + \exp\left(-\frac{\pi t R_{BC,DA}}{\sqrt{\rho_1 \rho_2}}\right) = 1$$

Eq. (7.1.4)

where ρ_1 and ρ_2 are the components of principal resistivity.

Price [81-82] developed the resistance equations for rectangular isotropic conductors:

$$R_{AB,CD} = -\frac{8\rho}{\pi t} \ln \prod_{n=0}^{\infty} \left\{ \tanh\left[\frac{BC}{AB}(2n+1)\frac{\pi}{2}\right] \right\}$$

Eq. (7.1.5)

$$R_{AD,CB} = -\frac{8\rho}{\pi t} \ln \prod_{n=0}^{\infty} \left\{ \tanh\left[\frac{AB}{BC}(2n+1)\frac{\pi}{2}\right] \right\}$$

Eq. (7.1.6)

where $AB = a$ and $BC = b$ are the length of the sides of the rectangle shown in Fig. 7.3.
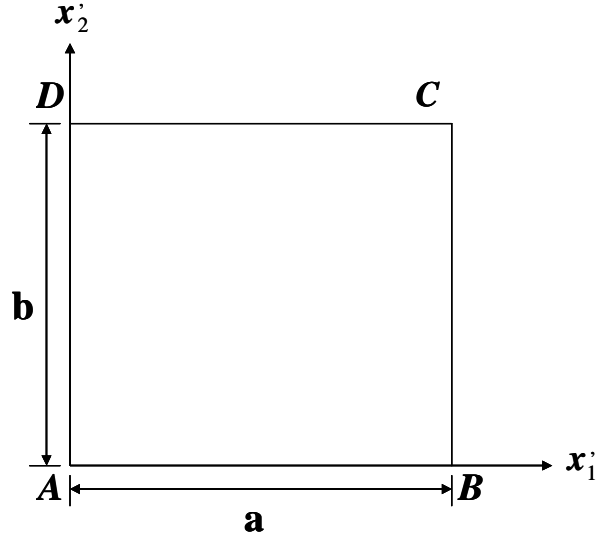
Fig. 7.3 - Isotropic rectangular VDP structure

For anisotropic conductors, Price [81-82] extended Eq. (7.1.5) and Eq. (7.1.6) as follows:

$$R_{AB,CD} = -\frac{8\sqrt{\rho'_{11}\rho'_{22}}}{\pi t}\ln\prod_{n=0}^{\infty}\{\tanh[\sqrt{\frac{\rho'_{22}}{\rho'_{11}}}\frac{BC}{AB}(2n+1)\frac{\pi}{2}]\} \qquad \text{Eq. (7.1.7)}$$

$$R_{AD,BC} = -\frac{8\sqrt{\rho'_{11}\rho'_{22}}}{\pi t}\ln\prod_{n=0}^{\infty}\{\tanh[\sqrt{\frac{\rho'_{11}}{\rho'_{22}}}\frac{AB}{BC}(2n+1)\frac{\pi}{2}]\} \qquad \text{Eq. (7.1.8)}$$

where ρ'_{11} and ρ'_{22} are resistivity components of the principal axes.

Mian [49-50] demonstrated that the resistance of $0°$ and $90°$ VDP can be represented as

$$R_0 = -\frac{8\sqrt{\rho'_{11}\rho'_{22} - \rho'_{12}}}{\pi t}\ln\prod_{n=0}^{\infty}\{\tanh[\sqrt{\frac{\rho'_{22}}{\rho'_{11}}}\frac{BC}{AB}(2n+1)\frac{\pi}{2}]\} \qquad \text{Eq. (7.1.9)}$$

$$R_{90} = -\frac{8\sqrt{\rho'_{11}\rho'_{22} - \rho'_{12}}}{\pi t}\ln\prod_{n=0}^{\infty}\{\tanh[\sqrt{\frac{\rho'_{11}}{\rho'_{22}}}\frac{AB}{BC}(2n+1)\frac{\pi}{2}]\} \qquad \text{Eq. (7.1.10)}$$

Similarly, for $\phi = 45$ ($+45°/-45°$ VDP) [49-50],

117

$$R_{45} = -\frac{8\sqrt{\rho_{11}'\rho_{22}' - \rho_{12}'}}{\pi t} \ln \prod_{n=0}^{\infty} \{\tanh[\sqrt{\frac{\rho_{11}' + \rho_{22}' - 2\rho_{12}'}{\rho_{11}' + \rho_{22}' + 2\rho_{12}'}} \frac{BC}{AB}(2n+1)\frac{\pi}{2}]\} \quad \text{Eq. (7.1.11)}$$

$$R_{-45} = -\frac{8\sqrt{\rho_{11}'\rho_{22}' - \rho_{12}'}}{\pi t} \ln \prod_{n=0}^{\infty} \{\tanh[\sqrt{\frac{\rho_{11}' + \rho_{22}' + 2\rho_{12}'}{\rho_{11}' + \rho_{22}' - 2\rho_{12}'}} \frac{AB}{BC}(2n+1)\frac{\pi}{2}]\} \quad \text{Eq. (7.1.12)}$$

For the (001) silicon wafer, in-plane components of resistivity tensor are [49-50]

$$\rho_{11}' = \rho[1 + \frac{\pi_{11} + \pi_{12} + \pi_{44}}{2}\sigma_{11}' + \frac{\pi_{11} + \pi_{12} - \pi_{44}}{2}\sigma_{22}' + \pi_{12}\sigma_{33}']$$

$$\rho_{22}' = \rho[1 + \frac{\pi_{11} + \pi_{12} - \pi_{44}}{2}\sigma_{11}' + \frac{\pi_{11} + \pi_{12} + \pi_{44}}{2}\sigma_{22}' + \pi_{12}\sigma_{33}'] \qquad \text{Eq. (7.1.13)}$$

$$\rho_{12}' = \rho[(\pi_{11} - \pi_{12})\sigma_{12}']$$

where π_{11}, π_{12}, and π_{44} are the unique piezoresistive coefficients of silicon. Also, σ_{ij}' are the stress components in the primed coordinate system. The function of temperature coefficient of resistance (TCR) is $f(\Delta T)$, and ΔT is the temperature change from the reference temperature where the isotropic resistivity ρ is evaluated.

For the (111) silicon wafer in-plane components of resistivity tensor are given by [49-50]

$$\rho_{11}' = \rho[1 + B_1\sigma_{11}' + B_2\sigma_{22}' + B_3\sigma_{33}' - 2\sqrt{2}(B_2 - B_3)\sigma_{23}']$$

$$\rho_{22}' = \rho[1 + B_2\sigma_{11}' + B_1\sigma_{22}' + B_3\sigma_{33}' + 2\sqrt{2}(B_2 - B_3)\sigma_{23}'] \qquad \text{Eq. (7.1.14)}$$

$$\rho_{12}' = \rho[2\sqrt{2}(B_3 - B_2)\sigma_{13}' + (B_1 - B_2)\sigma_{12}']$$

where B_1, B_2, and B_3 are a set of combined piezoresistive parameters that are related with the on-axis piezoresistive coefficients by

$$B_1 = \frac{\pi_{11} + \pi_{12} + \pi_{44}}{2}, \ B_2 = \frac{\pi_{11} + 5\pi_{12} - \pi_{44}}{6}, \ B_3 = \frac{\pi_{11} + 2\pi_{12} - \pi_{44}}{3} \quad \text{Eq. (7.1.15)}$$

The resistivity values change with applied stress in Eq. (7.1.13) and Eq. (7.1.14), which makes the resistance of a given VDP structure change with applied stress. This fact indicates that VDP stress sensors may be used as potential sensors.

7.2   Experimental Results for the (111) Silicon

Figure 7.4 shows the layout of the BMW-2.1 test chip in which the resistor rosette sensors and VDP test structures are fabricated on the (111) silicon surfaces. Rectangular strips, each strip containing a series of chips, are cut along x'_{11} axis (σ'_{11} direction in Fig. 7.4) from BMW-2.1 test wafers. Measurements are performed by loading a strip in a four-point bending fixture to apply uniaxial stress. For the VDP sensors as well as resistor sensors, R_0 and R_{90} are measured at various load conditions and are plotted as a function of the applied stress. Injected through one pair of electrodes is 100 μA in Fig. 7.4 in which 4 pads (electrodes) are numbered from 1 to 4. For example, in the case of R_0 of the VDP sensors, a current is injected through 1 and 4 or 2 and 3. Similarly, for R_{90} of the VDP sensors, a current is injected through 1 and 2 or 3 and 4. The potential difference between two electrodes is measured and the VDP resistance R_ϕ is calculated by dividing the potential difference by the injected current. All the steps are controlled by using a parametric analyzer.
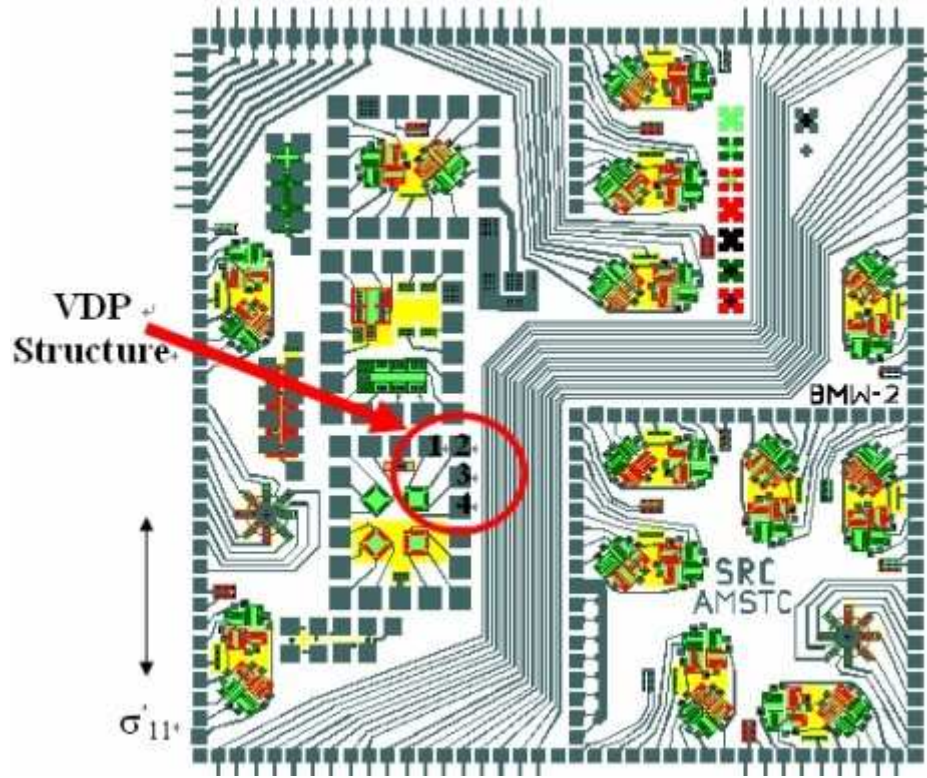
Fig. 7.4 - The (111) silicon test chip, BMW-2.1

The resistances of VDP sensors, as well as resistor sensors, are measured under unstressed and stressed conditions. The normalized resistance changes are evaluated using

$$\frac{\Delta R_\phi}{R_\phi} \equiv \frac{R_\phi(\sigma, \Delta T) - R_\phi(0,0)}{R_\phi(0,0)} \qquad \text{Eq. (7.2.1)}$$

where $R_\phi(0,0)$ is the unstressed resistance. For sensors on the (111) surface, the expression for a resistor sensor at angle ϕ with respect to the $x_1^{'}$ axis is given as follows:

$$\frac{\Delta R}{R} = [B_1\sigma_{11}^{'} + B_2\sigma_{22}^{'} + B_3\sigma_{33}^{'} - 2\sqrt{2}(B_2 - B_3)\sigma_{23}^{'}]\cos^2\phi$$
$$+ [B_2\sigma_{11}^{'} + B_1\sigma_{22}^{'} + B_3\sigma_{33}^{'} + 2\sqrt{2}(B_2 - B_3)\sigma_{23}^{'}]\sin^2\phi \qquad \text{Eq. (7.2.2)}$$
$$+ [2\sqrt{2}(B_3 - B_2)\sigma_{13}^{'} + (B_1 - B_2)\sigma_{12}^{'}]\sin 2\phi + f(\Delta T)$$

120

For uniaxial stress $\sigma = \sigma_{11}'$ with neglect of $f(\Delta T)$, Eq. (7.2.2.) simplifies to

$$\frac{\Delta R_0}{R_0} = B_1 \sigma \qquad\qquad \text{Eq. (7.2.3)}$$

$$\frac{\Delta R_{90}}{R_{90}} = B_2 \sigma \qquad\qquad \text{Eq. (7.2.4)}$$

in which the stress sensitivity is B_1 and B_2, respectively. Note that B_1 and B_2 are calculated from separate tests for resistor sensors on the same wafer lot. Subtraction of Eq. (7.2.4) from Eq. (7.2.3) leads to

$$\frac{\Delta R_0}{R_0} - \frac{\Delta R_{90}}{R_{90}} = (B_1 - B_2) \sigma \qquad\qquad \text{Eq. (7.2.5)}$$

in which the stress sensitivity is $(B_1 - B_2)$.

Typical results for the normalized resistance changes of R_0 and R_{90} as a function of an applied stress for p- and n-type resistor sensors are shown in Figs. 7.5 through 7.8. Note that the stress sensitivity of #1 specimen in Tables 7.1 and 7.2 is plotted in Figs. 7.5 and 7.6 for p-type sensors, whereas Figs. 7.7 and 7.8 are for n-type sensors.
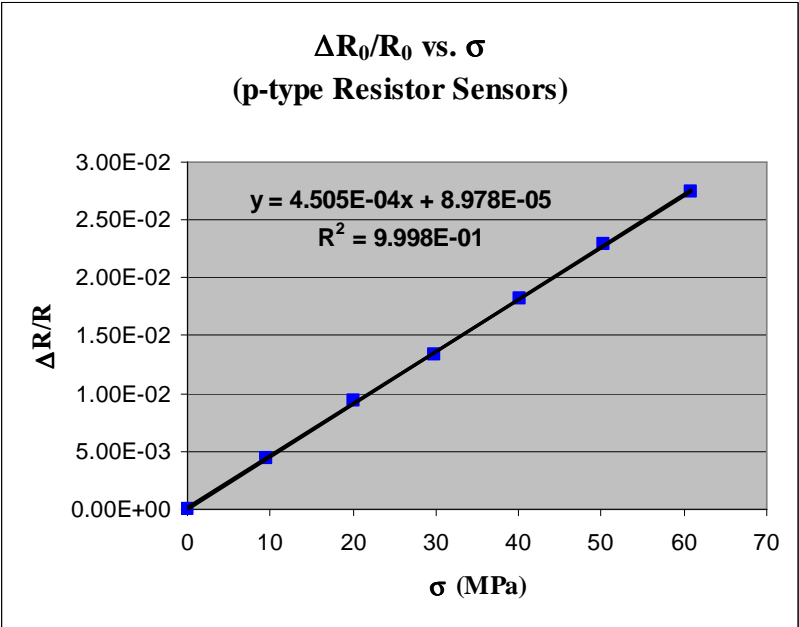
Fig. 7.5 - Typical stress sensitivity of p-type resistor sensors (R_0)
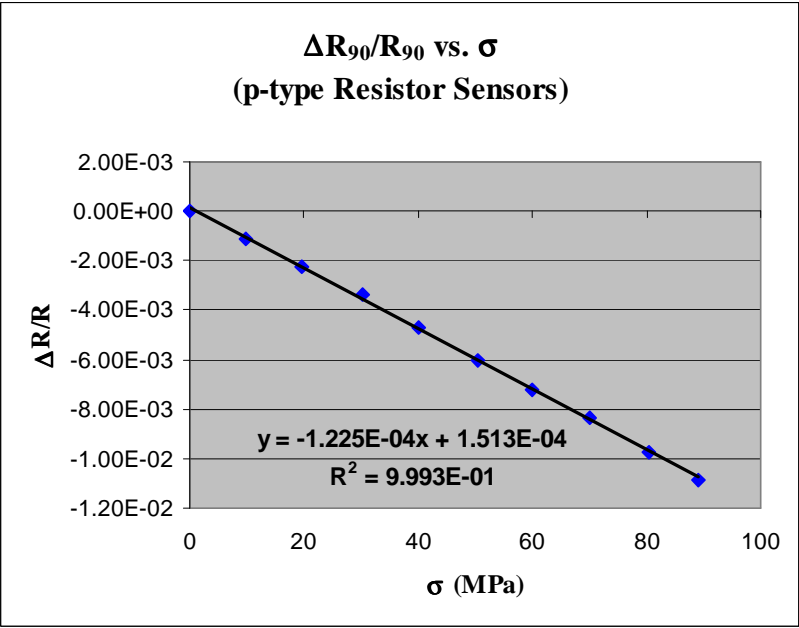
Fig. 7.6 - Typical stress sensitivity of p-type resistor sensors (R_{90})
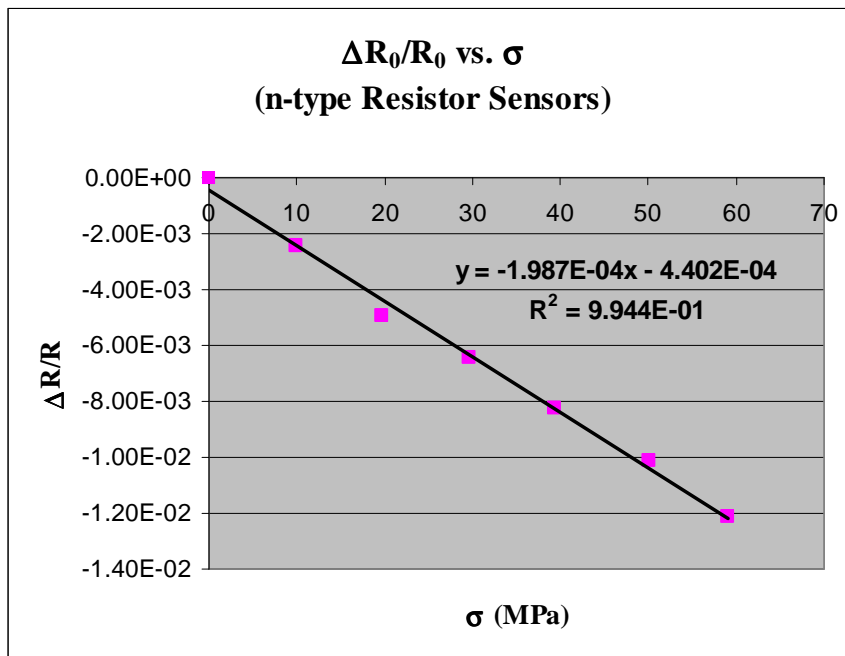
Fig. 7.7 - Typical stress sensitivity of n-type resistor sensors (R_0)
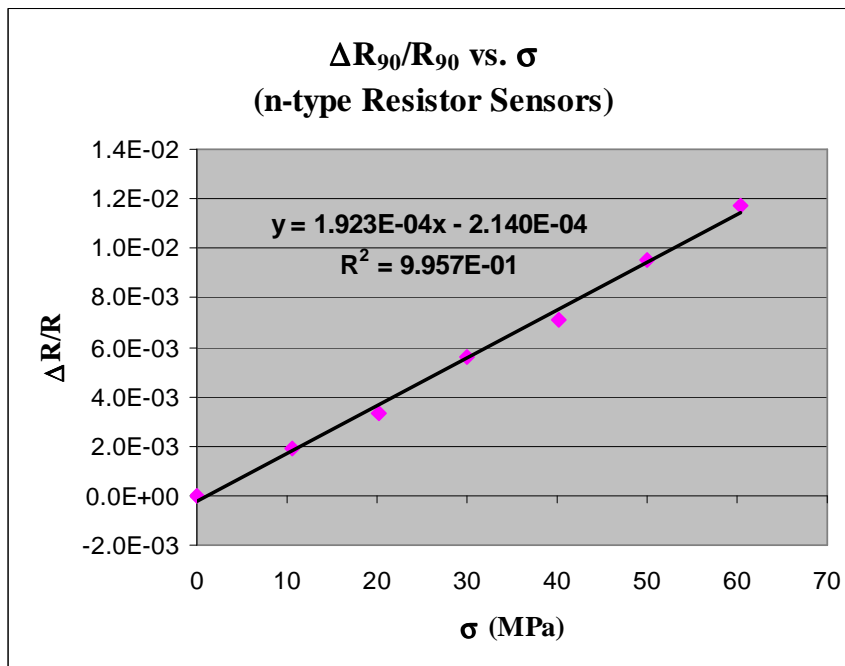
Fig. 7.8- Typical stress sensitivity of n-type resistor sensors (R_{90})

Note that Table 7.1 represents the values of 10 experiments performed using different resistor sensors of p-type silicon from the same wafer.

Table 7.1 – Stress sensitivities of the (111) p-type resistor sensors (Unit: MPa^{-1})			
Specimen	Slope of $\Delta R_0/R_0$ vs. σ	Slope of $\Delta R_{90}/R_{90}$ vs. σ	Slope of $\Delta R_0/R_0$-$\Delta R_{90}/R_{90}$ vs. σ
#1	450.5	-122.5	573.0
#2	479.1	-130.7	609.8
#3	442.4	-127.7	570.1
#4	465.4	-117.4	582.8
#5	428.5	-125.4	553.9
#6	487.6	-132.0	619.6
#7	465.5	-115.9	581.4
#8	468.6	-122.5	591.1
#9	465.7	-126.1	591.8
#10	435.1	-128.6	563.7
Average	458.8	-124.9	583.7
Std. Dev.	19.12	5.33	20.23

Similarly, the results of 10 experiments of n-type silicon are presented in Table 7.2.

Table 7.2 – Stress sensitivities of the (111) n-type resistor sensors (Unit: MPa^{-1})			
Specimen	Slope of $\Delta R_0/R_0$ vs. σ	Slope of $\Delta R_{90}/R_{90}$ vs. σ	Slope of $\Delta R_0/R_0$-$\Delta R_{90}/R_{90}$ vs. σ
#1	-198.7	192.3	-391.0
#2	-201.8	200.0	-401.8
#3	-214.7	203.7	-418.4
#4	-201.7	197.2	-398.9
#5	-197.8	201.6	-399.4
#6	-206.6	187.5	-394.1
#7	-198.3	189.6	-387.9
#8	-202.7	199.7	-402.4
#9	-211.0	201.6	-412.6
#10	-197.7	193.8	-391.5
Average	-203.1	196.7	-399.8
Std. Dev.	5.89	5.58	9.67

Similar tests are performed on several VDP sensors from the same wafer. The measured

stress sensitivities for ten experiments are presented in Tables 7.3 and 7.4. Averages of the

measurements and the corresponding standard deviation are also presented in the tables,

where the magnification factor M is defined as the ratio of the sensitivity of VDP sensors to

the sensitivity of resistor sensors, which will be discussed in the next section.

Table 7.3 - Stress sensitivities of the (111) p-type silicon VDP structures (Unit: MPa^{-1})				
Specimen	Slope of $\Delta R_0/R_0$ vs. σ	Slope of $\Delta R_{90}/R_{90}$ vs. σ	Slope of $\Delta R_0/R_0 - \Delta R_{90}/R_{90}$ vs. σ	M	Modified M
#1	1261.5	-869.4	2130.9	3.651	3.202
#2	1227.5	-874.1	2101.6	3.600	3.158
#3	1285.0	-882.3	2167.3	3.713	3.257
#4	1304.0	-870.7	2174.7	3.726	3.268
#5	1277.5	-863.5	2141.0	3.668	3.218
#6	1266.0	-883.0	2149.0	3.682	3.230
#7	1285.5	-865.4	2150.9	3.685	3.232
#8	1329.5	-832.3	2161.8	3.704	3.249
#9	1279.5	-825.6	2105.1	3.606	3.164
#10	1325.5	-843.4	2168.9	3.716	3.259
Average	1284.2	-861.0	2145.1	3.675	3.224
Std. Dev.	30.33	20.24	25.76	0.044	0.039

Table 7.4 - Stress sensitivities of the (111) n-type silicon VDP structures (Unit: MPa^{-1})				
Specimen	Slope of $\Delta R_0/R_0$ vs. σ	Slope of $\Delta R_{90}/R_{90}$ vs. σ	Slope of $\Delta R_0/R_0 - \Delta R_{90}/R_{90}$ vs. σ	M	Modified M
#1	-687.1	686.8	-1373.9	3.436	3.014
#2	-680.0	688.4	-1368.4	3.423	3.002
#3	-675.3	704.3	-1379.6	3.451	3.027
#4	-693.8	694.8	-1388.6	3.473	3.047
#5	-703.4	727.5	-1430.9	3.579	3.140
#6	-715.5	694.6	-1410.1	3.527	3.094
#7	-673.0	700.5	-1373.5	3.435	3.014
#8	-690.7	728.2	-1418.9	3.549	3.113
#9	-690.4	700.5	-1390.9	3.479	3.052
#10	-654.5	699.3	-1353.8	3.386	2.970
Average	-686.4	702.5	-1388.9	3.474	3.047
Std. Dev.	16.95	14.43	24.31	0.061	0.053

Typical results for the normalized resistance changes of R_0 and R_{90} as a function of an applied stress for p- and n-type VDP sensors are shown in Figs. 7.9 through 7.12. For R_0 of the VDP sensors, we have two pairs (see Fig. 7.4)--that is, a current is injected through 1 and 4 or 2 and 3. Similarly, for R_{90} of the VDP sensors, a current is injected through 1 and 2 or 3 and 4. The value in Tables 7.3 and 7.4 is an average of two pairs. Figures 7.9 and 7.10 are for p-type VDP sensors, whereas Figs. 7.11 and 7.12 are for n-type VDP sensors.
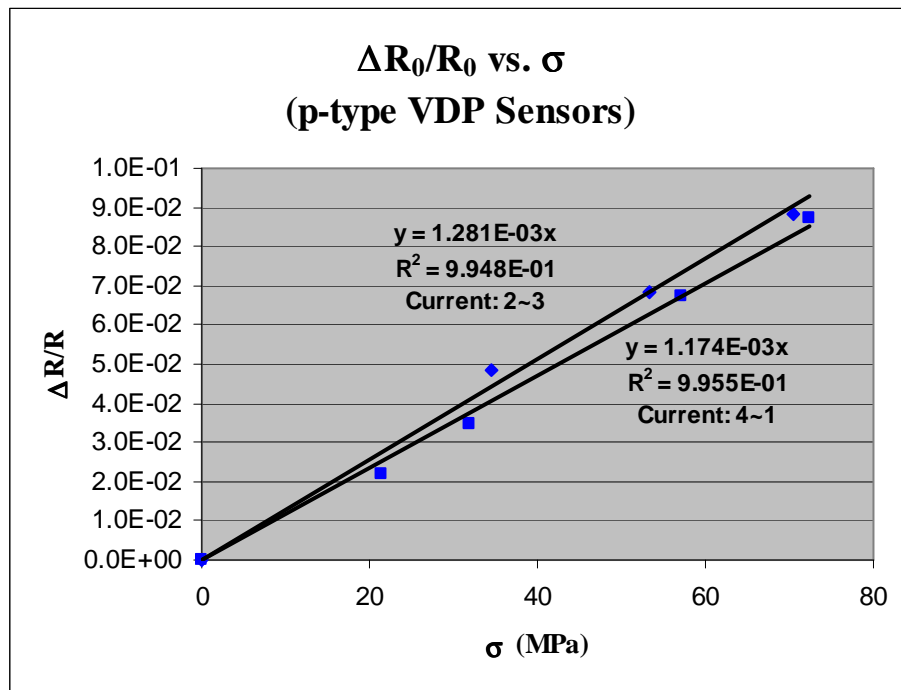
Fig. 7.9 - Typical stress sensitivity of p-type VDP sensors (R_0)

126
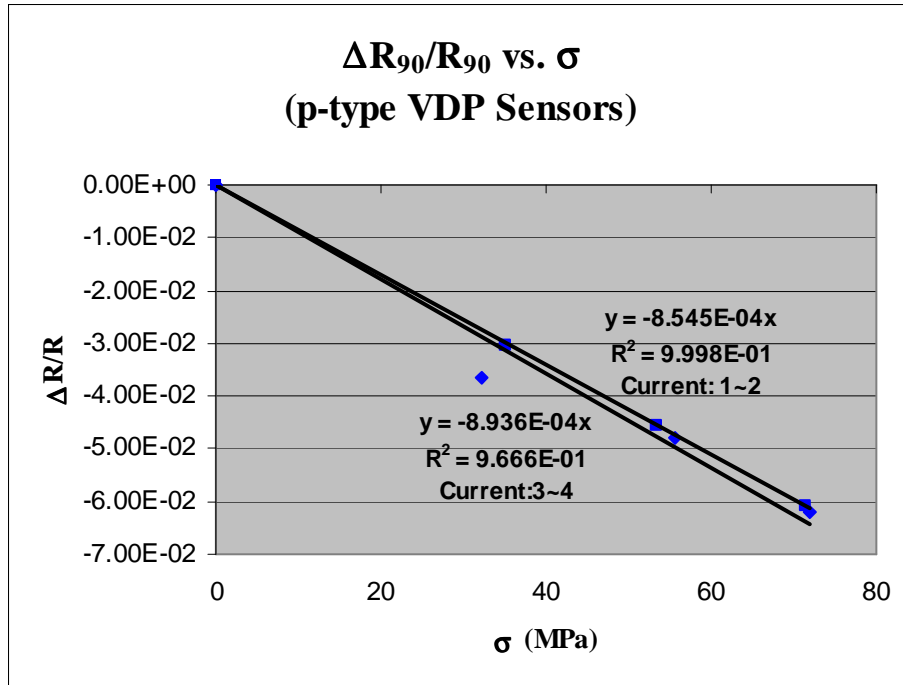
Fig. 7.10 - Typical stress sensitivity of p-type VDP sensors (R_{90})
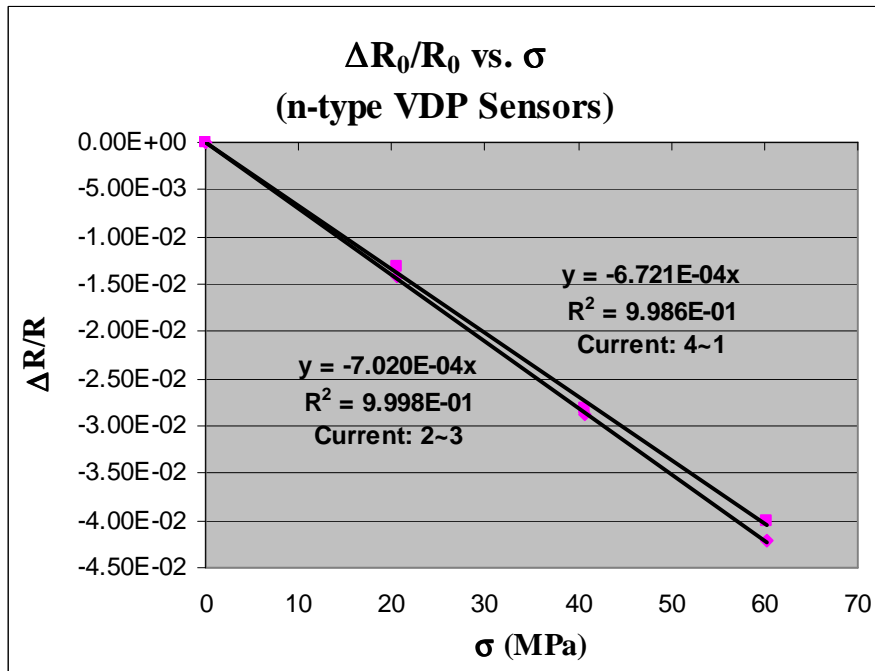
Fig. 7.11 - Typical stress sensitivity of n-type VDP sensors (R_0)
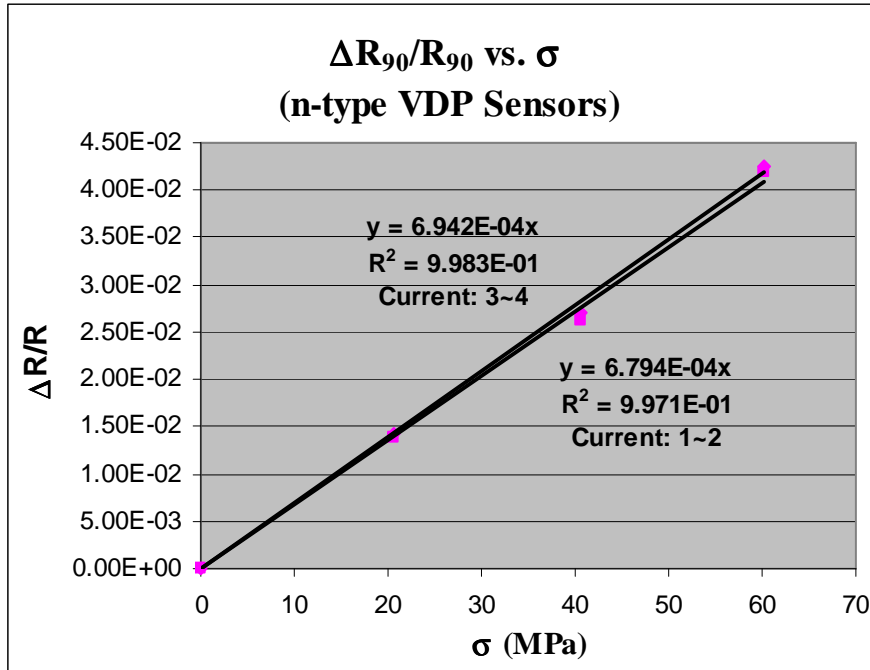
Fig. 7.12- Typical stress sensitivity of n-type VDP sensors (R_{90})

As observed in the resistor sensors, the experimental response of the VDP sensors to the applied stress is also linear. It is apparent that the results of two pairs match well as expected. As shown in Tables 7.3 and 7.4, p- and n-type sensors, the responses of the difference of the normalized resistance changes versus stress is several times higher than the responses experienced by the analogous 0° and 90° resistor sensors. For p-type sensors, the sensitivity of VDP sensors is 3.68 times higher than that of corresponding resistor sensors. However, for n-type sensors, it is found to be 3.47 times higher. The measured magnification of p-type senosrs is observed to be higher than that of n-type sensors.

7.3   Sensitivity Magnification Factor and γ

Mian [50] described how to calculate the modified magnification factor in the serpentine resistors connected with doped resistive material. Mian [50] also presented the value of magnification factor by the analytical and numerical methods. In our studies, we checked and verified the magnification factor to be about 3.157 numerically by using a MATLAB software program. The following notations are adopted in our work.

$$N = \frac{L}{W}$$ Eq. (7.3.1)

N represents the number of squares and L and W, respectively, represent the length and width of the resistance R of the rectangular block of uniformly doped material. N_{axial} and $N_{transverse}$ represent the number of squares in the axial and transverse parts of the resistance R.

$$\gamma = \frac{N_{axial}}{N_{axial} + N_{transverse}}$$ Eq. (7.3.2)

in which γ is the ratio of axial part to the sum of axial part and transverse part. If we consider the resistor R_{0_eff}, it is actually composed of resistor segments oriented in the 0° and 90° directions, Hence

$$R_{0\_eff} = \gamma R_0 + (1 - \gamma)R_{90}$$ Eq. (7.3.3)

The normalized change in resistance may be expressed as

$$\frac{\Delta R_0}{R_0} = B_1 \sigma_{11}' + B_2 \sigma_{22}' + B_3 \sigma_{33}' - 2\sqrt{2}(B_2 - B_3)\sigma_{23}' + f(\Delta T)$$

$$\frac{\Delta R_{90}}{R_{90}} = B_2 \sigma_{11}' + B_1 \sigma_{22}' + B_3 \sigma_{33}' + 2\sqrt{2}(B_2 - B_3)\sigma_{23}' + f(\Delta T)$$

Eq. (7.3.4)

in which $f(\Delta T) = \alpha_1 \Delta T + \alpha_2 \Delta T^2 + ...$

Thus

$$\frac{\Delta R_{0\_eff}}{R_{0\_eff}} = \gamma \frac{\Delta R_0}{R_0} + (1-\gamma)\frac{\Delta R_{90}}{R_{90}} \qquad \text{Eq. (7.3.5)}$$

Similar calculation may be performed for the serpentine resistor at 90° orientation with respect to the x_1' axis. The expression is

$$\frac{\Delta R_{90\_eff}}{R_{90\_eff}} = (1-\gamma)\frac{\Delta R_0}{R_0} + \gamma \frac{\Delta R_{90}}{R_{90}} \qquad \text{Eq. (7.3.6)}$$

In our cases, N_{axial} and $N_{transverse}$ are estimated to be 143.2 and 9.37 squares, respectively. Hence $\gamma = 0.939$.

According to Eq. (7.3.5) and Eq. (7.3.6), the results below can be found:

$$\frac{\Delta R_{0\_eff}}{R_{0\_eff}} - \frac{\Delta R_{90\_eff}}{R_{90\_eff}} = (2\gamma\text{-}1)(\frac{\Delta R_0}{R_0} - \frac{\Delta R_{90}}{R_{90}}) \qquad \text{Eq. (7.3.7)}$$

$$\frac{\Delta R_{0\_eff}}{R_{0\_eff}} + \frac{\Delta R_{90\_eff}}{R_{90\_eff}} = (\frac{\Delta R_0}{R_0} + \frac{\Delta R_{90}}{R_{90}}) \qquad \text{Eq. (7.3.8)}$$

Assuming uniaxial stress σ_{11}' in Eq. (7.3.4) leads to

$$\frac{\Delta R_0}{R_0} = B_1\sigma_{11}'$$
$$\frac{\Delta R_{90}}{R_{90}} = B_2\sigma_{11}' \qquad \text{Eq. (7.3.9)}$$

Substitution of Eq. (7.3.9) into Eqs. (7.3.7) and (7.3.8) yields

$$\frac{\Delta R_{0\_eff}}{R_{0\_eff}} - \frac{\Delta R_{90\_eff}}{R_{90\_eff}} = (2\gamma\text{-}1)(B_1\text{-}B_2)\sigma_{11}' = (B_{1\_eff} \text{-} B_{2\_eff})\sigma_{11}' \qquad \text{Eq. (7.3.10)}$$

$$\frac{\Delta R_{0\_eff}}{R_{0\_eff}} + \frac{\Delta R_{90\_eff}}{R_{90\_eff}} = (B_1 + B_2)\sigma_{11}' = (B_{1\_eff} + B_{2\_eff})\sigma_{11}' \qquad \text{Eq. (7.3.11)}$$

By Eqs. (7.3.10) and (7.3.11),

$$B_{1\_eff} = \gamma B_1 + (1 - \gamma)B_2 \qquad \text{Eq. (7.3.12)}$$

$$B_{2\_eff} = (1 - \gamma)B_1 + \gamma B_2 \qquad \text{Eq. (7.3.13)}$$

Thus

$$B_1 = \frac{\gamma B_{1\_eff} + (\gamma\text{-}1)B_{2\_eff}}{2\gamma\text{-}1} \qquad \text{Eq. (7.3.14)}$$

$$B_2 = \frac{\gamma B_{2\_eff} + (\gamma\text{-}1)B_{1\_eff}}{2\gamma\text{-}1} \qquad \text{Eq. (7.3.15)}$$

Subtraction and addition of Eq. (7.3.14) and Eq. (7.3.15) yield

$$B_1 + B_2 = B_{1\_eff} + B_{2\_eff} \qquad \text{Eq. (7.3.16)}$$

$$B_1 - B_2 = \frac{B_{1\_eff} - B_{2\_eff}}{2\gamma - 1} \qquad \text{Eq. (7.3.17)}$$

Substitution $\gamma = 0.939$ into Eq. (7.3.17) yields $(B_{1\_eff} - B_{2\_eff}) = 0.878(B_1 - B_2)$. Therefore,

the measured coefficients must be multiplied by the factor $1/0.878$ (= 1.139). In the

previous section, the measured magnification factor is 3.675 for p-type silicon and 3.474

for n-type silicon. The modified magnification factors are 3.224 for the p-type and 3.047

for the n-type coefficients. These results still show discrepancies with the analytical value

of 3.157. Reasons for these discrepancies will be discussed in the next section where the effects of dimensional changes during loading are considered.

7.4   Effects of Dimensional Changes of VDP and Resistor during Loading

Dimensional changes in VDP structures and resistors during loading have been neglected in the analysis up to here. Strain-effects of VDP structures and resistor sensors on piezoresistive coefficients and sensitivity magnifications will be discussed and compared with the cases in which strain-effects are not considered.

7.4.1   Strain-effects of VDP Structures

Consider again the case in which uniaxial stress $\sigma_{11}^{'} = \sigma$ is applied as shown in Fig. 7.13. Application of load induces the change in the side length of the VDP.
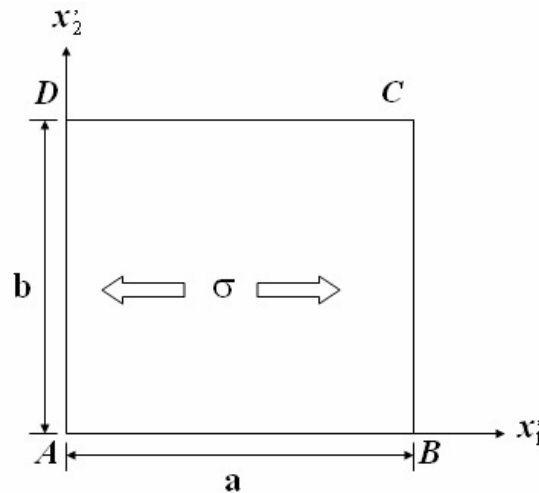
Fig. 7.13 - Isotropic rectangular VDP structure under uniaxial stress

The relation between stress and strain is given by

$$\sigma = \varepsilon E = (\frac{\Delta L}{L})E \qquad\qquad \text{Eq. (7.4.1)}$$

in which L is the unstressed side-length and E is the Young's modulus. By Eq. (7.4.1),

$$L^{'} = L + \Delta L \qquad\qquad \text{Eq. (7.4.2)}$$

in which $L^{'}$ is the stressed side-length. After application of uniaxial stress $\sigma_{11}^{'}$, the side length of the VDP structure is given by combining Eqs. (7.4.1) and (7.4.2):

$$L^{'} = L(1 + \frac{\Delta L}{L}) = L(1 + \frac{\sigma}{E}) \qquad\qquad \text{Eq. (7.4.3)}$$

If the sides of the unstressed square VDP structure are L_{AB} and L_{BC}, respectively, the length of the stressed side AB is defined as AB and is given by

$$AB = L_{AB}(1 + \frac{\sigma}{E}) \qquad\qquad \text{Eq. (7.4.4)}$$

in which L_{AB} is the length of the unstressed side AB. Poisson's ratio is a measure of the simultaneous change in elongation and in the cross-sectional area within the elastic range during a tensile or compressive test. During a tensile test, the reduction in the cross-sectional area is proportional to the increase in length in the elastic range by a dimensionless factor called Poisson's ratio, defined as a ratio of sideways contraction to length extension ($v = - \varepsilon_{22}/\varepsilon_{11}$). Therefore, the length of the side BC is expressed as

$$BC = L_{BC}(1 - \frac{v\sigma}{E}) \qquad\qquad \text{Eq. (7.4.5)}$$

in which L_{BC} is the length of the unstressed side BC. Likewise, the thickness $t^{'}$ of VDP structure under stressed condition is given by

133

$$t' = t(1 - \frac{v\sigma}{E})$$

Eq. (7.4.6)

in which t is the unstressed thickness of VDP structure. Combining Eqs. (7.4.4) and (7.4.5) yields

$$\frac{AB}{BC} = \frac{L_{AB}}{L_{BC}}(\frac{E+\sigma}{E-v\sigma})$$

Eq. (7.4.7)

Plugging Eqs. (7.4.6) and (7.4.7) into Eqs. (7.1.7) and (7.1.8) yields

$$R_{AB,CD} = -\frac{8E\sqrt{\rho'_{11}\rho'_{22}}}{\pi t(E-v\sigma)} \ln \prod_{n=0}^{\infty} \{\tanh[\sqrt{\frac{\rho'_{22}}{\rho'_{11}}} \frac{L_{BC}}{L_{AB}}(\frac{E-v\sigma}{E+\sigma})(2n+1)\frac{\pi}{2}]\}$$

Eq. (7.4.8)

$$R_{AD,BC} = -\frac{8E\sqrt{\rho'_{11}\rho'_{22}}}{\pi t(E-v\sigma)} \ln \prod_{n=0}^{\infty} \{\tanh[\sqrt{\frac{\rho'_{11}}{\rho'_{22}}} \frac{L_{AB}}{L_{BC}}(\frac{E+\sigma}{E-v\sigma})(2n+1)\frac{\pi}{2}]\}$$

Eq. (7.4.9)

in which ρ'_{11} and ρ'_{22} are resistivity components of the principal axes x'_1 and x'_2 that are parallel and perpendicular to the wafer flat of the silicon. The nonzero resistivity components are given by

$$\rho'_{11} = \rho[1 + B_1\sigma'_{11} + B_2\sigma'_{22} + B_3\sigma'_{33} - 2\sqrt{2}(B_2 - B_3)\sigma'_{23}]$$
$$\rho'_{22} = \rho[1 + B_2\sigma'_{11} + B_1\sigma'_{22} + B_3\sigma'_{33} + 2\sqrt{2}(B_2 - B_3)\sigma'_{23}]$$
$$\rho'_{12} = \rho[2\sqrt{2}(B_3 - B_2)\sigma'_{13} + (B_1-B_2)\sigma'_{12}]$$

Eq. (7.4.10)

For uniaxial stress $\sigma = \sigma'_{11}$, Eq. (7.4.10) reduces to

$$\rho'_{11} = \rho(1+B_1\sigma)$$
$$\rho'_{22} = \rho(1+B_2\sigma)$$
$$\rho'_{12} = 0$$

Eq. (7.4.11)

134

Equation (7.4.11) is substituted into Eqs. (7.4.8) and (7.4.9). By an analytic approach, the normalized change in $R_{AB,CD}$ and $R_{AD,BC}$ may be calculated. In our case, $R_{AB,CD} = R_0$ and $R_{AD,BC} = R_{90}$, and the normalized resistance equation with $\Delta T = 0$ is

$$\frac{\Delta R_\phi}{R_\phi} = \frac{R_\phi(\sigma, \Delta T) - R_\phi(0,0)}{R_\phi(0,0)} = \frac{R_\phi(\sigma,0) - R_\phi(0,0)}{R_\phi(0,0)} \qquad \text{Eq. (7.4.12)}$$

where $R(0,0)$ and $R(\sigma,0)$ are the unstressed and stressed resistances, respectively. It is obvious that the normalized resistance may be evaluated without knowing thickness t as shown in the following equations:

$$\frac{\Delta R_0}{R_0} = \frac{\dfrac{E\sqrt{(1+B_1\sigma)(1+B_2\sigma)}}{(E-\nu\sigma)} \ln\prod_{n=0}^{\infty}\{\tanh[\sqrt{\dfrac{(1+B_2\sigma)}{(1+B_1\sigma)}}\dfrac{L_{BC}}{L_{AB}}(\dfrac{E-\nu\sigma}{E+\sigma})(2n+1)\dfrac{\pi}{2}]\}}{\ln\prod_{n=0}^{\infty}\{\tanh[\dfrac{L_{BC}}{L_{AB}}(2n+1)\dfrac{\pi}{2}]\}} - 1 \qquad \text{Eq. (7.4.13)}$$

$$\frac{\Delta R_{90}}{R_{90}} = \frac{\dfrac{E\sqrt{(1+B_1\sigma)(1+B_2\sigma)}}{(E-\nu\sigma)} \ln\prod_{n=0}^{\infty}\{\tanh[\sqrt{\dfrac{(1+B_1\sigma)}{(1+B_2\sigma)}}\dfrac{L_{AB}}{L_{BC}}(\dfrac{E-\nu\sigma}{E+\sigma})(2n+1)\dfrac{\pi}{2}]\}}{\ln\prod_{n=0}^{\infty}\{\tanh[\dfrac{L_{AB}}{L_{BC}}(2n+1)\dfrac{\pi}{2}]\}} - 1 \qquad \text{Eq. (7.4.14)}$$

For $+45^\circ/-45^\circ$ VDP, through the proper coordinate transformation described in Section 7.2, the normalized change in resistance may be expressed as the following:

$$\frac{\Delta R_{45}}{R_{45}} = \frac{\dfrac{E\sqrt{(1+B_1\sigma)(1+B_2\sigma)}}{(E-\nu\sigma)} \ln\prod_{n=0}^{\infty}\{\tanh[\dfrac{BC}{AB}(2n+1)\dfrac{\pi}{2}]\} - \ln\prod_{n=0}^{\infty}\{\tanh[\dfrac{BC}{AB}(2n+1)\dfrac{\pi}{2}]\}}{\ln\prod_{n=0}^{\infty}\{\tanh[\dfrac{BC}{AB}(2n+1)\dfrac{\pi}{2}]\}}$$

$$= \frac{E\sqrt{(1+B_1\sigma)(1+B_2\sigma)}}{(E-\nu\sigma)} - 1$$

$$\text{Eq. (7.4.15)}$$

$$\frac{\Delta R_{-45}}{R_{-45}} = \frac{\dfrac{E\sqrt{(1+B_1\sigma)(1+B_2\sigma)}}{(E-\nu\sigma)}\ln\prod_{n=0}^{\infty}\{\tanh[\dfrac{AB}{BC}(2n+1)\dfrac{\pi}{2}]\}-\ln\prod_{n=0}^{\infty}\{\tanh[\dfrac{AB}{BC}(2n+1)\dfrac{\pi}{2}]\}}{\ln\prod_{n=0}^{\infty}\{\tanh[\dfrac{AB}{BC}(2n+1)\dfrac{\pi}{2}]\}}$$

$$= \frac{E\sqrt{(1+B_1\sigma)(1+B_2\sigma)}}{(E-\nu\sigma)}-1$$

<div align="right">Eq. (7.4.16)</div>

For $+45^{o}/-45^{o}$ VDP, AB = BC because of the symmetrical geometry, and the change in thickness of the VDP structure is reflected as shown in Eqs. (7.4.15) and (7.4.16). Also, it is to be emphasized that the normalized change in resistance has the same formula for $+45^{o}$ VDP and -45° VDP.

For a square of VDP structure, $L_{AB} = L_{BC}$. Also, $B_1^{p} = 458.8$ TPa^{-1}, $B_2^{p} = -124.9$ TPa^{-1}, $B_1^{n} = -203.1$ TPa^{-1}, and $B_2^{n} = 196.7$ TPa^{-1} are substituted into Eqs. (7.4.13) through (7.4.16). Note that E = 169.1 GPa and $\nu = 0.262$ on the (111) silicon surface. In addition, σ may be determined by the equation in the four-point bending fixture:

$$\sigma = \frac{3F(L-d)}{t^2 h} \qquad \text{Eq. (7.4.17)}$$

where uniaxial stress $\sigma'_{11} = \sigma$ is applied in the x'_1-direction. Hence, all the parameters in Eqs. (7.4.13) through (7.4.16) are known. The normalized resistance values may be calculated analytically. The following table presents the analytic value of the magnification factor M with/without considering the strain effect. It is observed that VDP sensors offer 3.157 times higher sensitivity than their analogous resistor sensors. However, considering

the strain effects leads M to 3.238 for p-type sensors and 3.039 for n-type sensors as shown

in Table 7.5.

Table 7.5 - Analytically calculated magnification factor, M		
Type	M with neglect of E and ν	M with consideration of E and ν
p	3.157	3.238
n	3.157	3.039

Table 7.6 - Experimental values of M				
Type	B_1-B_2	Slope of $\Delta R_0/R_0$-$\Delta R_{90}/R_{90}$ vs. σ	M	Modified M
p	583.7	2145.2	3.675	3.224
n	-399.8	-1388.9	3.474	3.047

In Table 7.6, the modified M is calculated by considering γ for the serpentine resistors. In

addition, analytic results are compared with experimental results as shown in Table 7.7.

Table 7.7 - Comparison between Analytic and Experimental M		
Type	Analytic M	Experimental M
p	3.238	3.224
n	3.039	3.047

It is observed that analytic results are now in good agreement with experimental

results. For p-type sensors, M is observed to be higher than 3.157. On the other hand, for n-

type sensors, M shows the result lower than 3.157. Reasons for these discrepancies will be

discussed later.

7.4.2 Strain-effects of Resistor Sensors

Before describing the strain-effects of resistor sensors, how γ responds to the applied stress should be mentioned. When the chip is unstressed ,

$$\gamma = \frac{N_{axial}}{N_{axial} + N_{transverse}} \qquad \text{Eq. (7.4.18)}$$

In our case, $N_{axial} = 143.2$ squares and $N_{transverse} = 9.37$ squares. Therefore $\gamma = 0.939$. When the chip is stressed, γ changes with the applied stress, whereas γ is constant under an unstressed condition. For R_0, γ is given by

$$\gamma = \frac{C_a N_{axial}}{C_a N_{axial} + C_t N_{transverse}} = \frac{N_{axial}}{N_{axial} + \dfrac{C_t}{C_a} N_{transverse}} \qquad \text{Eq. (7.4.19)}$$

in which C_a and C_t are modifying coefficients defined as follows:

$$C_a = \frac{(E + \sigma)}{(E - \nu\sigma)}, C_t = \frac{(E - \nu\sigma)}{(E + \sigma)} \qquad \text{Eq. (7.4.20)}$$

For R_{90},

$$\gamma = \frac{C_t N_{axial}}{C_t N_{axial} + C_a N_{transverse}} = \frac{N_{axial}}{N_{axial} + \dfrac{C_a}{C_t} N_{transverse}} \qquad \text{Eq. (7.4.21)}$$

Table 7.8 - γ_0 and γ_{90} at various stress levels				
σ (MPa)	c_a	c_t	γ_0	γ_{90}
0	1.0000E+00	1.0000E+00	9.4338E-01	9.4338E-01
20	1.0001E+00	9.9985E-01	9.4340E-01	9.4337E-01
40	1.0003E+00	9.9970E-01	9.4341E-01	9.4335E-01
60	1.0004E+00	9.9955E-01	9.4343E-01	9.4333E-01
80	1.0006E+00	9.9940E-01	9.4345E-01	9.4332E-01
100	1.0007E+00	9.9925E-01	9.4346E-01	9.4330E-01

In Table 7.8, γ_0 and γ_{90} denote γ for 0° and 90° resistors. Further, the plots of γ_0 and γ_{90} are shown in Fig. 7.14.
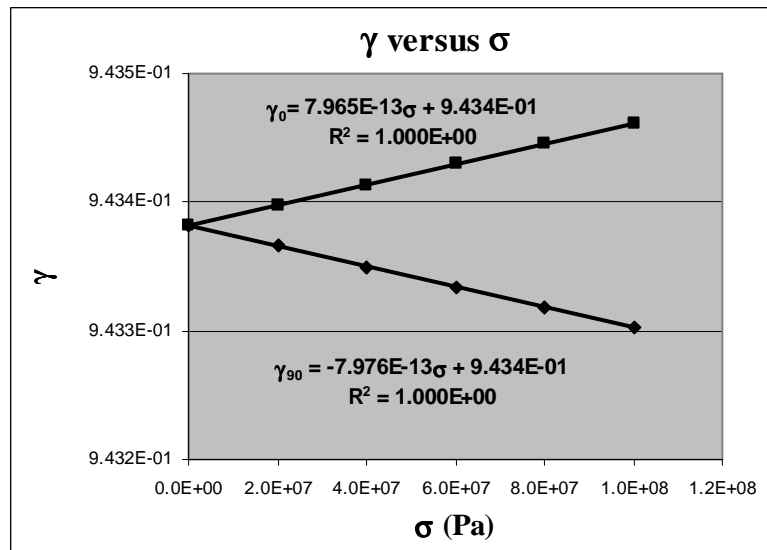
Fig. 7.14 - The plot of γ_0 and γ_{90} at various stress levels

As shown in Fig. 7.14, γ_0 and γ_{90} do not change much with varying stress. For instance, the normalized change in γ_0 and γ_{90} during application of 100MPa uniaxial stress is about 8.4×10^{-3} %. Hence γ_0 and γ_{90} may be assumed to be constant during application of stress.

The strain-effects in resistor sensors are described nest. The resistance R of a rectangular conductor is expressed as

$$R = \rho \frac{l}{A} = \rho \frac{l}{wt}$$

Eq. (7.4.22)

In the formula, ρ is the resistivity, and l, w, and t are the length, width, and thickness of the conductor, respectively. When the resistor is stretched by applying stress, the normalized change in resistance is given by

$$\frac{\Delta R}{R} \cong \frac{\Delta l}{l} - \frac{\Delta w}{w} - \frac{\Delta t}{t} + \frac{\Delta \rho}{\rho}$$

Eq. (7.4.23)

For convenience, the new notations are adopted

$$[\frac{\Delta R}{R}]_{dim} = \frac{\Delta l}{l} - \frac{\Delta w}{w} - \frac{\Delta t}{t}, \quad [\frac{\Delta R}{R}]_{res} = \frac{\Delta \rho}{\rho}$$

Eq. (7.4.24)

Equation (7.4.24) reflects the normalized change in resistance as follows:

$$\frac{\Delta R}{R} = [\frac{\Delta R}{R}]_{dim} + [\frac{\Delta R}{R}]_{res}$$

Eq. (7.4.25)

Generally dimensional change is neglected in the calculation of the normalized resistance change:

$$\frac{\Delta R}{R} \cong [\frac{\Delta R}{R}]_{res} = \frac{\Delta \rho}{\rho}$$

Eq. (7.4.26)

If the uniaxial stress $\sigma'_{11} (= \sigma)$ is applied,

$$\frac{\Delta R_0}{R_0} \cong [\frac{\Delta R_0}{R_0}]_{res} = \gamma B_1 \sigma + (1 - \gamma) B_2 \sigma$$

Eq. (7.4.27)

$$\frac{\Delta R_{90}}{R_{90}} \cong [\frac{\Delta R_{90}}{R_{90}}]_{res} = (1-\gamma) B_1 \sigma + \gamma B_2 \sigma$$

Eq. (7.4.28)

In addition, if we consider the effects of dimensional change, the results are

$$[\frac{\Delta R_0}{R_0}]_{dim} = \gamma[(\frac{\sigma}{E}) - (\frac{-\nu\sigma}{E}) - (\frac{-\nu\sigma}{E})] + (1-\gamma)[(\frac{-\nu\sigma}{E}) - (\frac{\sigma}{E}) - (\frac{-\nu\sigma}{E})]$$
$$= \frac{\sigma[2\gamma(1+\nu)-1]}{E}$$

Eq. (7.4.29)

$$[\frac{\Delta R_{90}}{R_{90}}]_{dim} = \gamma[(\frac{-\nu\sigma}{E}) - (\frac{\sigma}{E}) - (\frac{-\nu\sigma}{E})] + (1-\gamma)[(\frac{\sigma}{E}) - (\frac{-\nu\sigma}{E}) - (\frac{-\nu\sigma}{E})]$$
$$= \frac{\sigma[(1-2\gamma) + 2\nu(1-\gamma)]}{E}$$

Eq. (7.4.30)

Substitution of E = 169.1 GPa, $\nu = 0.262$, and $\gamma = 0.939$ into Eqs. (7.4.29) and (7.4.30)

yields

$$[\frac{\Delta R_0}{R_0}]_{dim} = 8.102 \times 10^{-12} \sigma$$

Eq. (7.4.31)

$$[\frac{\Delta R_{90}}{R_{90}}]_{dim} = -5.003 \times 10^{-12} \sigma$$

Eq. (7.4.32)

For p-type sensors, the calibration result of the normalized resistance change is

$$\frac{\Delta R_0}{R_0} = 458.8 \times 10^{-12} \sigma$$

Eq. (7.4.33)

$$\frac{\Delta R_{90}}{R_{90}} = -124.9 \times 10^{-12} \sigma$$

Eq. (7.4.34)

Substitution of the results of Eqs. (7.4.31) and (7.4.32) into Eq. (7.4.25) leads to

$$[\frac{\Delta R_0}{R_0}]_{res} = 450.7 \times 10^{-12} \sigma$$

Eq. (7.4.35)

$$[\frac{\Delta R_{90}}{R_{90}}]_{res} = -119.9 \times 10^{-12} \sigma$$

Eq. (7.4.36)

Similarly, for n-type sensors,

$$\frac{\Delta R_0}{R_0} = -203.1 \times 10^{-12} \sigma \qquad \text{Eq. (7.4.37)}$$

$$\frac{\Delta R_{90}}{R_{90}} = 196.7 \times 10^{-12} \sigma \qquad \text{Eq. (7.4.38)}$$

Hence

$$[\frac{\Delta R_0}{R_0}]_{res} = -211.2 \times 10^{-12} \sigma \qquad \text{Eq. (7.4.39)}$$

$$[\frac{\Delta R_{90}}{R_{90}}]_{res} = 211.7 \times 10^{-12} \sigma \qquad \text{Eq. (7.4.40)}$$

Tables 7.9 and 7.10 present the values of B_1 and B_2 with neglect of the dimensional change of resistors, whereas Tables 7.11 and 7.12 includes the effect of the dimensional change of resistors. Note that γ is considered in Tables 7.10 and 7.12.

Table 7.9 - The effective B_1 and B_2 (Unit: TPa^{-1})			
$B_{1\_eff}^{p}$	$B_{2\_eff}^{p}$	$B_{1\_eff}^{n}$	$B_{2\_eff}^{n}$
458.8	-124.9	-203.1	196.7

Table 7.10 - Modified B_1 and B_2 (Unit: TPa^{-1})			
B_1^{p}	B_2^{p}	B_1^{n}	B_2^{n}
499.4	-165.5	-230.9	224.5

Table 7.11 - The effective B_1 and B_2 (Unit: TPa^{-1})			
$B_{1\_eff}^p$	$B_{2\_eff}^p$	$B_{1\_eff}^n$	$B_{2\_eff}^n$
450.7	-119.9	-211.2	201.7

Table 7.12 - Modified B_1 and B_2 (Unit: TPa^{-1})			
B_1^p	B_2^p	B_1^n	B_2^n
490.3	-159.5	-240.6	230.4

As compared in Tables 7.9 and 7.11, B_{1_eff} and B_{2_eff} have discrepancies about 2~4 %.

Also, B_1 and B_2 in Tables 7.10 and 7.12, have discrepancies approximately of 1.6~3.2 %.

Substitution of the modified values of B_1 and B_2 in Table 7.12 into Eqs. (7.4.13) and

(7.4.14) yields M shown in the last column in Table 7.13.

Table 7.13 - Analytically calculated magnification factor, M, through the use of modified B_1 and B_2		
Type	M with neglect of E and ν	M with consideration of E and ν
p	3.157	3.231
n	3.157	3.057

If we compare the values in Tables 7.5 and 7.13, the magnification factor M is almost

constant. The observed discrepancies are less than 0.13 % for all cases. Thus, the

dimensional change of resistors may be neglected. However, in this work, the modified

values of B_1 and B_2 in Table 7.12 are considered in analytical calculations for

completeness and accuracy: $B_1^p = 490.3$ TPa^{-1}, $B_2^p = -159.5$ TPa^{-1}, $B_1^n = -240.6$ TPa^{-1}, and $B_2^n = 230.4$ TPa^{-1}.

In the simulations, 0.9~1.1 times of B_1 and B_2 is also assumed to consider the errors induced from measurements. In the cases where the strain effects are neglected, the magnification factor is close to 3.157 for all cases. In the cases where the strain effects are considered, the magnification factor is observed to be 3.22~3.29 for p-type sensors and 3.05~3.08 for n-type sensors, respectively. If we compare these results with the values in Table 7.13 (3.231 for p-type sensors and 3.057 for n-type sensors), the effects of aspect ratio, the magnitude of stress, and overestimation/underestimation of B_1 and B_2 do not seem to significantly affect the magnification factor. On the other hand, the strain effects should be considered.

7.5   Summary

In summary,

- In this work, the sensitivity of VDP sensors has been calculated/measured both analytically and experimentally.

- VDP sensors offer 3.157 times higher sensitivity than an analogous two element resistor sensor rosette. However, considering strain effects leads M to 3.231 for p-type sensors and 3.057 for n-type sensors.

- Dimensional changes of VDP sensors should be considered in the calculation of M. However, for resistor sensors, the dimensional changes may be neglected.

CHAPTER 8

TRANSVERSE STRESS ANALYSIS AND ERRORS ASSOCIATED WITH MISALIGNMENT

8.1   Transverse Stress Analysis

8.1.1   Resistor Sensors on the (111) Silicon

The effects of transverse stress on piezoresistive coefficient measurements are described in the previous chapter in which uniaxial stress is considered in only the (111) silicon surface. In this chapter two-dimensional states of stress are considered in the (001) silicon surface as well as the (111) silicon surface. A special (111) silicon test chip JSE-WB100C is used in the analysis. Each chip incorporates an array of the optimized eight-element dual polarity measurement rosettes. Experiments are performed with chips cut from JSE-WB100C test chip wafers. For sensors on the (111) surface, the expression for a resistor sensor at angle ϕ with respect to the $x_1^{'}$ axis is given by the following formula:

$$\frac{\Delta R_\phi}{R_\phi} = [B_1\sigma_{11}^{'} + B_2\sigma_{22}^{'} + B_3\sigma_{33}^{'} - 2\sqrt{2}(B_2 - B_3)\sigma_{23}^{'}]\cos^2\phi$$
$$+ [B_2\sigma_{11}^{'} + B_1\sigma_{22}^{'} + B_3\sigma_{33}^{'} + 2\sqrt{2}(B_2 - B_3)\sigma_{23}^{'}]\sin^2\phi \qquad \text{Eq. (8.1.1)}$$
$$+ [2\sqrt{2}(B_3 - B_2)\sigma_{13}^{'} + (B_1 - B_2)\sigma_{12}^{'}]\sin 2\phi + f(\Delta T)$$

Just as for the BMW-2.1 test chip discussed in Chapter 7, the JSE-WB100C sensors are composed of resistor segments oriented in the 0° and 90° directions because of the

145

serpentine resistor pattern. For the JSE-WB100C, $(\frac{L}{W})_{axial} = 96.455$ squares, and $(\frac{L}{W})_{transverse} = 10.313$ squares, resulting in $\gamma = 0.9034$. For two-dimensional states of stress on the surface of the die, with neglect of the out-of-plane stresses and temperature term $f(\Delta T)$, Eq. (8.1.1) yields

$$\frac{\Delta R_0}{R_0} = \gamma(B_1\sigma_{11}^{'} + B_2\sigma_{22}^{'}) + (1-\gamma)(B_2\sigma_{11}^{'} + B_1\sigma_{22}^{'})$$
$$= [\gamma B_1 + (1-\gamma)B_2]\sigma_{11}^{'} + [\gamma B_2 + (1-\gamma)B_1]\sigma_{22}^{'}$$

Eq. (8.1.2)

Similarly, for $\phi = 90^o$

$$\frac{\Delta R_{90}}{R_{90}} = (1-\gamma)(B_1\sigma_{11}^{'} + B_2\sigma_{22}^{'}) + \gamma(B_2\sigma_{11}^{'} + B_1\sigma_{22}^{'})$$
$$= [(1-\gamma)B_1 + \gamma B_2]\sigma_{11}^{'} + [(1-\gamma)B_2 + \gamma B_1]\sigma_{22}^{'}$$

Eq. (8.1.3)

Re-using the notation in Chapter 7,

$$B_{1\_(eff)} = \gamma B_1 + (1-\gamma)B_2$$
$$B_{2\_(eff)} = \gamma B_2 + (1-\gamma)B_1$$

Eq. (8.1.4)

we arrive at the result below:

$$\frac{\Delta R_0}{R_0} = B_{1\_(eff)}\sigma_{11}^{'} + B_{2\_(eff)}\sigma_{22}^{'}$$

Eq. (8.1.5)

$$\frac{\Delta R_{90}}{R_{90}} = B_{2\_(eff)}\sigma_{11}^{'} + B_{1\_(eff)}\sigma_{22}^{'}$$

Eq. (8.1.6)

From the notation above,

$$B_1 = \frac{\gamma B_{1\_(eff)} + (\gamma\text{-}1)B_{2\_(eff)}}{2\gamma\text{-}1}$$
$$B_2 = \frac{\gamma B_{2\_(eff)} + (\gamma\text{-}1)B_{1\_(eff)}}{2\gamma\text{-}1}$$

Eq. (8.1.7)

146

In Table 8.1, B_1 and B_2 with varying temperatures are presented without considering the effect of γ. On the other hand, the effect of γ is considered in the calculation of B_1 and B_2 in Table 8.2 in which $\gamma = 0.9034$ is substituted.

Table 8.1 - Extracted $B_{1\_(eff)}$ and $B_{2\_(eff)}$ versus temperature (Unit: TPa^{-1})				
T(^{o}C)	$B_{1\_(eff)}^{p}$	$B_{2\_(eff)}^{p}$	$B_{1\_(eff)}^{n}$	$B_{2\_(eff)}^{n}$
-133.4	608.2	-179.6	-166.2	135.3
-93.2	542.1	-157.3	-155.4	127.3
-48.2	447.3	-154.9	-152.7	112.7
-23.6	422.8	-148.6	-146.8	105.7
0.6	398.7	-142.6	-141.0	101.0
25.1	366.2	-133.9	-133.7	97.4
49.9	315.3	-117.3	-114.5	88.1
75.1	271.0	-100.1	-102.5	78.9
100.6	239.6	-92.4	-93.2	70.2

Table 8.2 - Modified B_1 and B_2 versus temperature with consideration of γ (Unit: TPa^{-1})				
T(^{o}C)	B_1^{p}	B_2^{p}	B_1^{n}	B_2^{n}
-133.4	702.5	-273.9	-202.3	171.4
-93.2	625.8	-241.0	-189.2	161.1
-48.2	519.4	-227.0	-184.5	144.5
-23.6	491.2	-217.0	-177.0	135.9
0.6	463.5	-207.4	-170.0	130.0
25.1	426.1	-193.8	-161.4	125.1
49.9	367.1	-169.1	-138.8	112.4
75.1	315.4	-144.5	-124.2	100.6
100.6	279.4	-132.2	-112.8	89.8

As seen in Table 8.1 and Table 8.2, considering γ leads to an increase in temperature sensitivity of B_1 and B_2. Also, addition and subtraction of equations in Eq. (8.1.7) yield

$$B_1 + B_2 = B_{1\_(eff)} + B_{2\_(eff)}$$

$$B_1 - B_2 = \frac{B_{1\_(eff)} - B_{2\_(eff)}}{2\gamma - 1} \qquad \text{Eq. (8.1.8)}$$

in which $(B_1 + B_2)$ is independent of γ. However, $(B_1 - B_2)$ depends on γ as shown in Tables 8.3 and 8.4.

Table 8.3 - Addition and subtraction of $B_{1\_(eff)}$ and $B_{2\_(eff)}$ versus temperature (Unit: TPa^{-1})				
$T(^oC)$	$B_{1\_(eff)}^{p} + B_{2\text{-}(eff)}^{p}$	$B_{1\_(eff)}^{p} - B_{2\_(eff)}^{p}$	$B_{1\_(eff)}^{n} + B_{2\_(eff)}^{n}$	$B_{1\_(eff)}^{n} - B_{2\_(eff)}^{n}$
-133.4	428.6	787.8	-30.9	-301.5
-93.2	384.8	699.4	-28.1	-282.7
-48.2	292.4	602.2	-40.0	-265.4
-23.6	274.2	571.4	-41.1	-252.5
0.6	256.1	541.3	-40.0	-242.0
25.1	232.3	501.0	-36.3	-231.1
49.9	198.0	432.6	-26.4	-202.6
75.1	170.9	371.1	-23.6	-181.4
100.6	147.2	332.0	-23.0	-163.4

Table 8.4 - Addition and subtraction of B_1 and B_2 versus temperature (Unit: TPa^{-1})				
$T(^oC)$	$B_1^{p} + B_2^{p}$	$B_1^{p} - B_2^{p}$	$B_1^{n} + B_2^{n}$	$B_1^{n} - B_2^{n}$
-133.4	428.6	976.5	-30.9	-373.7
-93.2	384.8	866.9	-28.1	-350.4
-48.2	292.4	746.4	-40.0	-329.0
-23.6	274.2	708.2	-41.1	-313.0
0.6	256.1	670.9	-40.0	-300.0
25.1	232.3	619.9	-36.3	-286.4
49.9	198.0	536.2	-26.4	-251.1
75.1	170.9	460.0	-23.6	-224.8
100.6	147.2	411.5	-23.0	-202.5

If a sensor is subjected to hydrostatic pressure ($\sigma'_{11} = \sigma'_{22} = \sigma'_{33} = -p$) with consideration of γ, the normalized resistance change is expressed as shown below:

For $\phi = 0$,

$$
\begin{aligned}
\frac{\Delta R_0}{R_0} &= \gamma\,[\,B_1\sigma'_{11} + B_2\sigma'_{22} + B_3\sigma'_{33}\,] + (1\text{-}\gamma)\,[\,B_2\sigma'_{11} + B_1\sigma'_{22} + B_3\sigma'_{33}] + f(\Delta T) \\
&= B_{1\_(eff)}\,\sigma'_{11} + B_{2\_(eff)}\,\sigma'_{22} + B_3\sigma'_{33} + f(\Delta T) \\
&= -(B_{1\_(eff)} + B_{2\_(eff)} + B_3)p + f(\Delta T)
\end{aligned}
$$

Eq. (8.1.9)

Similarly, for $\phi = 90^\circ$

$$
\begin{aligned}
\frac{\Delta R_{90}}{R_{90}} &= (1\text{-}\gamma)\,[\,B_1\sigma'_{11} + B_2\sigma'_{22} + B_3\sigma'_{33}\,] + \gamma\,[\,B_2\sigma'_{11} + B_1\sigma'_{22} + B_3\sigma'_{33}] + f(\Delta T) \\
&= B_{2\_(eff)}\,\sigma'_{11} + B_{1\_(eff)}\,\sigma'_{22} + B_3\sigma'_{33} + f(\Delta T) \\
&= -(B_{1\_(eff)} + B_{2\_(eff)} + B_3)p + f(\Delta T)
\end{aligned}
$$

Eq. (8.1.10)

It is important to emphasize that pressure coefficient π_p is independent of γ because $B_1 + B_2 = B_{1\_(eff)} + B_{2\_(eff)}$.

During diffusion in the fabrication processes, impurities diffuse laterally as well as vertically. If lateral diffusion is assumed in this study, we arrive at the following results:

For BMW-2.1 test chip:

Table 8.5 - γ with lateral diffusion (BMW-2.1)				
	Axial (L/W)	Transverse (L/W)	γ	$(2\gamma\text{-}1)^{-1}$
$x = 0\ \mu m$	143.2	9.37	0.939	1.140
$x = 1.5\ \mu m$	95.8	7.64	0.926	1.173
$x = 2.0\ \mu m$	86.3	7.20	0.923	1.182

Similarly, for JSE-WB 100C test chip:

Table 8.6 - γ from lateral diffusion (JSE-WB100C)				
	Axial (L/W)	Transverse (L/W)	γ	$(2γ\text{-}1)^{-1}$
$x = 0$ μm	96.46	10.31	0.903	1.239
$x = 1.5$ μm	70.89	9.13	0.886	1.296
$x = 2.0$ μm	65.16	8.84	0.881	1.314

As shown in Table 8.5 and Table 8.6, γ decreases with increasing lateral diffusion because the relative rate of number of squares is higher for the part of transverse direction.

8.1.2 Resistor Sensors on the (001) Silicon

- With respect to the unprimed axes

For the unprimed axes, the expression for a resistor sensor at angle ϕ with respect to the x_1 axis is given by

$$\frac{\Delta R}{R} = [\pi_{11}\sigma_{11} + \pi_{12}(\sigma_{22} + \sigma_{33})]\cos^2\phi + [\pi_{11}\sigma_{22} + \pi_{12}(\sigma_{11} + \sigma_{33})]\sin^2\phi$$

Eq. (8.1.11)

$$+ \pi_{44}\sigma_{12} \sin 2\phi + [\alpha_1\Delta T + \alpha_2\Delta T^2 + ...]$$

Using γ and neglecting the out-of-plane stresses and temperature terms gives

$$\frac{\Delta R_0}{R_0} = \gamma[\pi_{11}\sigma_{11} + \pi_{12}\sigma_{22}] + (1-\gamma)[\pi_{11}\sigma_{22} + \pi_{12}\sigma_{11}]$$

$$= [\gamma\pi_{11} + (1-\gamma)\,\pi_{12}]\sigma_{11} + [\gamma\,\pi_{12} + (1-\gamma)\,\pi_{11}]\sigma_{22}$$

Eq. (8.1.12)

$$\frac{\Delta R_{90}}{R_{90}} = (1-\gamma)[\pi_{11}\sigma_{11} + \pi_{12}\sigma_{22}] + \gamma[\pi_{11}\sigma_{22} + \pi_{12}\sigma_{11}]$$

$$= [(1\text{-}\gamma)\,\pi_{11} + \gamma\,\pi_{12}]\sigma_{11} + [(1\text{-}\gamma)\,\pi_{12} + \gamma\,\pi_{11}]\sigma_{22}$$

Eq. (8.1.13)

150

in which the new notations are adopted as follows:

$$\pi_{11\_(eff)} = \gamma\pi_{11} + (1-\gamma)\,\pi_{12} \qquad\qquad \text{Eq. (8.1.14)}$$

$$\pi_{12\_(eff)} = \gamma\pi_{12} + (1-\gamma)\,\pi_{11} \qquad\qquad \text{Eq. (8.1.15)}$$

Then subtraction and addition of two equations above, respectively, yield

$$\pi_{11\_(eff)} + \pi_{12\_(eff)} = \pi_{11} + \pi_{12} \qquad\qquad \text{Eq. (8.1.16)}$$

$$\pi_{11\_(eff)} - \pi_{12\_(eff)} = (2\gamma - 1)(\pi_{11} - \pi_{12}) \qquad\qquad \text{Eq. (8.1.17)}$$

From Eq. (8.1.16) and Eq. (8.1.17),

$$\pi_{11} = \frac{\gamma}{2\gamma - 1}\pi_{11\_(eff)} + \frac{\gamma - 1}{2\gamma - 1}\pi_{12\_(eff)} \qquad\qquad \text{Eq. (8.1.18)}$$

$$\pi_{12} = \frac{\gamma\text{-}1}{2\gamma - 1}\pi_{11\_(eff)} + \frac{\gamma}{2\gamma - 1}\pi_{12\_(eff)} \qquad\qquad \text{Eq. (8.1.19)}$$

It can be seen that $\pi_S = \pi_{11} + \pi_{12}$ is independent of γ. However, π_{11}, π_{12}, and

$\pi_D = \pi_{11} - \pi_{12}$ depend on γ.

- With respect to the primed axes

Similarly, for the primed axes, the expression for a resistor sensor at angle ϕ with

respect to the x_1' axis is given by

$$\frac{\Delta R}{R} = \left[\left(\frac{\pi_{11} + \pi_{12} + \pi_{44}}{2}\right)\sigma_{11}' + \left(\frac{\pi_{11} + \pi_{12} - \pi_{44}}{2}\right)\sigma_{22}'\right]\cos^2\phi$$

$$+ \left[\left(\frac{\pi_{11} + \pi_{12} - \pi_{44}}{2}\right)\sigma_{11}' + \left(\frac{\pi_{11} + \pi_{12} + \pi_{44}}{2}\right)\sigma_{22}'\right]\sin^2\phi \quad \text{Eq. (8.1.20)}$$

$$+ \ \pi_{12}\sigma_{33} + (\pi_{11}\text{-}\pi_{12})\sigma_{12}' \ \sin 2\phi + [\alpha_1\Delta T + \alpha_2\Delta T^2 + ...]$$

151

Including the effect of γ and neglecting the out-of-plane stresses and temperature terms in

Eq. (8.1.20) yield the following:

$$\frac{\Delta R_0}{R_0} = \gamma[\left(\frac{\pi_{11} + \pi_{12} + \pi_{44}}{2}\right)\sigma'_{11} + \left(\frac{\pi_{11} + \pi_{12} - \pi_{44}}{2}\right)\sigma'_{22}]$$

$$+ (1-\gamma)[\left(\frac{\pi_{11} + \pi_{12} - \pi_{44}}{2}\right)\sigma'_{11} + \left(\frac{\pi_{11} + \pi_{12} + \pi_{44}}{2}\right)\sigma'_{22}] \quad \text{Eq. (8.1.21)}$$

$$= [\frac{\pi_{11} + \pi_{12} + (2\gamma-1)\pi_{44}}{2}]\sigma'_{11} + [\frac{\pi_{11} + \pi_{12} + (1-2\gamma)\pi_{44}}{2}]\sigma'_{22}$$

Similarly, for $\phi = 90^o$

$$\frac{\Delta R_{90}}{R_{90}} = (1-\gamma)[\left(\frac{\pi_{11} + \pi_{12} + \pi_{44}}{2}\right)\sigma'_{11} + \left(\frac{\pi_{11} + \pi_{12} - \pi_{44}}{2}\right)\sigma'_{22}]$$

$$+ \gamma[\left(\frac{\pi_{11} + \pi_{12} - \pi_{44}}{2}\right)\sigma'_{11} + \left(\frac{\pi_{11} + \pi_{12} + \pi_{44}}{2}\right)\sigma'_{22}] \quad \text{Eq. (8.1.22)}$$

$$= [\frac{\pi_{11} + \pi_{12} + (1-2\gamma)\pi_{44}}{2}]\sigma'_{11} + [\frac{\pi_{11} + \pi_{12} + (2\gamma-1)\pi_{44}}{2}]\sigma'_{22}$$

Here the new notations are:

$$\frac{\pi_{S\_(eff)} + \pi_{44\_(eff)}}{2} = \frac{\pi_{11} + \pi_{12} + (2\gamma-1)\pi_{44}}{2} \quad \text{Eq. (8.1.23)}$$

$$\frac{\pi_{S\_(eff)} - \pi_{44\_(eff)}}{2} = \frac{\pi_{11} + \pi_{12} + (1-2\gamma)\pi_{44}}{2} \quad \text{Eq. (8.1.24)}$$

Subtraction and addition of both equations above, respectively, yield

$$\pi_{S\_(eff)} = \pi_S \quad \text{Eq. (8.1.25)}$$

$$\pi_{44\_(eff)} = (2\gamma-1)\pi_{44} \quad \text{Eq. (8.1.26)}$$

By Eq. (8.1.25) and Eq. (8.1.26),

$$\pi_S = \pi_{S\_(eff)} \quad \text{Eq. (8.1.27)}$$

$$\pi_{44} = \frac{1}{(2\gamma\text{-}1)} \pi_{44\_(\text{eff})} \qquad\qquad \text{Eq. (8.1.28)}$$

It is found that π_S is independent of γ. However, π_{44} depends on γ.

8.2 Off-Axis Alignment Error on the (001) Silicon Plane

The rosette configuration on the (001) plane silicon consists of 0°, 90°, 45°, and -45° resistors relative to the x_1 axis [100] (or $x_1^{'}$ axis [110]). The strip is cut along $x^{''} - y^{''}$ axes counter-clockwise rotated θ from $x - y$ axes [100] (or $x^{'} - y^{'}$ axes [110]). If we use the double-primed notation instead of the unprimed (or primed) notation, the equations change as discussed below.

- With respect to the unprimed axes

For the unprimed axes on the (001) plane silicon, the general equation for counter-clockwise rotation of the $x^{''} - y^{''}$ axes by an angle of θ from the $x - y$ axes, is given as follows:

$$\frac{\Delta R}{R} = \{\pi_{11}[(1-\frac{1}{2}\sin^2 2\theta)\ \sigma_{11}'' + \frac{1}{2}\sin^2 2\theta\ \sigma_{22}'' - \frac{\sin 4\theta}{2}\ \sigma_{12}'']$$

$$+\pi_{12}[\ \frac{1}{2}\sin^2 2\theta\ \sigma_{11}'' + (1-\frac{1}{2}\sin^2 2\theta)\sigma_{22}'' + \sigma_{33}'' + \frac{\sin 4\theta}{2}\ \sigma_{12}'']$$

$$+\pi_{44}[\ \frac{1}{2}\sin^2 2\theta\ \sigma_{11}'' - \frac{1}{2}\sin^2 2\theta\ \sigma_{22}'' + \frac{\sin 4\theta}{2}\ \sigma_{12}'']\}\ l''^2$$

$$+\{\pi_{11}[\frac{1}{2}\sin^2 2\theta\ \sigma_{11}'' + (1-\frac{1}{2}\sin^2 2\theta)\ \sigma_{22}'' + \frac{\sin 4\theta}{2}\ \sigma_{12}'']$$

$$+\pi_{12}[\ (1-\frac{1}{2}\sin^2 2\theta)\ \sigma_{11}'' + \frac{1}{2}\sin^2 2\theta\ \sigma_{22}'' + \sigma_{33}'' - \frac{\sin 4\theta}{2}\ \sigma_{12}'']$$

$$+\pi_{44}[\ -\frac{1}{2}\sin^2 2\theta\ \sigma_{11}'' + \frac{1}{2}\sin^2 2\theta\ \sigma_{22}'' - \frac{\sin 4\theta}{2}\ \sigma_{12}'']\}\ m''^2$$

$$+[\pi_{11}(\ \sigma_{33}'' + \frac{1}{2}\sin 4\theta\ \sigma_{12}'') + \pi_{12}(\ \sigma_{11}'' + \sigma_{22}'' - \frac{1}{2}\sin 4\theta\ \sigma_{12}'') - \pi_{44}\frac{\sin 4\theta}{2}\ \sigma_{12}'']\ n''^2$$

$$+2\ \pi_{44}(\sigma_{13}''l''n'' + \sigma_{23}''m''n'')$$

$$+2\{\pi_{11}[\ \frac{\sin 4\theta}{4}\ (\sigma_{22}'' - \sigma_{11}'') +\ \sin^2 2\theta\ \sigma_{12}'']$$

$$+\pi_{12}[\ -\frac{\sin 4\theta}{4}\ (\sigma_{22}'' - \sigma_{11}'') -\ \sin^2 2\theta\ \sigma_{12}'']$$

$$+\pi_{44}[\ -\frac{\sin 4\theta}{4}\ (\sigma_{22}'' - \sigma_{11}'') +\ \cos^2 2\theta\ \sigma_{12}'']\}\ l''m''$$

$$+[\alpha_1\Delta T + \alpha_2\Delta T^2 + ...\ ]$$

Eq. (8.2.1)

In the case of $\theta = 0$, the double-primed axes are aligned with the unprimed axes, and Eq. (8.2.1) simplifies to

$$\frac{\Delta R}{R} = [\pi_{11}\sigma_{11} + \pi_{12}(\sigma_{22} + \sigma_{33})]l^2 + [\pi_{11}\sigma_{22} + \pi_{12}(\sigma_{11} + \sigma_{33})]m^2$$

$$+ [\pi_{11}\sigma_{33} + \pi_{12}(\sigma_{11} + \sigma_{22})]n^2 + 2\pi_{44}(\sigma_{12}lm + \sigma_{13}ln + \sigma_{23}mn)$$

$$+ [\alpha_1\Delta T + \alpha_2\Delta T^2 + ...\ ]$$

Eq. (8.2.2)

By introducing $l = \cos\phi$, $m = \sin\phi$, and $n = 0$, Eq. (8.2.2) is expressed as

$$\frac{\Delta R}{R} = [\pi_{11}\sigma_{11} + \pi_{12}(\sigma_{22} + \sigma_{33})]\cos^2\phi$$

$$+ [\pi_{11}\sigma_{22} + \pi_{12}(\sigma_{11} + \sigma_{33})]\sin^2\phi$$

$$+ 2\pi_{44}\ \sigma_{12}\ \cos\phi\sin\phi$$

$$+ [\alpha_1\Delta T + \alpha_2\Delta T^2 + ...\ ]$$

Eq. (8.2.3)

Considering θ and assuming uniaxial stress $\sigma_{11}^{''}$ with neglect of temperature terms gives

$$\frac{\Delta R_0}{R_0} = [\pi_{11}(1 - \frac{1}{2}\sin^2 2\theta) + \pi_{12}\frac{1}{2}\sin^2 2\theta + \pi_{44}\frac{1}{2}\sin^2 2\theta]\,\sigma_{11}^{''}$$

$$= [\pi_{11} - (\frac{\pi_{11} - \pi_{12} - \pi_{44}}{2})\sin^2 2\theta]\,\sigma_{11}^{''} \qquad \text{Eq. (8.2.4)}$$

$$= \pi_{11}^{\theta}\sigma_{11}^{''}$$

$$\frac{\Delta R_{90}}{R_{90}} = [\pi_{11}\frac{1}{2}\sin^2 2\theta + \pi_{12}(1 - \frac{1}{2}\sin^2 2\theta) + \pi_{44}(-\frac{1}{2})\sin^2 2\theta]\,\sigma_{11}^{''}$$

$$= [\pi_{12} + (\frac{\pi_{11} - \pi_{12} - \pi_{44}}{2})\sin^2 2\theta]\,\sigma_{11}^{''} \qquad \text{Eq. (8.2.5)}$$

$$= \pi_{12}^{\theta}\sigma_{11}^{''}$$

$$\frac{\Delta R_{45}}{R_{45}} = [\pi_{11}(\frac{1 - \sin 2\theta \cos 2\theta}{2}) + \pi_{12}(\frac{1 + \sin 2\theta \cos 2\theta}{2}) + \pi_{44}(\frac{\sin 2\theta \cos 2\theta}{2})]\,\sigma_{11}^{''}$$

$$= [(\frac{\pi_{11} + \pi_{12}}{2}) - (\frac{\pi_{11} - \pi_{12} - \pi_{44}}{2})\sin 2\theta \cos 2\theta]\,\sigma_{11}^{''}$$

$$\text{Eq. (8.2.6)}$$

$$\frac{\Delta R_{-45}}{R_{-45}} = [\pi_{11}(\frac{1 + \sin 2\theta \cos 2\theta}{2}) + \pi_{12}(\frac{1 - \sin 2\theta \cos 2\theta}{2}) - \pi_{44}(\frac{\sin 2\theta \cos 2\theta}{2})]\,\sigma_{11}^{''}$$

$$= [(\frac{\pi_{11} + \pi_{12}}{2}) + (\frac{\pi_{11} - \pi_{12} - \pi_{44}}{2})\sin 2\theta \cos 2\theta]\,\sigma_{11}^{''}$$

$$\text{Eq. (8.2.7)}$$

From these equations, we find that the $0^{o}/90^{o}$ and $\pm 45^{o}$ pairs are insensitive to rotational alignment error. For $\theta = 0$, assuming uniaxial stress $\sigma_{11}^{''}$ with neglect of temperature terms gives

$$\frac{\Delta R_0}{R_0} = \pi_{11}\sigma''_{11} \qquad \text{Eq. (8.2.8)}$$

$$\frac{\Delta R_{90}}{R_{90}} = \pi_{12}\sigma''_{11} \qquad \text{Eq. (8.2.9)}$$

$$\frac{\Delta R_{45}}{R_{45}} = \frac{\Delta R_{-45}}{R_{-45}} = (\frac{\pi_{11} + \pi_{12}}{2})\sigma''_{11} \qquad \text{Eq. (8.2.10)}$$

where $\sigma''_{11} = \sigma_{11}$ since the doubled primed axes are aligned with the unprimed axes for

$\theta = 0$. In Eq. (8.2.4), π_{11}^{θ} is defined as

$$\pi_{11}^{\theta} = \pi_{11} - (\frac{\pi_{11} - \pi_{12} - \pi_{44}}{2})\sin^2 2\theta \qquad \text{Eq. (8.2.11)}$$

Similarly, in Eq. (8.2.5), π_{12}^{θ} is defined as

$$\pi_{12}^{\theta} = \pi_{12} + (\frac{\pi_{11} - \pi_{12} - \pi_{44}}{2})\sin^2 2\theta \qquad \text{Eq. (8.2.12)}$$

For $\phi = 0$ and $\phi = 90^{\circ}$, the normalized error in $\Delta R/R$ induced by θ is given by

$$\frac{[\frac{\Delta R_0}{R_0}]_{\theta} - [\frac{\Delta R_0}{R_0}]_{\theta=0}}{[\frac{\Delta R_0}{R_0}]_{\theta=0}} = (\frac{-\pi_{11} + \pi_{12} + \pi_{44}}{2\pi_{11}})\sin^2 2\theta \qquad \text{Eq. (8.2.13)}$$

$$= -(\frac{\pi_D - \pi_{44}}{2\pi_{11}})\sin^2 2\theta$$

$$\frac{[\frac{\Delta R_{90}}{R_{90}}]_{\theta} - [\frac{\Delta R_{90}}{R_{90}}]_{\theta=0}}{[\frac{\Delta R_{90}}{R_{90}}]_{\theta=0}} = (\frac{\pi_{11} - \pi_{12} - \pi_{44}}{2\pi_{12}})\sin^2 2\theta \qquad \text{Eq. (8.2.14)}$$

$$= (\frac{\pi_D - \pi_{44}}{2\pi_{12}})\sin^2 2\theta$$

where $\pi_D = \pi_{11} - \pi_{12}$. For $\phi = \pm 45^{\circ}$, the normalized error in $\Delta R/R$ induced by θ is given by

$$\frac{[\frac{\Delta R_{45}}{R_{45}}]_{\theta} - [\frac{\Delta R_{45}}{R_{45}}]_{\theta=0}}{[\frac{\Delta R_{45}}{R_{45}}]_{\theta=0}} = -(\frac{\pi_{11} - \pi_{12} - \pi_{44}}{\pi_S}) \sin 2\theta \cos 2\theta \qquad \text{Eq. (8.2.15)}$$

$$= (\frac{\pi_{44} - \pi_D}{2\pi_S}) \sin 4\theta$$

$$\frac{[\frac{\Delta R_{-45}}{R_{-45}}]_{\theta} - [\frac{\Delta R_{-45}}{R_{-45}}]_{\theta=0}}{[\frac{\Delta R_{-45}}{R_{-45}}]_{\theta=0}} = (\frac{\pi_{11} - \pi_{12} - \pi_{44}}{\pi_S}) \sin 2\theta \cos 2\theta \qquad \text{Eq. (8.2.16)}$$

$$= (\frac{\pi_D - \pi_{44}}{2\pi_S}) \sin 4\theta$$

For p-type silicon, $|\pi_{44}| \gg |\pi_{11}|$ and $|\pi_{44}| \gg |\pi_{12}|$ give [6], [98]

$$\frac{[\frac{\Delta R_0}{R_0}]_{\theta} - [\frac{\Delta R_0}{R_0}]_{\theta=0}}{[\frac{\Delta R_0}{R_0}]_{\theta=0}} \cong \frac{\pi_{44}}{2\pi_{11}} \sin^2 2\theta \qquad \text{Eq. (8.2.17)}$$

$$\frac{[\frac{\Delta R_{90}}{R_{90}}]_{\theta} - [\frac{\Delta R_{90}}{R_{90}}]_{\theta=0}}{[\frac{\Delta R_{90}}{R_{90}}]_{\theta=0}} \cong \frac{-\pi_{44}}{2\pi_{12}} \sin^2 2\theta \qquad \text{Eq. (8.2.18)}$$

$$\frac{[\frac{\Delta R_{45}}{R_{45}}]_{\theta} - [\frac{\Delta R_{45}}{R_{45}}]_{\theta=0}}{[\frac{\Delta R_{45}}{R_{45}}]_{\theta=0}} \cong \frac{1}{2} \frac{\pi_{44}}{\pi_S} \sin 4\theta \qquad \text{Eq. (8.2.19)}$$

157

$$\frac{[\frac{\Delta R_{-45}}{R_{-45}}]_{\theta} - [\frac{\Delta R_{-45}}{R_{-45}}]_{\theta=0}}{[\frac{\Delta R_{-45}}{R_{-45}}]_{\theta=0}} \cong -\frac{1}{2}(\frac{\pi_{44}}{\pi_S})\sin 4\theta \qquad \text{Eq. (8.2.20)}$$

For n-type silicon, the approximation $\pi_{11} \cong -2\pi_{12}$ [23] yields

$$\frac{[\frac{\Delta R_0}{R_0}]_{\theta} - [\frac{\Delta R_0}{R_0}]_{\theta=0}}{[\frac{\Delta R_0}{R_0}]_{\theta=0}} \cong -(\frac{3\pi_{12} + \pi_{44}}{4\pi_{12}})\sin^2 2\theta \qquad \text{Eq. (8.2.21)}$$

$$\frac{[\frac{\Delta R_{90}}{R_{90}}]_{\theta} - [\frac{\Delta R_{90}}{R_{90}}]_{\theta=0}}{[\frac{\Delta R_{90}}{R_{90}}]_{\theta=0}} \cong -(\frac{3\pi_{12} + \pi_{44}}{2\pi_{12}})\sin^2 2\theta \qquad \text{Eq. (8.2.22)}$$

$$\frac{[\frac{\Delta R_{45}}{R_{45}}]_{\theta} - [\frac{\Delta R_{45}}{R_{45}}]_{\theta=0}}{[\frac{\Delta R_{45}}{R_{45}}]_{\theta=0}} \cong -\frac{1}{2}(\frac{\pi_{44} + 3\pi_{12}}{\pi_{12}})\sin 4\theta \qquad \text{Eq. (8.2.23)}$$

$$\frac{[\frac{\Delta R_{-45}}{R_{-45}}]_{\theta} - [\frac{\Delta R_{-45}}{R_{-45}}]_{\theta=0}}{[\frac{\Delta R_{-45}}{R_{-45}}]_{\theta=0}} \cong \frac{1}{2}(\frac{\pi_{44} + 3\pi_{12}}{\pi_{12}})\sin 4\theta \qquad \text{Eq. (8.2.24)}$$

In the equations, for p-type sensors, the normalized % error in $\Delta R/R$ induced by θ can have a considerable value because of $|\pi_{44}| \gg |\pi_{11}|$ and $|\pi_{44}| \gg |\pi_{12}|$. For $\phi = 0$, $\phi = 90^o$, and $\phi = \pm45^o$, the normalized % error in $\Delta R/R$ versus θ is presented in Tables 8.7 and 8.8, whose plots are shown in Figs. 8.1 through 8.4.

Table 8.7 - Normalized % error in π_{11}^{θ} and π_{12}^{θ} versus θ				
	π_{11}^{θ}		π_{12}^{θ}	
θ	P-type sensors	N-type sensors	P-type sensors	N-type sensors
-10	1.16E+02	-8.13E+00	6.94E+02	-1.56E+01
-9	9.44E+01	-6.63E+00	5.66E+02	-1.27E+01
-8	7.50E+01	-5.27E+00	4.50E+02	-1.01E+01
-7	5.79E+01	-4.07E+00	3.47E+02	-7.79E+00
-6	4.27E+01	-3.00E+00	2.56E+02	-5.75E+00
-5	2.98E+01	-2.09E+00	1.79E+02	-4.01E+00
-4	1.91E+01	-1.35E+00	1.15E+02	-2.58E+00
-3	1.08E+01	-7.63E-01	6.45E+01	-1.46E+00
-2	4.85E+00	-3.42E-01	2.91E+01	-6.55E-01
-1	1.21E+00	-8.81E-02	7.27E+00	-1.69E-01
0	0.00E+00	0.00E+00	0.00E+00	0.00E+00
1	1.21E+00	-8.81E-02	7.27E+00	-1.69E-01
2	4.85E+00	-3.42E-01	2.91E+01	-6.55E-01
3	1.08E+01	-7.63E-01	6.45E+01	-1.46E+00
4	1.91E+01	-1.35E+00	1.15E+02	-2.58E+00
5	2.98E+01	-2.09E+00	1.79E+02	-4.01E+00
6	4.27E+01	-3.00E+00	2.56E+02	-5.75E+00
7	5.79E+01	-4.07E+00	3.47E+02	-7.79E+00
8	7.50E+01	-5.27E+00	4.50E+02	-1.01E+01
9	9.44E+01	-6.63E+00	5.66E+02	-1.27E+01
10	1.16E+02	-8.13E+00	6.94E+02	-1.56E+01
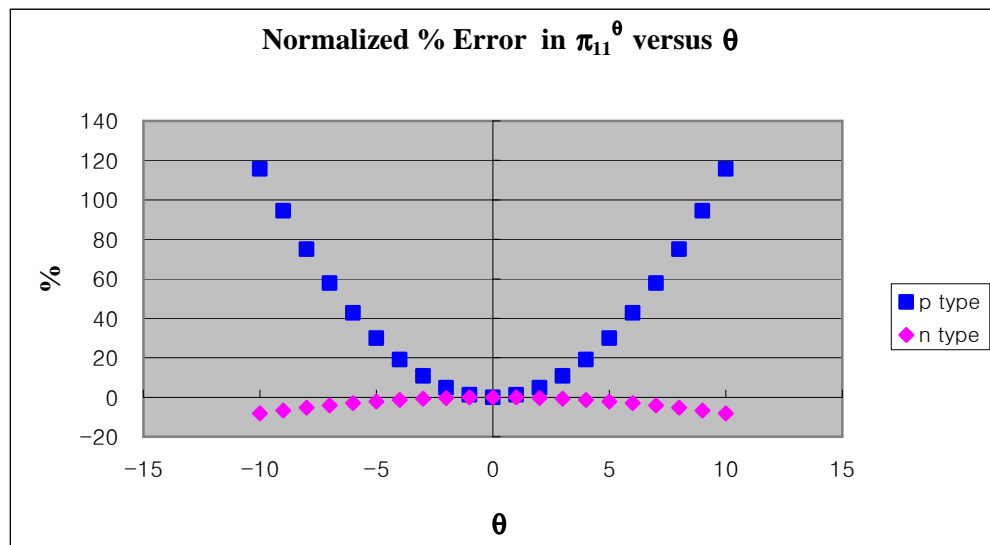
Fig. 8.1 - Normalized % error in π_{11}^{θ} versus θ
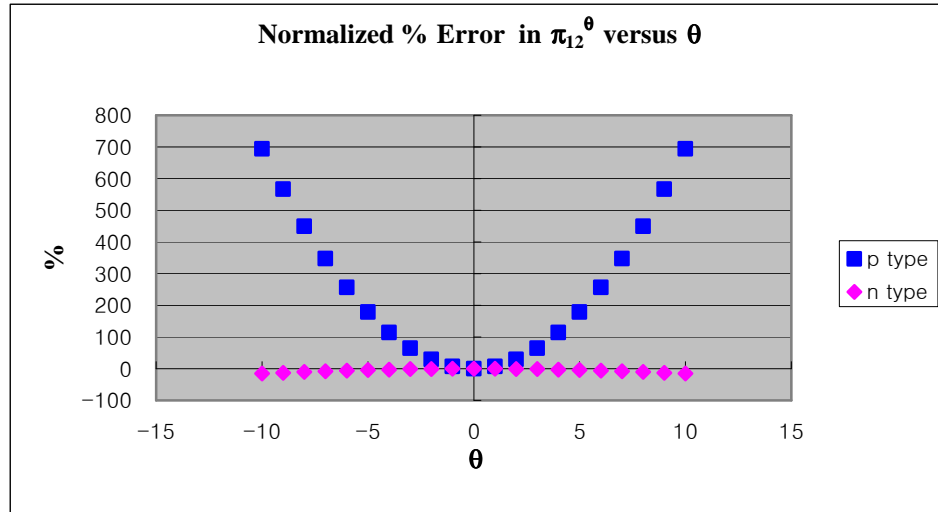
Fig. 8.2 - Normalized % error in π_{12}^{θ} versus θ

Table 8.8 - Normalized % error in $\Delta R_{45}/R_{45}$ and $\Delta R_{-45}/R_{-45}$ versus θ				
	$\phi = 45^o$		$\phi = -45^o$	
θ	P-type sensors	N-type sensors	P-type sensors	N-type sensors
-10	-7.62E+02	9.35E+01	7.62E+02	-9.35E+01
-9	-6.97E+02	8.55E+01	6.97E+02	-8.55E+01
-8	-6.28E+02	7.71E+01	6.28E+02	-7.71E+01
-7	-5.57E+02	6.83E+01	5.57E+02	-6.83E+01
-6	-4.82E+02	5.92E+01	4.82E+02	-5.92E+01
-5	-4.05E+02	4.98E+01	4.05E+02	-4.98E+01
-4	-3.27E+02	4.01E+01	3.27E+02	-4.01E+01
-3	-2.46E+02	3.02E+01	2.46E+02	-3.02E+01
-2	-1.65E+02	2.02E+01	1.65E+02	-2.02E+01
-1	-8.27E+01	1.01E+01	8.27E+01	-1.01E+01
0	0.00E+00	0.00E+00	0.00E+00	0.00E+00
1	8.27E+01	-1.01E+01	-8.27E+01	1.01E+01
2	1.65E+02	-2.02E+01	-1.65E+02	2.02E+01
3	2.46E+02	-3.02E+01	-2.46E+02	3.02E+01
4	3.27E+02	-4.01E+01	-3.27E+02	4.01E+01
5	4.05E+02	-4.98E+01	-4.05E+02	4.98E+01
6	4.82E+02	-5.92E+01	-4.82E+02	5.92E+01
7	5.57E+02	-6.83E+01	-5.57E+02	6.83E+01
8	6.28E+02	-7.71E+01	-6.28E+02	7.71E+01
9	6.97E+02	-8.55E+01	-6.97E+02	8.55E+01
10	7.62E+02	-9.35E+01	-7.62E+02	9.35E+01

Fig. 8.3 - Normalized % error in $\Delta R_{45}/R_{45}$ versus θ
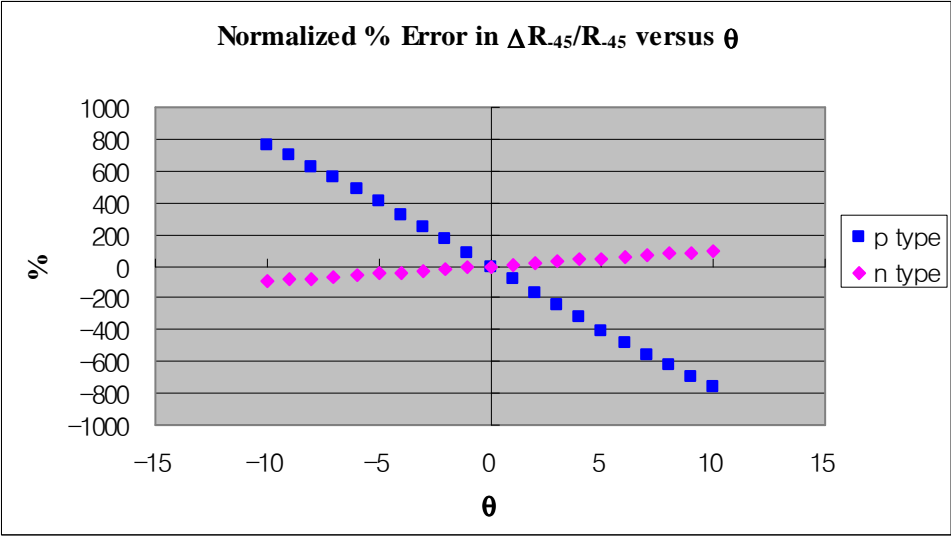
Fig. 8.4 - Normalized % error in $\Delta R_{-45}/R_{-45}$ versus θ

161

Through Figs. 8.1 and 8.4, it can be seen that p-type sensors have larger normalized % error compared with n-type sensors as described above.

- With respect to the primed axes

For the case of $\theta = 45^o$, the double-primed axes are aligned with the primed axes, and Eq. (8.2.1) simplifies to

$$\frac{\Delta R}{R} = \left[\left(\frac{\pi_{11} + \pi_{12} + \pi_{44}}{2} \right) \sigma_{11}' + \left(\frac{\pi_{11} + \pi_{12} - \pi_{44}}{2} \right) \sigma_{22}' \right] \cos^2 \phi$$

$$+ \left[\left(\frac{\pi_{11} + \pi_{12} - \pi_{44}}{2} \right) \sigma_{11}' + \left(\frac{\pi_{11} + \pi_{12} + \pi_{44}}{2} \right) \sigma_{22}' \right] \sin^2 \phi \quad \text{Eq. (8.2.25)}$$

$$+ \pi_{12} \sigma_{33} + (\pi_{11} - \pi_{12}) \sigma_{12}' \sin 2\phi + [\alpha_1 \Delta T + \alpha_2 \Delta T^2 + ...]$$

where $l' = \cos\phi$, $m' = \sin\phi$, and $n' = 0$ has been introduced, and ϕ is the angle between the x_1'-axis and the resistor orientation. The stress components are now measured in the double-primed coordinate system, and $\sigma_{33}'' = \sigma_{33}' = 0$ has been assumed.

For the primed axes on the (001) plane silicon, the general equation for counter-clockwise rotation of the $x'' - y''$ axes by an angle of θ from the $x' - y'$ axes [110], is given as follows:

162

$$\frac{\Delta R}{R} = \{\pi_{11}[(1-\frac{1}{2}\cos^2 2\theta)\,\sigma_{11}^{''} + \frac{1}{2}\cos^2 2\theta\,\sigma_{22}^{''} + \frac{\sin 4\theta}{2}\,\sigma_{12}^{''}]$$

$$+ \pi_{12}[\frac{1}{2}\cos^2 2\theta\,\sigma_{11}^{''} + (1-\frac{1}{2}\cos^2 2\theta)\sigma_{22}^{''} + \sigma_{33}^{''} - \frac{\sin 4\theta}{2}\,\sigma_{12}^{''}]$$

$$+ \pi_{44}[\frac{1}{2}\cos^2 2\theta\,\sigma_{11}^{''} - \frac{1}{2}\cos^2 2\theta\,\sigma_{22}^{''} - \frac{\sin 4\theta}{2}\,\sigma_{12}^{''}]\}\,l^{''2}$$

$$+ \{\pi_{11}[\frac{1}{2}\cos^2 2\theta\,\sigma_{11}^{''} + (1-\frac{1}{2}\cos^2 2\theta)\,\sigma_{22}^{''} - \frac{\sin 4\theta}{2}\,\sigma_{12}^{''}]$$

$$+ \pi_{12}[(1-\frac{1}{2}\cos^2 2\theta)\,\sigma_{11}^{''} + \frac{1}{2}\cos^2 2\theta\,\sigma_{22}^{''} + \sigma_{33}^{''} + \frac{\sin 4\theta}{2}\,\sigma_{12}^{''}]$$

$$+ \pi_{44}[-\frac{1}{2}\cos^2 2\theta\,\sigma_{11}^{''} + \frac{1}{2}\cos^2 2\theta\,\sigma_{22}^{''} + \frac{\sin 4\theta}{2}\,\sigma_{12}^{''}]\}\,m^{''2}$$

$$+ [\pi_{11}(\sigma_{33}^{''} - \frac{1}{2}\sin 4\theta\,\sigma_{12}^{''}) + \pi_{12}(\sigma_{11}^{''} + \sigma_{22}^{''} + \frac{1}{2}\sin 4\theta\,\sigma_{12}^{''}) + \pi_{44}\frac{\sin 4\theta}{2}\,\sigma_{12}^{''}]\,n^{''2}$$

$$+ 2\pi_{44}(\sigma_{13}^{''}l^{''}n^{''} + \sigma_{23}^{''}m^{''}n^{''})$$

$$+ 2\{\pi_{11}[\frac{\sin 4\theta}{4}(\sigma_{11}^{''} - \sigma_{22}^{''}) + \cos^2 2\theta\,\sigma_{12}^{''}]$$

$$+ \pi_{12}[\frac{\sin 4\theta}{4}(\sigma_{22}^{''} - \sigma_{11}^{''}) - \cos^2 2\theta\,\sigma_{12}^{''}]$$

$$+ \pi_{44}[\frac{\sin 4\theta}{4}(\sigma_{22}^{''} - \sigma_{11}^{''}) + \sin^2 2\theta\,\sigma_{12}^{''}]\}\,l^{''}m^{''}$$

$$+ [\alpha_1\Delta T + \alpha_2\Delta T^2 + ...]$$

Eq. (8.2.26)

In the formula, $(\theta - 45)^\circ$ instead of θ is substituted into Eq. (8.2.1) in order to consider the fact that the [110] axis is counter-clockwise rotated by 45° from the [100] axis. In the case of $\theta = 0$, the double-primed axes are aligned with the primed axes, and Eq. (8.2.26) simplifies to

$$\frac{\Delta R}{R} = [\pi_{11}(\frac{1}{2}\sigma'_{11} + \frac{1}{2}\sigma'_{22}) + \pi_{12}(\frac{1}{2}\sigma'_{11} + \frac{1}{2}\sigma'_{22} + \sigma'_{33}) + \pi_{44}(\frac{1}{2}\sigma'_{11} - \frac{1}{2}\sigma'_{22})]l'^2$$

$$+ [\pi_{11}(\frac{1}{2}\sigma'_{11} + \frac{1}{2}\sigma'_{22}) + \pi_{12}(\frac{1}{2}\sigma'_{11} + \frac{1}{2}\sigma'_{22} + \sigma'_{33}) + \pi_{44}(-\frac{1}{2}\sigma'_{11} + \frac{1}{2}\sigma'_{22})]m'^2$$

$$+ [\pi_{11}\sigma'_{33} + \pi_{12}(\sigma'_{11} + \sigma'_{22})]n'^2$$

$$+ 2\pi_{44}(\sigma'_{13}l'n' + \sigma'_{23}m'n') + 2(\pi_{11} - \pi_{12})\sigma'_{12}l'm'$$

$$+ [\alpha_1\Delta T + \alpha_2\Delta T^2 + ...]$$

<div align="right">Eq. (8.2.27)</div>

By introducing $l' = \cos\phi$, $m' = \sin\phi$, and $n' = 0$, Eq. (8.2.27) is expressed as

$$\frac{\Delta R}{R} = [(\frac{\pi_{11} + \pi_{12} + \pi_{44}}{2})\sigma'_{11} + (\frac{\pi_{11} + \pi_{12} - \pi_{44}}{2})\sigma'_{22}]\cos^2\phi$$

$$+ [(\frac{\pi_{11} + \pi_{12} - \pi_{44}}{2})\sigma'_{11} + (\frac{\pi_{11} + \pi_{12} + \pi_{44}}{2})\sigma'_{22}]\sin^2\phi$$

$$+ \pi_{12}\sigma'_{33} + 2(\pi_{11} - \pi_{12})\sigma'_{12}\cos\phi\sin\phi$$

$$+ [\alpha_1\Delta T + \alpha_2\Delta T^2 + ...]$$

<div align="right">Eq. (8.2.28)</div>

It may be noted that Eq. (8.2.28) is the same as Eq. (8.2.25). Considering θ and assuming

uniaxial stress σ''_{11} in Eq. (8.2.26) with neglect of temperature terms gives

$$\frac{\Delta R_0}{R_0} = [\pi_{11}(1 - \frac{1}{2}\cos^2 2\theta) + \frac{\pi_{12}}{2}\cos^2 2\theta + \frac{\pi_{44}}{2}\cos^2 2\theta]\sigma''_{11} \qquad \text{Eq. (8.2.29)}$$

$$\frac{\Delta R_{90}}{R_{90}} = [\frac{\pi_{11}}{2}\cos^2 2\theta + \pi_{12}(1 - \frac{1}{2}\cos^2 2\theta) - \frac{\pi_{44}}{2}\cos^2 2\theta]\sigma''_{11} \qquad \text{Eq. (8.2.30)}$$

$$\frac{\Delta R_{45}}{R_{45}} = [\frac{\pi_S}{2} + (\pi_D - \pi_{44})\frac{\sin 4\theta}{4}]\sigma''_{11} \qquad \text{Eq. (8.2.31)}$$

$$\frac{\Delta R_{-45}}{R_{-45}} = [\frac{\pi_S}{2} - (\pi_D - \pi_{44})\frac{\sin 4\theta}{4}]\sigma''_{11} \qquad \text{Eq. (8.2.32)}$$

It may be stressed that the $0^o/90^o$ and $\pm 45^o$ pairs are insensitive to rotational alignment error. In addition, Eqs. (8.2.6) and (8.2.7) are equal to Eqs. (8.2.32) and (8.2.31), respectively. For $\theta = 0$, assuming uniaxial stress $\sigma_{11}^{''}$ with neglect of temperature terms gives

$$\frac{\Delta R_0}{R_0} = (\frac{\pi_{11} + \pi_{12} + \pi_{44}}{2})\sigma_{11}^{''} \qquad \text{Eq. (8.2.33)}$$

$$\frac{\Delta R_{90}}{R_{90}} = (\frac{\pi_{11} + \pi_{12} - \pi_{44}}{2})\sigma_{11}^{''} \qquad \text{Eq. (8.2.34)}$$

$$\frac{\Delta R_{45}}{R_{45}} = \frac{\Delta R_{-45}}{R_{-45}} = (\frac{\pi_{11} + \pi_{12}}{2})\sigma_{11}^{''} \qquad \text{Eq. (8.2.35)}$$

In the equations, $\sigma_{11}^{''} = \sigma_{11}$ because the doubled primed axes are aligned with the primed axes for $\theta = 0$.

Subtraction of Eq. (8.2.30) from Eq. (8.2.29) leads to

$$\frac{\Delta R_0}{R_0} - \frac{\Delta R_{90}}{R_{90}} = [\pi_D (1 - \cos^2 2\theta) + \pi_{44} \cos^2 2\theta] \, \sigma_{11}^{''}$$
$$= \pi_{44}^{\theta} \, \sigma_{11}^{''} \qquad \text{Eq. (8.2.36)}$$

In Eq. (8.2.36), π_{44}^{θ} is defined as

$$\pi_{44}^{\theta} = \pi_D (1 - \cos^2 2\theta) + \pi_{44} \cos^2 2\theta \qquad \text{Eq. (8.2.37)}$$

Combining Eqs. (8.2.29) and (8.2.30) yields the normalized % error in π_{44}^{θ} versus θ as presented in Table 8.9, whose plots are shown in Fig. 8.5.

Table 8.9 - Normalized % error in π_{44}^{θ} versus θ		
θ	P-type sensors	N-type sensors
-10	-1.10E+01	1.22E+02
-9	-9.02E+00	9.97E+01
-8	-7.17E+00	7.93E+01
-7	-5.53E+00	6.11E+01
-6	-4.08E+00	4.51E+01
-5	-2.85E+00	3.15E+01
-4	-1.83E+00	2.02E+01
-3	-1.03E+00	1.14E+01
-2	-4.59E-01	5.08E+00
-1	-1.15E-01	1.27E+00
0	0.00E+00	0.00E+00
1	-1.15E-01	1.27E+00
2	-4.59E-01	5.08E+00
3	-1.03E+00	1.14E+01
4	-1.83E+00	2.02E+01
5	-2.85E+00	3.15E+01
6	-4.08E+00	4.51E+01
7	-5.53E+00	6.11E+01
8	-7.17E+00	7.93E+01
9	-9.02E+00	9.97E+01
10	-1.10E+01	1.22E+02

Fig. 8.5 - Normalized % error in π_{44}^{θ} versus θ

For $\phi = 0$, $\phi = 90°$, and $\phi = \pm 45°$, the normalized % error in $\Delta R/R$ versus θ is given by

$$\frac{[\frac{\Delta R_0}{R_0}]_\theta - [\frac{\Delta R_0}{R_0}]_{\theta=0}}{[\frac{\Delta R_0}{R_0}]_{\theta=0}} = (\frac{\pi_{11} - \pi_{12} - \pi_{44}}{\pi_{11} + \pi_{12} + \pi_{44}}) \sin^2 2\theta \qquad \text{Eq. (8.2.38)}$$

$$= (\frac{\pi_D - \pi_{44}}{\pi_S + \pi_{44}}) \sin^2 2\theta$$

$$\frac{[\frac{\Delta R_{90}}{R_{90}}]_\theta - [\frac{\Delta R_{90}}{R_{90}}]_{\theta=0}}{[\frac{\Delta R_{90}}{R_{90}}]_{\theta=0}} = (\frac{-\pi_{11} + \pi_{12} + \pi_{44}}{\pi_{11} + \pi_{12} - \pi_{44}}) \sin^2 2\theta \qquad \text{Eq. (8.2.39)}$$

$$= -(\frac{\pi_D - \pi_{44}}{\pi_S - \pi_{44}}) \sin^2 2\theta$$

$$\frac{[\frac{\Delta R_{45}}{R_{45}}]_\theta - [\frac{\Delta R_{45}}{R_{45}}]_{\theta=0}}{[\frac{\Delta R_{45}}{R_{45}}]_{\theta=0}} = \frac{(\pi_{11} - \pi_{12} - \pi_{44})}{2(\pi_{11} + \pi_{12})} \sin 4\theta \qquad \text{Eq. (8.2.40)}$$

$$= (\frac{\pi_D - \pi_{44}}{2\pi_S}) \sin 4\theta$$

$$\frac{[\frac{\Delta R_{-45}}{R_{-45}}]_\theta - [\frac{\Delta R_{-45}}{R_{-45}}]_{\theta=0}}{[\frac{\Delta R_{-45}}{R_{-45}}]_{\theta=0}} = \frac{-\pi_{11} + \pi_{12} + \pi_{44}}{2(\pi_{11} + \pi_{12})} \sin 4\theta \qquad \text{Eq. (8.2.41)}$$

$$= -(\frac{\pi_D - \pi_{44}}{2\pi_S}) \sin 4\theta$$

Assuming $|\pi_{44}| \gg |\pi_{11}|$ and $|\pi_{44}| \gg |\pi_{12}|$ for p-type silicon [6], [98] yields

$$\frac{[\frac{\Delta R_0}{R_0}]_\theta - [\frac{\Delta R_0}{R_0}]_{\theta=0}}{[\frac{\Delta R_0}{R_0}]_{\theta=0}} \cong -\sin^2 2\theta \qquad \text{Eq. (8.2.42)}$$

$$\frac{[\frac{\Delta R_{90}}{R_{90}}]_\theta - [\frac{\Delta R_{90}}{R_{90}}]_{\theta=0}}{[\frac{\Delta R_{90}}{R_{90}}]_{\theta=0}} \cong -\sin^2 2\theta \qquad \text{Eq. (8.2.43)}$$

$$\frac{[\frac{\Delta R_{45}}{R_{45}}]_\theta - [\frac{\Delta R_{45}}{R_{45}}]_{\theta=0}}{[\frac{\Delta R_{45}}{R_{45}}]_{\theta=0}} \cong \frac{-\pi_{44}}{2\pi_S} \sin 4\theta \qquad \text{Eq. (8.2.44)}$$

$$\frac{[\frac{\Delta R_{-45}}{R_{-45}}]_\theta - [\frac{\Delta R_{-45}}{R_{-45}}]_{\theta=0}}{[\frac{\Delta R_{-45}}{R_{-45}}]_{\theta=0}} \cong \frac{\pi_{44}}{2\pi_S} \sin 4\theta \qquad \text{Eq. (8.2.45)}$$

For n-type silicon, assuming the approximation $\pi_{11} \cong -2\pi_{12}$ [23] yields

$$\frac{[\frac{\Delta R_0}{R_0}]_\theta - [\frac{\Delta R_0}{R_0}]_{\theta=0}}{[\frac{\Delta R_0}{R_0}]_{\theta=0}} \cong (\frac{3\pi_{12} + \pi_{44}}{\pi_{12} - \pi_{44}}) \sin^2 2\theta \qquad \text{Eq. (8.2.46)}$$

$$\frac{[\frac{\Delta R_{90}}{R_{90}}]_\theta - [\frac{\Delta R_{90}}{R_{90}}]_{\theta=0}}{[\frac{\Delta R_{90}}{R_{90}}]_{\theta=0}} \cong -(\frac{3\pi_{12} + \pi_{44}}{\pi_{12} + \pi_{44}}) \sin^2 2\theta \qquad \text{Eq. (8.2.47)}$$

$$\frac{[\frac{\Delta R_{45}}{R_{45}}]_\theta - [\frac{\Delta R_{45}}{R_{45}}]_{\theta=0}}{[\frac{\Delta R_{45}}{R_{45}}]_{\theta=0}} = \frac{(3\pi_{12} + \pi_{44})}{2\pi_{12}} \sin 4\theta \qquad \text{Eq. (8.2.48)}$$

$$\frac{[\frac{\Delta R_{-45}}{R_{-45}}]_{\theta} - [\frac{\Delta R_{-45}}{R_{-45}}]_{\theta=0}}{[\frac{\Delta R_{-45}}{R_{-45}}]_{\theta=0}} = \frac{-(3\pi_{12} + \pi_{44})}{2\pi_{12}} \sin 4\theta \qquad \text{Eq. (8.2.49)}$$

For $\phi = 0$, $\phi = 90°$, and $\phi = \pm 45$, the normalized % error in $\Delta R/R$ versus θ is presented

in Tables 8.10 and 8.11, whose plots are shown in Figs. 8.6 through 8.9.

Table 8.10 - Normalized % error in $\Delta R/R$ versus θ for $\phi = 0$ and $\phi = 90°$				
	$0°$ sensors: $(\frac{\pi_{11} - \pi_{12} - \pi_{44}}{\pi_{11} + \pi_{12} + \pi_{44}})\sin^2 2\theta$		$90°$ sensors: $(\frac{-\pi_{11} + \pi_{12} + \pi_{44}}{\pi_{11} + \pi_{12} - \pi_{44}})\sin^2 2\theta$	
θ	P-type sensors	N-type sensors	P-type sensors	N-type sensors
-10	-10.6	13.3	-11.5	-47.2
-9	-8.7	10.9	-9.4	-38.5
-8	-6.9	8.6	-7.5	-30.6
-7	-5.3	6.7	-5.8	-23.6
-6	-3.9	4.9	-4.3	-17.4
-5	-2.7	3.4	-3.0	-12.2
-4	-1.8	2.2	-1.9	-7.8
-3	-1.0	1.2	-1.1	-4.4
-2	-0.4	0.6	-0.5	-2.0
-1	-0.1	0.1	-0.1	-0.5
0	0.0	0.0	0.0	0.0
1	-0.1	0.1	-0.1	-0.5
2	-0.4	0.6	-0.5	-2.0
3	-1.0	1.2	-1.1	-4.4
4	-1.8	2.2	-1.9	-7.8
5	-2.7	3.4	-3.0	-12.2
6	-3.9	4.9	-4.3	-17.4
7	-5.3	6.7	-5.8	-23.6
8	-6.9	8.6	-7.5	-30.6
9	-8.7	10.9	-9.4	-38.5
10	-10.6	13.3	-11.5	-47.2
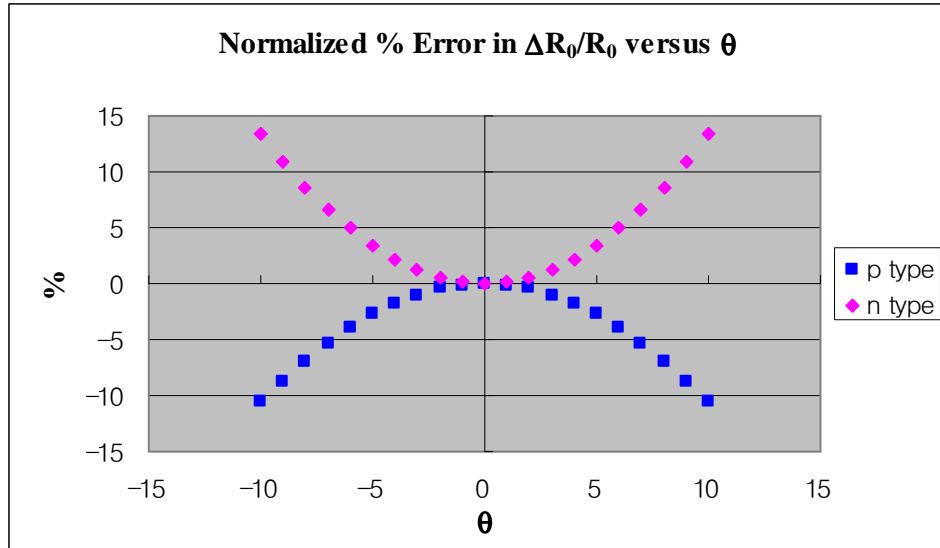
Fig. 8.6 - Normalized % error in $\Delta R_0/R_0$ versus θ
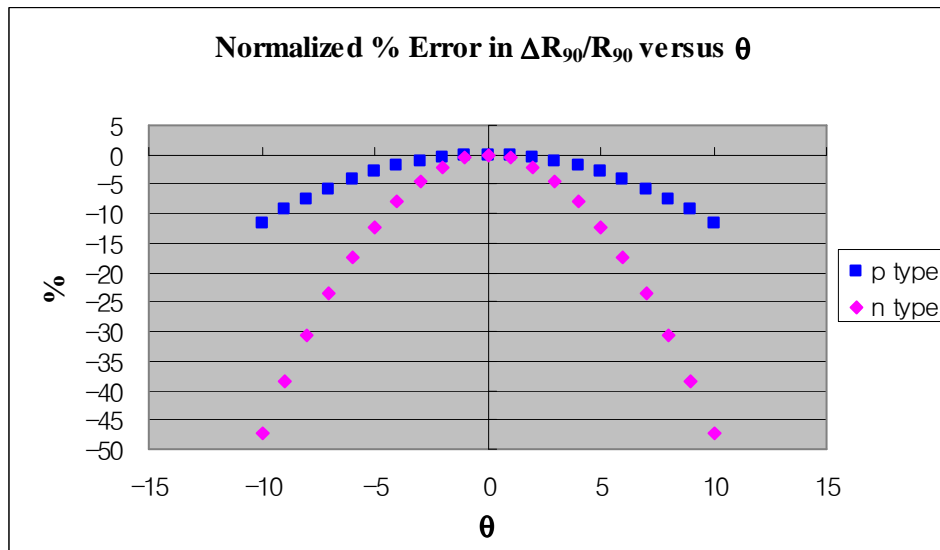
Fig. 8.7 - Normalized % error in $\Delta R_{90}/R_{90}$ versus θ

170

Table 8.11 - Normalized % error in $\Delta R_{45}/R_{45}$ and $\Delta R_{-45}/R_{-45}$ versus θ				
	$\phi = 45^o$		$\phi = -45^o$	
θ	P-type sensors	N-type sensors	P-type sensors	N-type sensors
-10	7.62E+02	-9.35E+01	-7.62E+02	9.35E+01
-9	6.97E+02	-8.55E+01	-6.97E+02	8.55E+01
-8	6.28E+02	-7.71E+01	-6.28E+02	7.71E+01
-7	5.57E+02	-6.83E+01	-5.57E+02	6.83E+01
-6	4.82E+02	-5.92E+01	-4.82E+02	5.92E+01
-5	4.05E+02	-4.98E+01	-4.05E+02	4.98E+01
-4	3.27E+02	-4.01E+01	-3.27E+02	4.01E+01
-3	2.46E+02	-3.02E+01	-2.46E+02	3.02E+01
-2	1.65E+02	-2.02E+01	-1.65E+02	2.02E+01
-1	8.27E+01	-1.01E+01	-8.27E+01	1.01E+01
0	0.00E+00	0.00E+00	0.00E+00	0.00E+00
1	-8.27E+01	1.01E+01	8.27E+01	-1.01E+01
2	-1.65E+02	2.02E+01	1.65E+02	-2.02E+01
3	-2.46E+02	3.02E+01	2.46E+02	-3.02E+01
4	-3.27E+02	4.01E+01	3.27E+02	-4.01E+01
5	-4.05E+02	4.98E+01	4.05E+02	-4.98E+01
6	-4.82E+02	5.92E+01	4.82E+02	-5.92E+01
7	-5.57E+02	6.83E+01	5.57E+02	-6.83E+01
8	-6.28E+02	7.71E+01	6.28E+02	-7.71E+01
9	-6.97E+02	8.55E+01	6.97E+02	-8.55E+01
10	-7.62E+02	9.35E+01	7.62E+02	-9.35E+01

Fig. 8.8 - Normalized % error in $\Delta R_{45}/R_{45}$ versus θ
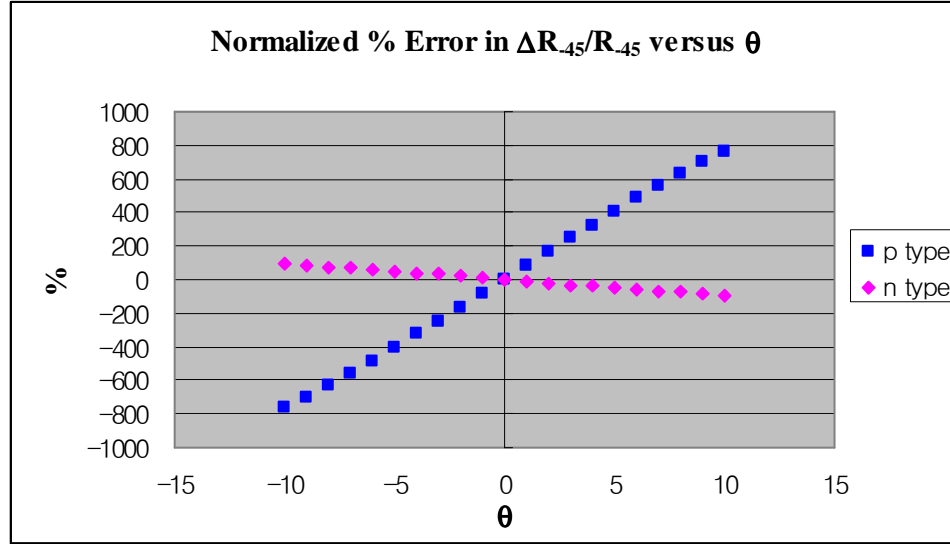
Fig. 8.9 - Normalized % error in $\Delta R_{-45}/R_{-45}$ versus θ

As depicted in Figs. 8.6 through 8.9, n-type sensors have larger normalized % error than p-type sensors.

Besides, it should be noted that Eq. (8.2.3) and Eq. (8.2.28) can be also derived using the standard equations for transforming the in-plane stress components from one coordinate system to another [12-13]:

- With respect to the unprimed coordinate system

For θ, the angle of counter-clockwise rotation of the $x^{''}$ - $y^{''}$ coordinate system with respect to the x - y coordinate system, the double-primed stress componenets are given as

$$\begin{bmatrix} \sigma_{11}^{''} \\ \sigma_{22}^{''} \\ \sigma_{12}^{''} \end{bmatrix} = \begin{bmatrix} \cos^2\theta & \sin^2\theta & 2\sin\theta\cos\theta \\ \sin^2\theta & \cos^2\theta & -2\sin\theta\cos\theta \\ -\sin\theta\cos\theta & \sin\theta\cos\theta & \cos^2\theta - \sin^2\theta \end{bmatrix} \begin{bmatrix} \sigma_{11} \\ \sigma_{22} \\ \sigma_{12} \end{bmatrix} \qquad \text{Eq. (8.2.50)}$$

172

The stress components are now measured in the new double-primed coordinate system instead of the unprimed coordinate system.

- With respect to the primed coordinate system

$$\begin{bmatrix} \sigma_{11}^{"} \\ \sigma_{22}^{"} \\ \sigma_{12}^{"} \end{bmatrix} = \begin{bmatrix} \cos^2\theta & \sin^2\theta & 2\sin\theta\cos\theta \\ \sin^2\theta & \cos^2\theta & -2\sin\theta\cos\theta \\ -\sin\theta\cos\theta & \sin\theta\cos\theta & \cos^2\theta - \sin^2\theta \end{bmatrix} \begin{bmatrix} \sigma_{11}^{'} \\ \sigma_{22}^{'} \\ \sigma_{12}^{'} \end{bmatrix}$$ Eq. (8.2.51)

Likewise, θ represents the angle of counter-clockwise rotation of the $x^{"}$ - $y^{"}$ coordinate system with respect to the x' - y' coordinate system. The stress components are measured in the new double-primed coordinate system instead of the primed coordinate system. In addition, it maybe be noted that Eq. (8.2.4) and Eq. (8.2.5) can be derived by combining the inverse of Eq. (8.2.50) with Eq. (8.2.3) for $\phi = \theta$ and $\phi = \theta + 90$, respectively. Similarly, Eq. (8.2.29) and Eq. (8.2.30) can be obtained by combining the inverse of Eq. (8.2.51) with Eq. (8.2.28) for $\phi = \theta$ and $\phi = \theta + 90$, respectively. Calibration of the off-axis rosettes can be accomplished by using a uniaxial stress applied along the $x_1^{"}$ or $x_2^{"}$ axis.

8.3 Off-Axis Error on the (111) Silicon Plane

On the (111) plane silicon, the rosette configuration consists of 0°, 90°, 45°, and -45° resistors relative to the $[1\bar{1}0]$ axis. The strip is cut along the axis $x^{"} - y^{"}$ counter-clockwise rotated θ from the primed axis $[1\bar{1}0]$. The off-axis piezoresistive coefficients can be determined by using the transformation

173

$$\pi'_{\alpha\beta} \;=\; T_{\alpha\gamma}\,\pi_{\gamma\delta}\,T^{-1}_{\delta\beta} \qquad\qquad \text{Eq. (8.3.1)}$$

The appropriate direction cosines for the (111) silicon wafer is given as follows:

$$
\begin{bmatrix} l_1 & m_1 & n_1 \\[4pt] l_2 & m_2 & n_2 \\[4pt] l_3 & m_3 & n_3 \end{bmatrix}
=
\begin{bmatrix}
\dfrac{\cos\theta}{\sqrt{2}}+\dfrac{\sin\theta}{\sqrt{6}} & -\dfrac{\cos\theta}{\sqrt{2}}+\dfrac{\sin\theta}{\sqrt{6}} & \dfrac{-2\sin\theta}{\sqrt{6}} \\[10pt]
\dfrac{\cos\theta}{\sqrt{6}}-\dfrac{\sin\theta}{\sqrt{2}} & \dfrac{\cos\theta}{\sqrt{6}}+\dfrac{\sin\theta}{\sqrt{2}} & \dfrac{-2\cos\theta}{\sqrt{6}} \\[10pt]
\dfrac{1}{\sqrt{3}} & \dfrac{1}{\sqrt{3}} & \dfrac{1}{\sqrt{3}}
\end{bmatrix}
\qquad \text{Eq. (8.3.2)}
$$

If $\theta = 0$,

$$
\begin{bmatrix} l_1 & m_1 & n_1 \\[4pt] l_2 & m_2 & n_2 \\[4pt] l_3 & m_3 & n_3 \end{bmatrix}
=
\begin{bmatrix}
\dfrac{1}{\sqrt{2}} & -\dfrac{1}{\sqrt{2}} & 0 \\[10pt]
\dfrac{1}{\sqrt{6}} & \dfrac{1}{\sqrt{6}} & \dfrac{-2}{\sqrt{6}} \\[10pt]
\dfrac{1}{\sqrt{3}} & \dfrac{1}{\sqrt{3}} & \dfrac{1}{\sqrt{3}}
\end{bmatrix}
\qquad \text{Eq. (8.3.3)}
$$

and $\pi'_{\alpha\beta}$ is given as follows:

$$
\pi'_{\alpha\beta}=
\begin{bmatrix}
\dfrac{\pi_{11}+\pi_{12}+\pi_{44}}{2} & \dfrac{\pi_{11}+5\pi_{12}-\pi_{44}}{6} & \dfrac{\pi_{11}+2\pi_{12}-\pi_{44}}{3} & 0 & \dfrac{\sqrt{2}(-\pi_{11}+\pi_{12}+\pi_{44})}{3} & 0 \\[10pt]
\dfrac{\pi_{11}+5\pi_{12}-\pi_{44}}{6} & \dfrac{\pi_{11}+\pi_{12}+\pi_{44}}{2} & \dfrac{\pi_{11}+2\pi_{12}-\pi_{44}}{3} & 0 & \dfrac{\sqrt{2}(\pi_{11}-\pi_{12}-\pi_{44})}{3} & 0 \\[10pt]
\dfrac{\pi_{11}+2\pi_{12}-\pi_{44}}{3} & \dfrac{\pi_{11}+2\pi_{12}-\pi_{44}}{3} & \dfrac{\pi_{11}+2\pi_{12}-\pi_{44}}{3} & 0 & 0 & 0 \\[10pt]
0 & 0 & 0 & \dfrac{2\pi_{11}-2\pi_{12}+\pi_{44}}{3} & 0 & \dfrac{\sqrt{2}(\pi_{11}-\pi_{12}-\pi_{44})}{3} \\[10pt]
\dfrac{\sqrt{2}(\pi_{11}-\pi_{12}-\pi_{44})}{6} & \dfrac{-\sqrt{2}(\pi_{11}-\pi_{12}-\pi_{44})}{6} & 0 & 0 & \dfrac{2\pi_{11}-2\pi_{12}+\pi_{44}}{3} & 0 \\[10pt]
0 & 0 & 0 & \dfrac{\sqrt{2}(\pi_{11}-\pi_{12}-\pi_{44})}{3} & 0 & \dfrac{\pi_{11}-\pi_{12}+2\pi_{44}}{3}
\end{bmatrix}
$$

Eq. (8.3.4)

As described in Chapter 3, the normalized change in resistance can be expressed as

$$\frac{\Delta R}{R} = [B_1\sigma'_{11} + B_2\sigma'_{22} + B_3\sigma'_{33} - 2\sqrt{2}(B_2 - B_3)\sigma'_{23}]\cos^2\phi$$
$$+ [B_2\sigma'_{11} + B_1\sigma'_{22} + B_3\sigma'_{33} + 2\sqrt{2}(B_2 - B_3)\sigma'_{23}]\sin^2\phi \qquad \text{Eq. (8.3.5)}$$
$$+ [2\sqrt{2}(B_3 - B_2)\sigma'_{13} + (B_1 - B_2)\sigma'_{12}]\sin 2\phi + [\alpha_1\Delta T + \alpha_2\Delta T^2 + \dots]$$

In addition, the normalized change in resistance can be expressed in terms of the off-axis stress components using

$$\frac{\Delta R}{R} = (\pi''_{1\alpha}\sigma''_\alpha)l''^2 + (\pi''_{2\alpha}\sigma''_\alpha)m''^2 + (\pi''_{3\alpha}\sigma''_\alpha)n''^2$$

$$+ 2(\pi''_{4\alpha}\sigma''_\alpha)l''n'' + 2(\pi''_{5\alpha}\sigma''_\alpha)m''n'' + 2(\pi''_{6\alpha}\sigma''_\alpha)l''m'' \qquad \text{Eq. (8.3.6)}$$

$$+ [\alpha_1\Delta T + \alpha_2\Delta T^2 + \dots]$$

Assuming $\sigma''_4 = \sigma''_5 = \sigma''_6 = 0$ ($\sigma''_{13} = \sigma''_{23} = \sigma''_{12} = 0$) in Eq. (8.3.6) yields

$$\frac{\Delta R}{R} = (\pi''_{11}\sigma''_{11} + \pi''_{12}\sigma''_{22} + \pi''_{13}\sigma''_{33})l''^2$$

$$+ (\pi''_{21}\sigma''_{11} + \pi''_{22}\sigma''_{22} + \pi''_{23}\sigma''_{33})m''^2$$

$$+ (\pi''_{31}\sigma''_{11} + \pi''_{32}\sigma''_{22} + \pi''_{33}\sigma''_{33})n''^2 \qquad \text{Eq. (8.3.7)}$$

$$+ 2(\pi''_{61}\sigma''_{11} + \pi''_{62}\sigma''_{22} + \pi''_{63}\sigma''_{33})l''m''$$

$$+ [\alpha_1\Delta T + \alpha_2\Delta T^2 + \dots]$$

Introducing $l'' = \cos\phi$, $m'' = \sin\phi$, and $n'' = 0$ yields

$$\frac{\Delta R}{R} = (\pi_{11}^{''}\sigma_{11}^{''} + \pi_{12}^{''}\sigma_{22}^{''} + \pi_{13}^{''}\sigma_{33}^{''})\cos^2\phi$$

$$+ (\pi_{21}^{''}\sigma_{11}^{''} + \pi_{22}^{''}\sigma_{22}^{''} + \pi_{23}^{''}\sigma_{33}^{''})\sin^2\phi$$

Eq. (8.3.8)

$$+ 2(\pi_{61}^{''}\sigma_{11}^{''} + \pi_{62}^{''}\sigma_{22}^{''} + \pi_{63}^{''}\sigma_{33}^{''})\cos\phi\sin\phi$$

$$+ [\alpha_1\Delta T + \alpha_2\Delta T^2 + ...]$$

and then combining Eq. (8.3.1) and Eq. (8.3.2) yields

$$\pi_{11}^{''} = [(\frac{\cos\theta}{\sqrt{2}} + \frac{\sin\theta}{\sqrt{6}})^4 + (\frac{\cos\theta}{\sqrt{2}} - \frac{\sin\theta}{\sqrt{6}})^4 + \frac{4}{9}\sin^4\theta]\,\pi_{11}$$

$$+ [2(\frac{\cos\theta}{\sqrt{2}} + \frac{\sin\theta}{\sqrt{6}})^2(\frac{\cos\theta}{\sqrt{2}} - \frac{\sin\theta}{\sqrt{6}})^2 + \frac{8}{3}\sin^2\theta\,(\frac{\cos^2\theta}{2} + \frac{\sin^2\theta}{6})]\,\pi_{12} + \frac{(\cos^2\theta + \sin^2\theta)^2}{2}\,\pi_{44}$$

$$= \frac{\pi_{11} + \pi_{12} + \pi_{44}}{2}$$

Eq. (8.3.9)

$$\pi_{12}^{''} = \{\frac{1}{6}[(\cos\theta - \sqrt{3}\sin\theta)^2(\frac{\cos\theta}{\sqrt{2}} + \frac{\sin\theta}{\sqrt{6}})^2 + (\cos\theta + \sqrt{3}\sin\theta)^2(\frac{\cos\theta}{\sqrt{2}} - \frac{\sin\theta}{\sqrt{6}})^2] + \frac{4}{9}\cos^2\theta\sin^2\theta\,\}\pi_{11}$$

$$+ \{\frac{1}{6}[(\cos\theta - \sqrt{3}\sin\theta)^2(\frac{\cos\theta}{\sqrt{2}} - \frac{\sin\theta}{\sqrt{6}})^2 + (\cos\theta + \sqrt{3}\sin\theta)^2(\frac{\cos\theta}{\sqrt{2}} + \frac{\sin\theta}{\sqrt{6}})^2]$$

$$+ \frac{6(\cos^4\theta + \sin^4\theta) + 4\cos^2\theta\sin^2\theta}{9}\,\}\pi_{12} - \frac{(\cos^2\theta + \sin^2\theta)^2}{6}\,\pi_{44}$$

$$= \frac{\pi_{11} + 5\pi_{12} - \pi_{44}}{6}$$

Eq. (8.3.10)

$$\pi_{13}^{''} = \frac{(\cos^2\theta + \sin^2\theta)^2}{3}(\pi_{11} + 2\,\pi_{12} - \pi_{44}) = \frac{\pi_{11} + 2\,\pi_{12} - \pi_{44}}{3} \qquad \text{Eq. (8.3.11)}$$

$$\pi_{21}^{"} = [(\frac{\cos\theta}{\sqrt{6}} - \frac{\sin\theta}{\sqrt{2}})^2 (\frac{\cos\theta}{\sqrt{2}} + \frac{\sin\theta}{\sqrt{6}})^2 + (\frac{\cos\theta}{\sqrt{6}} + \frac{\sin\theta}{\sqrt{2}})^2 (\frac{\cos\theta}{\sqrt{2}} - \frac{\sin\theta}{\sqrt{6}})^2] + \frac{4}{9}\cos^2\theta \sin^2\theta \,]\pi_{11}$$

$$+ [(\frac{\cos\theta}{\sqrt{6}} + \frac{\sin\theta}{\sqrt{2}})^2 (\frac{\cos\theta}{\sqrt{2}} + \frac{\sin\theta}{\sqrt{6}})^2 + (\frac{\cos\theta}{\sqrt{6}} - \frac{\sin\theta}{\sqrt{2}})^2 (\frac{\cos\theta}{\sqrt{2}} - \frac{\sin\theta}{\sqrt{6}})^2$$

$$+ \frac{6(\cos^4\theta + \sin^4\theta) + 4\cos^2\theta \sin^2\theta}{9}]\pi_{12} - \frac{(\cos^2\theta + \sin^2\theta)^2}{6}\pi_{44}$$

$$= \frac{\pi_{11} + 5\pi_{12} - \pi_{44}}{6}$$

Eq. (8.3.12)

$$\pi_{22}^{"} = [(\frac{\cos\theta}{\sqrt{6}} + \frac{\sin\theta}{\sqrt{2}})^4 + (\frac{\cos\theta}{\sqrt{6}} - \frac{\sin\theta}{\sqrt{2}})^4 + \frac{4}{9}\cos^4\theta]\,\pi_{11}$$

$$+ [2(\frac{\cos^2\theta}{6} - \frac{\sin^2\theta}{2})^2 + \frac{8}{3}\cos^2\theta(\frac{\cos^2\theta}{6} + \frac{\sin^2\theta}{2})]\pi_{12} + \frac{(\cos^2\theta + \sin^2\theta)^2}{2}\pi_{44}$$

$$= \frac{\pi_{11} + \pi_{12} + \pi_{44}}{2}$$

Eq. (8.3.13)

$$\pi_{23}^{"} = \frac{(\cos^2\theta + \sin^2\theta)^2}{3}(\pi_{11} + 2\pi_{12} - \pi_{44}) = \frac{\pi_{11} + 2\pi_{12} - \pi_{44}}{3} \qquad \text{Eq. (8.3.14)}$$

$$\pi_{61}^{"} = \pi_{62}^{"} = \pi_{63}^{"} = 0 \qquad \text{Eq. (8.3.15)}$$

It is apparent that all the pi-coefficients ($\pi_{11}^{"}$, $\pi_{22}^{"}, \pi_{12}^{"}, \pi_{13}^{"}, \pi_{21}^{"}, \pi_{23}^{"}, \pi_{61}^{"}, \pi_{62}^{"}$ and $\pi_{63}^{"}$) are independent of θ. For any θ the following findings are yielded:

$$\pi_{11}^{''} = \frac{\pi_{11} + \pi_{12} + \pi_{44}}{2}, \ \pi_{12}^{''} = \frac{\pi_{11} + 5\pi_{12} - \pi_{44}}{6}, \ \pi_{13}^{''} = \frac{\pi_{11} + 2\pi_{12} - \pi_{44}}{3}$$

$$\pi_{21}^{''} = \frac{\pi_{11} + 5\pi_{12} - \pi_{44}}{6}, \ \pi_{22}^{''} = \frac{\pi_{11} + \pi_{12} + \pi_{44}}{2}, \ \pi_{23}^{''} = \frac{\pi_{11} + 2\pi_{12} - \pi_{44}}{3} \quad \text{Eq. (8.3.16)}$$

$$\pi_{61}^{''} = 0, \ \pi_{62}^{''} = 0, \ \pi_{63}^{''} = 0$$

A set of linearly independent temperature dependent combined piezoresistive parameters, B_1, B_2, and B_3 [26] are given as follows:

$$B_1 = \frac{\pi_{11} + \pi_{12} + \pi_{44}}{2}, \ B_2 = \frac{\pi_{11} + 5\pi_{12} - \pi_{44}}{6} \ \text{and} \ B_3 = \frac{\pi_{11} + 2\pi_{12} - \pi_{44}}{3} \quad \text{Eq. (8.3.17)}$$

Hence any θ using the notations above gives

$$\pi_{11}^{''} = \pi_{22}^{''} = B_1$$

$$\pi_{12}^{''} = \pi_{21}^{''} = B_2$$

$$\pi_{13}^{''} = \pi_{31}^{''} = \pi_{23}^{''} = \pi_{32}^{''} = B_3 \quad \text{Eq. (8.3.18)}$$

$$\pi_{61}^{''} = 0, \ \pi_{62}^{''} = 0, \ \pi_{63}^{''} = 0$$

Substitution of Eq. (8.3.18) into Eq. (8.3.8) with neglect of the out-of-plane normal stress $\sigma_3^{''}$ and the terms of temperature coefficients of resistance leads to

$$\frac{\Delta R}{R} = [B_1 \sigma_1^{''} + B_2 \sigma_2^{''}] \cos^2 \phi + [B_2 \sigma_1^{''} + B_1 \sigma_2^{''}] \sin^2 \phi \quad \text{Eq. (8.3.19)}$$

For $\phi = 0$ and $\phi = 90^\circ$, the expressions for the stress-induced resistance changes

$$\frac{\Delta R_0}{R_0} = \pi_{11}^{''} \sigma_{11}^{''} + \pi_{12}^{''} \sigma_{22}^{''} \quad \text{Eq. (8.3.20)}$$

$$\frac{\Delta R_{90}}{R_{90}} = \pi_{21}^{''} \sigma_{11}^{''} + \pi_{22}^{''} \sigma_{22}^{''} \quad \text{Eq. (8.3.21)}$$

It is to be emphasized that, for the (111) silicon surface, normalized % error in $\Delta R/R$ versus θ is zero due to the isotropic characteristics of the (111) silicon. Note that Eqs. (8.3.20) and (8.3.21) may be derived also combining the inverse of Eq. (8.2.51) with Eq. (8.3.5) for $\phi = \theta$ and $\phi = \theta + 90$, respectively. The stress components are measured in the new double-primed coordinate system instead of the primed coordinate system.

In addition, the errors in piezoresistive coefficients induced by the rotational misalignment of strip on the supports by an angle θ with respect to the ideal longitudinal axis of strip will be explained in Appendix D.

8.4 Summary

Parameter γ is defined as the ratio of the axial portion to the sum of axial and transverse portion of the diffused serpentine resistor. On the (111) silicon surface, $(B_1 + B_2)$ is constant with γ. However, $(B_1 - B_2)$ depends on γ. Likewise, for sensors on the (001) surface, π_S is constant with γ. On the other hand, π_{44} depends on γ.

In addition, errors in misalignment with the given crystallographic axes are described and analyzed. Precise determination of the crystallographic orientation in (001) silicon wafers is found to be essential for extraction of piezoresistive coefficients of silicon. However, for the (111) silicon wafers, errors associated with misalignment are observed to have no effect on the determination of piezoresistive coefficients of silicon due to the isotropic characteristics of the (111) silicon.

In order to extract a complete set of pi-coefficients (π_{11}, π_{12}, and π_{44}) for both p- and n-type sensors, hydrostatic tests are required for the (111) silicon. On the other hand, those tests are not needed for stress sensors on the (001) silicon. Instead, cutting the (001) wafers along two directions (e.g., the unprimed axis [100] and the primed axis [110]) and then combining both can give a complete set of pi-coefficients. In addition, by using off-axis sensor rosettes [29], experimental calibration results for the piezoresistive coefficients of silicon may be determined.

CHAPTER 9

(001) TEST CHIP DESIGN AND CALIBRATION

9.1   Mask Alignment Using Wet Anisotropic Etching

The main objective of this work is to detect the orientation with the highest precision possible. As described in Chapter 8, the normalized error induced by rotational misalignment is zero for the (111) silicon surface. On the other hand, rotational misalignment can be a very important source of error on the (001) surface.

For precise determination of the crystallographic orientation in the (001) silicon wafers, anisotropic wet etching is used. It may be noted that our proposed design takes advantage of the symmetric under-etching behavior around the [110] direction. Also, it includes alignment marks for aligning subsequent masks. In our cases, mask alignment of the (001) silicon needs high precision because off-axis induced error cannot be neglected, as described in Chapter 8. To determine the crystallographic directions, x-ray diffraction is commonly used to determine the crystallographic properties with very high precision. However, it would be difficult to put x-ray equipment into a mask aligner. Since the eye is very sensitive to symmetries, it is not difficult to find two points symmetrically distributed around a [110] direction. As shown in Fig. 9.1, we introduced alignment forks that are repeated with an angular increment of 0.25^{o} in the range of $\pm 5°$ from the

presumed [110] direction. In addition, alignment marks for aligning subsequent masks (active region, contact, and metal) with the correct crystallographic direction are included in the design (see Fig. 9.2).
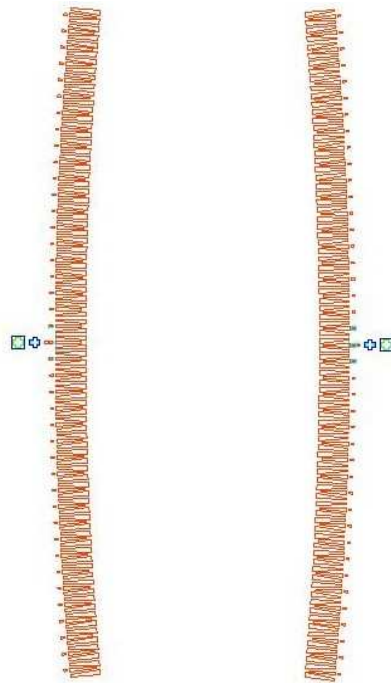
Fig. 9.1 - The alignment forks of both sides on silicon surface
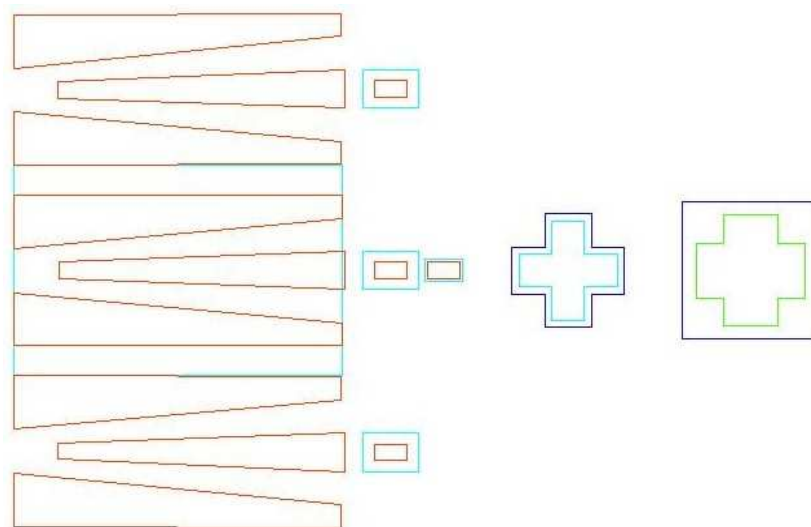
Fig. 9.2 - Alignment marks for subsequent masks

To determine the [110] direction, the etched structure of alignment forks formed using wet anisotropic etching is checked. In principle, the alignment fork is etched symmetrically when perfectly aligned with the [110] direction. In this work, KOH (Potassium Hydroxide) is used as an etchant. When the etch rate is plotted in regard to the degree from the [110] direction, the minimum occurs for the [110] direction. The exact behavior at the minimum has not been fully investigated, but a linear dependence somewhat off the minimum is observed. A symmetric etch rate is observed from the [110] direction, and it monotonically rises with increasing rotation from the [110] direction. If alignment forks are patterned symmetrically from the [110] direction as shown in Fig. 9.1, the under-etching will cut equal length. Asymmetric under-etch, on the other hand will give different lengths. Hence, among the pair of alignment forks, it is easy to select the one that is symmetrically etched. In our layout, the angular increment of alignment fork is 0.25^{o}. In order to re-align subsequent masks, every alignment mark should be affixed with an alignment mark on the previous mask as shown in Fig. 9.2.

In this work, we limit ourselves to stating a precision of $\pm\,0.125°$, which leads to a negligible error. For instance, $\pm\,0.125°$ misalignment produces the following % error:

- With respect to the unprimed axes on the (001) silicon surface

For $\phi = 0$ and $\phi = 90°$, the normalized error induced by θ is given by

$$\frac{[\dfrac{\Delta R_0}{R_0}]_{\theta=0.125} - [\dfrac{\Delta R_0}{R_0}]_{\theta=0}}{[\dfrac{\Delta R_0}{R_0}]_{\theta=0}} = -(\frac{\pi_{11} - \pi_{12} - \pi_{44}}{2\pi_{11}})\sin^2 2(0.125) \qquad \text{Eq. (9.1.1)}$$

$$= 1.88 \times 10^{-2} \% \text{ for p-type sensors}$$

$$= -1.32 \times 10^{-3} \% \text{ for n-type sensors}$$

$$\frac{[\frac{\Delta R_{90}}{R_{90}}]_{\theta=0.125} - [\frac{\Delta R_{90}}{R_{90}}]_{\theta=0}}{[\frac{\Delta R_{90}}{R_{90}}]_{\theta=0}} = (\frac{\pi_{11} - \pi_{12} - \pi_{44}}{2\pi_{12}})\sin^2 2(0.125) \qquad \text{Eq. (9.1.2)}$$

$$= 1.13 \times 10^{-1} \% \text{ for p-type sensors}$$

$$= -2.53 \times 10^{-3} \% \text{ for n-type sensors}$$

- With respect to the primed axes on the (001) silicon surface

For $\phi = 0$ and $\phi = 90°$, the normalized error induced by θ is given by

$$\frac{[\frac{\Delta R_0}{R_0}]_{\theta=0.125} - [\frac{\Delta R_0}{R_0}]_{\theta=0}}{[\frac{\Delta R_0}{R_0}]_{\theta=0}} = (\frac{\pi_{11} - \pi_{12} - \pi_{44}}{\pi_{11} + \pi_{12} + \pi_{44}})\sin^2 2(0.125) \qquad \text{Eq. (9.1.3)}$$

$$= -1.73 \times 10^{-3} \% \text{ for p-type sensors}$$

$$= 4.33 \times 10^{-3} \% \text{ for n-type sensors}$$

$$\frac{[\frac{\Delta R_{90}}{R_{90}}]_{\theta=0.125} - [\frac{\Delta R_{90}}{R_{90}}]_{\theta=0}}{[\frac{\Delta R_{90}}{R_{90}}]_{\theta=0}} = (\frac{-\pi_{11} + \pi_{12} + \pi_{44}}{\pi_{11} + \pi_{12} - \pi_{44}})\sin^2 2(0.125) \qquad \text{Eq. (9.1.4)}$$

$$= -1.87 \times 10^{-3} \% \text{ for p-type sensors}$$

$$= -7.68 \times 10^{-3} \% \text{ for n-type sensors}$$

where the normalized errors induced by 0.125^o misalignment with the appropriate axes are negligible in all cases. It should be noted that pi-coefficients in this calculation are from Smith [6]:

$\pi_{11} = 66$ (1/TPa), $\pi_{12} = -11$ (1/TPa), and $\pi_{44} = 1381$ (1/TPa) for p-type silicon

$\pi_{11} = -1022$ (1/TPa), $\pi_{12} = 534$ (1/TPa), and $\pi_{44} = -136$ (1/TPa) for n-type silicon

In the case of KOH etching, temperature affects the etch time, and the etched cutback rises with an increasing etch temperature for fixed duration. In our process, the etch time is about 45 minutes at 65^oC to obtain comparable etch depths. Inspection of the etching is made in an optical microscope. A typical example of etched test structure is shown in Fig. 9.3. The easiest way to find the alignment is to use human eye.

As seen in Fig. 9.3, the asymmetric etched structures are observed in the upper and lower parts since two ridges are patterned symmetrically with respect to an axis which is off the [110] direction. On the other hand in the central part, we can see almost symmetric etching because two ridges are patterned symmetrically near the [110] direction and the under-etching will cut the arms to equal length.

(Upper Part)   (Central Part)   (Lower Part)
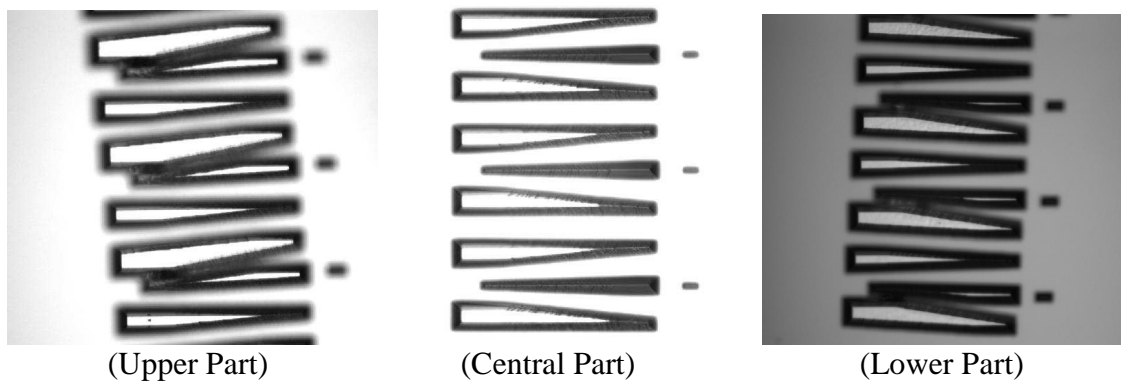
Fig. 9.3 - An example of an etched structure of alignment forks in one wafer

9.2   The (001) Silicon Test Chips

A special test chip was designed and fabricated. The test chip contains p-type and n-type sensor sets, each with resistor elements making angles of $\phi = 0$, $\pm 45^{\circ}$, and 90° with respect to the x_1 (or $x_1^{'}$) axis. The layout of the test chip in which the resistor rosette sensors and VDP test structures are fabricated on the (001) silicon surfaces is shown in Fig. 9.4. It is noteworthy that three different cells are repeated in the layout of our test chip.
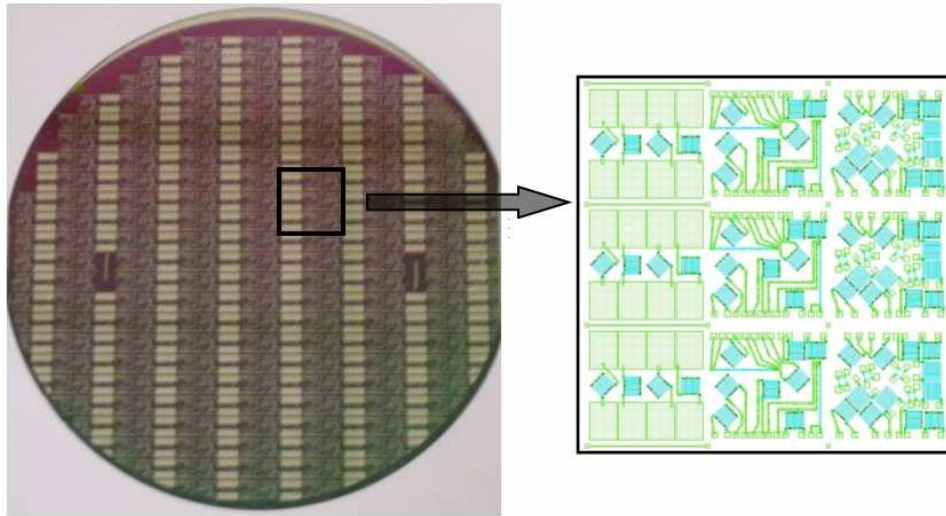
Fig. 9.4(a) - The test chip on the (001) silicon surfaces
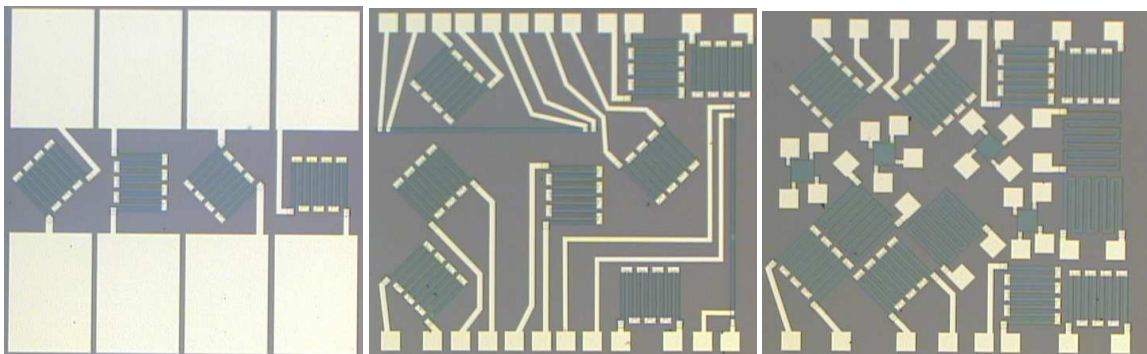
Fig. 9.4(b) - Microphoto of the test chip on the (001) silicon surfaces

186

Each test chip has only one type (p-type or n-type sensors). Resistors are often designed with relatively large meandering patterns to achieve acceptable resistance levels for measurement. However, as discussed in Chapter 8, they suffer from transverse sensitivity which is difficult to estimate because of the lateral diffusion that occurs during the fabrication process. In order to minimize transverse stress sensitivity, resistor legs are interconnected with metal links, but interconnections require additional contacts that further increase resistor size. For the comparison of transverse stress sensitivity, one pair of 0°, 90°, $+45^o$, and -45° resistors without metal link are also contained in the layout. The large pads in the left hand cell are designed for more convenient calibration of the sensitivity. The metallurgical junction depth at which the impurity profile intersects the background concentration is approximately 1.7 μm for p-type sensors and 1.2 μm for n-type sensors.

As displayed in Table 9.1, the sheet resistance measured by Van der Pauw's method is about 211.5 ohms per square for p-type sensors and 122.8 ohms per square for n-type sensors, respectively. Since $\dfrac{L}{W} = 105.5$ in the layout of our test chip, the unstressed resistance is expected to be $22.3\,\text{k}\Omega$ and $13.0\,\text{k}\Omega$ for p- and n-type sensors, respectively (see Table 9.2), which are in good with the calibration results of resistors ($22.8\,\text{k}\Omega$ for p-type resistors and $13.2\,\text{k}\Omega$ for n-type resistors). It is noteworthy that no lateral diffusion is assumed in the calculation of $\dfrac{L}{W}$. The expected resistance should be smaller with consideration of the lateral diffusion.

Table 9.1 - Sheet resistance measured by Van der Pauw's method (Unit: ohms per square)				
VDP-type	P-type	P-type	N-type	N-type
Injection pair	#1	#2	#1	#2
1~2	205.7	206.0	122.0	116.6
1~4	216.5	213.6	137.6	129.4
2~3	214.7	211.8	108.4	111.0
3~4	213.4	210.6	124.3	133.0
Average	212.5	210.5	123.1	122.5
Std.Dev	4.7	3.2	12.0	10.4

Table 9.2 - Expected resistance (Unit: ohm)				
VDP-type	P-type	P-type	N-type	N-type
Injection pair	#1	#2	#1	#2
1~2	21699	21735	12867	12298
1~4	22836	22531	14522	13656
2~3	22646	22345	11433	11715
3~4	22511	22217	13116	14029
Average	22423	22207	12985	12925
Std.Dev	501	340	1265	1097

Ion implantation is used as the method of introducing impurities such as boron and phosphorous into the surface of silicon target wafers, followed by drive-in step used to move the diffusion front to the desired depth. After annealing, *I-V* characteristics for p- and n-type silicon are tested and shown in Figs. 9.5 and 9.6.

P-type Resistor

$$y = 4.282E+01x$$
$$R^2 = 1.000E+00$$
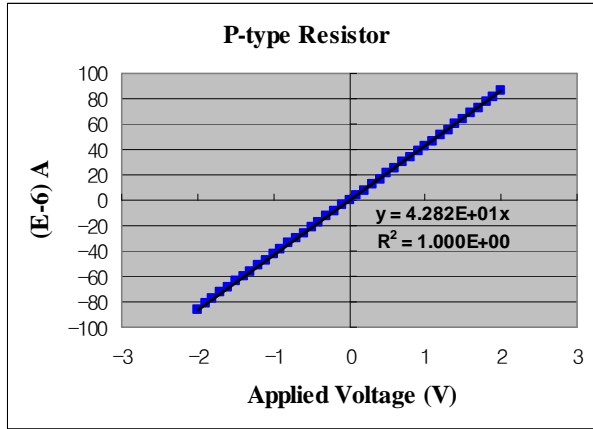
Fig. 9.5 - *I-V* characteristics of a p-type resistor after annealing

N-type Resistor

N-type Resistor (PtSi)

N-type Resistor
(PtSi and diffusion)

$$y = 7.610E+01x$$
$$R^2 = 9.993E-01$$
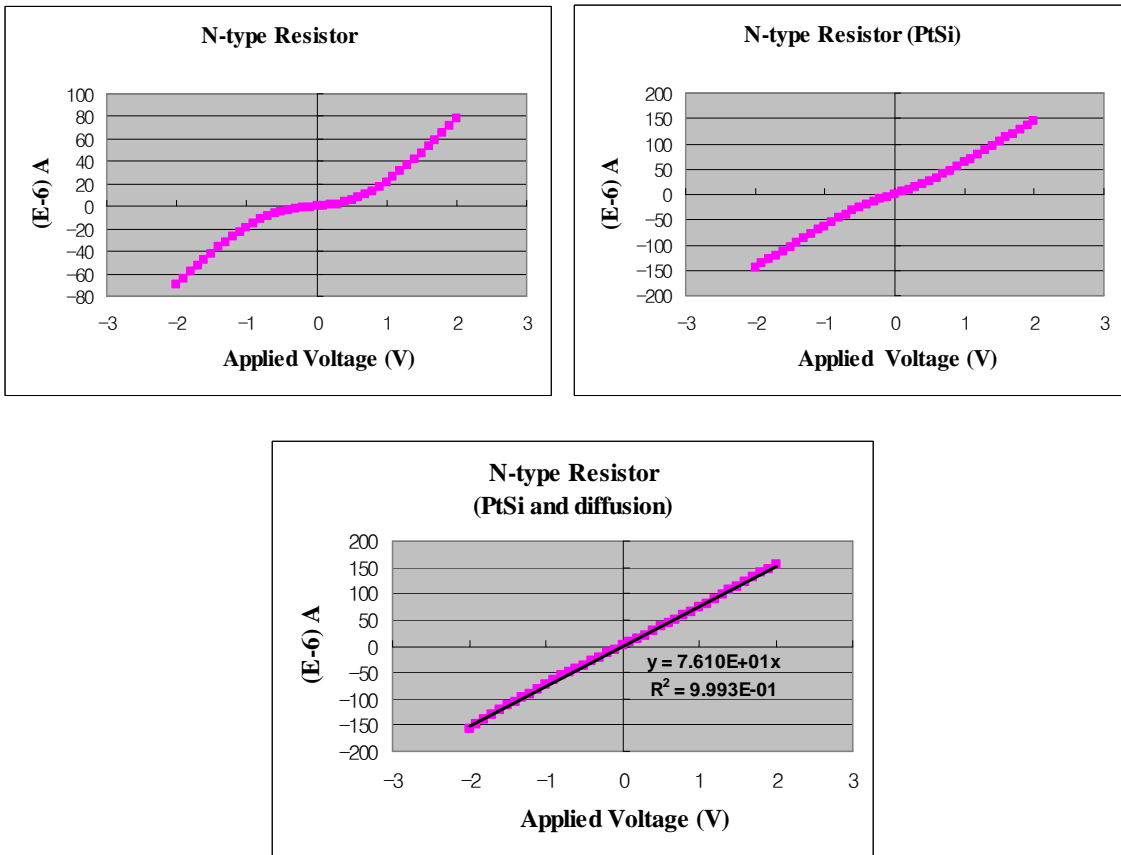
Fig. 9.6 - *I-V* characteristics of an n-type resistor after annealing

Obviously, it is desirable to form *ohmic* contacts between the metal and semiconductor. As shown in Fig. 9.5, p-type resistor exhibits a straight line I-V characteristic. However, a problem arises in trying to contact n-type silicon as shown in Fig. 9.6, since aluminum may form a metal-semiconductor Schottky diode rather than an ohmic contact. In order to resolve the problem for n-type silicon, PtSi (platinum silicide) contact metallurgy is used. In the process, a 200 nm Pt film is deposited by electron-beam evaporation onto the (001) Si substrates which have been pre-cleaned in buffered HF. The wafer is then sintered at $400^{o}C$ for 10 minutes in order to form a high quality layer of PtSi. Next, the Pt film is stripped off with aqua regia (a mixture of nitric and hydrochloric acids that dissolves gold or platinum) in which silicon, silicon dioxide, and nitride will not be etched. Furthermore, in order to form desirable *ohmic* contacts, heavy impurities of phosphorous are introduced into the surface of the contacts by diffusion before forming the layer of PtSi. For electrical testing, connections between the strip and the PC board utilize wire-bonding between inner pads on the board and the pads on the silicon strip, as shown in Fig. 9.7.
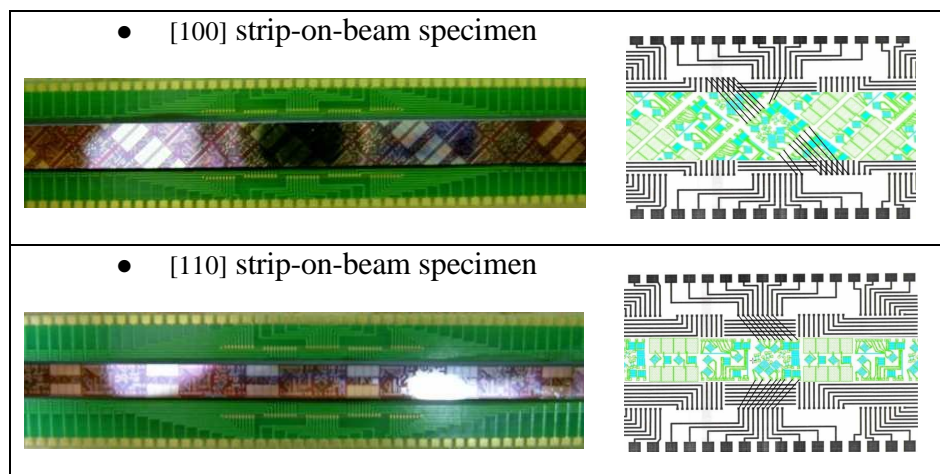
Fig. 9.7 - The [100] and [110] strip-on-beam specimens

9.3 Resistance Equations for the (001) Silicon

The piezoresistive coefficients for the (001) surface are π_{11}, π_{12}, and π_{44}. A wafer plot showing the two directions that are cut from the (001) wafer is presented in Fig. 9.8. If a wafer strip along the x_1 direction (or x_1' direction) is subjected to four-point-bending, and a known uniaxial stress $\sigma_{11} = \sigma$ (or $\sigma_{11}' = \sigma$) is applied in the x_1 (or x_1') direction on the (001) silicon surface, the simplified normalized equations are expressed as follows:
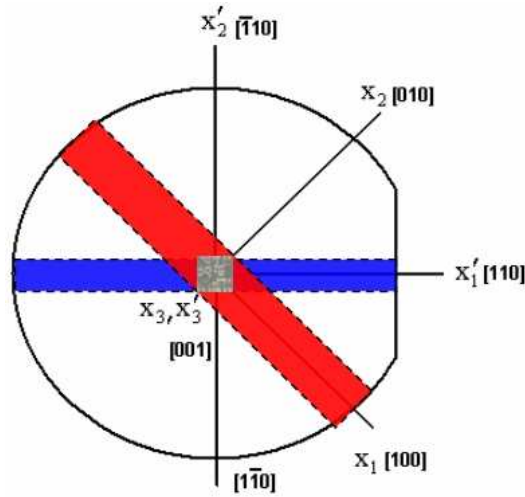
Fig. 9.8 - Two directions cut from the (001) silicon wafer

- With respect to the unprimed axes

$$\frac{\Delta R}{R} = [\pi_{11}\sigma_{11} + \pi_{12}(\sigma_{22} + \sigma_{33})]\cos^2\phi + [\pi_{11}\sigma_{22} + \pi_{12}(\sigma_{11} + \sigma_{33})]\sin^2\phi$$

Eq. (9.3.1)

$$+ \pi_{44}\sigma_{12}\sin2\phi + [\alpha_1\Delta T + \alpha_2\Delta T^2 + ...]$$

where ϕ is the angle between the x_1 axis and the resistor orientation. The normalized resistance equations for 0° and 90° sensors can determine π_{11} and π_{12} directly.

191

$$\frac{\Delta R_0}{R_0} = \pi_{11}\sigma_{11} \qquad \text{Eq. (9.3.2)}$$

$$\frac{\Delta R_{90}}{R_{90}} = \pi_{12}\sigma_{11} \qquad \text{Eq. (9.3.3)}$$

$$\frac{\Delta R_{45}}{R_{45}} = \frac{\Delta R_{-45}}{R_{-45}} = (\frac{\pi_{11} + \pi_{12}}{2})\sigma_{11} \qquad \text{Eq. (9.3.4)}$$

Addition of Eqs. (9.3.2) and (9.3.3) yields

$$\frac{\Delta R_0}{R_0} + \frac{\Delta R_{90}}{R_{90}} = (\pi_{11} + \pi_{12})\,\sigma_{11} = 2(\frac{\Delta R_{45}}{R_{45}}) = 2(\frac{\Delta R_{-45}}{R_{-45}}) \qquad \text{Eq. (9.3.5)}$$

- With respect to the primed axes

$$\frac{\Delta R}{R} = \left[\left(\frac{\pi_{11} + \pi_{12} + \pi_{44}}{2}\right)\sigma_{11}' + \left(\frac{\pi_{11} + \pi_{12} - \pi_{44}}{2}\right)\sigma_{22}'\right]\cos^2\phi$$

$$+ \left[\left(\frac{\pi_{11} + \pi_{12} - \pi_{44}}{2}\right)\sigma_{11}' + \left(\frac{\pi_{11} + \pi_{12} + \pi_{44}}{2}\right)\sigma_{22}'\right]\sin^2\phi \qquad \text{Eq. (9.3.6)}$$

$$+ \ \pi_{12}\sigma_{33} + (\pi_{11} - \pi_{12})\sigma_{12}' \ \sin2\phi + [\alpha_1\Delta T + \alpha_2\Delta T^2 + ...]$$

where ϕ is the angle between the x_1' axis and the resistor orientation. The normalized resistance equations are given by

$$\frac{\Delta R_0}{R_0} = (\frac{\pi_{11} + \pi_{12} + \pi_{44}}{2})\sigma_{11}' \qquad \text{Eq. (9.3.7)}$$

$$\frac{\Delta R_{90}}{R_{90}} = (\frac{\pi_{11} + \pi_{12} - \pi_{44}}{2})\sigma_{11}' \qquad \text{Eq. (9.3.8)}$$

$$\frac{\Delta R_{45}}{R_{45}} = \frac{\Delta R_{-45}}{R_{-45}} = (\frac{\pi_{11} + \pi_{12}}{2})\sigma_{11}' \qquad \text{Eq. (9.3.9)}$$

Subtraction Eq. (9.3.8) from Eq. (9.3.7) determine π_{44} as follows:

192

$$\frac{\Delta R_0}{R_0} - \frac{\Delta R_{90}}{R_{90}} = \pi_{44} \, \sigma_{11}'$$

<div align="right">Eq. (9.3.10)</div>

Addition of Eqs. (9.3.7) and (9.3.8) yields

$$\frac{\Delta R_0}{R_0} + \frac{\Delta R_{90}}{R_{90}} = (\pi_{11} + \pi_{12}) \, \sigma_{11}' = 2(\frac{\Delta R_{45}}{R_{45}}) = 2(\frac{\Delta R_{-45}}{R_{-45}})$$

<div align="right">Eq. (9.3.11)</div>

Through the use of four-point bending tests, all pi-coefficients may be determined without hydrostatic tests. If we consider two-dimensional states of stress, the normalized resistance equations are expressed as follows:

- With respect to the unprimed axes

$$\frac{\Delta R_0}{R_0} = \pi_{11}\sigma_{11} + \pi_{12}\sigma_{22}$$

<div align="right">Eq. (9.3.12)</div>

$$\frac{\Delta R_{90}}{R_{90}} = \pi_{12}\sigma_{11} + \pi_{11}\sigma_{22}$$

<div align="right">Eq. (9.3.13)</div>

$$\frac{\Delta R_{45}}{R_{45}} = \frac{\pi_{11} + \pi_{12}}{2} (\sigma_{11} + \sigma_{22}) + \pi_{44}\sigma_{12}$$

<div align="right">Eq. (9.3.14)</div>

$$\frac{\Delta R_{-45}}{R_{-45}} = \frac{\pi_{11} + \pi_{12}}{2} (\sigma_{11} + \sigma_{22}) - \pi_{44}\sigma_{12}$$

<div align="right">Eq. (9.3.15)</div>

It is apparent that π_{11} and π_{12} can be determined by adding and subtracting Eqs. (9.3.12) and (9.3.13). In order to express two-dimensional states of stress as a function of force F, we adopt the notations as cited previously in Chapter 4:

$$\sigma_{11} \equiv \sigma_{11F}F, \ \sigma_{22} \equiv \sigma_{22F}F, \text{ and } S_\phi \equiv \frac{d}{dF}(\frac{\Delta R_\phi}{R_\phi})$$

<div align="right">Eq. (9.3.16)</div>

The results are

$$\pi_{11} = \frac{\sigma_{11F}S_0 - \sigma_{22F}S_{90}}{(\sigma_{11F})^2 - (\sigma_{22F})^2}$$

Eq. (9.3.17)

$$\pi_{12} = \frac{\sigma_{11F}S_{90} - \sigma_{22F}S_0}{(\sigma_{11F})^2 - (\sigma_{22F})^2}$$

Eq. (9.3.18)

In the equations, σ_{11F} and σ_{22F} may be obtained by the finite element simulation, in which σ_{11} and σ_{22} are the same as σ_{11F} and σ_{22F} for a 1-N force, respectively. In addition, π_S can be determined as follows:

$$\pi_S = \frac{S_0 + S_{90}}{\sigma_{11F} + \sigma_{22F}} = \frac{S_{45} + S_{-45}}{\sigma_{11F} + \sigma_{22F}}$$

Eq. (9.3.19)

- With respect to the primed axes

$$\frac{\Delta R_0}{R_0} = (\frac{\pi_{11} + \pi_{12} + \pi_{44}}{2}) \sigma_{11}' + (\frac{\pi_{11} + \pi_{12} - \pi_{44}}{2}) \sigma_{22}'$$

Eq. (9.3.20)

$$\frac{\Delta R_{90}}{R_{90}} = (\frac{\pi_{11} + \pi_{12} - \pi_{44}}{2}) \sigma_{11}' + (\frac{\pi_{11} + \pi_{12} + \pi_{44}}{2}) \sigma_{22}'$$

Eq. (9.3.21)

$$\frac{\Delta R_{45}}{R_{45}} = (\frac{\pi_{11} + \pi_{12}}{2}) \ (\sigma_{11}' + \sigma_{22}') + (\pi_{11} - \pi_{12})\sigma_{12}'$$

Eq. (9.3.22)

$$\frac{\Delta R_{-45}}{R_{-45}} = (\frac{\pi_{11} + \pi_{12}}{2}) \ (\sigma_{11}' + \sigma_{22}') - (\pi_{11} - \pi_{12})\sigma_{12}'$$

Eq. (9.3.23)

Note that π_{44} can be determined by adding and subtracting Eqs. (9.3.20) and (9.3.21). The results are

$$\pi_{44} = \frac{S_0 - S_{90}}{\sigma_{11F}' - \sigma_{22F}'}$$

Eq. (9.3.24)

$$\pi_S = \frac{S_0 + S_{90}}{\sigma_{11F}' + \sigma_{22F}'}$$

Eq. (9.3.25)

194

In the equations, σ_{11F}' and σ_{22F}' may be obtained by the finite element simulation, in which σ_{11}' and σ_{22}' are the same as σ_{11F}' and σ_{22F}' for a 1-N force, respectively. In addition, in the cases of the primed axes, $S_0 + S_{90} = S_{45} + S_{-45}$. Hence π_S may be given by

$$\pi_S = \frac{S_0 + S_{90}}{\sigma_{11F}' + \sigma_{22F}'} = \frac{S_{45} + S_{-45}}{\sigma_{11F}' + \sigma_{22F}'} \qquad \text{Eq. (9.3.26)}$$

By Eqs. (9.3.17), (9.3.18), and (9.3.24), all the piezoresistive coefficients π_{11}, π_{12}, and π_{44} can be determined for the (001) silicon surface.

The details of errors in piezoresistive coefficients induced by the rotational misalignment of strips on the supports by an angle θ with respect to the ideal longitudinal axis of the strips are analyzed in Appendix D. It is noteworthy that π_S is not influenced by any rotational error only in the form of $(S_0 + S_{90})$ or $(S_{45} + S_{-45})$. On the other hand, rotational error affects all individual pi-coefficients (π_{11}, π_{12}, and π_{44}) on the (001) surface.

9.4   Strip-on-beam Test Samples

Our first attempt at building strip-on-beam samples used a single strip on one side of the PCB beam. However, as shown in Fig. 9.9, the single-sided silicon strip-on-beam samples were significantly warped after cooling from their assembly temperature, resulting from the mismatch in the coefficients of expansion of the various packaging materials. The warpage shifts the initial resistance values due to the induced stresses. In order to minimize the warpage, the double-sided silicon strip-on-beam samples were used (see Fig. 9.10). A second dummy strip was mounted on the back of the beam resulting in

a symmetrical structure. Theses samples achieve an almost "stress free" condition before applying the force in 4PB apparatus because of their symmetrical structure.

From the simulation results in the next section, it can be seen that the stress in the direction of the beam is uniform between the inner 4PB supports, and the transverse component is negligible. Thus, from a stress uniformity point of view, the double-sided strip-on-beam technique is very similar to just having a silicon beam directly in the 4PB fixture.
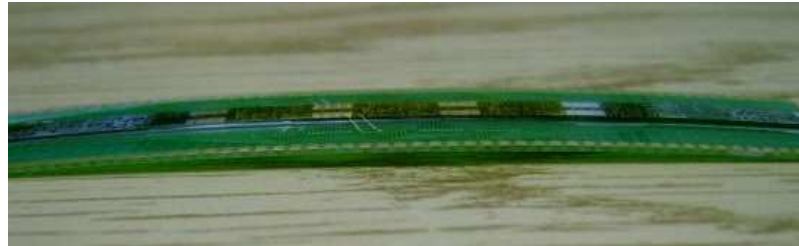
Fig. 9.9 - The obvious warp of a single-sided silicon strip-on-beam sample after cooling from 150°C to room temperature

Fig. 9.10 - The almost warp-free double-sided silicon strip-on-beam sample after cooling from 150°C to room temperature

9.5   Simulation Results for the (001) Silicon Test Chips

Meshes for the [100] and [110] silicon strip-on-beam sample are shown in Figs. 9.11 through 9.14. Double-sided silicon strip-on-beam samples are used in order to minimize the deformation that occurs upon cooling from the assembly temperature and to maintain an almost "stress free" condition before applying the force in 4PB apparatus.

The central quarter-die size part of silicon strip was meshed into 12 x 12 x 5 elements for the [100] directional strip-on-beam (8 x 8 x 5 for the [110] directional strip-on-beam). Note that quarter-model was used due to the limitations of number of elements and the duration of simulations. The other parts were meshed less densely compared with the central part. The meshes for both types ([100] and [110] silicon strip-on-beam) are very similar other than the number of elements.
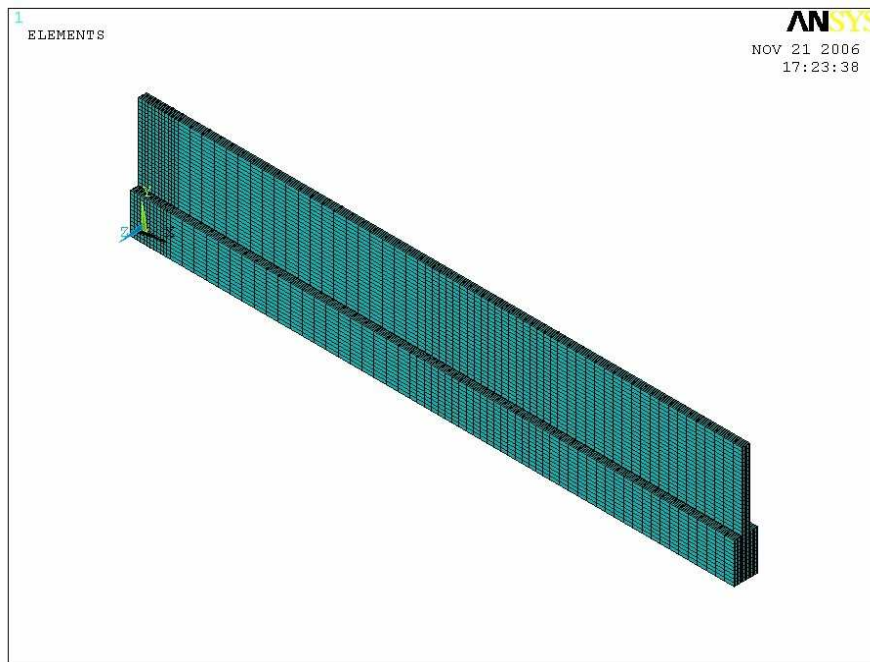
Fig. 9.11 - Mesh plots of the [100] silicon strip-on-beam sample (quarter model)

197

Fig. 9.12 - Mesh plots of the [100] silicon strip (central part)
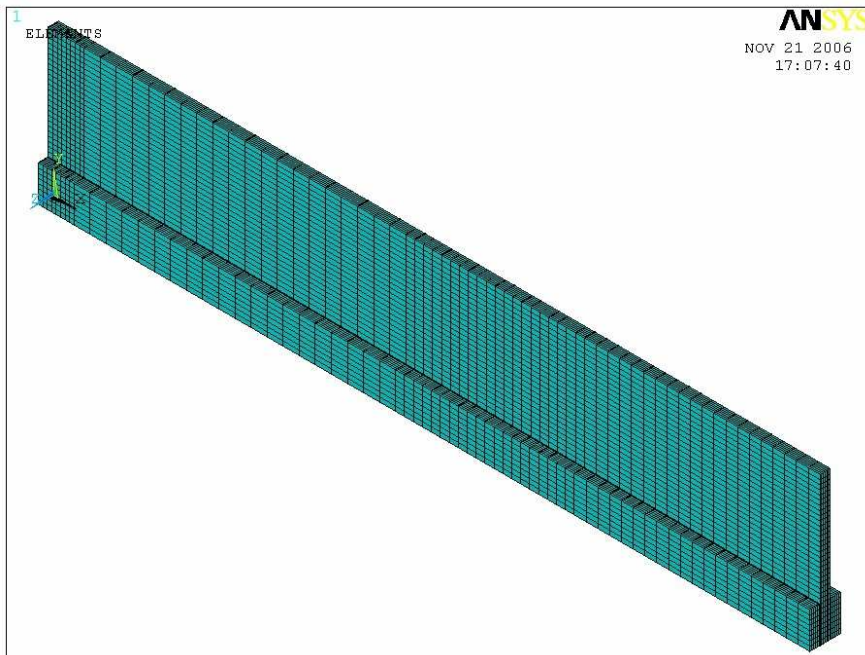
Fig. 9.13 - Mesh plots of the [110] silicon strip-on-beam sample (quarter model)

198

Fig. 9.14 - Mesh plots of the [110] silicon strip (central part)

The calculated contour plots of σ_{11} and σ_{22} (σ'_{11} and σ'_{22}) in the double-sided silicon strip-on-beam are presented for a 1-N force in Figs. 9.15 through 9.18. Note that the direction of σ_{11} (or σ'_{11}) is parallel to the direction of the beam in our tests.
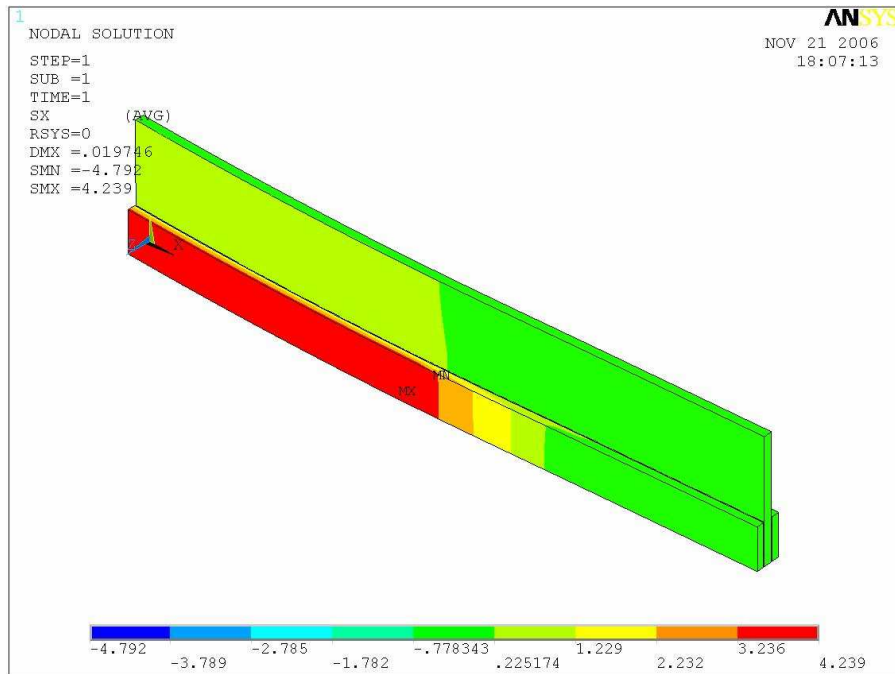
Fig. 9.15 - Contour plot of σ_{11} on [100] silicon strip-on-beam at 25°C
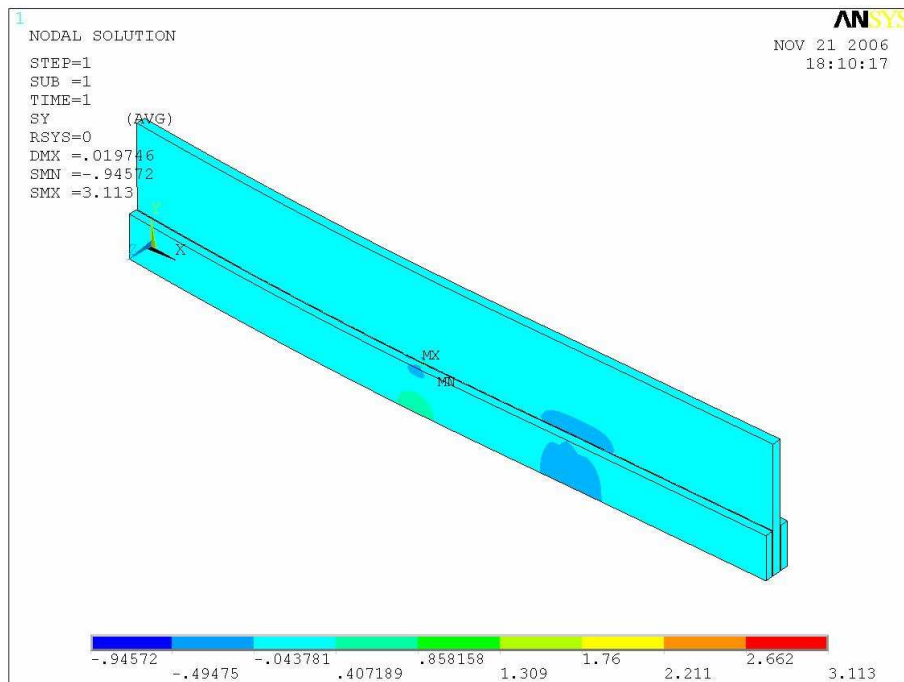
Fig. 9.16 - Contour plot of σ_{22} on [100] silicon strip-on-beam at 25°C
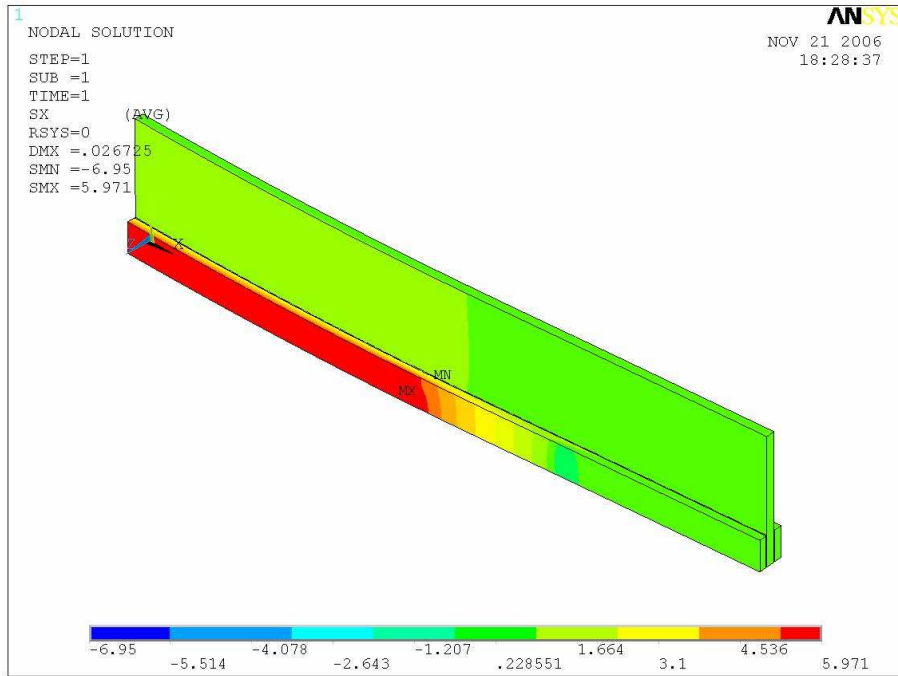
Fig. 9.17 - Contour plot of σ'_{11} on [110] silicon strip-on-beam at 25$^{\text{o}}$C
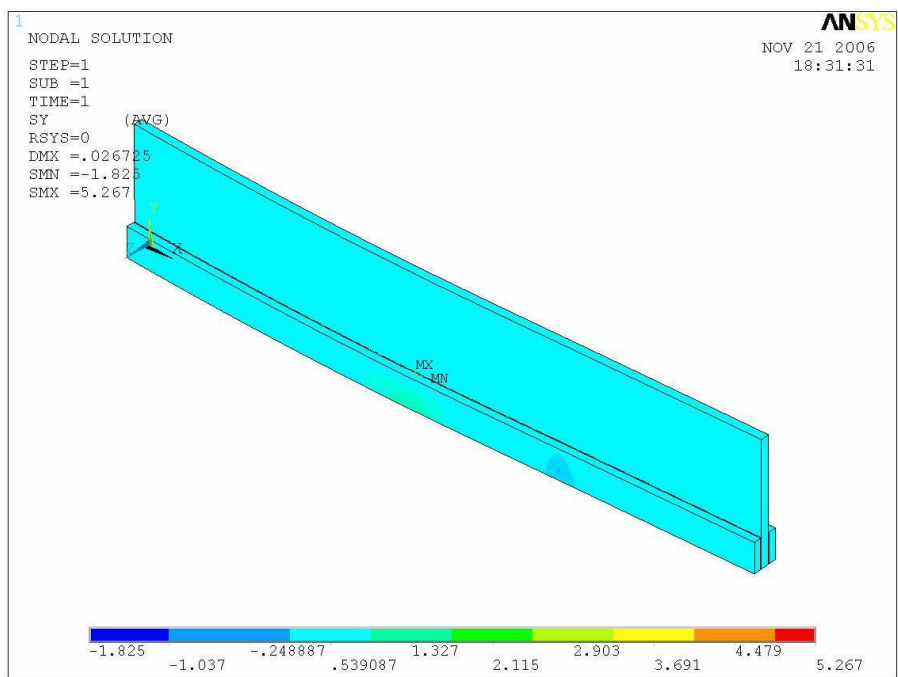
Fig. 9.18 - Contour plot of σ'_{22} on [110] silicon strip-on-beam at 25$^{\text{o}}$C

Stresses, σ_{11} and σ_{22} (σ_{11}' and σ_{22}') at the location of sensor over the temperature

range -150°C to +125°C appear in Table 9.3.

Table 9.3 - σ_{11} and σ_{22} (σ_{11}' and σ_{22}') at the sensor location with temperature (Unit: MPa)				
T(^{o}C)	σ_{11}	σ_{22}	σ_{11}'	σ_{22}'
-151.0	3.7727	0.00534	5.3222	-0.00669
-133.4	3.7784	0.00510	5.3303	-0.00629
-113.4	3.7822	0.00495	5.3355	-0.00602
-93.2	3.7865	0.00481	5.3413	-0.00564
-71.4	3.7881	0.00481	5.3432	-0.00541
-48.2	3.7897	0.00480	5.3440	-0.00540
-23.6	3.7913	0.00477	5.3472	-0.00500
0.6	3.7923	0.00478	5.3486	-0.00485
25.1	3.7968	0.00462	5.3547	-0.00450
49.9	3.8029	0.00429	5.3635	-0.00423
75.1	3.8098	0.00395	5.3748	-0.00387
100.6	3.8164	0.00360	5.3836	-0.00354
125.9	3.8164	0.00306	5.3986	-0.00322

The primary normal stress component σ_{11} (and/or σ_{11}') is almost constant with varying

temperatures. The second normal stress component σ_{22} (and/or σ_{22}') is negligible over

the whole temperature range because of their symmetrical structure. Note that they are

relatively small compared with the chip-on-beam cases in Chapter 4. In the simulations,

the mechanical properties (E) of composite materials are reflected in Table 9.4. Also, the

generally accepted values of ν are 0.278 and 0.062 respectively for the [100] silicon and

[110] silicon over the whole range of temperature.

Table 9.4 - Measurements of E with temperature (Unit: GPa)				
T(^{o}C)	ME525	Silicon [100]	Silicon [110]	FR-406
-151.0	19.81	131.6	172.9	28.82
-133.4	18.46	131.4	172.4	27.41
-113.4	17.53	131.3	172.0	26.49
-93.2	15.99	131.2	171.5	25.57
-71.4	14.90	131.0	171.0	25.35
-48.2	13.70	130.8	170.6	25.12
-23.6	12.85	130.5	170.0	24.80
0.6	12.00	130.2	169.7	24.68
25.1	10.43	130.1	169.1	23.73
49.9	9.85	130.0	168.4	22.05
75.1	8.75	129.6	167.9	20.26
100.6	7.72	129.4	167.3	18.55
125.9	4.98	129.0	166.8	16.37

Tables 9.5 and 9.6 give the dimensions of materials of strip-on-beam structure representing the average values of 10 specimens. These were obtained by microscope measurement with a resolution of 0.05 mil.

Table 9.5 - Dimensions of composite materials of [100] silicon strip-on-beam (Unit: mil)			
	Beam material	(001) silicon: [100]	Adhesive material
Length (l)	3400	3400	3400
Width (b)	650	226	226
Thickness (h)	22.67	20	2.5

Table 9.6 - Dimensions of composite materials of [110] silicon strip-on-beam (Unit: mil)			
	Beam material	(001) silicon: [110]	Adhesive material
Length (l)	3400	3400	3400
Width (b)	650	160	160
Thickness (h)	22.67	20	2.5

9.6 Sensor Calibration for the (001) Silicon Test Chips

The 4PB apparatus has been used to generate the required stress. However, due to the mismatch of mechanical properties such as E and ν among silicon, die attachment adhesive (ME 525), and PCB material (FR-406), two-dimensional states of stress are induced. For the double-sided silicon strip-on-beam cases, considering only σ_{11} (and/or σ'_{11}) is enough for determination of pi-coefficients because the second normal stress component σ_{22} (and/or σ'_{22}) is negligible. However, in this work, a two-dimensional state of stress is still considered for completeness and accuracy. The characterization results are displayed with respect to applied force F instead of uniaxial stress. As discussed in section 9.3, the stress-induced resistance changes for the (001) silicon are given as follows:

- With respect to the unprimed axes

$$\pi_{11} = \frac{\sigma_{22F}S_{90} - \sigma_{11F}S_0}{(\sigma_{22F})^2 - (\sigma_{11F})^2} \quad, \quad \pi_{12} = \frac{\sigma_{22F}S_0 - \sigma_{11F}S_{90}}{(\sigma_{22F})^2 - (\sigma_{11F})^2} \qquad \text{Eq. (9.5.1)}$$

$$\pi_S = \frac{S_0 + S_{90}}{\sigma_{11F} + \sigma_{22F}} = \frac{S_{45} + S_{-45}}{\sigma_{11F} + \sigma_{22F}} \qquad \text{Eq. (9.5.2)}$$

- With respect to the primed axes

$$\pi_{44} = \frac{S_0 - S_{90}}{\sigma'_{11F} - \sigma'_{22F}} \qquad \text{Eq. (9.5.3)}$$

$$\pi_S = \frac{S_0 + S_{90}}{\sigma'_{11F} + \sigma'_{22F}} = \frac{S_{45} + S_{-45}}{\sigma'_{11F} + \sigma'_{22F}} \qquad \text{Eq. (9.5.4)}$$

The slopes of the resistance versus force curves, S_0, S_{90}, S_{45}, and S_{-45} for the (001) silicon have been measured over temperature, and the average of 10 specimens is presented in

Tables 9.7 through 9.10. Temperature was measured directly using a Type-T (-270°C to +300°C) thermocouple inserted into the Delta Design 2850 test chamber. The details of S_0, S_{90}, S_{45}, S_{-45}, and pi-coefficients for the (001) silicon over temperature are presented in Appendix E.

Table 9.7 - S_0, S_{90}, S_{45}, and S_{-45} for [100] p-type silicon with temperature (Unit: 10^{-6} N^{-1})

T (°C)	S_0	S_{90}	S_{45}	S_{-45}
-151.0	203.8	-55.7	79.6	78.5
-133.4	184.7	-46.5	77.3	73.5
-113.4	168.7	-47.7	60.9	65.6
-93.2	163.6	-44.2	63.0	60.8
-71.4	150.2	-36.7	53.5	56.4
-48.2	136.7	-35.7	54.4	48.9
-23.6	123.8	-29.2	48.6	47.7
0.6	116.2	-27.3	39.2	53.5
25.1	111.5	-23.4	40.4	37.1
49.9	98.2	-21.6	36.0	35.7
75.1	83.5	-17.1	30.3	24.2
100.6	70.8	-10.1	31.1	28.5
125.9	68.3	-9.7	32.6	22.6

Table 9.8 - S_0, S_{90}, S_{45}, and S_{-45} for [110] p-type silicon with temperature (Unit: 10^{-6} N^{-1})

T (°C)	S_0	S_{90}	S_{45}	S_{-45}
-151.0	3831	-3598	134.2	131.3
-133.4	3602	-3377	126.8	124.4
-113.4	3369	-3171	111.8	123.5
-93.2	3193	-3005	111.9	122.7
-71.4	3094	-2894	102.9	108.0
-48.2	2891	-2726	91.3	100.5
-23.6	2737	-2612	86.0	79.5
0.6	2603	-2481	77.9	89.0
25.1	2456	-2366	69.5	72.5
49.9	2298	-2199	69.8	64.4
75.1	2077	-1984	54.2	55.5
100.6	1938	-1859	44.7	46.9
125.9	1777	-1731	44.5	43.2

Table 9.9 - S_0, S_{90}, S_{45}, and S_{-45} for [100] n-type silicon with temperature (Unit: 10^{-6} N^{-1})

T (^{o}C)	S_0	S_{90}	S_{45}	S_{-45}
-151.0	-4383	2443	-993	-975
-133.4	-4171	2333	-930	-900
-113.4	-3914	2210	-878	-857
-93.2	-3726	2103	-822	-821
-71.4	-3493	2001	-776	-795
-48.2	-3294	1887	-702	-707
-23.6	-3054	1732	-667	-667
0.6	-2856	1600	-627	-626
25.1	-2622	1478	-578	-569
49.9	-2456	1346	-529	-520
75.1	-2299	1258	-472	-484
100.6	-2067	1159	-438	-424
125.9	-1858	1032	-388	-401

Table 9.10 - S_0, S_{90}, S_{45}, and S_{-45} for [110] n-type silicon with temperature (Unit: 10^{-6} N^{-1})

T (^{o}C)	S_0	S_{90}	S_{45}	S_{-45}
-151.0	-1623	-983	-1322	-1284
-133.4	-1536	-918	-1267	-1166
-113.4	-1423	-849	-1142	-1134
-93.2	-1337	-810	-1088	-1051
-71.4	-1256	-736	-962	-1011
-48.2	-1185	-699	-941	-911
-23.6	-1117	-664	-858	-873
0.6	-1053	-632	-782	-806
25.1	-973	-577	-718	-766
49.9	-903	-523	-701	-686
75.1	-804	-464	-630	-634
100.6	-744	-422	-589	-560
125.9	-646	-356	-521	-519

Combining Eqs. (9.5.1) and (9.5.3) with the FEM results, we can determine all the pi-coefficients (π_{11}, π_{12}, and π_{44}) for p- and n-type material, and the extracted values appear

in Table 9.11 and Figs. 9.19 through 9.22. Our experimental results show that the magnitudes of the pi-coefficients, π_{11}, π_{12}, and π_{44} for p- and n-type silicon decrease monotonically with increasing temperature over the temperature range -150°C to $+125^{\circ}$C. The four coefficients exhibit an approximately linear variation with temperature over the full range.

Table 9.11 - $\pi_{11,}$ π_{12}, and π_{44} for (001) p- and n-type silicon with temperature (Unit: TPa^{-1})						
	P-type silicon			N-type silicon		
T(^{o}C)	π_{11}	π_{12}	π_{44}	π_{11}	π_{12}	π_{44}
-151.0	54.0	-14.8	1395.5	-1162.7	649.1	-120.1
-133.4	48.9	-12.4	1309.2	-1104.7	618.8	-115.7
-113.4	44.6	-12.7	1225.6	-1035.5	585.8	-107.5
-93.2	43.2	-11.7	1160.3	-984.8	556.5	-98.4
-71.4	39.7	-9.7	1120.8	-922.8	529.3	-97.2
-48.2	36.1	-9.5	1051.1	-869.9	498.9	-90.9
-23.6	32.7	-7.8	1000.2	-806.2	457.9	-84.6
0.6	30.7	-7.2	950.5	-753.6	422.7	-78.7
25.1	29.4	-6.2	898.5	-691.0	390.0	-73.9
49.9	25.8	-5.7	838.0	-646.2	354.7	-70.8
75.1	21.9	-4.5	755.0	-603.7	330.9	-63.3
100.6	18.5	-2.7	704.7	-541.9	304.2	-59.7
125.9	17.9	-2.5	649.0	-485.8	270.2	-53.7
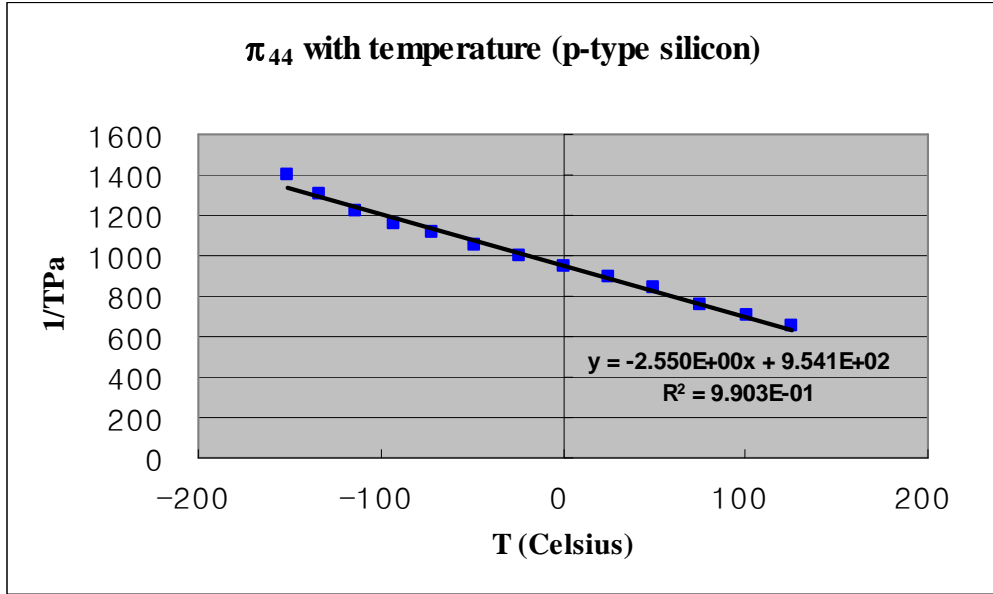
Figure 9.19 - π_{44} for the (001) p-type silicon with temperature
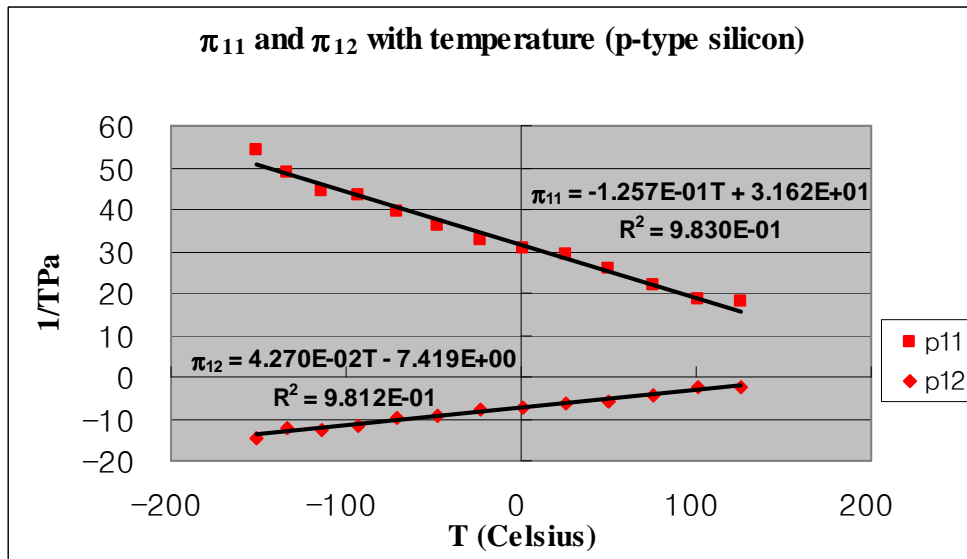
Figure 9.20 - π_{11} and π_{12} for the (001) p-type silicon with temperature
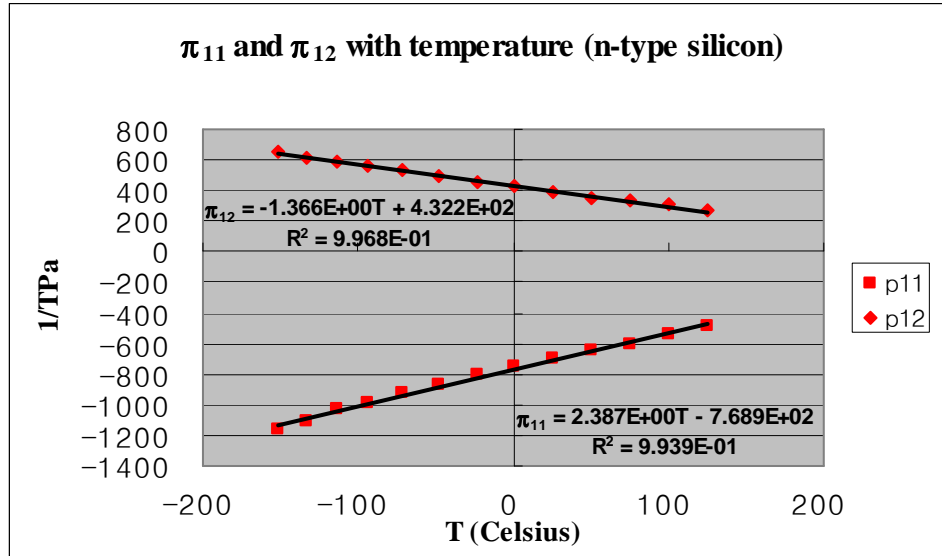
Figure 9.21 - π_{11} and π_{12} for the (001) n-type silicon with temperature
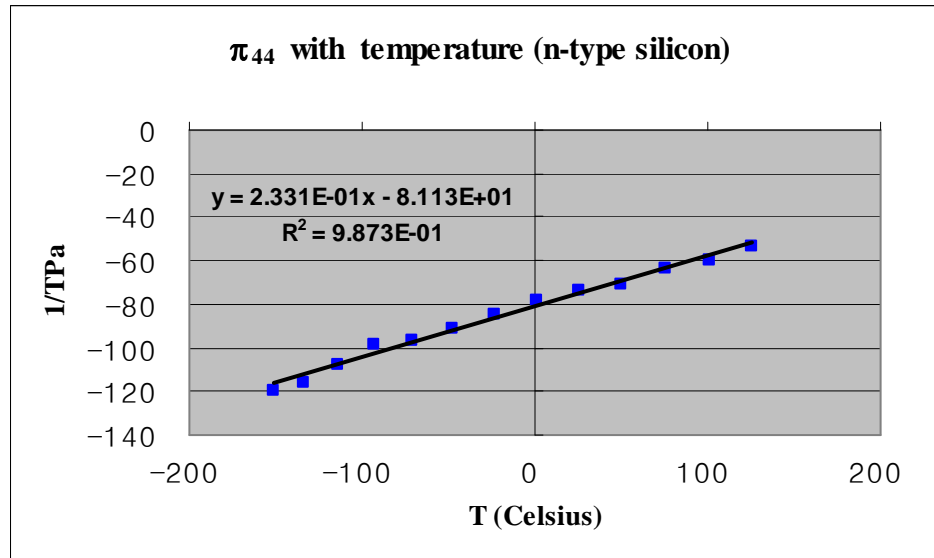
Fig. 9.22 - π_{44} for the (001) n-type silicon with temperature

Figure 9.23 plots the ratio π_{11}/π_{12} versus temperature. The ratio is observed to be

constant with $\pi_{11} \cong -1.8 \ \pi_{12}$. This result is in good agreement with the theoretical

prediction that $\pi_{11} \cong -2\ \pi_{12}$ based on the electron-transfer mechanism in n-type silicon [96].
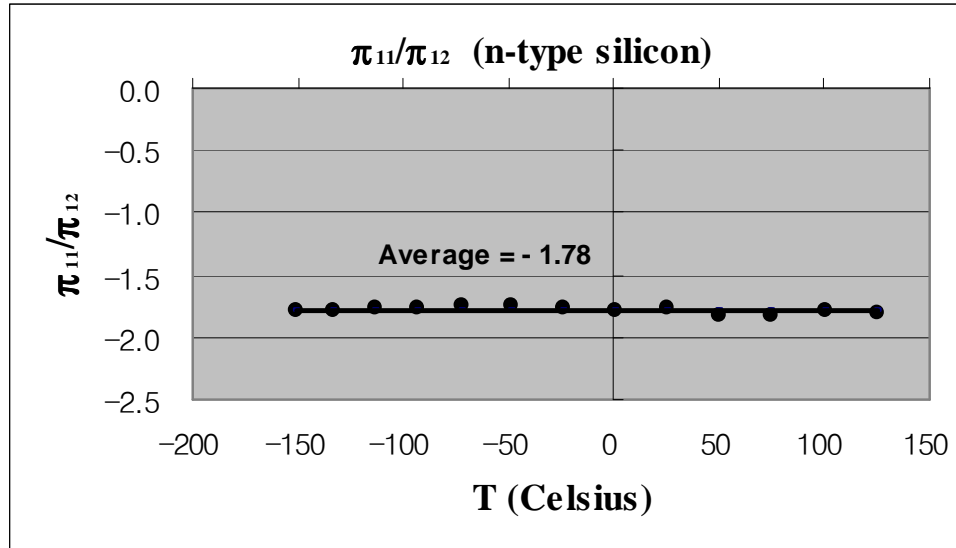
Fig. 9.23 - π_{11}/π_{12} for the (001) n-type silicon with temperature

The value of the combined coefficient $\pi_S = \pi_{11} + \pi_{12}$ may be determined from both the $\pm 45^\circ$ and $0^\circ/90^\circ$ resistor pairs for the unprimed and/or primed coordinate system as represented in Eqs. (9.5.2) and (9.5.4). The results appear in Tables 9.12 and 9.13 and Figs. 26 and 27. Both the $\pm 45^\circ$ and $0^\circ/90^\circ$ pairs are insensitive to rotational alignment error [58], and should yield the most precise measurements.

Table 9.12 - π_S for the (001) p-type silicon with temperature (Unit: TPa^{-1})						
T (^{o}C)	[110]: (+45,-45)	[110]: (0,90)	[100]: (+45,-45)	[100]: (0,90)	Average	Std.Dev
-151.0	50.0	44.0	41.9	39.2	43.8	4.6
-133.4	47.3	42.3	39.9	36.5	41.5	4.5
-113.4	44.2	37.3	33.4	32.0	36.7	5.5
-93.2	44.0	35.2	32.7	31.5	35.9	5.7
-71.4	39.6	37.5	29.0	29.9	34.0	5.3
-48.2	36.0	31.0	27.2	26.6	30.2	4.3
-23.6	31.0	23.4	25.3	24.9	26.2	3.4
0.6	31.3	22.9	24.4	23.4	25.5	3.9
25.1	26.6	16.9	20.4	23.2	21.8	4.1
49.9	25.1	18.5	18.8	20.1	20.6	3.0
75.1	20.5	17.4	14.3	17.4	17.4	2.5
100.6	17.1	14.7	15.6	15.9	15.8	1.0
125.9	16.3	8.5	14.4	15.3	13.6	3.5

Table 9.13 - π_S for the (001) n-type silicon with temperature (Unit: TPa^{-1})						
T (^{o}C)	[110]: (+45,-45)	[110]: (0,90)	[100]: (+45,-45)	[100]: (0,90)	Average	Std.Dev
-151.0	-490.3	-490.3	-521.1	-513.5	-503.8	15.9
-133.4	-456.8	-460.8	-483.7	-485.9	-471.8	15.1
-113.4	-427.0	-426.2	-458.0	-449.8	-440.2	16.1
-93.2	-400.9	-402.3	-433.5	-428.2	-416.2	17.0
-71.4	-369.7	-373.3	-414.1	-393.5	-387.6	20.5
-48.2	-347.0	-352.8	-371.5	-371.0	-360.6	12.5
-23.6	-324.0	-333.4	-351.2	-348.3	-339.2	12.8
0.6	-297.2	-315.2	-329.9	-330.8	-318.3	15.8
25.1	-277.3	-289.6	-301.9	-300.9	-292.4	11.5
49.9	-258.9	-266.1	-275.6	-291.5	-273.0	14.1
75.1	-235.3	-236.1	-250.6	-272.8	-248.7	17.6
100.6	-213.6	-216.6	-225.6	-237.7	-223.4	10.8
125.9	-192.7	-185.7	-205.9	-215.6	-200.0	13.4
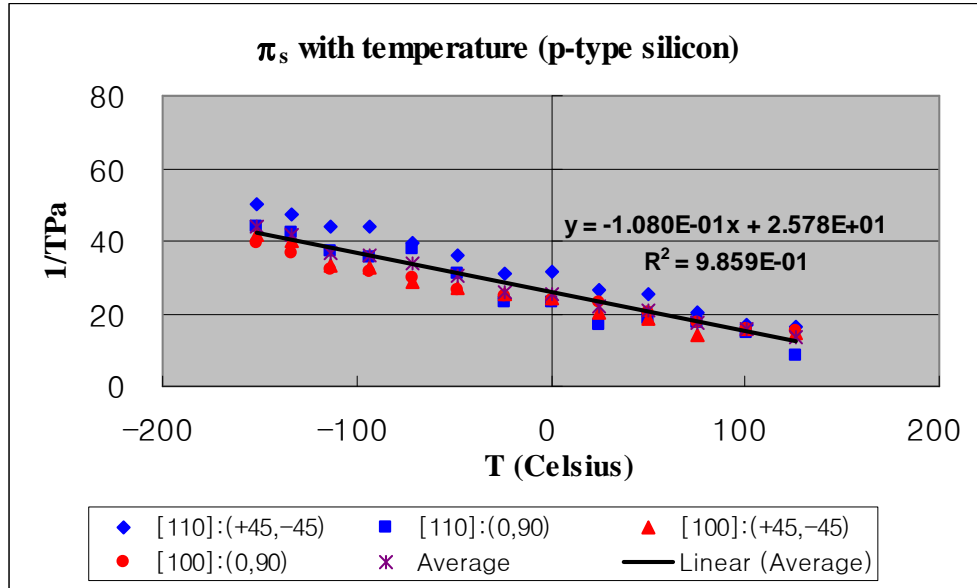
Fig. 9.24(a) - π_S for the (001) p-type silicon with temperature
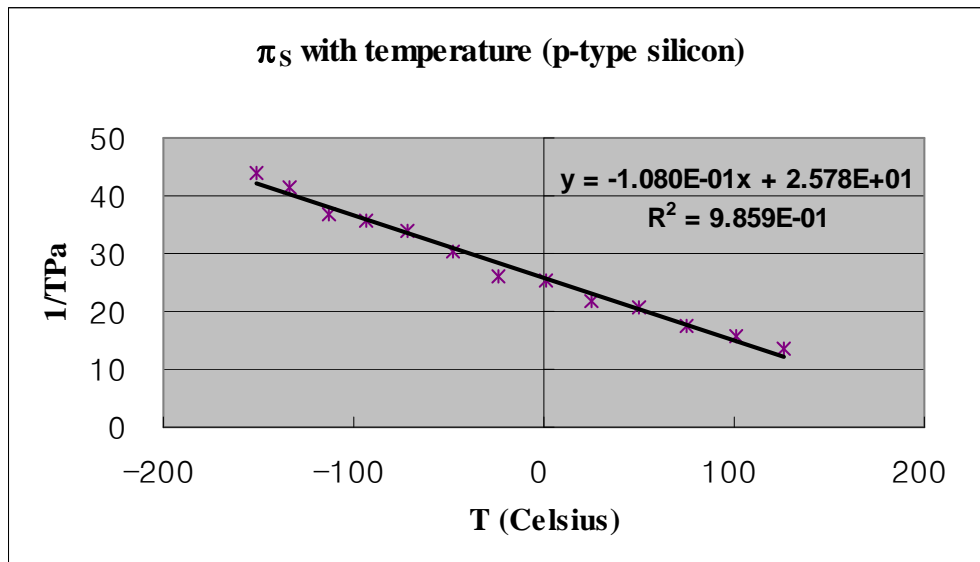
Fig. 9.24(b) - π_S for the (001) p-type silicon with temperature. Fit to the average values from Fig. 9.24(a).
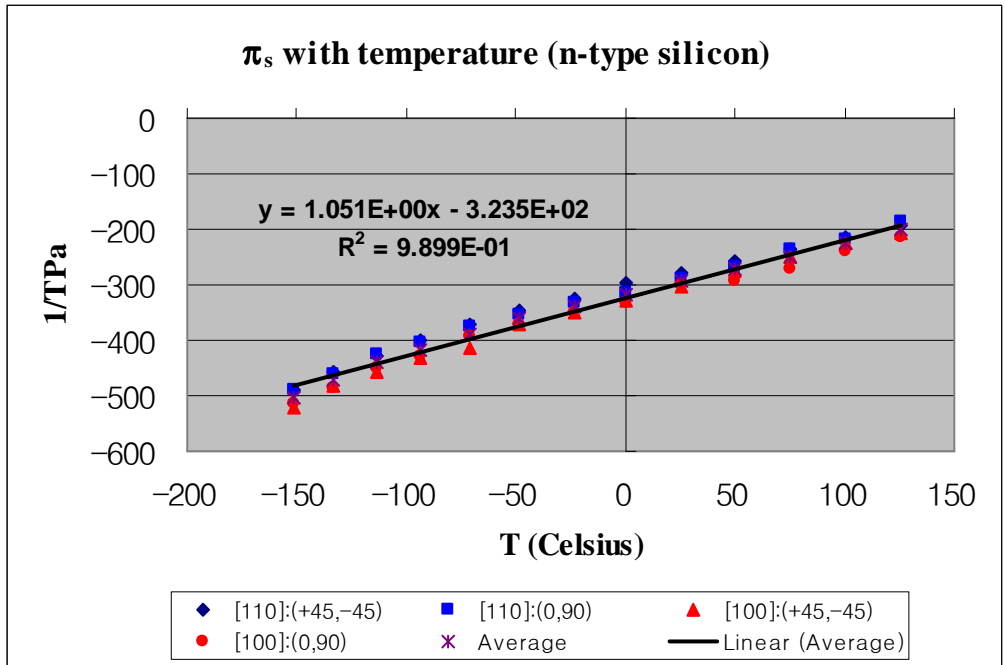
Fig. 9.25(a) - π_S for the (001) n-type silicon with temperature
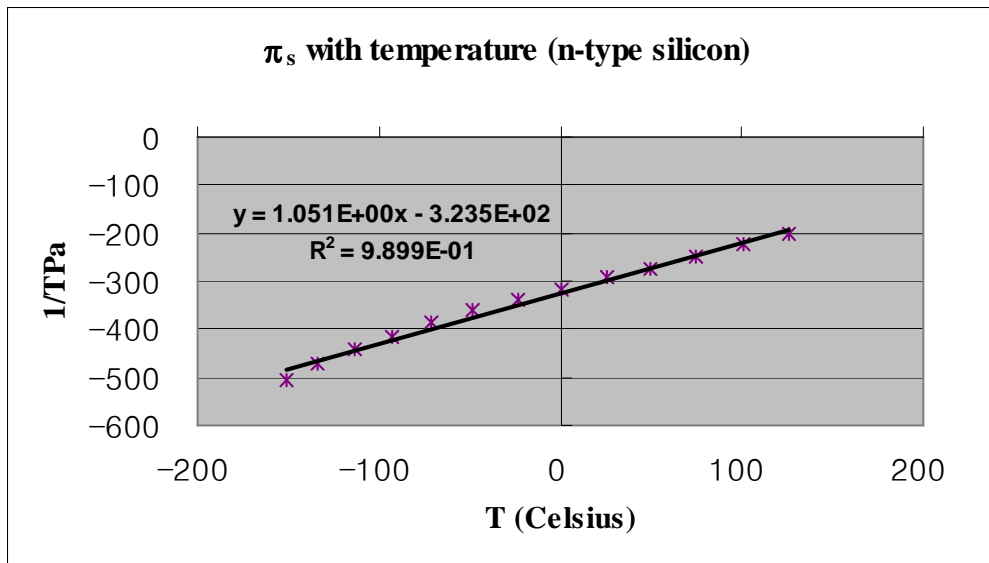
Fig. 9.25(b) - π_S for the (001) n-type silicon with temperature. Fit to the average values from Fig. 9.25(a).

The temperature variation of the three coefficients in p-type material is linear and monotonically decreases in magnitude over the full temperature range studied, -150$^{\mathrm{o}}$C to +125$^{\mathrm{o}}$C. π_{44} is large and positive in p-type material. For the small coefficients in p-type material, π_{11} is found to be positive and π_{12} is negative over the complete temperature range. These results are consistent in sign and magnitude with the room temperature results originally presented by Smith [6].

The three pi-coefficients are larger and more easily measured in n-type material. The variation of the coefficients in n-type material is also linear and monotonically decreases in magnitude over the full temperature range as for the p-type coefficients. π_{11} and π_{44} are clearly negative, and π_{12} is positive over the measured temperature range. Our test results of π_{44} for p-type silicon and π_{11} for n-type silicon versus temperature are compared with the collected data from the literature as shown in Figs. 9.26 and 9.27, respectively.
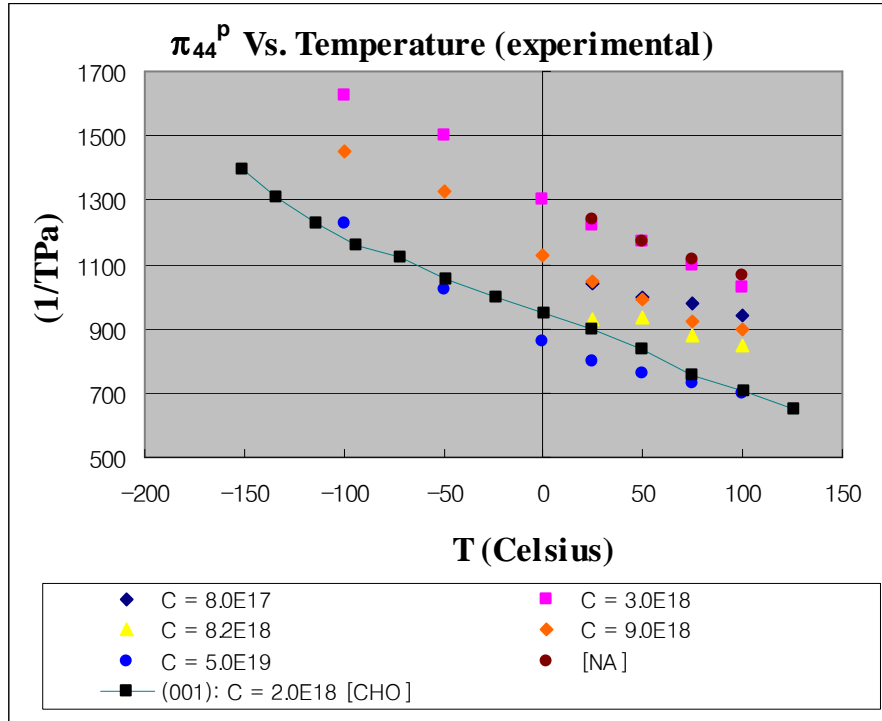
Fig. 9.26 - Experimental data for π_{44} versus temperature with different doping concentration for p-type silicon
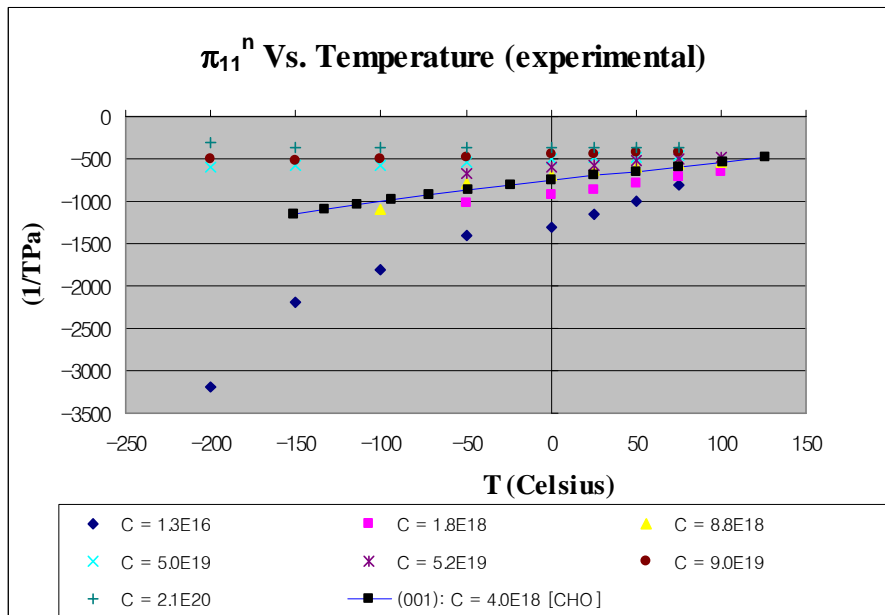
Fig. 9.27 - Experimental data for π_{11} versus temperature with different doping concentration for n-type silicon

9.7   Summary

The flat on silicon wafers that is normally used for alignment purposes can be off by 1-2 degrees, and any misalignment of the resistors with the crystallographic axes will lead to errors in the measured piezoresistive coefficients. In this work, a method for precise determination of the crystallographic orientation [110] in the (001) silicon wafer is used. The design takes advantage of the symmetric KOH under-etching behavior around [110] direction, and the resulting misalignment obtained is less than 0.125^{o}.

Piezoresistive coefficients for the (001) silicon can be determined by direct calibration. Through the use of four-point bending tests, all pi-coefficients may be determined without hydrostatic tests. On the other hand, (111) silicon sensors need hydrostatic tests in order to extract a complete set of pi-coefficients (π_{11}, π_{12}, and π_{44}).

By using the sensors on the (001) silicon strip cut along the unprimed axis [110], π_{44} can be determined by combining the normalized resistance equations for 0° and 90° sensors. Also, it is apparent that π_{11} and π_{12} can be determined by the equations from the sensors on the (001) silicon strip cut along the unprimed axis [100]. The value of the combined coefficient $\pi_{S} = \pi_{11} + \pi_{12}$ may be determined from both the $\pm 45^{o}$ and $0^{o}/90^{o}$ resistor pairs for the unprimed and/or primed coordinate system. Both the $\pm 45^{o}$ and $0^{o}/90^{o}$ pairs are insensitive to rotational alignment error.

In order to get data, experimental apparatus has been built for characterizing the temperature dependencies of the piezoresistive coefficients of silicon. A four-point-bending fixture has been configured to operate over a wide temperature range. In our work, we used the double-sided silicon strip-on-beam samples because the primary

normal stress component σ_{11} (and/or σ'_{11}) is uniform and independent of the location as long as the sensor is located between the inner supports and their secondary normal stress components are negligible because of their symmetrical structure. Experimental measurements have been combined with finite element simulations to produce the temperature dependence of the piezoresistive coefficients.

Our test results show that the pi-coefficients in both p- and n-type silicon exhibit an approximately linear variation with temperature over the measurement range. All the pi-coefficients decrease with rising temperatures.

CHAPTER 10

SUMMARY AND CONCLUSIONS

This work presents an extensive experimental study of the temperature dependence of the piezoresistive coefficients of silicon. Measurements were performed using stress sensors fabricated on both (001) and (111) silicon mounted on PCB material including both chip-on-beam and strip-on-beam mounting techniques. Four-point bending (4PB) was used to generate the required stress, and finite element simulations have been used to determine the actual states of stress applied to the calibration samples. Stress sensors fabricated on the surface of the (111) silicon wafers offer the advantage of being able to measure the complete stress state on the silicon surface, but they require use of hydrostatic measurement of the silicon "pressure" coefficients for calibration. On the other hand, all these coefficients can be measured on the (001) surface using judicious application of uniaxial stress. Hydrostatic experiments were performed on the test chips over the temperature range of -25$^\text{o}$C to 100$^\text{o}$C. By subtraction of the temperature-induced resistance change $f(\Delta T)$ from the total resistance change at each data point, adjusted resistance versus pressure data are obtained. The pressure coefficients of p- and n-type silicon versus temperature are calibrated. For n-type silicon, π_p is very small, as expected from the approximation $\pi_{11} \cong -2\pi_{12}$ [96], so direct measurement of these values

is quite difficult. For both p- and n-type sensors, π_p decreases in magnitude with rising temperature.

A special four-point bending (4PB) apparatus has been constructed and integrated into an environmental chamber capable of temperatures from -155 to +300°C. Force generated by a vertical translation stage is applied to the four-point bending fixture inside the chamber through a ceramic rod penetrating the bottom side of the chamber. During experiments, a chip-on-beam (and/or a double-sided strip-on-beam) specimen is placed on the bottom supports of the four-point bending fixture.

The hydrostatic pressure apparatus has been developed to make measurements at elevated and reduced temperature. In order to increase the temperature of fluid, a resistance heater is used inside the pressure vessel. To lower the temperature of fluid, liquid nitrogen is injected into a specially designed box surrounding the pressure vessel.

E (*Young's modulus*) and ν (*Poisson's ratio*) of silicon are dependent on direction because the anisotropic nature of the single crystal silicon. For any crystallographic direction of silicon, the expression of E and ν by compliance coefficients (s_{11}, s_{12}, and s_{44}) were presented. In this work, E of silicon and the other composite materials of chip-on-beam samples were calculated analytically and found to be in good agreement with experimental values obtained by using the "*Deflection of Beams*" method. For the (111) silicon surface, E and ν were observed to be isotropic.

The VDP sensor has been identified to have higher sensitivity than a conventional resistor sensor [49-50]. In this work, the effects of dimensional changes during loading were considered. It was observed that VDP sensors offer 3.157 times higher sensitivity than

an analogous two element resistor sensors. On the other hand, considering strain effects changes the magnification factor M to 3.23 for p-type sensors and 3.06 for n-type sensors. However, the strain effects were observed to be negligible for resistor sensors, so dimensional changes should be considered in the calculation of M for the VDP sensors.

In most prior investigations, calibration of the piezoresistive coefficients has been performed neglecting the error in misalignment. Literature values exhibit wide discrepancies in magnitude as well as disagreement in signs. Thus the literature data limits the accuracy of test chip stress measurements. From the analysis of off-axis sensors, misalignment with the crystallographic axes may lead to an enormous error in determining the pi-coefficients for the (001) silicon surface, whereas misalignment has no effect on the pi-coefficients for the (111) silicon surface because of its isotropic characteristics. In this work, for precise determination of the crystallographic orientation in silicon wafers, anisotropic wet etching is used. Furthermore, experimental calibration results for the piezoresistive coefficients of silicon as a function of temperature are presented and compared and contrasted with existing values from the literature. Our test results show that the temperature variation of the three coefficients in p- and n-type material is linear and monotonically decreases in magnitude over the full temperature range studied, -150°C to 125°C. π_{44} is large and positive in p-type material. For the small coefficients in p-type silicon, π_{11} is found to be positive and π_{12} is negative over the complete temperature range. The three pi-coefficients are larger and more easily measured in n-type material. π_{11} and π_{44} are clearly negative, and π_{44} is positive over the measured temperature range. These results are consistent in sign and magnitude with the room temperature results originally presented by Smith [6].

220

The double-sided silicon strip-on-beam method was developed to eliminate curvature problems. By this technique, the samples achieve an almost "stress free" condition before applying the force in 4PB apparatus because of their symmetrical structure. In addition, this technique offers stress uniformity in the 4PB fixture.

BIBLIOGRAPHY

1. Bridgman, P. W., "The Effect of Tension on the Electrical Resistance of Certain Abnormal Metals," *Proceedings of the American Academy of Arts and Sciences*, Vol. 57(3), pp. 41-66, 1922.

2. Bridgman, P. W., "The Effect of Tension on the Transverse and Longitudinal Resistance of Metals," *Proceedings of the American Academy of Arts and Sciences*, Vol. 60(8), pp. 423-449, 1925.

3. Bridgman, P. W., "The Effect of Homogeneous Mechanical Stress on the Electrical Resistance of Crystals, " *Physical Review*, Vol.42, pp. 858-863, 1932.

4. Taylor, J. H., "Pressure Dependence of Resistance of Germanium," *Physical Review*, Vol. 80, pp. 919-920, 1950.

5. Bridgman, P. W., "The Effect of Pressure on the Electrical Resistance of Certain Semiconductors, " *Proceedings of the American Academy of Arts and Sciences*, Vol. 79(3), pp. 127-148, 1951.

6. Smith, C. S., "Piezoresistance effects in Germanium and Silicon," *Physical Review*, Vol. 94(1), pp. 42-49, December, 1953.

7. Paul, W., Pearson, G. L., "Pressure Dependence of the Resistivity of Silicon," *Physical Review*, Vol. 98, pp. 1755-1757, 1955.

8. Pfann, W. G., Thurston, R. N., "Semiconducting Stress Transducers Utilizing the Transverse and Shear Piezoresistance Effects," *Journal of Applied Physics*, Vol. 32(10), pp. 2008-2019, October, 1961.

9. Mason, W. P., Thurston, R. N., "Use of Piezoresistive Materials in the Measurement of Displacement, Force and Torque," *Journal of the Acoustical Society of America*, Vol. 29(10), pp. 1096-1101, 1957.

10. Thurston, R. N., "Use of Semiconductor Transducers in Measuring Strains, Accelerations, and Displacements," *Physical Acoustics*, Edited by W. P. Mason, Academic Press, pp. 215-235, 1964.

11. Smith, C. S., "Macroscopic Symmetry and Properties of Crystals," *Solid State Physics*, Vol. 6, Edited by Seitz, F., Turnbull, D., Academic Press, pp. 175-249, 1958.

12. Bittle, D. A., Piezoresistive Stress Sensors for Integrated Circuits, M.S. Thesis, Auburn University, Auburn, Alabama, 1990.

13. Bittle, D. A., Suhling, J. C., Beaty, R. E., Jaeger, R. C., Johnson, R. W., "Piezoresistive Stress Sensors for Structural Analysis of Electronic Packaging," *M.S. Journal of Electronic Packaging*, pp. 203-215, September, 1991.

14. Bittle, D. A., Suhling, J. C., Beaty, R. E., Jaeger, R. C., and Johnson, R. W., "Piezoresistive Stress Sensors for Structural Analysis of Electronic Packages," *Journal of Electronic Packaging,* Vol. 113(3), pp. 203-215, 1991.

15. Kang, Y., Piezoresistive Stress Sensors for Advanced Semiconductor Materials, Ph.D. Dissertation, Auburn University, Auburn, AL, 1997.

16. Vangbo, Mattias., Baecklund, Ylva., "Precise Mask Alignment to the Crystallographic Orientation of Silicon Wafers Using Wet Anisotropic Etching," *J. Micromech. Microeng*. 6, pp.279-284, 1996.

17. Jaeger, R. C., Suhling, J. C., "Thermally induced Errors in the Calibration and Application of Silicon Piezoresistive Stress Sensors," *Advance in Electronic Packaging*, ASME, EEP-Vol.4-1, pp. 457-470, 1993.

18. Cordes, R. A., Suhling, J. C., Kang, Y., and Jaeger, R. C., "Optimal Temperature Compensated Piezoresistive Stress Sensor Rosettes," *Proceedings of the Symposium on Applications of Experimental Mechanics to Electronic Packaging*, ASME, EEP-Vol. 13, pp. 109-116, 1995.

19. Matsuda, Kazunori., "Nonlinear Piezoresistance Effects in Silicon," *J. Appl. Phys.*,vol.73(4), pp. 1838-1847, February, 1993.

20. Kanda, Y., "Graphical Representation of the Piezoresistance Coefficients in Silicon," *IEEE Transactions on Electron Devices*, vol. 29(1), pp. 64-70, January, 1982.

21. Richter, J., Hansen, O., "Piezoresistance of Silicon and Strained $Si_{0.9}Ge_{0.1}$," preprint submitted to Elsevier Preprint, pp. 1-18,2004

22. Vladimir, A. K., "Numerical Simulation of the Nonlinearity of the Piezoresistive Effect in the p-Type Silicon," *Siberian Russian Student Workshop on Electron Devices and Materials*, pp. 103-110, 2000.

23. Morin, F. J., Geballe, T. H., Herring, C., "Temperature Dependence of the Piezoresistance of High-Purity Silicon and Germanium," *Physical Review*, vol. 10, no. 2, pp. 525-539, 1956.

24. Tufte, O. N., Stelzer, E. L., "Piezoresistive Properties of Silicon Diffused Layers," *Journal of Applied Physics*, vol.34, no. 2, pp. 3322-3327, February, 1963.

25. Tufte, O. N., Stelzer, E. L., "Piezoresistive Properties of Heavily Doped n-Type Silicon," *Physical Review*, vol. 133, no. 6A, pp. A1705-A1716, March, 1964.

26. Suhling, J. C., Beaty, R. E., Jaeger, R. C., and Johnson, R. W., "Piezoresistive Sensors for Measurement of Thermally-Induced Stresses in Microelectronics," *Proceedings of the 1991 Spring Conference of the Society for Experimental Mechanics*, pp. 683-694, Milwaukee, WI, June 10-13, 1991.

27. Suhling, J. C., Carey, M. T., Johnson, R. W., and Jaeger, R. C., "Stress Measurement in Microelectronic Packages Subjected to High Temperature," in *Manufacturing, Processes and Materials Challenges in Microelectronic Packaging*, ASME, EEP-Vol. 1, pp. 143-152, 1991.

28. Lenkkeri, J. T., "Nonlinear effects in the Piezoresistivity of p-Type Silicon," *Phys. Stat. Sol.*, vol.136, no.1, pp. 373-385, July, 1986.

29. Jaeger, R. C., Suhling, J. C., "Off-Axis Sensor Rosettes for Measurement of the Piezoresistive Coefficients of Silicon," *IEEE Transactions on Components, Hybrids, and Manufacturing Technology*, vol. 16, no. 8, pp. 925-930, December, 1993

30. Lund, Einvind., Finstad, T., "Measurement of the Temperature Dependency of the Piezoresistance Coefficients in p-type Silicon," EEP-Vol.26-1, *Advances in Electronic Packaging*, vol. 1 ASME 1999, pp. 215-218, 1999.

31. Gniazdowski, Z., Kowalski, P., "Practical Approach to Extraction of Piezo-resistance of Piezoresistance Coefficient," *Sensors and Actuators* A68, pp. 329-332, 1998.

32. Toriyama, T., Sugiyama, S., "Analysis of Piezoresistance in p-Type Silicon for Mechanical Sensors," *Journal of Microelectromechanical Systems*, vol. 11, no. 5, pp. 598-604, October, 2002.

33. Kozlovskiy, S., Boiko, I., "First-order Piezoresistance Coefficients in Silicon Crystals," *Sensors and Actuators A118*, pp. 33-43,

34. Yamada, K., Nishihara, M., Shimada, S., Tanabe, M., Shimazoe, M., and Matsouka, Y., "Nonlinearity of the Piezoresistance Effect of P-Type Silicon Diffused Layers," *IEEE Transactions on Electron Devices*, Vol. 29(1), pp. 71-77. 1982.

35. Suhling, J. C., Jaeger, R. C., and Ramani, R., "Stress Measurement Using 0-90 Piezoresistive Rosettes on (111) Silicon," *Proceedings of the 1994 International Mechanical Engineering Congress and Exposition*, Chicago, IL, AMD-Vol. 195, pp. 65-73, 1994.

36. Suhling, J. C., Jaeger, R. C., Lin, S. T., Moral, R. J., and Zou, Y., "Measurement of the Complete Stress State in Plastic Encapsulated Packages," *Proceedings of INTERpack '97*, pp. 1741-1750, Kohala, HI, June 15-19, 1997.

37. Suhling, J. C., Jaeger, R. C., Wilamowski, B. M., Lin, S. T., Mian, A. K. M., and Cordes, R. A., "Design and Calibration of Optimized (111) Silicon Stress Sensing Test Chips," *Proceedings of INTERpack '97,* pp. 1723-1730, Kohala, HI, June 15-19, 1997.

38. Sweet, J. N., "Die Stress Measurement Using Piezoresistive Stress Sensors," *Thermal Stress and Strain in Microelectronics Packaging*, Edited by J. Lau, Von Nostrand Reinhold, 1993.

39. Bittle, D. A., Suhling, J. C., Beaty, R. E., Jaeger, R. C., and Johnson, R. W., "Piezoresistive Stress Sensors for Structural Analysis of Electronic Packages," *Journal of Electronic Packaging,* Vol. 113(3), pp. 203-215, 1991.

40. Miura, H., Kitano, M., Nishimura, A., and Kawai, S., "Thermal Stress Measurement in Silicon Chips Encapsulated in IC Plastic Packages under Thermal Cycling," *Journal of Electronic Packaging*, Vol. 115(1), pp. 9-15, 1993.

41. Jaeger, R. C., Ramani, R., and Suhling, J. C., "Effects of Stress-Induced Mismatches on CMOS Analog Circuits," *Proceedings of the International Symposium on VLSI Technology, Systems, and Applications*, pp. 354-360, Taipei, Taiwan, 1995.

42. Jaeger, R. C., Ramani, R., Suhling, J. C., and Kang, Y., "CMOS Stress Sensor Circuits Using Piezoresistive Field-Effect Transistors (PIFET's)," *Proceedings of 1995 Symposium on VLSI Circuit Design and Technology*, pp. 43-44, Kyoto, Japan, 1995.

43. Jaeger, R. C., and Suhling, J. C., "Advances in Stress Test Chips," *Application of Experimental Mechanics to Electronic Pakcaging-1997*, ASME, EEP-Vol. 22, pp.1-5, Dallas, TX, 1997.

44. Jaeger, R. C., Suhling, J. C., Bradley, A. T., and Xu, J., "Silicon Piezoresistive Stress Sensors Using MOS and Bipolar Transistors," *Proceeding of InterPack'99*, pp. 219-226, Lahaina, HI, June 13-19, 1999.

45. Jaeger, R. C., Suhling, J. C., Ramani, R., Bradley, A. T., and Xu, J., "CMOS Stress Sensors on (100) Silicon," *IEEE Journal of Solid-State Circuits*, Vol. 35(1), pp. 85-95, 2000.

46. Ramani, R., <u>Piezoresistive Behavior of MOSFET and FET-Based Stress Sensor Circuit</u>, Ph.D. Dissertation, Auburn University, 1996.

47. Bradley, A. T., <u>Piezoresistive Behavior of MOSFETs and MOS Circuits</u>, Ph.D. Dissertation, Auburn University, 1999.

48. Xu, J., <u>CMOS Piezoresistive Stress Sensors on (111) Silicon</u>, Ph.D. Dissertation, Auburn University, 2000.

49. Mian, A. K. M., Suhling, J. C., and Jaeger, R. C., "Sensitivity of Van der Pauw Sensors to Uniaxial Stress," *American Society of Mechanical Engineers*, ASME, EEP, Vol. 26(1), pp. 195-203, Jun 13-Jun 19 1999.

50. Mian, A. K. M., <u>Application of the Van der Pauw Structure as a Piezoresistive Stress Sensor</u>, Ph.D. Dissertation, Auburn University, 2000.

51. Beaty, R. E., Jaeger, R. C., Suhling, J. C., Johnson, R. W., Butler, R. D., "Piezoresistive Coefficient Variation in Silicon Stress Sensors Using a Four-Point Bending Test Fixture," *IEEE Transactions on Components, Hybrids, and Manufacturing Technology*, Vol. 15(5), pp. 904-914, 1992.

52. Jaeger, R. C., Suhling, J. C., Ramani, R., Anderson, A., "A (100) Silicon Stress Test Chip with Optimized Piezoresistive Sensor Rosettes," *Proceedings of the 44th Electronic Components and Technology Conference (ECTC)*, IEEE, pp. 741-749, 1994.

53. Van Gestel, R., <u>Reliability Related Research on Plastic IC-Packages: A Test Chip Approach</u>, Ph.D. Dissertation Delft Technical University, Delft University Press, 1994.

54. Cordes, R. A., <u>Wafer Level Calibration of Piezoresistive Stress Sensors</u>, M.S. Thesis, Auburn University, Auburn, Alabama, 1995.

55. Suhling, J. C., Jaeger, R. C., Kang, Y. L., Cordes, R. A., "A New Wafer-Level Calibration Procedure for Piezoresistive Stress Sensors," *Proceedings of the 1993 SEM Spring Conference on Experimental Mechanics*, pp. 977-987, Dearborn, MI, June 7-9, 1993.

56. Suhling, J. C., Cordes, R. A., Kang, Y. L., Jaeger, R. C., "Wafer-Level Calibration of Stress Sensing Test Chips," *Proceedings of the 44the Electronic Components and Technology Conference (ECTC)*, IEEE, pp. 1058-1070, 1994.

57. Cordes, R. A., Suhling, J. C., Kang, Y. L., Jaeger, R. C. "Application of a Wafer Level Calibration Technique for Stress Sensing Test Chips," *Applications of Experimental Mechanics to Electronic Packaging*, ASME International

Mechanical Engineering Congress and Expositions, EEP-Vol. 13, pp. 79-94, San Fransisco, CA, November 12-17, 1995.

58. Jaeger, R. C., Suhling, J. C., and Ramani, R., "Errors Associated with the Design and Calibration of Piezoresistive Stress Sensors in (100) Silicon," *Proceedings of the ASME/JSME Joint Conference on Electronic Packaging*, ASME, EEP-Vol. 1-1, pp. 447-456, Milpitas, CA, April 9-12, 1992.

59. Jaeger, R. C., Suhling, J. C., and Ramani, R., "Errors Associated with the Design, Calibration of Piezoresistive Stress Sensors in (100) Silicon," *IEEE Transactions on Components, Packaging, and Manufacturing Technology - Part B: Advanced Packaging*, Vol. 17(1), pp. 97-107, 1994.

60. Lo, T. C. P., Chan, P. C. H., and Tang, Z., "Design And Characterization of a Micro Strain Gauge," *Proceedings of the 1995 IEEE Region 10 International Conference on Microelectronics and VLSI, TENCON'95*, pp. 36-39, Hong Kong, 1995.

61. Lo, T. C. P., and Chan, P. C. H., "Design and Calibration of a 3-D Micro-Strain Gauge for In Situ on Chip Stress Measurements," *Proceedings of the 1996 IEEE International Conference on Semiconductor Electronics*, ICSE, pp 252-255, Penang, Malaysia, 1996.

62. Bossche, A., and Mollinger, J. R., "Calibration Procedure for Piezoresistance Coefficients of Polysilicon Sheets and Application to a Stress Test Chip," *Sensors & Actuators A-Physical*, Vol. 62(1-3), pp. 475-479, 1997.

63. Ducos, C. S., Christophe, E., Fremont, H., Kaoua, G., Pellet, C., and Danto, Y., "Evaluation of Stresses in Packaged ICs by In Situ Measurements with an Assembly Test Chip and Simulation," *Microelectronics and Reliability*, Vol. 37(10-11), pp. 1795-1798, 1997.

64. Nysaether, J. B., Larsen, A., Liverod, B., and Ohlckers, P., "Structures For Piezoresistive Measurement of Package Induced Stress in Transfer Molded Silicon Pressure Sensors," *Microelectronics & Reliability*, Vol. 38(6-8), pp. 1271-1276, 1998.

65. Palmer, D. W., Benson, D. A., Peterson, D. W., and Sweet, J. N., "IC Chip Stress During Plastic Package Molding," *Proceedings 48th Electronic Components and Technology Conference*, pp. 1326-1331, 1998.

66. Caruso, S., Frisina, F., Zafarana, R., and Raciti, A., "Induced Stresses on Silicon Die by the Molding Process: Experimental Investigation by Piezoresistive Elements in Case of a Power Device Package," *IAS Annual Meeting (IEEE Industry Applications Society)*, IEEE, pp. 2996-3002, 2000.

67. Kang, Y., Mian, A. K. M., Suhling, J. C., and Jaeger, R. C., "Hydrostatic Response of Piezoresistive Stress Sensors," *Application of Experimental Mechanics to Electronic Packaging - 1997*, ASME, EEP-Vol. 22, pp. 29-36, 1997.

68. Suhling, J. C., Jaeger, R. C., and Ramani, R., "Stress Measurement Using 0-90 Piezoresistive Rosettes on (111) Silicon," *Proceedings of the 1994 International Mechanical Engineering Congress and Exposition*. Chicago, IL, AMD-Vol. 195, pp. 65-73, 1994.

69. Kelly, G., Lyden, C., Mathuna, C. O., Campbell, J. S., "Investigation of Thermo-Mechanically Induced Stress in a PQFP 160 Using Finite Element Techniques," *Proceedings of 42th Electronic Components and Technology Conference*, IEEE, pp. 467-472, San Diego, CA, 1992

70. van Gestel, R., Schellekens, H., "3D Finite Element Simulation of the Delamination Behaviour of a PLCC Package in the Temperature Cycling Test," *Proceedings of the 31st Annual Reliability Physics Symposium*, pp. 108-121, Atlanta, GA, 1993

71. Sweetm J. N., Burchett, S. N., Peterson, D. W., Hsia, A. H. "Piezoresistive Measurement and FEM Analysis of Mechanical Stresses in 160L Plastic Quad Flat Packs," *Proceedings of INTERpack 1997*, pp. 1731-1740, Kohala, HI, June 15-19, 1997.

72. Mian, Ahsan, Piezoresistive Stress Sensors for Integrated Circuits, Ph.D. Dissertation, Auburn University, Auburn, Alabama, 2000.

73. Edwards, D. R., Heinen, G., Bednarz, G. A. and Schroen, W. H., "Test Structure Methodology of IC Package Material Characterization," *Proceedings of the 33rd Electronic Components Conference*, IEEE, pp. 386-393, 1983.

74. Miura, H., Nishimura, A., Kawai, S. And Murakami, G., "Structural Effect of IC Plastic Package on Residual Stress in Silicon Chips," *Proceedings of the 40th Electronic Components and Technology Conference*, IEEE, May 20-23, 1990, Las Vegas, NV, pp. 316-321, 1990.

75. Sweet, J. N., "Die Stress Measurement Using Piezoresistive Stress Sensors," *Thermal Stress and Strain in Microelectronics Packaging*, Edited by J. H. Lau, von Nostrand Rheinhold, pp. 221-271, 1993.

76. Suhling, J. C., Jaeger, R. C., Lin, S. T., Moral, R. J. and Zou, Y., "Measurement of the Complete Stress State in Plastic Encapsulated Packages," *Advances in Electronic Packaging 1997*, ASME EEP-Vol. 19-2, pp. 1741-1750, 1997.

77. Zou, Y., Suhling, J. C., Jaeger, R. C., and Ali, H., "Three-Dimensional Die Surface Stress Measurements in Delaminated and Non-Delaminated Plastic Packaging," *Proceedings of the 48th Electronic Components and Technology Conference (ECTC)*, Seattle, WA, May 25-28, pp. 1223-1234, 1998.

78. van der Pauw, L. J., "A Method of Measuring Specific Resistivity and Hall Effect of Discs of Arbitrary Shapes," Philips Research Reports, Vol. 13, pp. 1-9, 1958.

79. van der Pauw, L. J., "Determination of Resistivity Tensor and Hall Tensor of Anisotropic Shape," Philips Research Reports, Vol. 16, pp. 187-195, 1961.

80. Hornstra, J., van der Pauw, L. J., "Measurements of the Resistivity Constants of Anisotropic Conductors By Means of Plane-Parallel Discs of Arbitrary Shape," *Journal of Electronics and Control*, Vol. 7, pp. 169-171, 1959.

81. Price, W. L., "Extension of van der Pauw's Theorem for Measuring Specific Resistivity in Discs of Arbitrary Shape to Anisotropic Media," *Journal of Physics* D: Applied Physics, Vol. 5, pp. 1127-1132, 1971.

82. Price, W. L., "Electric Potential and Current Distribution in a Rectangular Sample of Anisotropic Material with Application to Measurement of the Principal Resistivities by an Extension of van der Pauw's Method," *Solid State Electronics*, Vol. 16(7), pp. 753-762, 1973.

83. Kinsler, M., Humurcik, L. V., Patton, J., "Van der Pauw Measurement of Metal Fiber Orientation in a Plastic-Metal Composite," *Journal of Materials Science*, Vol. 23, pp. 1425-1430, 1988.

84. Futamata, M., " A Computer-Controlled Measurement for Electrical Conductivity Using the van der Pauw Method at Various Temperatures," *Measurement Science and Technology*, Vol. 3, pp. 919-921, 1992.

85. Ramadan, A. A., Gould, R. D., Ashour, A., "On the van der Pauw Method of Resistivity Measurements," *Thin Solid Films*, Vol. 239, pp. 272-275, 1994.

86. Bartels, A., Peiner, E., Schlachetzki, A., "A Procedure for Temperature-Dependent, Differential van der Pauw Measurements," *Review of scientific Instruments*, Vol. 66(8), pp. 4271-4276, 1995.

87. Van Gelder, A. P., "A New Method for Measuring the Conductivity of Arbitrary Shaped Two-Dimensional Samples," *Physica* B. Vol. 204, pp. 149-152, 1995.

88. McSkimin, H. J., "Ultrasonic Measurement Techniques Applicable to Small Solid Specimens," *Journal of the Acoustical Society of America*, Vol. 22(4), pp. 413-418, 1950.

89. McSkimin, H. J., Bond, W. L., Buehler, E., Teal, G. K., "Measurement of the Elastic Constant of Silicon Single Crystals and Their Thermal Coefficients," *Physical Review*, Vol. 83, pp. 1080(L), 1951.

90. Wortman, J. J., Evans, R. A., "Young's Modulus, Shear Modulus, and Poisson's Ratio in Silicon and Germanium," *Journal of Applied Physics*, vol. 36(1), pp. 153-156, 1964.

91. Gere, J. M., Timoshenko, S. P., Thornes, S., Mechanics of Materials, Fourth SI edition.

92. J. C. Suhling and R. C. Jaeger, "Silicon Piezoresistive Stress Sensors and Their Application in Electronic Packaging," *IEEE Sensors Journal*, vol. 1, no. 1. , pp. 14-30, June 2001.

93. Perelomova, N. V., Tagieva, M. M., Problems in Crystal Physics with Solutions, Mir Publishers, 1983

94. Onsager, L., "Reciprocal Relations in Irreversible Process – I.," *Physical Review*, Vol. 37, pp. 405-426, 1931.

95. Onsager, L., "Reciprocal Relations in Irreversible Process – II.," *Physical Review*, Vol. 38, pp. 2265-2279, 1931.

96. Herring, C., "Transport Properties of a Many-Valley Semiconductor," *Bell System Tech. J.* 34, pp. 237-290, 1955.

97. http://isola-usa.com/images/uploaded/MechanicalProperties.pdf

98. Tufte, O. N., Chapman, P. W., Long, Donald., "Silicon Diffused-Element Piezoresistive Diaphragms," *Journal of Applied Physics*, Vol.33, Number 11, pp. 3322-3327, April, 1962.

99. Rahim, Md. S., Measurement of Stress in Electronic Packages Using Piezoresistive Sensors, Ph.D. Dissertation, Auburn University, 2005.

100. Pikus, G.. E., Bir, G. L., Symmetry and Strain-Induced Effects in Semi-conductors, New York: Wiley, 1974.

101. Sugiyama, S, Ph.D. Dissertation, Tokyo Inst. Technol., 1994.

102. Jaeger, R. C., Suhling, J. C., "Innovative Sensors for Stress Measurements in Packaged Integrated Circuits," 99-NJ-459-Third Year Report, SRC Packaging Multiple Contract Review, September 28, 1999.

103. Jaeger, R. C., "Introduction to Microelectronic Fabrication," *Modular Series on Solid State Devices*, vol. 5, pp. 60, Addison-Wesley Publishing Company, Inc, 1993.

104. Jaeger, R. C., Suhling, J. C., "Innovative Sensors for Stress Measurements in Packaged Integrated Circuits," 99-NJ-459-Third Year Report, SRC Packaging Multiple Contract Review, September 28, 1999.

105. Chen, Y., <u>A Chip-on-Beam Technique for Calibration of Piezoresistive Stress Sensors</u>, M.S. Thesis, Auburn University, Auburn, Alabama, 2003.

APPENDICES

APPENDIX A

TYPICAL RESULTS OF S_0 and S_{90} FOR THE (111) SILICON AT DIFFERENT

TEMPERATURES

Calibration results of S_0 and S_{90} for the (111) silicon for each temperature are displayed in this section. As mentioned in Chapter 4, the following notation is adopted:

$$S_\phi \equiv \frac{d}{dF}\left(\frac{\Delta R_\phi}{R_\phi}\right) \qquad \text{Eq. (A.1)}$$

Through Figs. A.1 and A.16, typical results of S_0 and S_{90} for the (111) silicon are shown for each temperature of calibration.
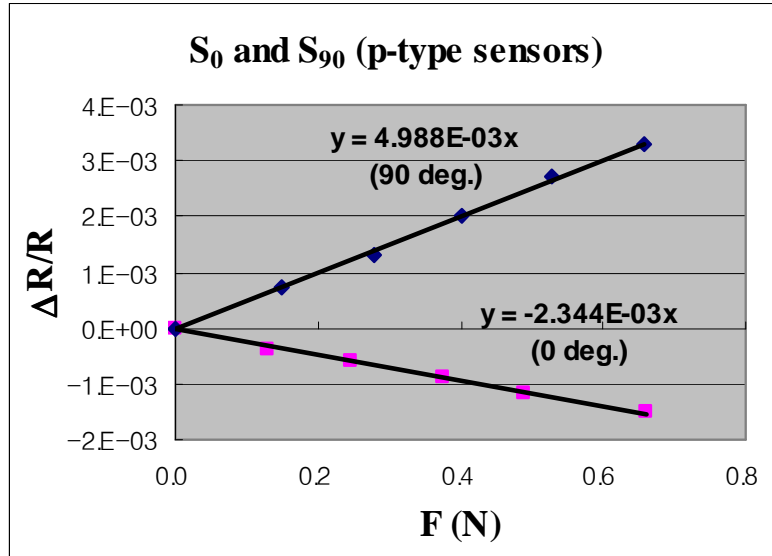
Fig. A.1 - S_0 and S_{90} for the (111) silicon at -133°C (p-type sensors)
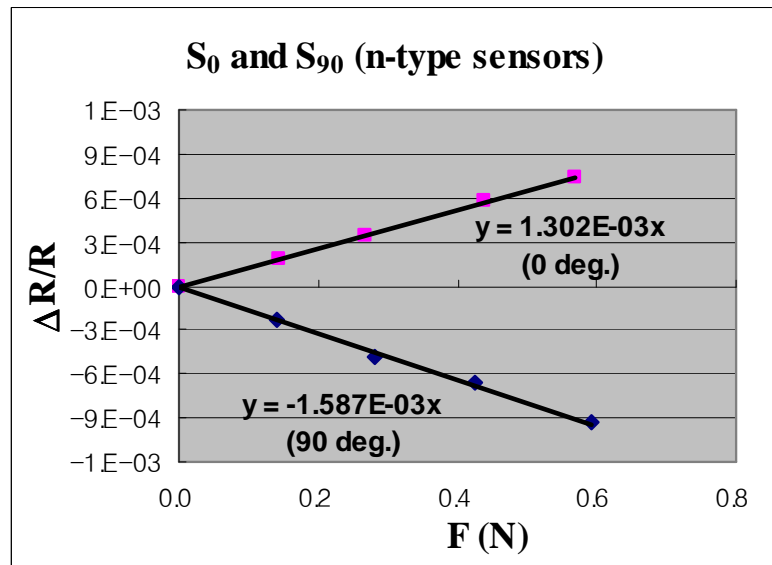
Fig. A.2 - S_0 and S_{90} for the (111) silicon at -133°C (n-type sensors)
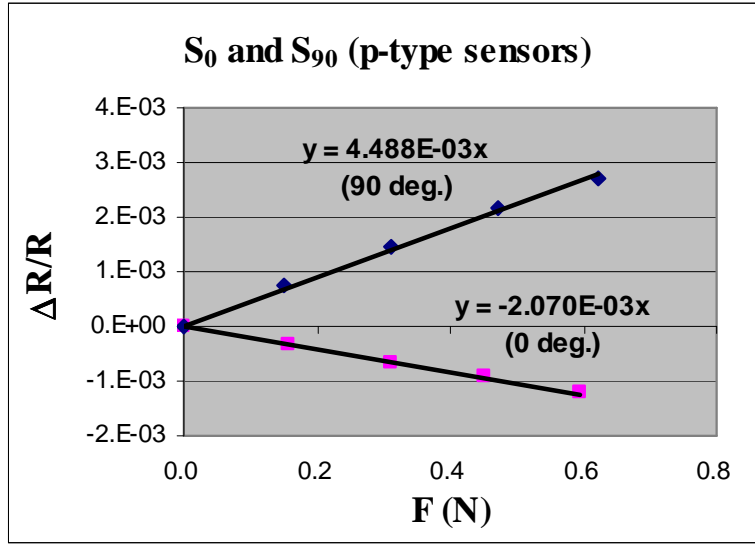
Fig. A.3 - S_0 and S_{90} for the (111) silicon at $-93{}^{\circ}$C (p-type sensors)
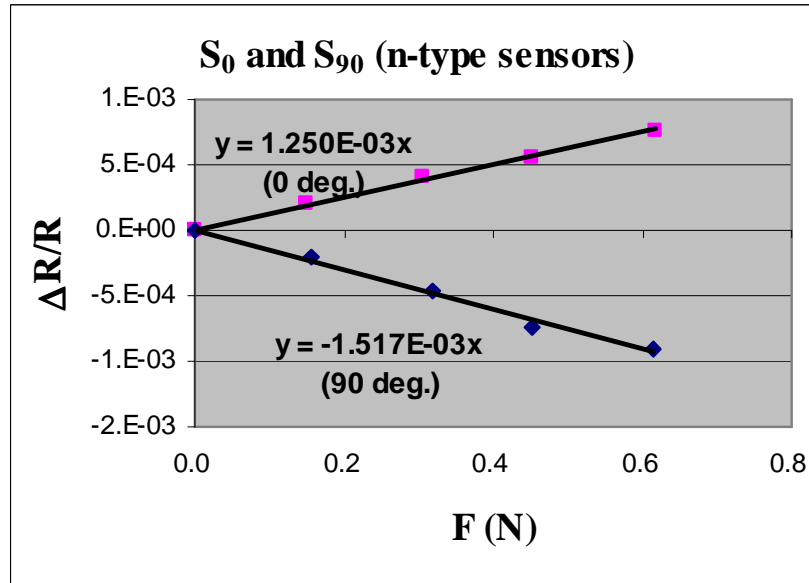
Fig. A.4 - S_0 and S_{90} for the (111) silicon at $-93{}^{\circ}$C (n-type sensors)
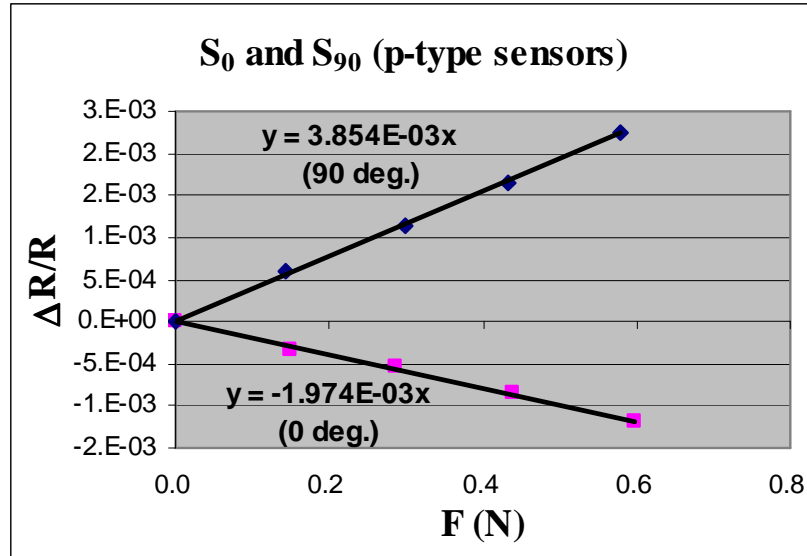
Fig. A.5 - S_0 and S_{90} for the (111) silicon at -48°C (p-type sensors)
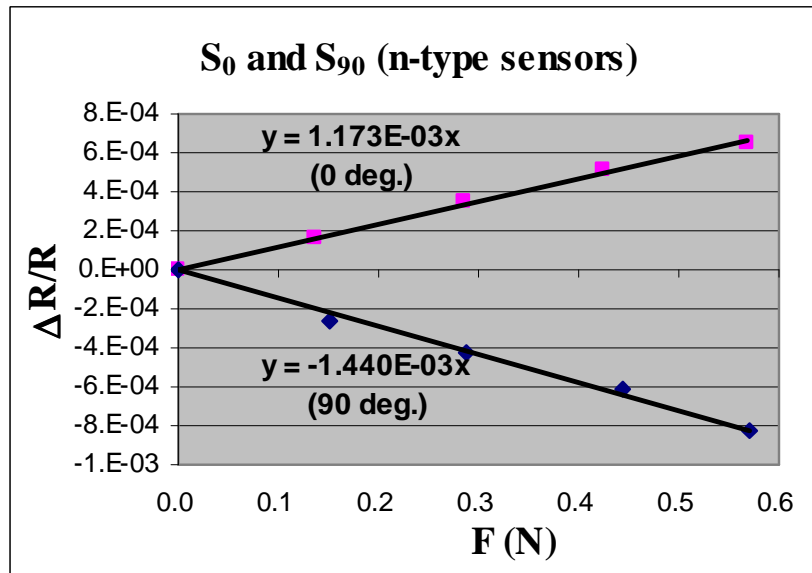
Fig. A.6 - S_0 and S_{90} for the (111) silicon at -48°C (n-type sensors)
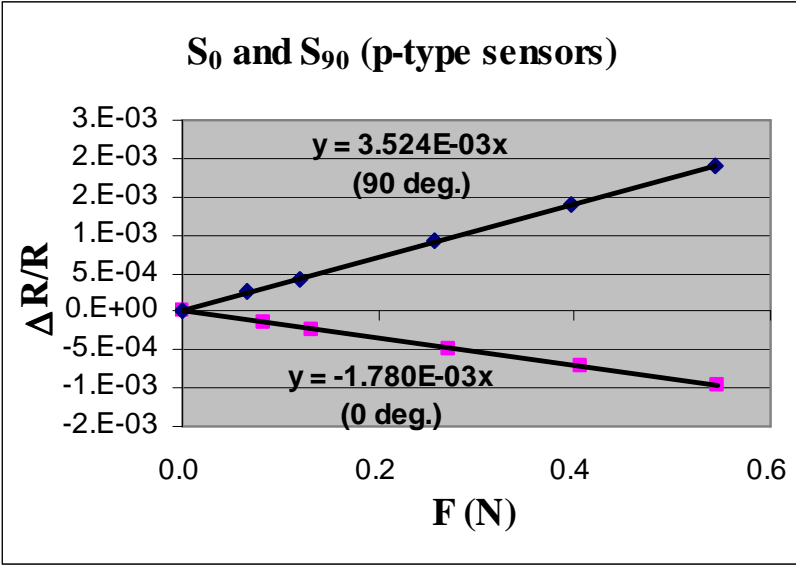
Fig. A.7 - S_0 and S_{90} for the (111) silicon at 0^oC (p-type sensors)
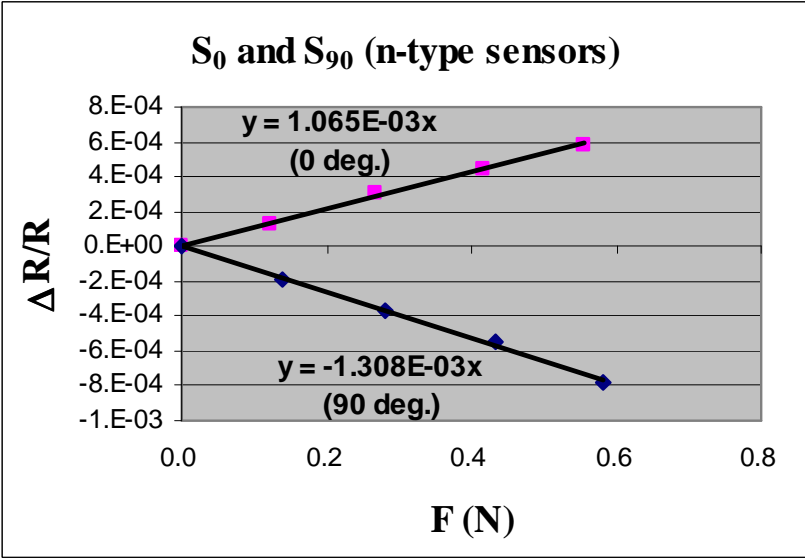
Fig. A.8 - S_0 and S_{90} for the (111) silicon at 0^oC (n-type sensors)
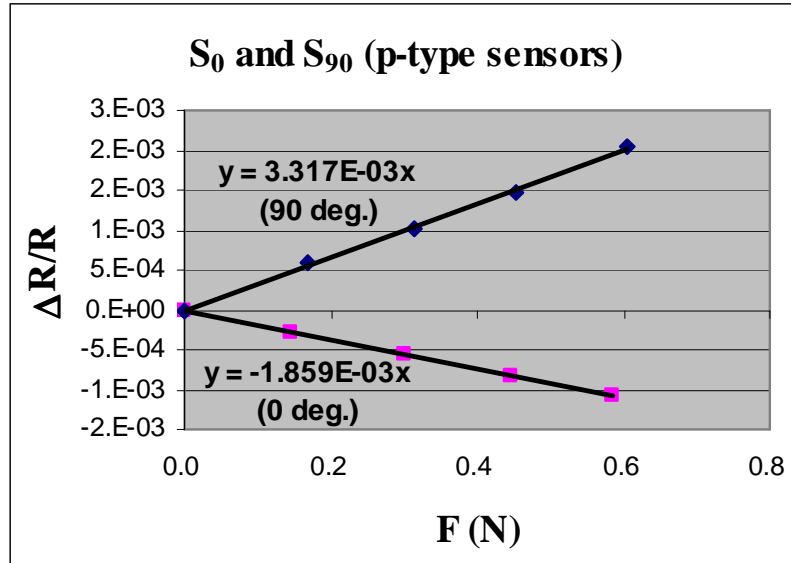
Fig. A.9 - S_0 and S_{90} for the (111) silicon at 25°C (p-type sensors)
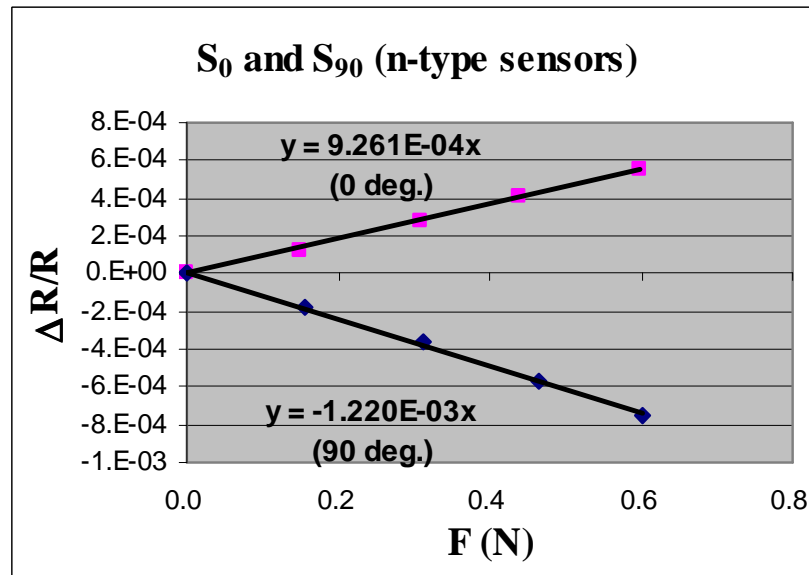
Fig. A.10 - S_0 and S_{90} for the (111) silicon at 25°C (n-type sensors)
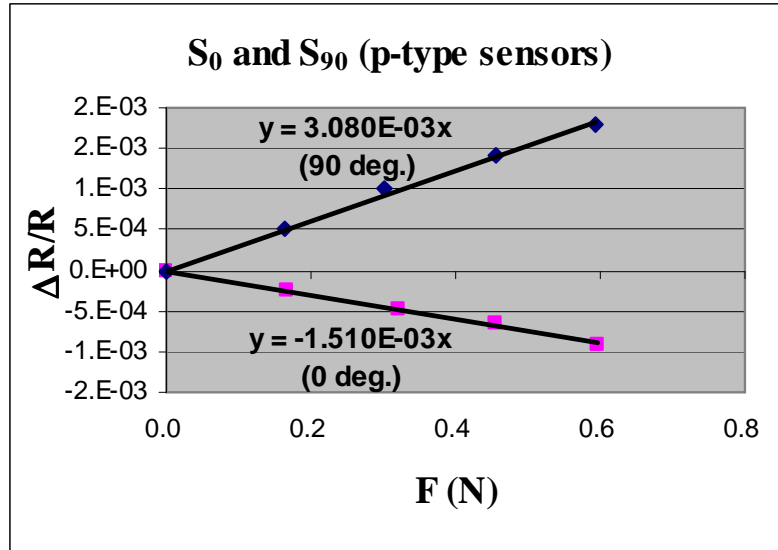
Fig. A.11 - S_0 and S_{90} for the (111) silicon at 50^oC (p-type sensors)
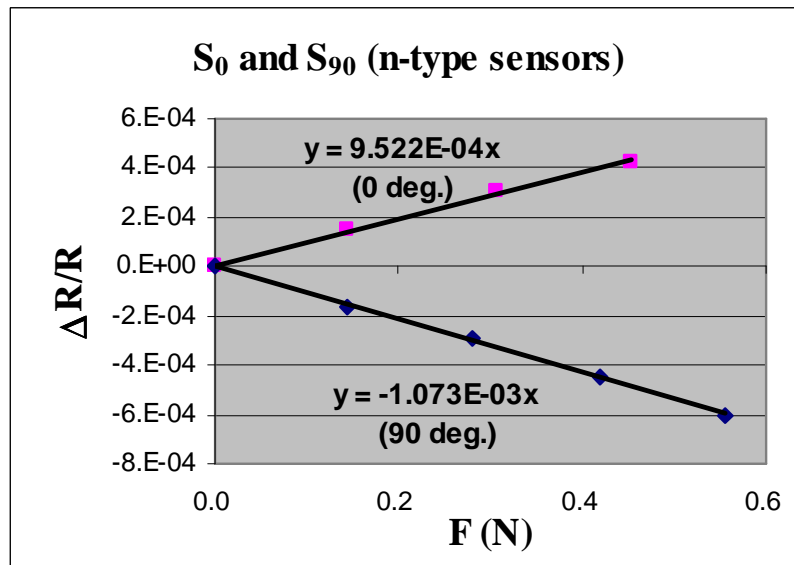
Fig. A.12 - S_0 and S_{90} for the (111) silicon at 50^oC (n-type sensors)
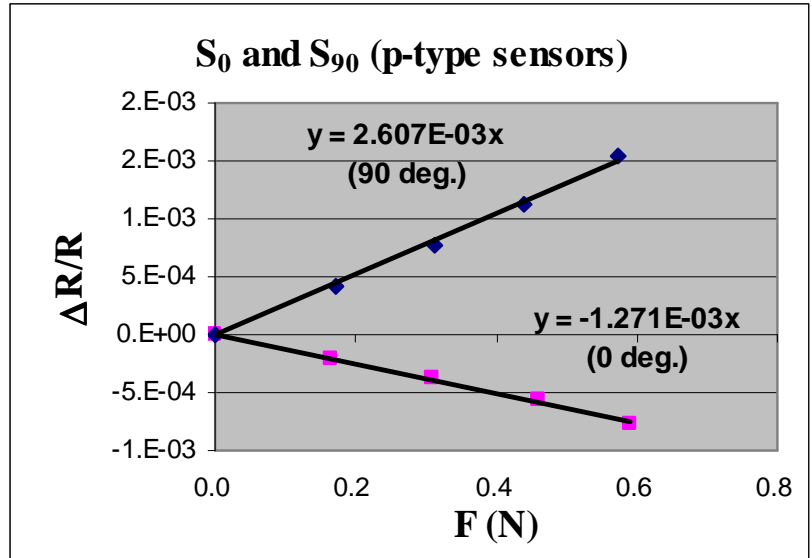
Fig. A.13 - S_0 and S_{90} for the (111) silicon at 75°C (p-type sensors)
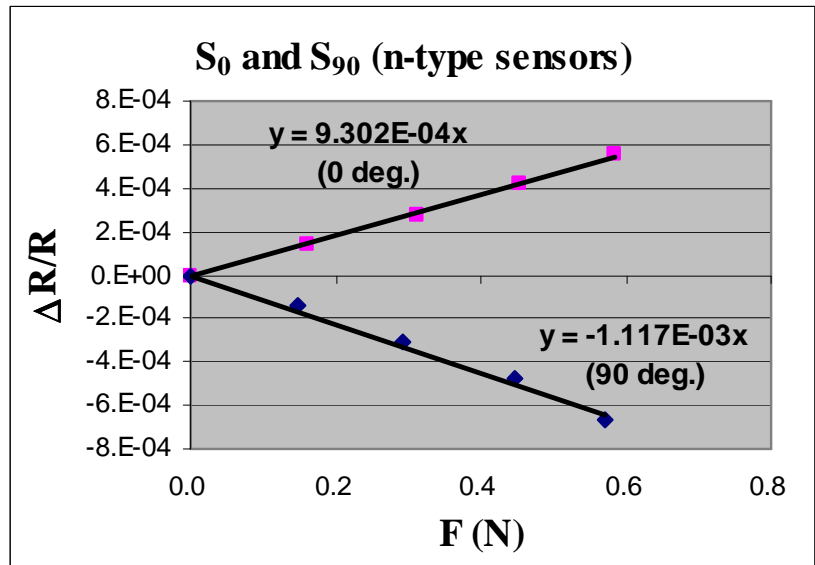
Fig. A.14 - S_0 and S_{90} for the (111) silicon at 75°C (n-type sensors)
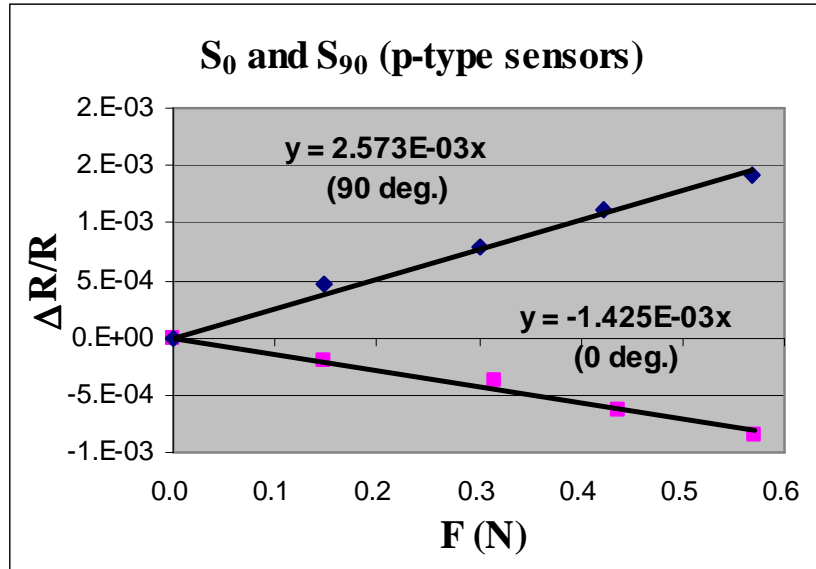
Fig. A.15 - S_0 and S_{90} for the (111) silicon at 100°C (p-type sensors)
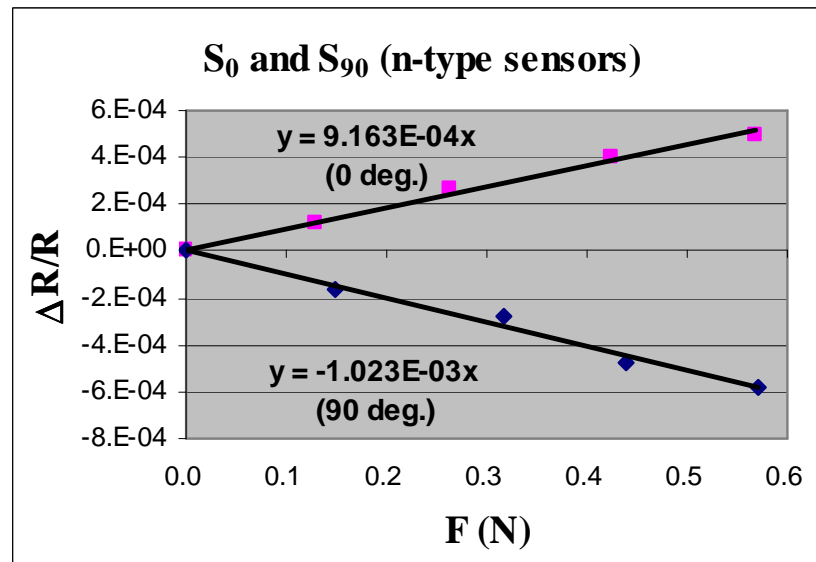
Fig. A.16 - S_0 and S_{90} for the (111) silicon at 100°C (n-type sensors)

DETERMINATION OF PIEZORESISTIVE COEFFICIENTS

A general plot of resistance with varying temperatures and applied force is shown in Fig. B.1, whose graphs may vary with the doping concentrations and the crystallographic orientations of sensors.
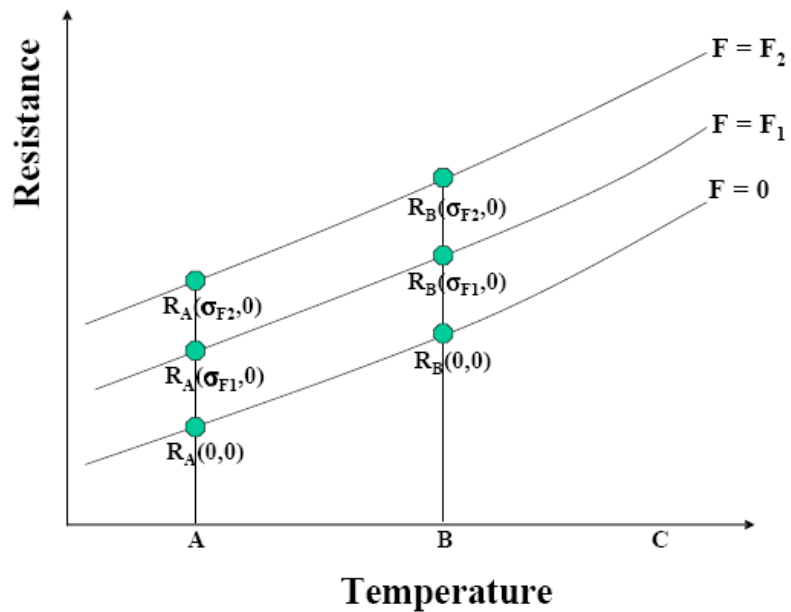
Fig. B.1 - Resistance change with temperature and stress

In Fig. B.1, σ_{F1} and σ_{F2} at a given temperature denote the corresponding stresses for $F = F_1$ and $F = F_2$, respectively. Also, it may be noted that R_T is defined as the resistance value at temperature T. Then we derive the relationship of piezoresistive coefficients between different temperatures as follows:

- The cases for $\Delta T = 0$

At reference temperature A, the general expression for resistance discussed in Chapter 4

$R(\sigma, \Delta T) = R(0,0)\{1 + f(\Delta T) + [\Pi + \beta(\Delta T)]\sigma\}$ can be expressed for two different stress

states (σ_{F1} and σ_{F2}) with $\Delta T = 0$:

$$\frac{R_A(\sigma_{F1},0) - R_A(0,0)}{R_A(0,0)} = \pi_A \, \sigma_{F1} \qquad \text{Eq. (B.1)}$$

$$\frac{R_A(\sigma_{F2},0) - R_A(0,0)}{R_A(0,0)} = \pi_A \, \sigma_{F2} \qquad \text{Eq. (B.2)}$$

where π_A is defined as π at temperature A. Subtraction of Eq. (B.1) from Eq. (B.2)

leads to

$$\frac{R_A(\sigma_{F2},0) - R_A(\sigma_{F1},0)}{R_A} = \pi_A (\sigma_{F2} - \sigma_{F1}) \qquad \text{Eq. (B.3)}$$

Hence, at reference temperature A, the slope of $\dfrac{\Delta R}{R}$ versus stress $(\sigma_{F2} - \sigma_{F1})$ is π_A as

shown in Fig. B.2
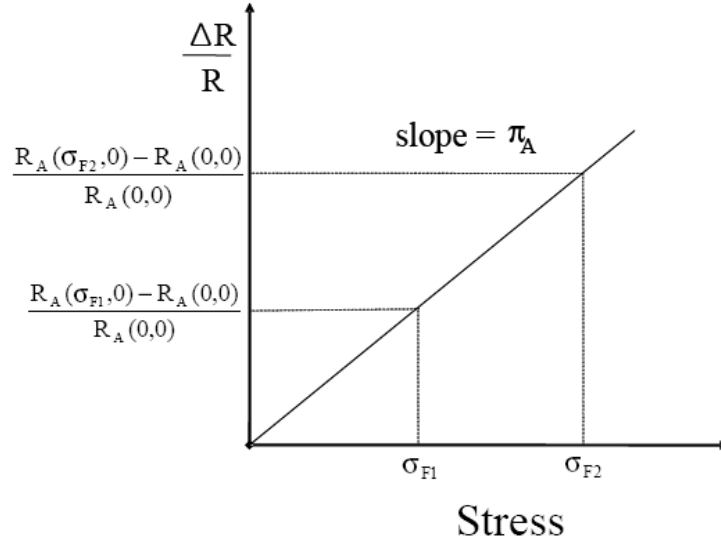
Fig. B.2 - $\dfrac{\Delta R}{R}$ versus stress at reference temperature A

Similarly, at reference temperature B,

$$\frac{R_B(\sigma_{F2},0) - R_B(\sigma_{F1},0)}{R_B(0,0)} = \pi_B(\sigma_{F2} - \sigma_{F1}) \qquad \text{Eq. (B.4)}$$

For $\Delta T = 0$, Π can be calculated directly.

- The cases for $\Delta T \neq 0$

By using $R(\sigma, \Delta T) = R(0,0)\{1 + f(\Delta T) + [\Pi + \beta(\Delta T)]\sigma\}$, R_B at reference temperature

A can be expressed for two different stress states (σ_{F1} and σ_{F2}) as the following:

$$\frac{R_B(\sigma_{F1},0) - R_A(0,0)}{R_A(0,0)} = f_A(B-A) + [\pi_A + \beta_A(B-A)]\sigma_{F1} \qquad \text{Eq. (B.5)}$$

$$\frac{R_B(\sigma_{F2},0) - R_A(0,0)}{R_A(0,0)} = f_A(B-A) + [\pi_A + \beta_A(B-A)]\sigma_{F2} \qquad \text{Eq. (B.6)}$$

Subtraction of Eq. (B.5) from Eq. (B.6) yields

244

$$\frac{R_B(\sigma_{F2},0) - R_B(\sigma_{F1},0)}{R_A(0,0)} = [\pi_A + \beta_A(B-A)](\sigma_{F2} - \sigma_{F1})$$

Eq. (B.7)
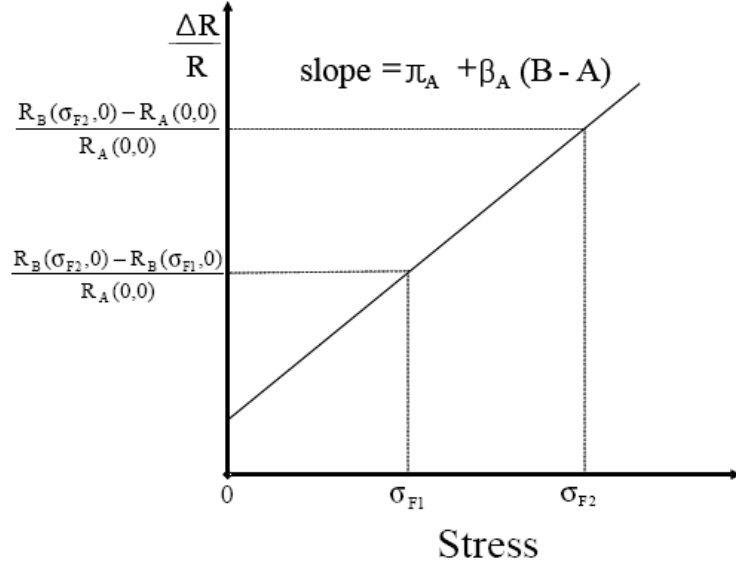
Fig. B.3 - $\dfrac{\Delta R}{R}$ versus stress at reference temperature A

For $\Delta T \neq 0$, direct calculation of Π is not possible. However, combining Eqs. (B.4) and (B.7), the relationship of Π can be determined between different temperatures. Hence it can be a proper method for relating coefficients at different temperatures. Equation (B.4) and Eq. (B.7) yielded the following result:

$$R_B(\sigma_{F2},0) - R_B(\sigma_{F1},0) = R_B(0,0)\pi_B(\sigma_{F2} - \sigma_{F1}) = R_A(0,0)[\pi_A + \beta_A(B-A)](\sigma_{F2} - \sigma_{F1})$$

Hence,

$$R_B(0,0)\pi_B = R_A(0,0)[\pi_A + \beta_A(B-A)]$$

APPENDIX C

TYPICAL RESULTS FOR THE PRESSURE COEFFICIENT OF (111) SILICON AT DIFFERENT TEMPERATURES

The pressure coefficients for the (111) silicon at different temperatures are shown in this section. As discussed in Chapter 5, subtraction of the effect of temperature from the resistance change determines the pressure coefficient. Through Figs. C.1 and C.6, adjusted hydrostatic calibrations for the (111) silicon are shown for each temperature of calibration. The slope of the curve corresponds to the piezoresistive coefficient π_p as presented in Chapter 5:

$$\frac{\Delta R}{R} - f(\Delta T) = -(\pi_{11} + 2\pi_{12})p = -(B_1 + B_2 + B_3)p = \pi_p p \qquad \text{Eq. (C.1)}$$
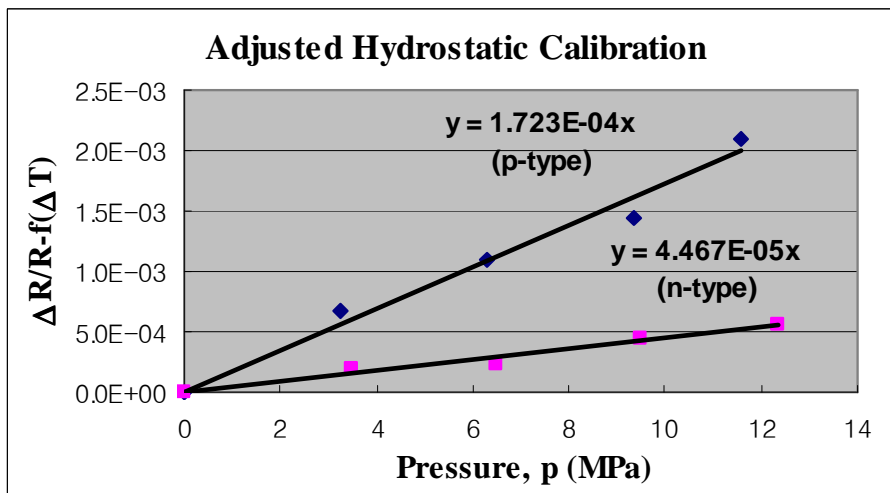
Fig. C.1 - Adjusted hydrostatic calibration for the (111) silicon at -25°C
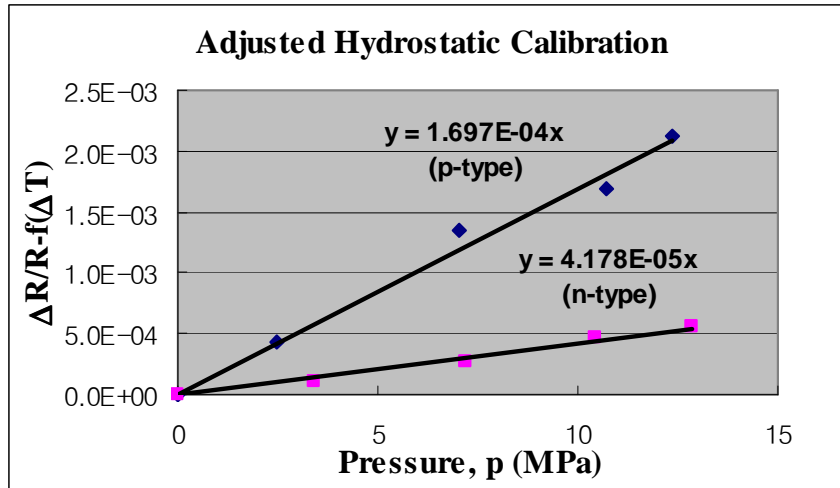
Fig. C.2 - Adjusted hydrostatic calibration for the (111) silicon at 0°C
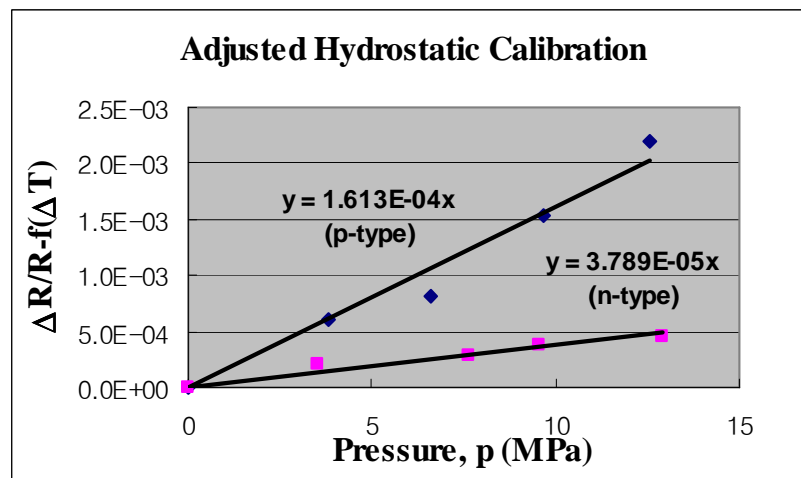
Fig. C.3 - Adjusted hydrostatic calibration for the (111) silicon at 25°C
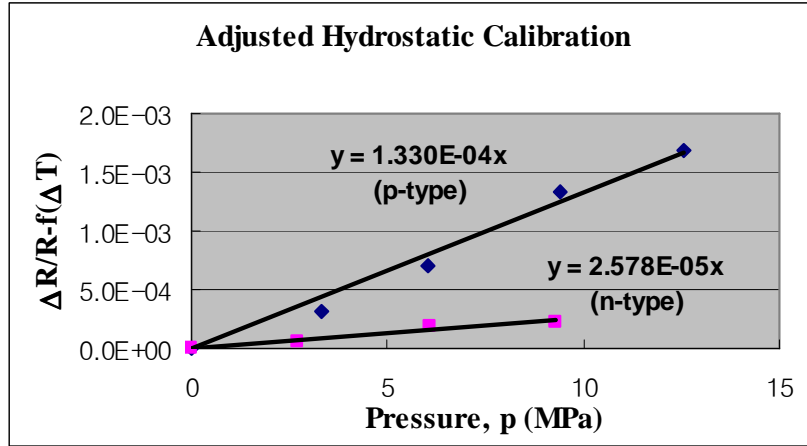
Fig. C.4 - Adjusted hydrostatic calibration for the (111) silicon at 50°C
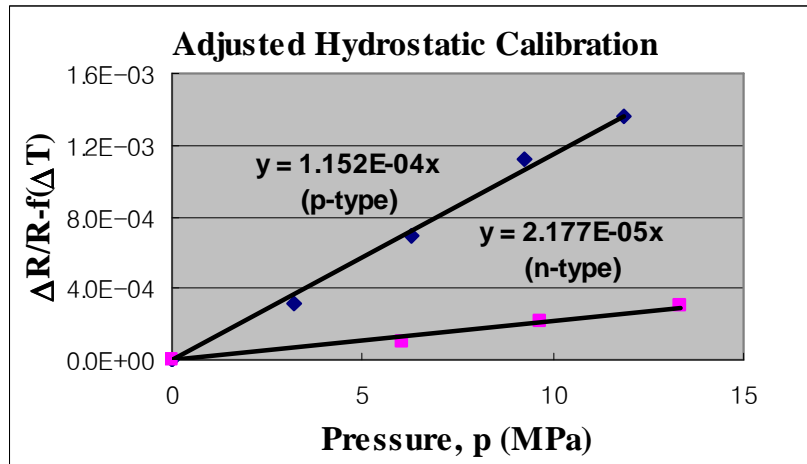
Fig. C.5 - Adjusted hydrostatic calibration for the (111) silicon at 75°C
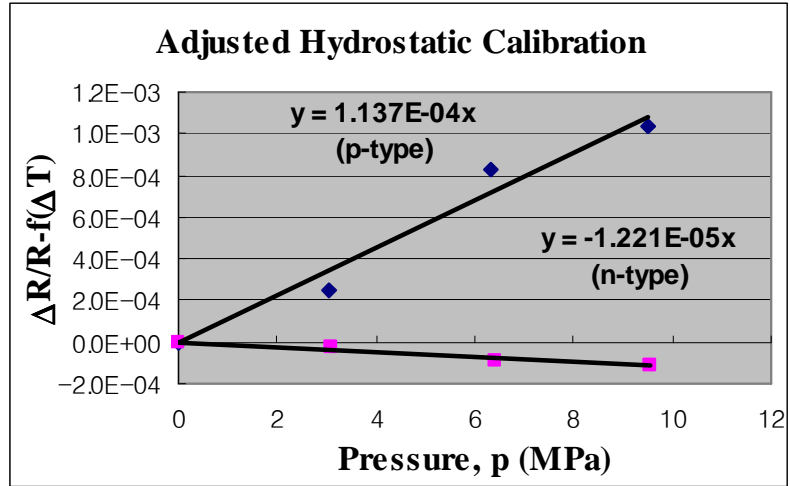
Fig. C.6 - Adjusted hydrostatic calibration for the (111) silicon at 100°C

APPENDIX D

BEAM ROTATIONAL ERROR

In Chapter 8, errors in misalignment with the given crystallographic axes are described and analyzed. Bittle, et al. [51] calculated percent error in the axial normal stress at the midpoint between the supports versus the angle of misalignment of the wafer strip in a four-point bending test fixture. In order to calculate error in the axial normal stress at the midpoint between the supports, a finite element numerical simulation was performed [51]. In addition, Bittle, et al. [51] showed that the error will be less than approximately 1% if the wafer strip can be aligned to within 5°. However, in our work, the errors in piezoresistive coefficients induced by the rotational misalignment of the strip on the supports by an angle θ with respect to the ideal longitudinal axis of the strip are explained:

- With respect to the unprimed coordinate system
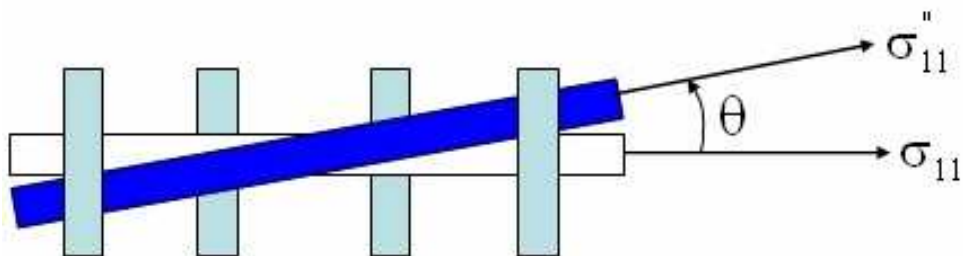
Fig. D.1 - Misalignment of the wafer strip in a four-point bending test fixture

For θ, the angle of counter-clockwise rotation of the $x^{''}$ - $y^{''}$ coordinate system relative to the x - y coordinate system, the double-primed stress componenets are given as [12-13]

$$\begin{bmatrix} \sigma_{11}^{''} \\ \sigma_{22}^{''} \\ \sigma_{12}^{''} \end{bmatrix} = \begin{bmatrix} \cos^2\theta & \sin^2\theta & 2\sin\theta\cos\theta \\ \sin^2\theta & \cos^2\theta & -2\sin\theta\cos\theta \\ -\sin\theta\cos\theta & \sin\theta\cos\theta & \cos^2\theta - \sin^2\theta \end{bmatrix} \begin{bmatrix} \sigma_{11} \\ \sigma_{22} \\ \sigma_{12} \end{bmatrix} \qquad \text{Eq. (D.1)}$$

Hence

$$\sigma_{11} = \cos^2\theta\,\sigma_{11}^{''} + \sin^2\theta\,\sigma_{22}^{''} - \sin2\theta\,\sigma_{12}^{''}$$

$$\sigma_{22} = \sin^2\theta\,\sigma_{11}^{''} + \cos^2\theta\,\sigma_{22}^{''} + \sin2\theta\,\sigma_{12}^{''} \qquad \text{Eq. (D.2)}$$

$$\sigma_{12} = \frac{1}{2}\sin2\theta\,\sigma_{11}^{''} - \frac{1}{2}\sin2\theta\,\sigma_{22}^{''} + \cos2\theta\,\sigma_{12}^{''}$$

Addition of the first two equations yields the finding below:

$$\sigma_{11} + \sigma_{12} = \sigma_{11}^{''} + \sigma_{22}^{''} \qquad \text{Eq. (D.3)}$$

The stress components are now measured in the new double-primed coordinate system instead of the unprimed coordinate system. The general resistance equation is given by

$$\begin{aligned} \frac{\Delta R}{R} &= [\pi_{11}\sigma_{11} + \pi_{12}\sigma_{22}]\cos^2\phi \\ &+ [\pi_{11}\sigma_{22} + \pi_{12}\sigma_{11}]\sin^2\phi \\ &+ 2\pi_{44}\,\sigma_{12}\,\cos\phi\sin\phi \\ &+ [\alpha_1\Delta T + \alpha_2\Delta T^2 + ...] \end{aligned} \qquad \text{Eq. (D.4)}$$

in which only in-plane stresses are assumed. If we consider θ with neglect of temperature terms, $\Delta R/R$ induced by θ relative to the actual longitudinal axis of strip for $\phi = 0$, $\phi = 90°$, and $\phi = \pm 45°$ is presented below:

$$\frac{\Delta R_0}{R_0} = \pi_{11}\sigma_{11} + \pi_{12}\sigma_{22}$$

$$= \pi_{11}(\cos^2\theta\,\sigma_{11}'' + \sin^2\theta\,\sigma_{22}'' - \sin2\theta\,\sigma_{12}'') + \pi_{12}(\sin^2\theta\,\sigma_{11}'' + \cos^2\theta\,\sigma_{22}'' + \sin2\theta\,\sigma_{12}'')$$

$$= (\pi_{11}\cos^2\theta + \pi_{12}\sin^2\theta)\sigma_{11}'' + (\pi_{11}\sin^2\theta + \pi_{12}\cos^2\theta)\sigma_{22}'' + (\pi_{12} - \pi_{11})\sin2\theta\,\sigma_{12}''$$

Eq. (D.5)

$$\frac{\Delta R_{90}}{R_{90}} = \pi_{12}\sigma_{11} + \pi_{11}\sigma_{22}$$

$$= \pi_{12}(\cos^2\theta\,\sigma_{11}'' + \sin^2\theta\,\sigma_{22}'' - \sin2\theta\,\sigma_{12}'') + \pi_{11}(\sin^2\theta\,\sigma_{11}'' + \cos^2\theta\,\sigma_{22}'' + \sin2\theta\,\sigma_{12}'')$$

$$= (\pi_{12}\cos^2\theta + \pi_{11}\sin^2\theta)\sigma_{11}'' + (\pi_{12}\sin^2\theta + \pi_{11}\cos^2\theta)\sigma_{22}'' + (\pi_{11} - \pi_{12})\sin2\theta\,\sigma_{12}''$$

Eq. (D.6)

$$\frac{\Delta R_{45}}{R_{45}} = (\frac{\pi_{11} + \pi_{12}}{2})(\sigma_{11} + \sigma_{22}) + \pi_{44}\sigma_{12}$$

$$= (\frac{\pi_{11} + \pi_{12}}{2})(\sigma_{11}'' + \sigma_{22}'') + \pi_{44}(\frac{1}{2}\sin2\theta\,\sigma_{11}'' - \frac{1}{2}\sin2\theta\,\sigma_{22}'' + \cos2\theta\,\sigma_{12}'')$$

$$= (\frac{\pi_{11} + \pi_{12}}{2} + \frac{\pi_{44}}{2}\sin2\theta)\sigma_{11}'' + (\frac{\pi_{11} + \pi_{12}}{2} - \frac{\pi_{44}}{2}\sin2\theta)\sigma_{22}'' + \pi_{44}\cos2\theta\,\sigma_{12}''$$

Eq. (D.7)

$$\frac{\Delta R_{-45}}{R_{-45}} = (\frac{\pi_{11} + \pi_{12}}{2})(\sigma_{11} + \sigma_{22}) - \pi_{44}\sigma_{12}$$

$$= (\frac{\pi_{11} + \pi_{12}}{2})(\sigma_{11}'' + \sigma_{22}'') - \pi_{44}(\frac{1}{2}\sin2\theta\,\sigma_{11}'' - \frac{1}{2}\sin2\theta\,\sigma_{22}'' + \cos2\theta\,\sigma_{12}'')$$

$$= (\frac{\pi_{11} + \pi_{12}}{2} - \frac{\pi_{44}}{2}\sin2\theta)\sigma_{11}'' + (\frac{\pi_{11} + \pi_{12}}{2} + \frac{\pi_{44}}{2}\sin2\theta)\sigma_{22}'' - \pi_{44}\cos2\theta\,\sigma_{12}''$$

Eq. (D.8)

Through the use of the equations,

$$\pi_{11} = \frac{\sigma_{11F}S_0 - \sigma_{22F}S_{90}}{(\sigma_{11F})^2 - (\sigma_{22F})^2}$$

$$= \frac{(\cos^2\theta\, \sigma_{11F}'' + \sin^2\theta\, \sigma_{22F}'' - \sin 2\theta\, \sigma_{12F}'')S_0 - (\sin^2\theta\, \sigma_{11F}'' + \cos^2\theta\, \sigma_{22F}'' + \sin 2\theta\, \sigma_{12F}'')S_{90}}{(\sigma_{11F}'' + \sigma_{22F}'')[\cos 2\theta(\sigma_{11F}'' - \sigma_{22F}'') - 2\sin 2\theta\, \sigma_{12F}'']}$$

<div align="right">Eq. (D.9)</div>

$$\pi_{12} = \frac{\sigma_{11F}S_{90} - \sigma_{22F}S_0}{(\sigma_{11F})^2 - (\sigma_{22F})^2}$$

$$= \frac{(\cos^2\theta\, \sigma_{11F}'' + \sin^2\theta\, \sigma_{22F}'' - \sin 2\theta\, \sigma_{12F}'')S_{90} - (\sin^2\theta\, \sigma_{11F}'' + \cos^2\theta\, \sigma_{22F}'' + \sin 2\theta\, \sigma_{12F}'')S_0}{(\sigma_{11F}'' + \sigma_{22F}'')[\cos 2\theta(\sigma_{11F}'' - \sigma_{22F}'') - 2\sin 2\theta\, \sigma_{12F}'']}$$

<div align="right">Eq. (D.10)</div>

$$\pi_S = \frac{S_0 + S_{90}}{\sigma_{11F} + \sigma_{22F}} = \frac{S_{45} + S_{-45}}{\sigma_{11F} + \sigma_{22F}} = \frac{S_0 + S_{90}}{\sigma_{11F}'' + \sigma_{22F}''} = \frac{S_{45} + S_{-45}}{\sigma_{11F}'' + \sigma_{22F}''} \qquad \text{Eq. (D.11)}$$

Note that Eq. (D.3) is used in the calculation of π_S in Eq. (D.11)

- With respect to the primed coordinate system
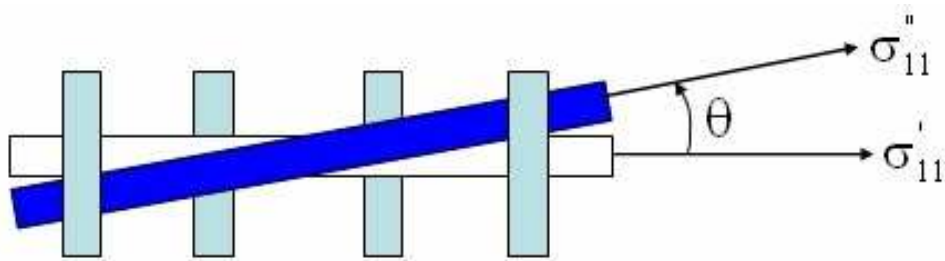
Fig. D.2 - Misalignment of the wafer strip in a four-point bending test fixture

By [12-13],

$$
\begin{bmatrix} \sigma_{11}^{''} \\ \sigma_{22}^{''} \\ \sigma_{12}^{''} \end{bmatrix} = \begin{bmatrix} \cos^2\theta & \sin^2\theta & 2\sin\theta\cos\theta \\ \sin^2\theta & \cos^2\theta & -2\sin\theta\cos\theta \\ -\sin\theta\cos\theta & \sin\theta\cos\theta & \cos^2\theta - \sin^2\theta \end{bmatrix} \begin{bmatrix} \sigma_{11}^{'} \\ \sigma_{22}^{'} \\ \sigma_{12}^{'} \end{bmatrix} \qquad \text{Eq. (D.12)}
$$

Hence

$$
\sigma_{11}^{'} = \cos^2\theta\,\sigma_{11}^{''} + \sin^2\theta\,\sigma_{22}^{''} - \sin2\theta\,\sigma_{12}^{''}
$$

$$
\sigma_{22}^{'} = \sin^2\theta\,\sigma_{11}^{''} + \cos^2\theta\,\sigma_{22}^{''} + \sin2\theta\,\sigma_{12}^{''} \qquad \text{Eq. (D.13)}
$$

$$
\sigma_{12}^{'} = \frac{1}{2}\sin2\theta\,\sigma_{11}^{''} - \frac{1}{2}\sin2\theta\,\sigma_{22}^{''} + \cos2\theta\,\sigma_{12}^{''}
$$

Addition of the first two equations yields the finding below:

$$
\sigma_{11}^{'} + \sigma_{22}^{'} = \sigma_{11}^{''} + \sigma_{22}^{''} \qquad \text{Eq. (D.14)}
$$

In Eq. (D.13), θ represents the angle of counter-clockwise rotation of the $x^{''} - y^{''}$ coordinate system with respect to the $x' - y'$ coordinate system. The stress components are measured in the new double-primed coordinate system instead of the primed coordinate system. The general resistance equation is expressed as the following:

$$
\begin{aligned}
\frac{\Delta R}{R} &= [(\frac{\pi_{11} + \pi_{12} + \pi_{44}}{2})\sigma_{11}^{'} + (\frac{\pi_{11} + \pi_{12} - \pi_{44}}{2})\sigma_{22}^{'}]\cos^2\phi \\
&+ [(\frac{\pi_{11} + \pi_{12} - \pi_{44}}{2})\sigma_{11}^{'} + (\frac{\pi_{11} + \pi_{12} + \pi_{44}}{2})\sigma_{22}^{'}]\sin^2\phi \\
&+ 2(\pi_{11} - \pi_{12})\,\sigma_{12}^{'}\cos\phi\sin\phi \\
&+ [\alpha_1\Delta T + \alpha_2\Delta T^2 + ...]
\end{aligned} \qquad \text{Eq. (D.15)}
$$

in which only in-plane stresses are assumed. If we consider θ with neglect of temperature terms, $\Delta R/R$ induced by θ with respect to the ideal longitudinal axis of strip for $\phi = 0$, $\phi = 90^\circ$, and $\phi = \pm45^\circ$ is presented below:

$$\frac{\Delta R_0}{R_0} = (\frac{\pi_{11} + \pi_{12} + \pi_{44}}{2})\sigma'_{11} + (\frac{\pi_{11} + \pi_{12} - \pi_{44}}{2})\sigma'_{22}$$

$$= (\frac{\pi_{11} + \pi_{12} + \pi_{44}}{2})(\cos^2\theta\,\sigma''_{11} + \sin^2\theta\,\sigma''_{22} - \sin2\theta\,\sigma''_{12})$$

$$+ (\frac{\pi_{11} + \pi_{12} - \pi_{44}}{2})(\sin^2\theta\,\sigma''_{11} + \cos^2\theta\,\sigma''_{22} + \sin2\theta\,\sigma''_{12})$$

$$= (\frac{\pi_{11} + \pi_{12} + \pi_{44}\cos2\theta}{2})\sigma''_{11} + (\frac{\pi_{11} + \pi_{12} - \pi_{44}\cos2\theta}{2})\sigma''_{22} - \pi_{44}\sin2\theta\,\sigma''_{12}$$

Eq. (D.16)

$$\frac{\Delta R_{90}}{R_{90}} = (\frac{\pi_{11} + \pi_{12} - \pi_{44}}{2})\sigma'_{11} + (\frac{\pi_{11} + \pi_{12} + \pi_{44}}{2})\sigma'_{22}$$

$$= (\frac{\pi_{11} + \pi_{12} - \pi_{44}}{2})(\cos^2\theta\,\sigma''_{11} + \sin^2\theta\,\sigma''_{22} - \sin2\theta\,\sigma''_{12})$$

$$+ (\frac{\pi_{11} + \pi_{12} + \pi_{44}}{2})(\sin^2\theta\,\sigma''_{11} + \cos^2\theta\,\sigma''_{22} + \sin2\theta\,\sigma''_{12})$$

$$= (\frac{\pi_{11} + \pi_{12} - \pi_{44}\cos2\theta}{2})\sigma''_{11} + (\frac{\pi_{11} + \pi_{12} + \pi_{44}\cos2\theta}{2})\sigma''_{22} + \pi_{44}\sin2\theta\,\sigma''_{12}$$

Eq. (D.17)

$$\frac{\Delta R_{45}}{R_{45}} = (\frac{\pi_{11} + \pi_{12}}{2})(\sigma'_{11} + \sigma'_{22}) + (\pi_{11} - \pi_{12})\,\sigma'_{12}$$

$$= (\frac{\pi_{11} + \pi_{12}}{2})(\sigma''_{11} + \sigma''_{22}) + (\pi_{11} - \pi_{12})(\frac{1}{2}\sin2\theta\,\sigma''_{11} - \frac{1}{2}\sin2\theta\,\sigma''_{22} + \cos2\theta\,\sigma''_{12})$$

$$= [(\frac{\pi_{11} + \pi_{12}}{2}) + \frac{1}{2}\sin2\theta\,(\pi_{11} - \pi_{12})]\sigma''_{11} + [(\frac{\pi_{11} + \pi_{12}}{2}) - \frac{1}{2}\sin2\theta\,(\pi_{11} - \pi_{12})]\sigma''_{22}$$

$$+ (\pi_{11} - \pi_{12})\cos2\theta\,\sigma''_{12}$$

Eq. (D.18)

$$\frac{\Delta R_{-45}}{R_{-45}} = (\frac{\pi_{11} + \pi_{12}}{2})(\sigma'_{11} + \sigma'_{22}) - (\pi_{11} - \pi_{12})\,\sigma'_{12}$$

$$= (\frac{\pi_{11} + \pi_{12}}{2})(\sigma''_{11} + \sigma''_{22}) - (\pi_{11} - \pi_{12})(\frac{1}{2}\sin 2\theta\,\sigma''_{11} - \frac{1}{2}\sin 2\theta\,\sigma''_{22} + \cos 2\theta\,\sigma''_{12})$$

$$= [(\frac{\pi_{11} + \pi_{12}}{2}) - \frac{1}{2}\sin 2\theta\,(\pi_{11} - \pi_{12})]\,\sigma''_{11} + [(\frac{\pi_{11} + \pi_{12}}{2}) + \frac{1}{2}\sin 2\theta\,(\pi_{11} - \pi_{12})]\,\sigma''_{22}$$

$$- (\pi_{11} - \pi_{12})\cos 2\theta\,\sigma''_{12}$$

Eq. (D.19)

Through the use of the equations,

$$\pi_{44} = \frac{S_0 - S_{90}}{\sigma'_{11F} - \sigma'_{22F}} = \frac{S_0 - S_{90}}{\cos 2\theta\,(\sigma''_{11F} - \sigma''_{22F}) - 2\sin 2\theta\,\sigma''_{12F}}$$

Eq. (D.20)

$$\pi_S = \frac{S_0 + S_{90}}{\sigma'_{11F} + \sigma'_{22F}} = \frac{S_{45} + S_{-45}}{\sigma'_{11F} + \sigma'_{22F}} = \frac{S_0 + S_{90}}{\sigma''_{11F} + \sigma''_{22F}} = \frac{S_{45} + S_{-45}}{\sigma''_{11F} + \sigma''_{22F}}$$

Eq. (D.21)

Note that Eq. (D.14) is used in the calculation of π_S in Eq. (D.21). As presented in Eqs.

(D.11) and (D.21), the $0^\circ/90^\circ$ and $\pm 45^\circ$ pairs are insensitive to beam rotational error and

should yield the precise measurement. It addition, the $0^\circ/90^\circ$ and $\pm 45^\circ$ pairs are

insensitive to rotational alignment error.

APPENDIX E

TYPICAL RESULTS FOR S_0, S_{90}, S_{45}, AND S_{-45} FOR THE (001) SILICON VERSUS TEMPERATURE

Typical results of S_0, S_{90}, S_{45}, and S_{-45} for the (001) silicon with temperature are displayed in this section. It may be noted that 10 samples were used for these calibrations.

- P-type: [100] direction

Table E.1 - S_0 for [100] p-type silicon with temperature (Unit: N^{-1})											
T (^{o}C)	#1	#2	#3	#4	#5	#6	#7	#8	#9	#10	Average	Std.Dev
-151.0	244.4	162.1	205.8	173.4	160.4	237.6	239.5	258.1	187.8	169.0	203.8	38.1
-133.4	197.1	171.4	179.3	198.2	149.6	187.9	219.2	147.3	193.4	203.7	184.7	23.1
-113.4	156.5	130.2	192.5	126.9	112.6	166.3	203.9	210.1	177.7	210.1	168.7	36.3
-93.2	168.6	162.0	200.2	149.1	145.0	157.4	130.3	146.8	150.2	226.5	163.6	28.8
-71.4	133.4	136.9	175.1	172.1	123.5	117.9	132.1	145.5	182.7	183.2	150.2	25.4
-48.2	111.4	156.3	163.0	177.0	131.4	105.9	107.0	95.2	138.5	180.8	136.7	31.4
-23.6	103.2	135.6	135.0	134.4	115.0	110.2	110.6	131.9	110.1	151.6	123.8	15.9
0.6	89.3	119.2	94.4	164.4	128.2	85.9	86.7	114.9	130.8	148.5	116.2	27.3
25.1	99.7	121.9	131.0	123.1	82.8	94.6	115.6	111.0	112.1	123.0	111.5	15.0
49.9	68.1	133.7	111.5	102.7	67.0	80.0	97.3	121.8	97.9	101.7	98.2	21.7
75.1	71.7	81.4	60.2	88.7	69.8	76.8	104.4	102.2	104.2	75.6	83.5	15.7
100.6	42.8	71.1	65.8	65.9	60.9	88.2	74.9	77.5	75.0	85.5	70.8	13.0
125.9	47.7	75.4	78.4	42.0	54.6	57.9	86.9	88.2	85.8	66.4	68.3	17.0

Table E.2 - S_{90} for [100] p-type silicon with temperature (Unit: N^{-1})											
T (°C)	#1	#2	#3	#4	#5	#6	#7	#8	#9	#10	Average	Std.Dev
-151.0	-69.6	-48.2	-53.6	-43.7	-50.2	-67.9	-67.2	-62.7	-50.7	-42.9	-55.7	10.3
-133.4	-46.7	-10.2	-49.8	-50.4	-31.4	-61.6	-47.7	-44.9	-56.0	-66.6	-46.5	16.0
-113.4	-42.7	-50.6	-58.4	-30.9	-20.3	-71.4	-55.6	-38.6	-46.6	-61.8	-47.7	15.2
-93.2	-53.8	-34.4	-48.1	-42.3	-29.0	-58.6	-38.4	-42.9	-36.2	-58.1	-44.2	10.2
-71.4	-42.8	-46.3	-60.4	-45.4	-13.0	-25.7	-32.1	-20.6	-35.0	-45.8	-36.7	14.2
-48.2	-33.9	-58.5	-27.2	-42.2	-38.3	-15.9	-36.7	-35.3	-28.5	-40.0	-35.7	11.1
-23.6	-32.0	-13.7	-30.9	-35.2	-31.0	-23.1	-35.2	-32.5	-32.6	-26.3	-29.2	6.6
0.6	-34.0	-35.0	5.1	-31.1	-40.0	-28.6	-29.1	-26.3	-25.4	-29.0	-27.3	12.2
25.1	-24.7	-30.9	-17.8	-25.5	-24.5	-19.4	-27.5	-18.6	-22.6	-22.9	-23.4	4.1
49.9	-43.3	-17.1	-25.7	-22.1	-16.7	-16.0	-19.6	-21.6	-12.5	-21.6	-21.6	8.5
75.1	-22.6	-31.3	-27.1	-11.8	-13.4	-14.9	-14.3	-10.7	-10.9	-14.0	-17.1	7.3
100.6	-9.4	-10.4	3.6	-7.5	-10.9	-8.0	-15.5	-15.7	-15.0	-11.7	-10.1	5.7
125.9	-10.7	-7.6	8.1	-12.1	7.0	-17.5	-18.1	-12.8	-18.6	-14.4	-9.7	9.7

Table E.3 - S_{45} for [100] p-type silicon with temperature (Unit: N^{-1})											
T (°C)	#1	#2	#3	#4	#5	#6	#7	#8	#9	#10	Average	Std.Dev
-151.0	64.4	67.2	66.8	40.7	70.7	118.2	93.6	115.4	82.5	76.8	79.6	23.9
-133.4	66.8	74.2	70.3	94.0	49.1	96.5	75.2	91.9	60.5	94.7	77.3	16.4
-113.4	47.2	55.0	63.7	28.6	52.4	69.6	91.6	64.4	49.4	87.3	60.9	18.9
-93.2	61.2	46.7	43.7	64.2	61.3	66.1	80.0	69.3	64.5	73.6	63.0	11.1
-71.4	45.7	60.3	50.8	54.1	42.7	45.5	44.3	69.1	54.6	67.5	53.5	9.6
-48.2	38.8	63.2	51.6	63.6	53.1	36.3	62.9	73.3	31.9	68.9	54.4	14.5
-23.6	31.3	59.6	48.1	35.2	54.5	47.2	47.8	72.3	42.9	46.8	48.6	11.7
0.6	46.4	42.5	16.6	48.2	36.7	44.8	46.7	33.7	33.1	43.4	39.2	9.6
25.1	54.6	54.2	15.7	40.3	47.7	43.7	43.7	30.2	37.9	35.8	40.4	11.6
49.9	39.4	42.9	12.9	55.6	39.5	29.9	29.9	30.4	32.9	46.3	36.0	11.6
75.1	24.1	27.4	12.0	32.3	32.8	39.4	39.7	30.9	27.4	36.8	30.3	8.3
100.6	29.3	30.4	33.2	27.1	22.6	33.3	37.0	33.6	34.4	29.8	31.1	4.1
125.9	23.7	33.9	47.9	29.0	25.1	35.4	36.2	36.1	26.8	32.4	32.6	7.1

Table E.4 - S_{-45} for [100] p-type silicon with temperature (Unit: N^{-1})											
T (ºC)	#1	#2	#3	#4	#5	#6	#7	#8	#9	#10	Average	Std.Dev
-151.0	81.1	122.1	61.6	50.2	59.3	83.8	112.9	84.4	47.2	82.6	78.5	25.0
-133.4	85.8	50.9	59.0	58.8	67.2	101.8	106.4	66.8	66.9	70.9	73.5	18.6
-113.4	61.1	32.6	59.8	61.3	40.0	78.1	91.2	85.3	71.9	74.7	65.6	18.7
-93.2	54.0	57.0	71.6	38.4	46.4	85.8	64.0	80.1	49.2	61.9	60.8	15.0
-71.4	48.3	40.7	60.8	40.0	64.9	58.4	82.1	68.7	44.3	55.5	56.4	13.5
-48.2	34.1	37.3	49.0	34.5	67.8	61.5	38.0	57.9	56.1	52.7	48.9	12.2
-23.6	48.3	52.0	21.9	67.1	38.8	50.6	51.0	50.3	30.6	66.2	47.7	14.2
0.6	38.0	54.5	62.3	79.6	43.6	58.9	58.6	55.2	33.5	51.0	53.5	13.2
25.1	41.1	37.4	25.8	47.8	34.0	32.3	32.3	48.1	29.1	43.5	37.1	7.7
49.9	30.4	39.2	35.9	27.6	29.3	43.1	43.1	43.6	30.6	34.3	35.7	6.2
75.1	-20.9	18.4	51.4	41.6	24.8	29.9	5.2	33.7	18.9	38.7	24.2	20.6
100.6	7.6	26.2	27.1	24.8	35.7	36.6	33.3	35.7	25.2	32.6	28.5	8.7
125.9	18.6	24.7	8.7	19.9	17.0	27.8	28.1	29.8	29.0	22.9	22.6	6.7

- P-type: [110] direction

Table E.5 - S_0 for [110] p-type silicon with temperature (Unit: N^{-1})											
T (ºC)	#1	#2	#3	#4	#5	#6	#7	#8	#9	#10	Average	Std.Dev
-151.0	4216	4149	3963	3592	4119	4069	3686	3456	3590	3468	3831	300.9
-133.4	3865	3702	3727	3365	3955	3768	3466	3358	3409	3401	3602	225.8
-113.4	3456	3452	3311	3284	3539	3400	3369	3236	3354	3293	3369	93.4
-93.2	3188	3160	3180	3237	3223	3187	3298	3173	3237	3042	3193	66.8
-71.4	3093	2874	3063	3180	3209	2982	3270	3064	3226	2980	3094	126.9
-48.2	2811	2719	2846	3029	2905	2688	3213	2892	2953	2858	2891	151.7
-23.6	2687	2685	2642	2820	2733	2461	3133	2723	2740	2744	2737	168.1
0.6	2632	2583	2418	2627	2550	2485	3045	2497	2518	2677	2603	173.9
25.1	2462	2419	2362	2306	2496	2340	2882	2376	2410	2507	2456	163.4
49.9	2348	2234	2197	2216	2295	2305	2520	2349	2353	2166	2298	103.3
75.1	2128	2130	1923	2138	2129	2141	2219	2263	2179	1519	2077	215.1
100.6	2047	1969	1806	1875	1984	2023	2091	2129	2025	1431	1938	202.2
125.9	1964	1903	1640	1638	1823	1870	1845	1829	1930	1324	1777	193.1

Table E.6 - S_{90} for [110] p-type silicon with temperature (Unit: N^{-1})											
T (ºC)	#1	#2	#3	#4	#5	#6	#7	#8	#9	#10	Average	Std.Dev
-151.0	-3930	-4038	-3804	-3360	-3868	-3812	-3541	-3259	-3345	-3019	-3598	339.7
-133.4	-3630	-3546	-3735	-3048	-3653	-3559	-3360	-3120	-3233	-2886	-3377	291.8
-113.4	-3276	-3330	-3220	-2966	-3362	-3200	-3265	-3047	-3190	-2854	-3171	164.3
-93.2	-2947	-3019	-2987	-2921	-3057	-3006	-3253	-3046	-3084	-2731	-3005	132.7
-71.4	-2834	-2770	-2842	-2895	-2981	-2759	-3188	-2880	-3074	-2720	-2894	147.9
-48.2	-2690	-2637	-2670	-2794	-2668	-2442	-3150	-2804	-2835	-2571	-2726	189.3
-23.6	-2516	-2591	-2500	-2618	-2589	-2440	-3005	-2711	-2695	-2459	-2612	165.6
0.6	-2457	-2484	-2261	-2462	-2604	-2320	-2923	-2457	-2439	-2404	-2481	180.8
25.1	-2247	-2293	-2150	-2240	-2420	-2232	-2848	-2400	-2376	-2451	-2366	195.4
49.9	-2217	-2204	-2017	-2094	-2247	-2203	-2465	-2283	-2299	-1964	-2199	145.3
75.1	-2113	-2105	-1824	-2049	-2015	-1902	-2227	-2106	-1992	-1504	-1984	203.6
100.6	-3930	-4038	-3804	-3360	-3868	-1938	-2076	-1980	-1865	-1337	-1859	205.7
125.9	-3630	-3546	-3735	-3048	-3653	-1800	-1923	-1847	-1899	-1181	-1731	225.2

Table E.7 - S_{45} for [110] p-type silicon with temperature (Unit: N^{-1})											
T (ºC)	#1	#2	#3	#4	#5	#6	#7	#8	#9	#10	Average	Std.Dev
-151.0	133.1	126.9	145.1	108.0	94.9	141.1	156.7	129.4	138.0	168.8	134.2	21.6
-133.4	107.9	110.9	135.1	117.5	83.0	139.3	136.6	132.1	126.1	179.1	126.8	25.2
-113.4	79.2	106.0	94.5	115.3	97.6	120.3	133.0	111.5	101.2	159.2	111.8	22.3
-93.2	95.4	96.7	114.8	102.9	98.0	125.1	123.4	113.7	101.6	147.8	111.9	16.6
-71.4	83.2	35.3	116.0	105.7	89.5	108.9	129.6	98.8	117.7	144.3	102.9	29.8
-48.2	67.7	90.4	84.6	82.9	87.6	115.8	108.2	71.3	94.2	109.9	91.3	16.1
-23.6	82.3	85.4	93.7	93.9	55.5	90.1	103.4	86.3	84.9	84.2	86.0	12.4
0.6	83.0	47.4	74.1	71.2	64.6	94.1	89.5	78.6	110.6	65.7	77.9	17.7
25.1	62.3	58.6	65.6	67.6	56.8	80.8	81.5	62.9	87.4	71.8	69.5	10.5
49.9	69.7	59.3	60.7	61.6	51.9	71.9	80.4	76.7	95.0	71.1	69.8	12.4
75.1	56.9	39.9	48.9	47.6	44.5	41.2	43.3	71.7	84.0	63.7	54.2	14.7
100.6	27.9	48.0	23.5	45.7	27.2	56.5	50.2	60.9	46.7	60.9	44.7	13.9
125.9	39.9	36.5	40.0	40.1	38.0	34.1	55.4	53.9	63.2	43.8	44.5	9.6

Table E.8 - S_{-45} for [110] p-type silicon with temperature (Unit: N^{-1})											
T (ºC)	#1	#2	#3	#4	#5	#6	#7	#8	#9	#10	Average	Std.Dev
-151.0	121.6	66.3	135.9	122.9	121.6	144.4	173.2	111.3	113.8	202.3	131.3	36.8
-133.4	113.5	114.7	128.6	115.8	110.1	132.2	146.2	110.0	114.3	158.7	124.4	16.8
-113.4	90.0	111.4	121.8	123.2	112.2	119.6	154.3	105.7	128.4	168.0	123.5	22.8
-93.2	106.4	118.4	119.6	141.4	106.4	133.0	138.5	106.5	116.9	140.2	122.7	14.4
-71.4	91.2	76.9	118.4	98.6	95.8	110.1	139.1	109.7	99.0	141.7	108.0	20.5
-48.2	83.6	75.8	103.4	95.1	104.4	117.2	106.9	101.0	89.4	128.4	100.5	15.5
-23.6	78.7	34.1	85.3	87.0	85.9	93.2	80.0	76.2	76.7	98.3	79.5	17.5
0.6	73.7	73.0	93.3	85.6	96.8	101.2	99.1	77.9	85.2	103.9	89.0	11.5
25.1	70.0	65.8	69.7	62.6	52.9	72.8	93.6	84.8	85.7	66.9	72.5	12.2
49.9	72.0	53.1	63.0	54.9	61.1	64.8	69.5	78.0	75.2	52.2	64.4	9.2
75.1	46.5	38.1	66.9	43.0	47.3	54.7	66.2	61.3	79.1	52.2	55.5	12.7
100.6	48.8	51.5	30.4	29.0	38.5	44.9	63.1	74.5	39.4	49.0	46.9	14.0
125.9	45.9	41.5	39.8	45.9	34.2	51.7	33.3	44.9	53.0	41.6	43.2	6.5

- N-type: [100] direction

Table E.9 – S_0 for [100] n-type silicon with temperature (Unit: N^{-1})											
T (ºC)	#1	#2	#3	#4	#5	#6	#7	#8	#9	#10	Average	Std.Dev
-151.0	-4550	-4648	-4120	-4547	-4232	-4318	-4367	-4735	-4262	-4050	-4383	228.7
-133.4	-4312	-4758	-3970	-4104	-3923	-3937	-4223	-4582	-3947	-3953	-4171	297.2
-113.4	-4105	-4229	-3851	-3922	-3697	-3668	-3804	-4319	-3753	-3788	-3914	227.4
-93.2	-3846	-4088	-3634	-3644	-3303	-3516	-3857	-4171	-3623	-3579	-3726	264.8
-71.4	-3583	-3717	-3332	-3438	-3200	-3327	-3613	-3949	-3451	-3322	-3493	224.6
-48.2	-3128	-3542	-3061	-3255	-3000	-3194	-3561	-3691	-3232	-3279	-3294	229.6
-23.6	-2766	-3256	-2899	-3101	-2874	-3091	-3291	-3322	-2937	-3006	-3054	190.8
0.6	-2626	-2896	-2825	-2903	-2697	-2928	-2987	-3130	-2809	-2756	-2856	146.3
25.1	-2399	-2600	-2717	-2723	-2433	-2606	-2716	-2642	-2734	-2647	-2622	119.2
49.9	-2201	-2570	-2552	-2540	-2270	-2502	-2455	-2518	-2518	-2432	-2456	124.4
75.1	-2094	-2327	-2356	-2362	-2121	-2315	-2331	-2414	-2342	-2326	-2299	104.8
100.6	-1858	-2241	-2039	-2060	-1823	-2124	-1991	-2244	-2163	-2128	-2067	144.4
125.9	-1671	-1920	-1826	-1857	-1690	-1874	-1840	-2006	-1955	-1939	-1858	108.8

T (^{o}C)	#1	#2	#3	#4	#5	#6	#7	#8	#9	#10	Average	Std.Dev
			Table E.10 – S_{90} for [100] n-type silicon with temperature (Unit: N^{-1})									
-151.0	2337	2716	2157	2540	2270	2391	2606	2865	2384	2162	2443	234.9
-133.4	2323	2625	2087	2264	2108	2215	2512	2782	2161	2248	2333	232.3
-113.4	2222	2512	1973	2209	1957	2057	2334	2581	2105	2153	2210	211.4
-93.2	2035	2478	1937	2108	1814	1972	2214	2352	2069	2046	2103	197.8
-71.4	1911	2214	1873	2030	1805	1857	2236	2173	1978	1929	2001	156.5
-48.2	1701	2092	1690	1936	1675	1805	2082	2061	1917	1907	1887	163.0
-23.6	1442	1927	1592	1821	1607	1758	1782	1911	1733	1750	1732	149.4
0.6	1364	1577	1510	1682	1466	1708	1657	1780	1636	1615	1600	123.8
25.1	1310	1455	1485	1474	1310	1434	1671	1623	1512	1504	1478	115.1
49.9	1198	1403	1298	1289	1208	1345	1437	1503	1323	1456	1346	102.9
75.1	1152	1353	1284	1196	1146	1264	1248	1406	1250	1285	1258	81.8
100.6	1035	1281	1163	1077	1040	1226	1130	1273	1154	1212	1159	89.6
125.9	912	1058	1027	1071	894	1034	1032	1147	1040	1107	1032	77.8

T (^{o}C)	#1	#2	#3	#4	#5	#6	#7	#8	#9	#10	Average	Std.Dev
			Table E.11 – S_{45} for [100] n-type silicon with temperature (Unit: N^{-1})									
-151.0	-1103	-1162	-936	-1069	-1187	-980	-851	-1008	-856	-783	-993	137.8
-133.4	-958	-804	-935	-924	-1022	-933	-973	-1092	-775	-881	-930	94.0
-113.4	-862	-814	-898	-867	-825	-944	-878	-923	-886	-879	-878	39.6
-93.2	-878	-887	-765	-833	-781	-925	-849	-732	-745	-832	-822	64.8
-71.4	-784	-725	-748	-782	-826	-767	-835	-777	-726	-788	-776	36.7
-48.2	-673	-740	-676	-699	-669	-714	-739	-692	-743	-678	-702	29.7
-23.6	-646	-689	-641	-663	-636	-664	-660	-690	-669	-708	-667	23.1
0.6	-634	-641	-612	-628	-606	-617	-655	-655	-611	-609	-627	18.8
25.1	-531	-582	-547	-592	-527	-614	-620	-591	-629	-550	-578	37.3
49.9	-487	-512	-534	-513	-513	-569	-538	-525	-561	-541	-529	24.6
75.1	-489	-513	-426	-454	-491	-490	-506	-468	-446	-440	-472	29.7
100.6	-417	-468	-422	-435	-448	-463	-462	-416	-430	-416	-438	20.8
125.9	-402	-435	-396	-358	-383	-412	-388	-366	-368	-370	-388	23.8

Table E.12 – S_{-45} for [100] n-type silicon with temperature (Unit: N^{-1})											
T (°C)	#1	#2	#3	#4	#5	#6	#7	#8	#9	#10	Average	Std.Dev
-151.0	-1290	-964	-1039	-913	-943	-1006	-949	-930	-794	-925	-975	127.9
-133.4	-1148	-1036	-810	-965	-927	-859	-733	-870	-924	-732	-900	130.2
-113.4	-923	-1044	-728	-963	-951	-882	-773	-853	-683	-768	-857	116.3
-93.2	-889	-827	-810	-845	-829	-820	-817	-893	-732	-749	-821	51.5
-71.4	-829	-971	-810	-729	-746	-840	-787	-837	-741	-659	-795	84.5
-48.2	-761	-696	-698	-666	-726	-671	-734	-766	-645	-714	-707	40.3
-23.6	-674	-660	-690	-641	-663	-633	-716	-682	-633	-674	-667	26.5
0.6	-579	-630	-623	-626	-647	-655	-599	-637	-649	-617	-626	23.5
25.1	-535	-588	-525	-514	-579	-631	-597	-617	-565	-543	-569	39.6
49.9	-516	-543	-473	-531	-496	-555	-519	-555	-509	-502	-520	26.6
75.1	-467	-508	-456	-444	-477	-521	-490	-505	-464	-506	-484	25.9
100.6	-437	-462	-368	-389	-420	-450	-413	-471	-402	-428	-424	32.3
125.9	-385	-468	-388	-376	-377	-441	-323	-444	-398	-404	-401	41.8

- N-type: [110] direction

Table E.13 – S_0 for [110] n-type silicon with temperature (Unit: N^{-1})											
T (°C)	#1	#2	#3	#4	#5	#6	#7	#8	#9	#10	Average	Std.Dev
-151.0	-1782	-1726	-1715	-1440	-1439	-1696	-1719	-1457	-1728	-1530	-1623	138.8
-133.4	-1620	-1770	-1599	-1367	-1391	-1522	-1603	-1403	-1613	-1467	-1536	128.4
-113.4	-1422	-1568	-1474	-1335	-1338	-1432	-1473	-1315	-1493	-1378	-1423	81.5
-93.2	-1375	-1439	-1334	-1275	-1266	-1323	-1386	-1249	-1406	-1312	-1337	63.7
-71.4	-1234	-1432	-1196	-1182	-1229	-1269	-1275	-1190	-1313	-1240	-1256	74.3
-48.2	-1173	-1343	-1127	-1144	-1169	-1215	-1112	-1126	-1236	-1203	-1185	69.2
-23.6	-1114	-1197	-1095	-1088	-1110	-1084	-1076	-1090	-1158	-1158	-1117	40.3
0.6	-1033	-1093	-1019	-1042	-1048	-1033	-1012	-1019	-1150	-1079	-1053	43.0
25.1	-941	-965	-952	-957	-981	-977	-946	-969	-1035	-1004	-973	28.8
49.9	-875	-910	-878	-904	-891	-876	-863	-915	-969	-952	-903	34.6
75.1	-771	-835	-744	-826	-774	-801	-771	-842	-813	-864	-804	38.5
100.6	-728	-746	-699	-759	-720	-737	-702	-776	-768	-800	-744	32.7
125.9	-618	-691	-583	-645	-634	-646	-618	-684	-679	-664	-646	34.2

Table E.14 – S_{90} for [110] n-type silicon with temperature (Unit: N^{-1})											
T (ºC)	#1	#2	#3	#4	#5	#6	#7	#8	#9	#10	Average	Std.Dev
-151.0	-1157	-1079	-1007	-827	-859	-928	-1023	-916	-1068	-968	-983	103.4
-133.4	-1005	-1129	-861	-789	-833	-865	-943	-882	-972	-901	-918	98.5
-113.4	-840	-879	-885	-745	-808	-890	-836	-813	-922	-867	-849	51.3
-93.2	-844	-836	-830	-717	-780	-818	-812	-775	-886	-805	-810	45.8
-71.4	-727	-854	-682	-668	-736	-777	-743	-703	-718	-755	-736	52.8
-48.2	-704	-778	-670	-689	-706	-721	-639	-681	-678	-720	-699	37.3
-23.6	-705	-708	-636	-654	-683	-627	-652	-647	-649	-683	-664	28.5
0.6	-660	-671	-608	-619	-628	-612	-619	-593	-653	-652	-632	25.9
25.1	-559	-572	-580	-583	-587	-583	-563	-568	-586	-587	-577	10.4
49.9	-501	-533	-529	-539	-514	-517	-502	-525	-528	-542	-523	14.2
75.1	-451	-479	-424	-501	-444	-469	-450	-481	-443	-495	-464	25.0
100.6	-417	-433	-402	-410	-421	-432	-424	-418	-416	-446	-422	12.5
125.9	-345	-391	-337	-333	-349	-358	-334	-378	-369	-364	-356	19.6

Table E.15 – S_{45} for [110] n-type silicon with temperature (Unit: N^{-1})											
T (ºC)	#1	#2	#3	#4	#5	#6	#7	#8	#9	#10	Average	Std.Dev
-151.0	-1705	-1227	-1258	-1059	-1044	-1644	-1243	-1310	-1423	-1304	-1322	217.8
-133.4	-1551	-1121	-1244	-1091	-1014	-1401	-1360	-1256	-1366	-1261	-1267	161.3
-113.4	-1357	-1093	-1186	-992	-886	-1254	-1222	-1224	-1089	-1117	-1142	136.5
-93.2	-1290	-1251	-934	-1008	-850	-1118	-1137	-1140	-1170	-979	-1088	141.1
-71.4	-1085	-1135	-928	-932	-863	-931	-900	-958	-934	-955	-962	83.3
-48.2	-945	-1018	-875	-910	-847	-1124	-874	-883	-966	-973	-941	83.7
-23.6	-962	-1011	-853	-811	-831	-848	-816	-753	-846	-848	-858	74.7
0.6	-859	-764	-790	-730	-778	-881	-791	-722	-725	-784	-782	53.4
25.1	-716	-719	-724	-759	-712	-692	-708	-711	-703	-737	-718	18.9
49.9	-699	-740	-709	-727	-713	-666	-715	-691	-671	-679	-701	24.2
75.1	-585	-624	-615	-600	-635	-616	-586	-717	-685	-638	-630	42.2
100.6	-518	-593	-578	-579	-609	-568	-539	-638	-632	-637	-589	41.2
125.9	-514	-533	-534	-485	-583	-453	-445	-586	-541	-536	-521	48.1

Table E.16 – S_{-45} for [110] n-type silicon with temperature (Unit: N^{-1})												
T (ºC)	#1	#2	#3	#4	#5	#6	#7	#8	#9	#10	Average	Std.Dev
-151.0	-1318	-1491	-1399	-1173	-1197	-1206	-1432	-1164	-1309	-1155	-1284	123.3
-133.4	-1156	-1450	-1332	-930	-933	-1223	-1223	-1188	-1140	-1082	-1166	160.9
-113.4	-1122	-1310	-1242	-956	-978	-1171	-1026	-1122	-1238	-1170	-1134	117.4
-93.2	-986	-1003	-1137	-935	-876	-1263	-967	-1198	-1069	-1080	-1051	121.5
-71.4	-1128	-940	-992	-919	-923	-1161	-932	-999	-1054	-1064	-1011	87.5
-48.2	-901	-1038	-904	-869	-830	-900	-823	-1024	-903	-921	-911	71.0
-23.6	-838	-886	-883	-872	-816	-909	-850	-860	-910	-909	-873	32.4
0.6	-772	-781	-852	-759	-808	-787	-799	-833	-833	-834	-806	31.3
25.1	-739	-776	-781	-698	-769	-782	-737	-809	-769	-799	-766	32.9
49.9	-620	-644	-674	-647	-664	-724	-706	-763	-718	-705	-686	44.0
75.1	-610	-641	-602	-649	-629	-598	-579	-704	-670	-653	-634	37.9
100.6	-509	-581	-472	-594	-553	-518	-521	-634	-608	-611	-560	53.4
125.9	-472	-602	-465	-527	-447	-547	-479	-581	-567	-500	-519	53.9

Typical results of S_0, S_{90}, S_{45}, and S_{-45} for the (001) p-type and n-type silicon at 25ºC are shown in Figs.E.6 through Fig.E.13.
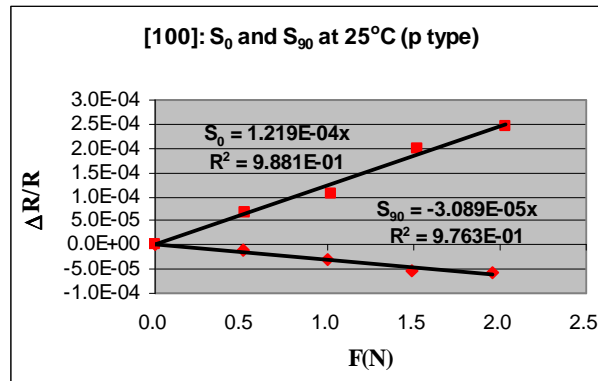
Fig. E.6 - S_0 and S_{90} for [100] p-type silicon at 25ºC (Unit: N^{-1})
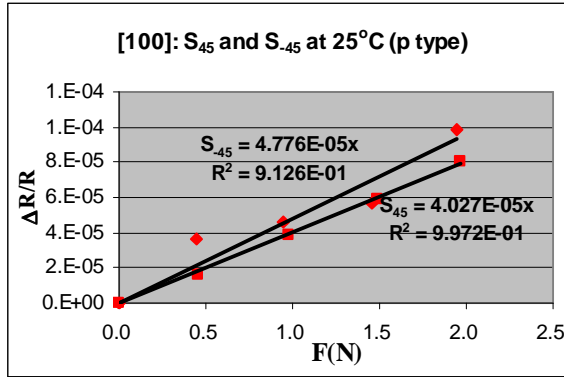
Fig. E.7 - S_{45} and S_{-45} for [100] p-type silicon at 25^oC (Unit: N^{-1})
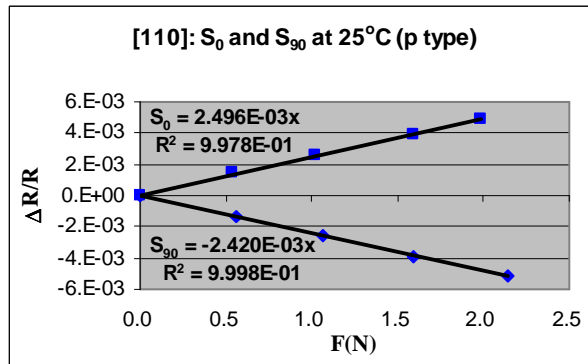
Fig. E.8 - S_0 and S_{90} for [110] p-type silicon at 25^oC (Unit: N^{-1})
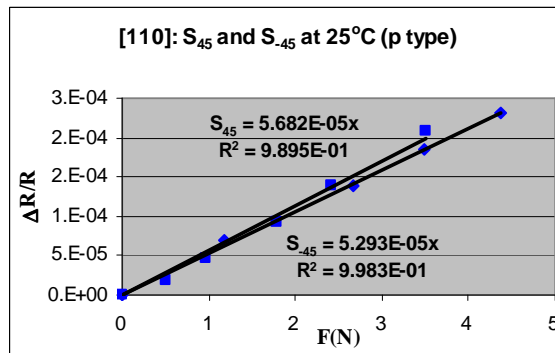
Fig. E.9 - S_{45} and S_{-45} for [110] p-type silicon at 25^oC (Unit: N^{-1})

266
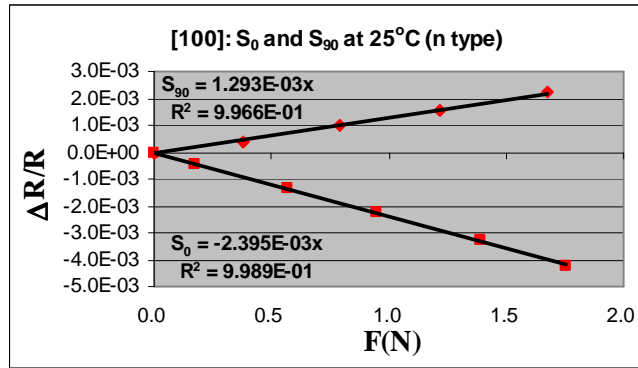
Fig. E.10 - S_0 and S_{90} for [100] n-type silicon at $25^{\circ}C$ (Unit: N^{-1})
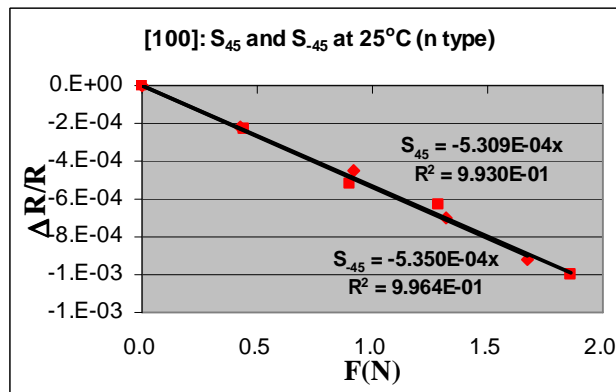
Fig. E.11 - S_{45} and S_{-45} for [100] n-type silicon at $25^{\circ}C$ (Unit: N^{-1})
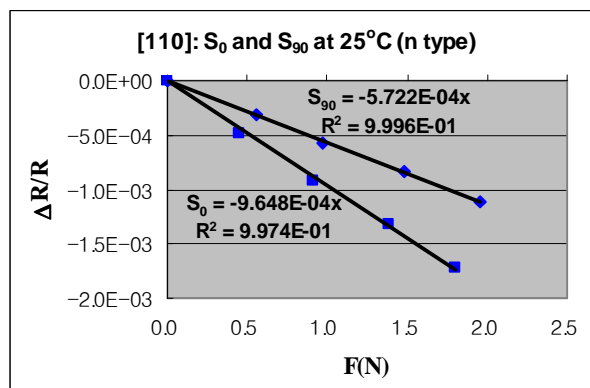
Fig. E.12 - S_0 and S_{90} for [110] n-type silicon at $25^{\circ}C$ (Unit: N^{-1})

267
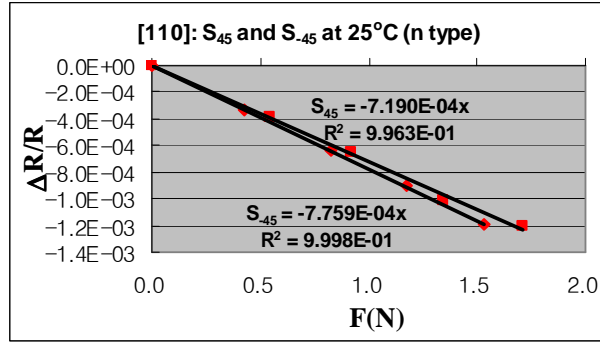
Fig. E.13 - S_{45} and S_{-45} for [110] n-type silicon at 25°C (Unit: N^{-1})

APPENDIX F

THE EFFECTS OF ERRORS ASSOCIATED WITH INITIAL RESISTANCE ON THE

DETERMINATION OF PI-COEFFICIENTS

The correct calibration of initial resistance is essential for the accurate determination of pi-coefficients. The incorrect initial values of resistance occur from uneven expansions and contractions during thermal expansion of the various materials which expand and contract at different rates and have different elastic moduli. Under heating and cooling of such assemblies of materials, the coefficient of thermal expansion mismatches lead to thermal stresses.

Figure F.1. is presented in order to help with the understanding of the effects of the incorrect initial resistance, as shown below.
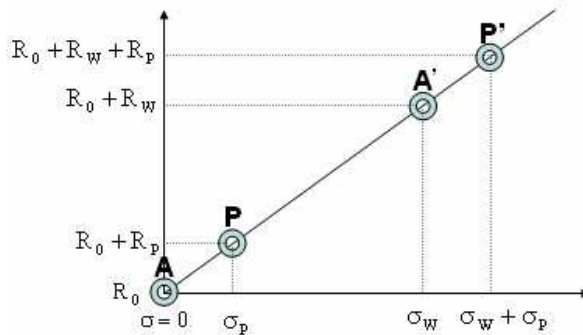
Fig. F.1 - Resistance at various stress levels

In Fig. F.1, σ_w denotes the stress induced by any warpage, for example, resulting from the mismatch in the coefficients of expansion of the various packaging materials, and σ_p denotes the stress that we want to apply on the sample, respectively. In Fig. F.1,

the linear relationship between the resistance and stress is established because the

piezoresistive effect has been observed to be linear in the applied stress. Through the use

of $\dfrac{\Delta R}{R} = \pi\sigma$, the resistance equation becomes:

- From A to P

$$\frac{(R_0 + R_P) - R_0}{R_0} = \pi\,\sigma_P \qquad \text{Eq. (F.1)}$$

Hence

$$\pi = \frac{1}{\sigma_P}\frac{R_P}{R_0} \qquad \text{Eq. (F.2)}$$

- From A' to P'

$$\frac{(R_0 + R_W + R_P) - (R_0 + R_W)}{(R_0 + R_W)} = \pi'\,(\sigma_W + \sigma_P - \sigma_W) \qquad \text{Eq. (F.3)}$$

Hence

$$\pi' = \frac{1}{\sigma_P}\left(\frac{R_P}{R_0 + R_W}\right) \qquad \text{Eq. (F.4)}$$

Dividing Eq. (F.2) by Eq. (F.4) yields

$$\frac{\pi}{\pi'} = \frac{R_0}{R_0 + R_W} \qquad \text{Eq. (F.5)}$$

Then it leads to

$$\pi' = \left(\frac{R_0 + R_W}{R_0}\right)\pi \qquad \text{Eq. (F.6)}$$

in which R_W is the resistance induced by σ_W. The initial resistance value is shifted from

R_0 to $R_0 + R_W$ due to the induced stresses σ_W. If $R_W \ll R_0$, Eq. (F.6) becomes

$$\pi^{'} \cong \pi \qquad\qquad\qquad \text{Eq. (F.7)}$$

However, as R_w becomes more comparable with R_0, the discrepancy between π and $\pi^{'}$ is exacerbated.

In Figs. F.2 and F.3, the contour plots of σ_{11} and σ_{22} in the single-sided silicon strip-on-beam from thermal simulations (from 150$^{\text{o}}$C to 25$^{\text{o}}$C) are presented. The colors of contour represent the stress value.
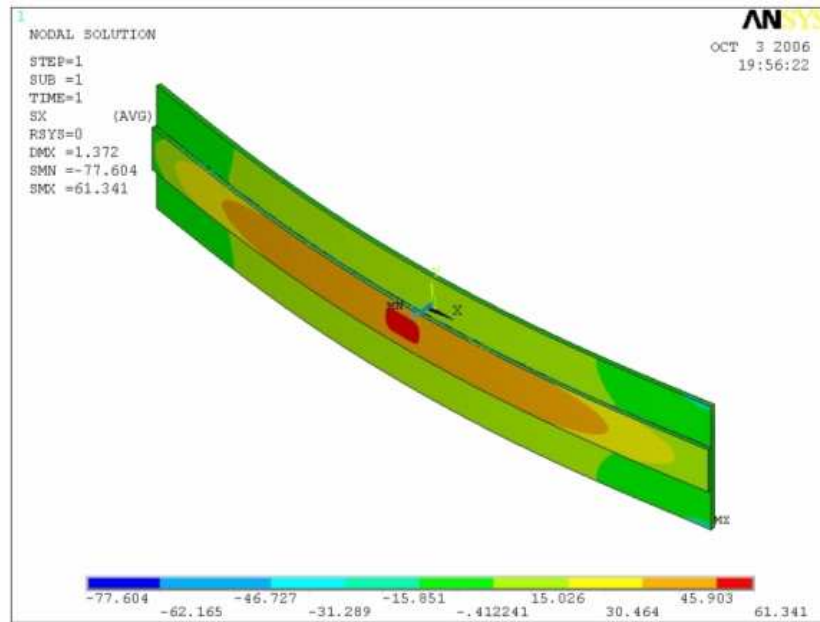
Fig. F.2 - Thermal simulation of σ_{11} for [100] strip-on-beam
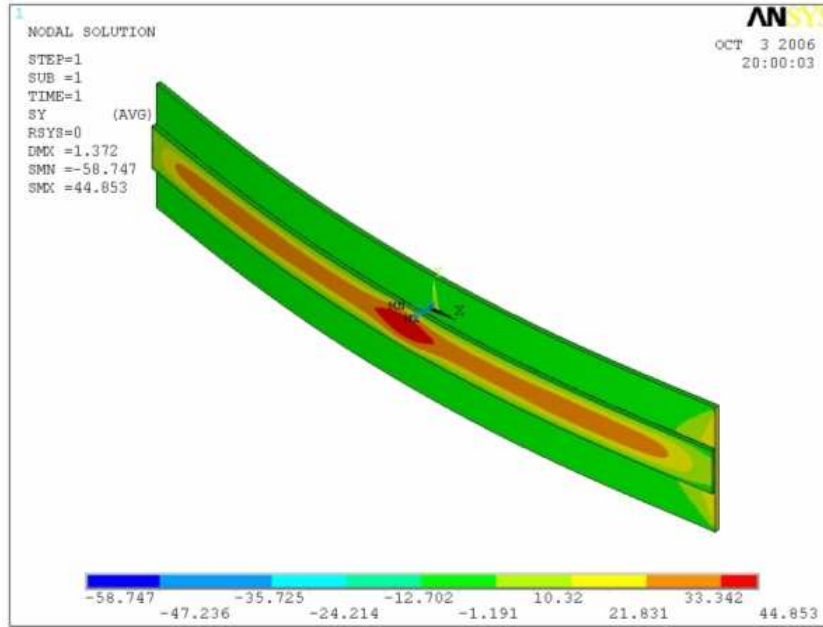
Fig. F.3 - Thermal simulation of σ_{22} for [100] strip-on-beam

Similarly, contour plots of σ'_{11} and σ'_{22} in the [100] double-sided silicon strip-on-beam from thermal simulations (from 150$^{\text{o}}$C to 25$^{\text{o}}$C) are presented as shown in Figs. F.4 and F.5.
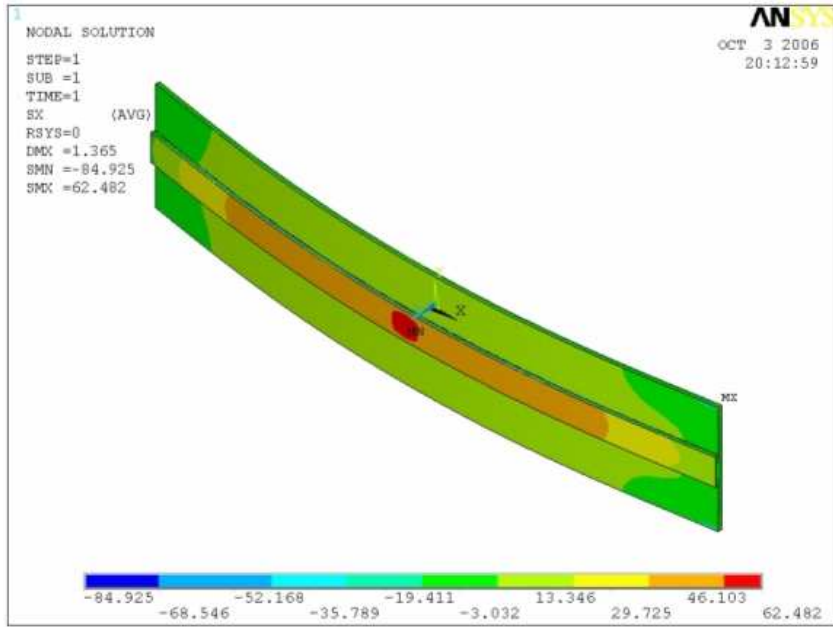
Fig. F.4 - Thermal simulation of σ'_{11} for [110] strip-on-beam
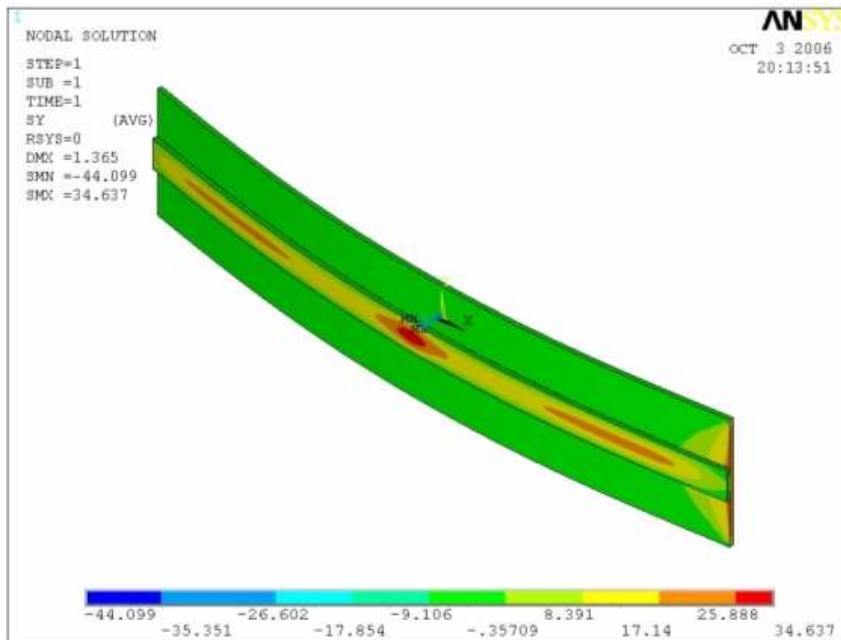
Fig. F.5 - Thermal simulation of σ'_{22} for [110] strip-on-beam

In addition, thermal simulations of z-directional displacement are performed from 150°C

to 25°C as shown in Figs. F.6 and F.7.
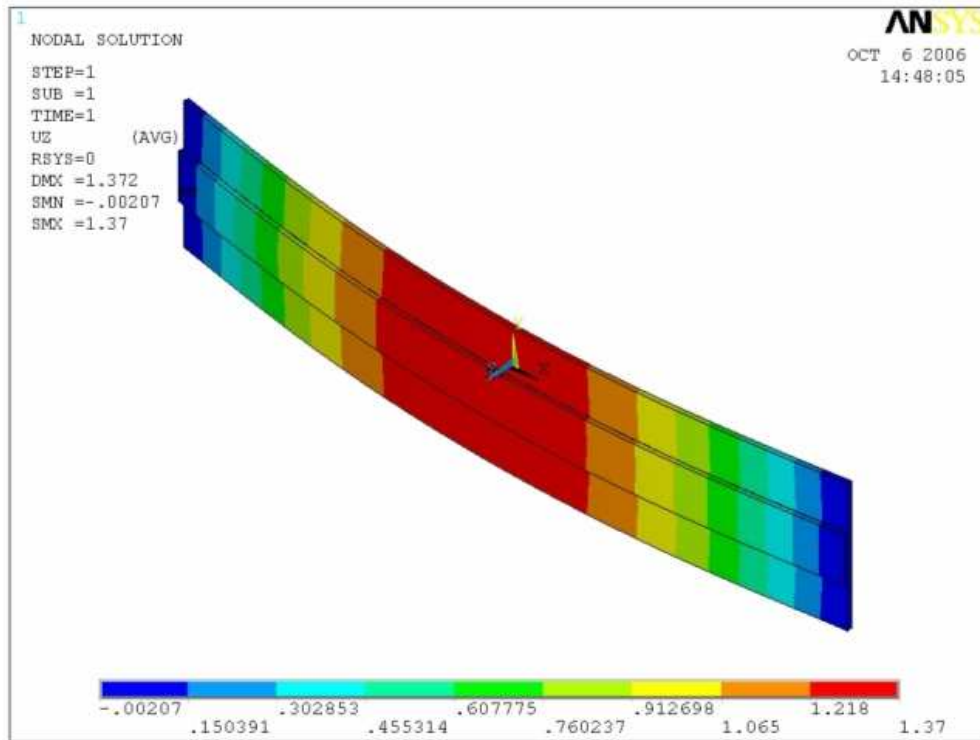
Fig. F.6 - Thermal simulation of z-displacement for [100] strip-on-beam
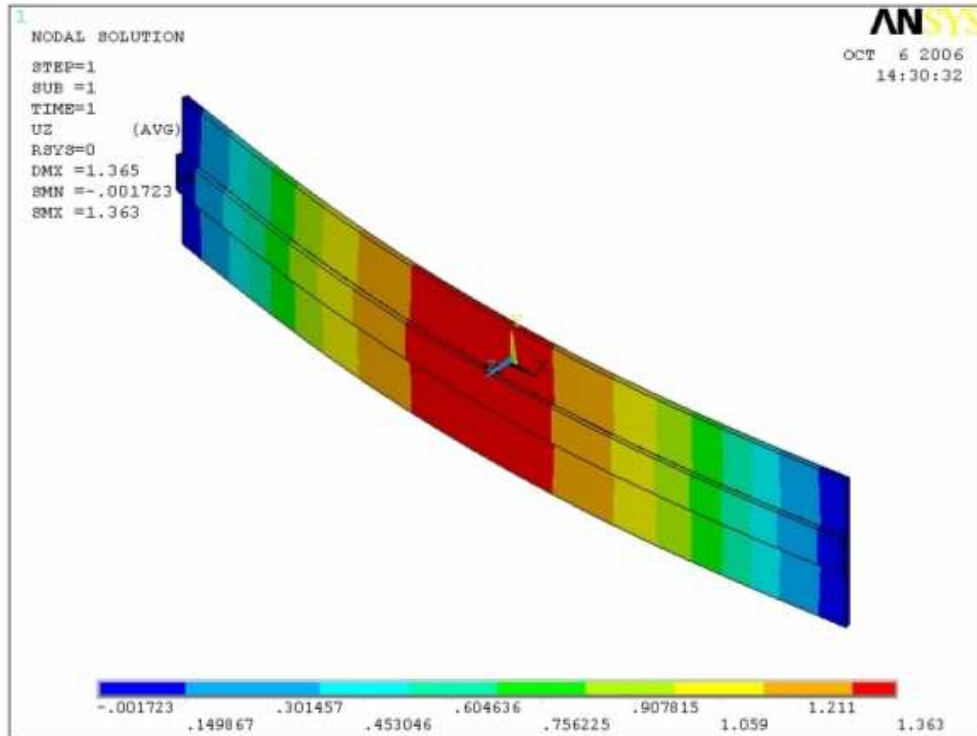
Fig. F.7 - Thermal simulation of z-displacement for [110] strip-on-beam

For both [100] and [110] strip-on-beam structures, the maximum change in z-directional displacement occurs at the central part. The maximum displacement of simulation is about 1.36~1.37 mm for both cases. The simulation result for the maximum change in z-directional displacement is in good agreement with the experimental result (about 1.3~1.5 mm) as shown in Fig. F.8. It can be seen that a single-sided silicon strip-on-beam sample was significantly warped after cooling from their assembly temperature, resulting from the mismatch in the coefficients of expansion of the various packaging materials.

Fig. F.8 - The obvious warp of a single-sided silicon strip-on-beam sample after cooling from 150°C to room temperature

From thermal simulations, the in-plane stresses at sensor location in [100] and [110] silicon strip-on-beam samples are displayed in Tables F.1 and F.2, respectively.

Table F.1 - In-plane stresses at sensor location in [100] silicon strip-on-beam (Unit: MPa)		
σ_{11}	σ_{22}	σ_{12}
57.63	44.85	-1.00E-08

Table F.2 - In-plane stresses at sensor location in [110] silicon strip-on-beam (Unit: MPa)		
σ'_{11}	σ'_{22}	σ'_{12}
60.31	34.64	3.81E-09

Pi-coefficients reflecting the average values of 10 specimens, as discussed in Chapter 9, are shown in Table F.3

Table F.3 - π_{11}, π_{12}, and π_{44} of (001) p- and n-type silicon at 25°C (Unit: TPa^{-1})			
Type	π_{11}	π_{12}	π_{44}
p	29.4	-6.2	898
n	-691	390	-73.9

The normalized change in resistance induced by thermal stresses, arising from the assembly operations, can be calculated by substitution of the values in Tables F.1 through F.3 into the equations below:

- With respect to the unprimed axes

$$\frac{\Delta R}{R} = [\pi_{11}\sigma_{11} + \pi_{12}(\sigma_{22} + \sigma_{33})]\cos^2\phi + [\pi_{11}\sigma_{22} + \pi_{12}(\sigma_{11} + \sigma_{33})]\sin^2\phi$$

Eq. (F.8)

$$+ \pi_{44}\sigma_{12} \sin2\phi + [\alpha_1\Delta T + \alpha_2\Delta T^2 + ...]$$

For p- and n-type sensors,

$$\frac{\Delta R_0}{R_0} = \pi_{11}\sigma_{11} + \pi_{12}\sigma_{22}$$

$$= 1.42 \times 10^{-3} \text{ for p - type sensors}$$ Eq. (F.9)
$$= -2.23 \times 10^{-2} \text{ for n - type sensors}$$

$$\frac{\Delta R_{90}}{R_{90}} = \pi_{12}\sigma_{11} + \pi_{11}\sigma_{22}$$

$$= 9.61 \times 10^{-4} \text{ for p - type sensors}$$ Eq. (F.10)
$$= -8.52 \times 10^{-3} \text{ for n - type sensors}$$

$$\frac{\Delta R_{45}}{R_{45}} = (\frac{\pi_{11} + \pi_{12}}{2})(\sigma_{11} + \sigma_{22})$$

$$= 1.19 \times 10^{-3} \text{ for p - type sensors}$$ Eq. (F.11)
$$= -1.54 \times 10^{-2} \text{ for n - type sensors}$$

$$\frac{\Delta R_{-45}}{R_{-45}} = (\frac{\pi_{11} + \pi_{12}}{2})(\sigma_{11} + \sigma_{22})$$

$$= 1.19 \times 10^{-3} \text{ for p - type sensors}$$ Eq. (F.12)
$$= -1.54 \times 10^{-2} \text{ for n - type sensors}$$

- With respect to the primed axes

$$\frac{\Delta R}{R} = \left[\left(\frac{\pi_{11} + \pi_{12} + \pi_{44}}{2} \right) \sigma'_{11} + \left(\frac{\pi_{11} + \pi_{12} - \pi_{44}}{2} \right) \sigma'_{22} \right] \cos^2 \phi$$

$$+ \left[\left(\frac{\pi_{11} + \pi_{12} - \pi_{44}}{2} \right) \sigma'_{11} + \left(\frac{\pi_{11} + \pi_{12} + \pi_{44}}{2} \right) \sigma'_{22} \right] \sin^2 \phi \qquad \text{Eq. (F.13)}$$

$$+ \pi_{12} \sigma_{33} + (\pi_{11} - \pi_{12}) \sigma'_{12} \sin 2\phi + + [\alpha_1 \Delta T + \alpha_2 \Delta T^2 + ...]$$

For p- and n-type sensors,

$$\frac{\Delta R_0}{R_0} = \left(\frac{\pi_{11} + \pi_{12} + \pi_{44}}{2} \right) \sigma'_{11} + \left(\frac{\pi_{11} + \pi_{12} - \pi_{44}}{2} \right) \sigma'_{22}$$

$$= 1.26 \times 10^{-2} \quad \text{for p - type sensors} \qquad \text{Eq. (F.14)}$$

$$= -1.52 \times 10^{-2} \quad \text{for n - type sensors}$$

$$\frac{\Delta R_{90}}{R_{90}} = \left(\frac{\pi_{11} + \pi_{12} - \pi_{44}}{2} \right) \sigma'_{11} + \left(\frac{\pi_{11} + \pi_{12} + \pi_{44}}{2} \right) \sigma'_{22}$$

$$= -1.04 \times 10^{-2} \quad \text{for p - type sensors} \qquad \text{Eq. (F.15)}$$

$$= -1.33 \times 10^{-2} \quad \text{for n - type sensors}$$

$$\frac{\Delta R_{45}}{R_{45}} = \left(\frac{\pi_{11} + \pi_{12}}{2} \right) (\sigma'_{11} + \sigma'_{22})$$

$$= 1.10 \times 10^{-3} \quad \text{for p - type sensors} \qquad \text{Eq. (F.16)}$$

$$= -1.43 \times 10^{-2} \quad \text{for n - type sensors}$$

$$\frac{\Delta R_{-45}}{R_{-45}} = \left(\frac{\pi_{11} + \pi_{12}}{2} \right) (\sigma'_{11} + \sigma'_{22})$$

$$= 1.10 \times 10^{-3} \quad \text{for p - type sensors} \qquad \text{Eq. (F.17)}$$

$$= -1.43 \times 10^{-2} \quad \text{for n - type sensors}$$

For p-type sensors, the normalized % changes in initial resistance for [100] and [110] silicon strip-on-beam compared with the corresponding silicon strip are summarized in Tables F.4 and F.5.

Table F.4 - Typical results of % change in initial resistance of [100] p-type silicon at 25°C				
Direction	Strip (Unit:kohm)	Single-sided strip-on-beam (Unit: kohm)	% change (Experimental)	% change (Analytic)
$\phi = 0$	22.351	22.387	0.16	0.14
$\phi = 90$	22.305	22.322	0.08	0.10
$\phi = +45$	22.325	22.332	0.03	0.12
$\phi = -45$	22.312	22.334	0.10	0.12

Table F.5 - Typical results of % change in initial resistance of [110] p-type silicon at 25°C				
Direction	Strip (Unit:kohm)	Single-sided strip-on-beam (Unit: kohm)	% change (Experimental)	% change (Analytic)
$\phi = 0$	23.051	23.396	1.49	1.26
$\phi = 90$	22.946	22.651	-1.29	-1.04
$\phi = +45$	23.084	23.098	0.06	0.11
$\phi = -45$	23.022	23.084	0.27	0.11

As shown in Table F.4, the normalized % change in initial resistance for [100] p-type sensors is negligible because all the related pi-coefficients π_{11}, π_{12}, and π_S for p-type silicon are very small. For the same reason, the last two rows in Table F.5 show the small % changes in initial resistance.

Similarly, for n-type sensors, the normalized % changes in initial resistance for [100] and [110] silicon strip-on-beam compared with the corresponding silicon strip are summarized in Tables F.6 and F.7.

Table F.6 - Typical results of % change in initial resistance of [100] n-type silicon at 25°C				
Direction	Strip (Unit:kohm)	Single-sided strip-on-beam (Unit: kohm)	% change (Experimental)	% change (Analytic)
$\phi = 0$	13.265	12.898	-2.77	-2.23
$\phi = 90$	13.351	13.135	-1.62	-0.85
$\phi = +45$	13.442	13.152	-2.16	-1.54
$\phi = -45$	13.368	13.138	-1.72	-1.54

Table F.7 - Typical results of % change in initial resistance of [110] n-type silicon at 25°C				
Direction	Strip (Unit:kohm)	Single-sided strip-on-beam (Unit: kohm)	% change (Experimental)	% change (Analytic)
$\phi = 0$	13.110	12.968	-1.08	-1.52
$\phi = 90$	12.883	12.663	-1.71	-1.33
$\phi = +45$	12.978	12.573	-3.12	-1.43
$\phi = -45$	13.345	13.184	-1.21	-1.43

Compared with p-type sensors, the normalized % changes in initial resistance for n-type sensors are relatively large because of the large pi-coefficients. It is observed that analytic results are in good agreement with experimental results for both p- and n-type sensors. In order to resolve the problems concerning the initial resistance, we use the double-sided silicon strip-on-beam samples.

APPENDIX G

THE COMPARISONS OF PI-COEFFICIENTS BETWEEN STRIPS AND DOUBLE-

SIDED SILICON STRIP-ON-BEAM SAMPLES

Typical results of pi-coefficients, which reflect the average values of 10 specimens, are presented in Chapter 9. For comparison purpose, stress test strips are calibrated and characterized. As discussed in Chapter 4, a rectangular strip containing a row of chips is cut from a wafer and is loaded in a four-point bending fixture to generate uniaxial stress state. Hence the variation of the resistance of sensors with applied uniaxial stress has been measured. Through the use of four-point bending test, we may determine all pi-coefficients and the values will be compared with those from double-sided silicon strip-on-beam samples. As discussed in Chapter 4, the induced uniaxial stress is given by

$$\sigma = \frac{3F(L-D)}{bh^2}$$ Eq. (G.1)

where F = 1N, (L-D) = 2.4 x 10^{-2} m and the dimensions of the (001) silicon strips are shown in Table G.1.

Table G.1 - Dimensions of the (001) silicon strips (Unit: mil)		
	(001) silicon:[100]	(001) silicon: [110]
Length (l)	3400	3400
Width (b)	226	160
Thickness (h)	20	20

Note that the dimensions of composite materials of strip-on-beam samples are presented in Tables 9.5 and 9.6.
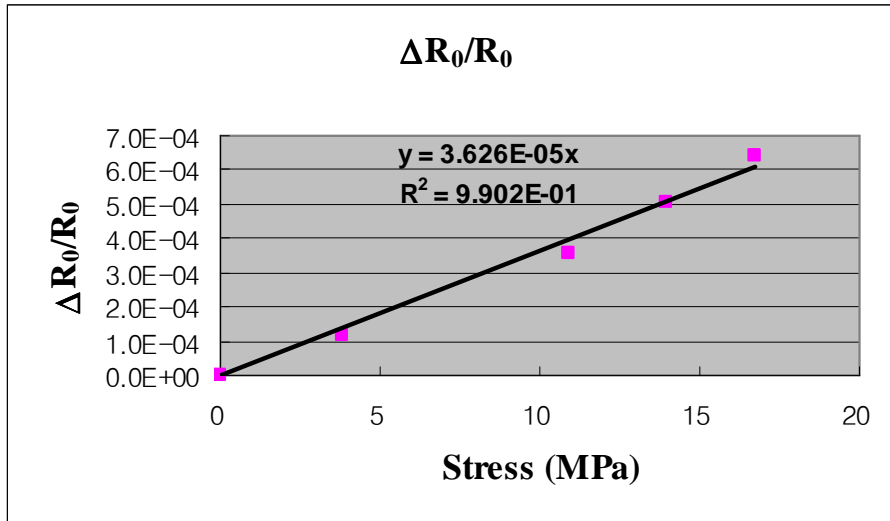
Fig. G.1 - Typical stress sensitivity of p-type resistors on the [100] silicon strip (R_0)
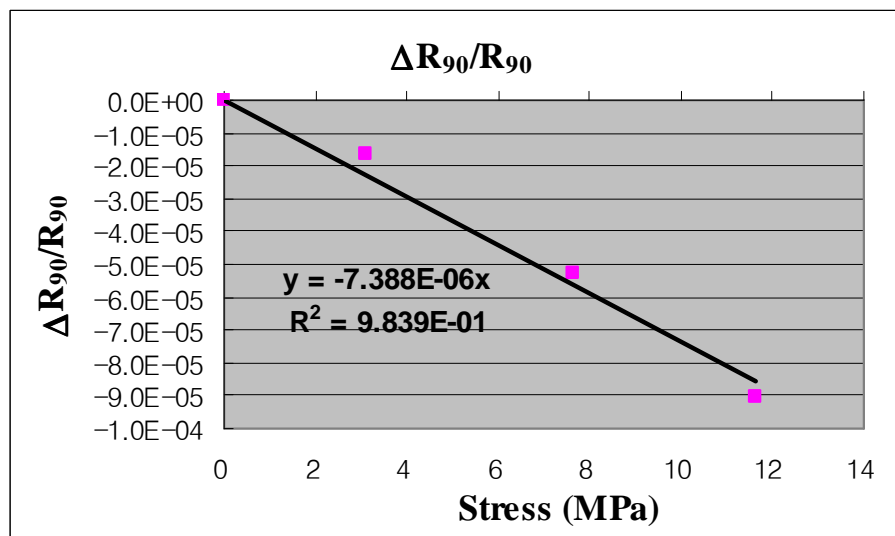
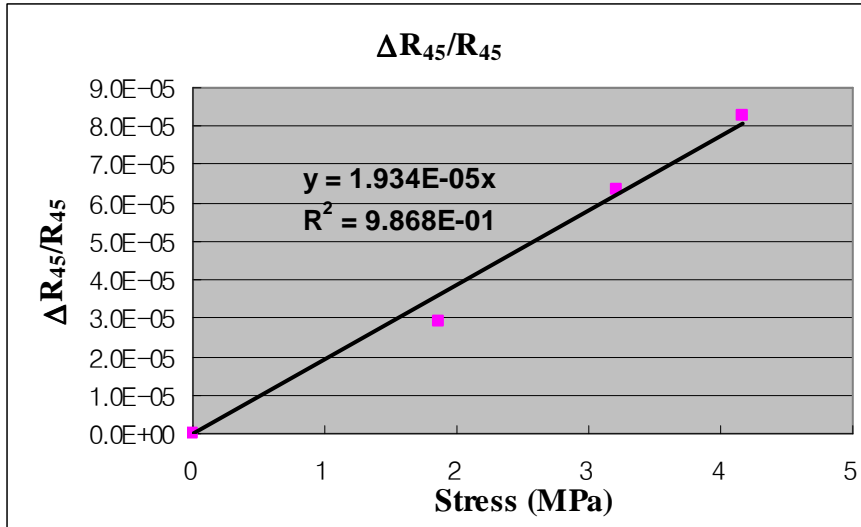Fig. G.2 - Typical stress sensitivity of p-type resistors on the [100] silicon strip (R_{90})
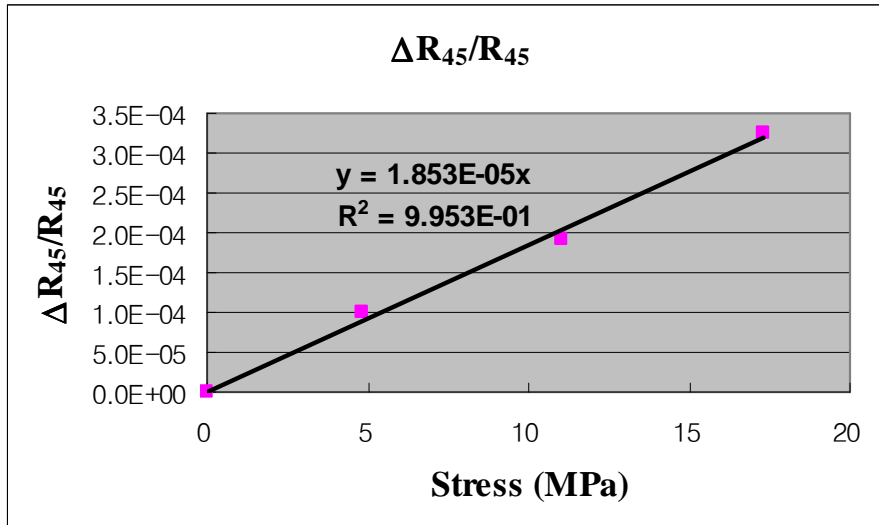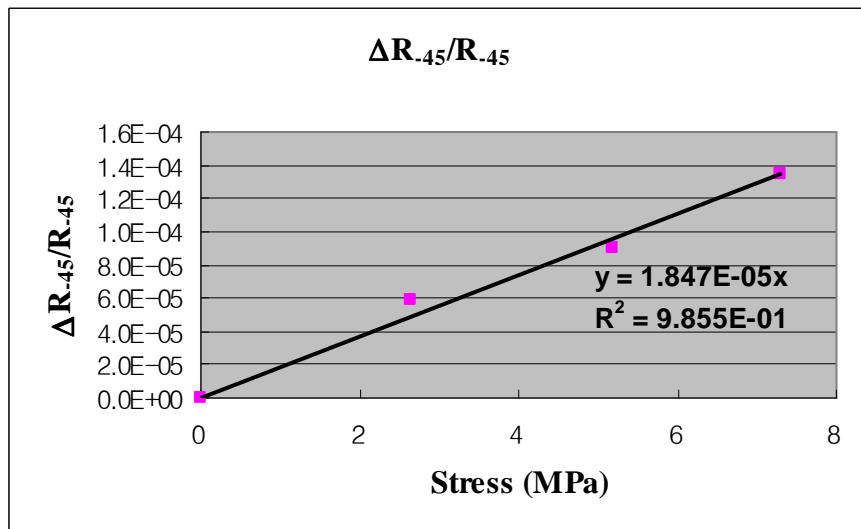
Fig. G.3 - Typical stress sensitivity of p-type resistors on the [100] silicon strip (R_{45})
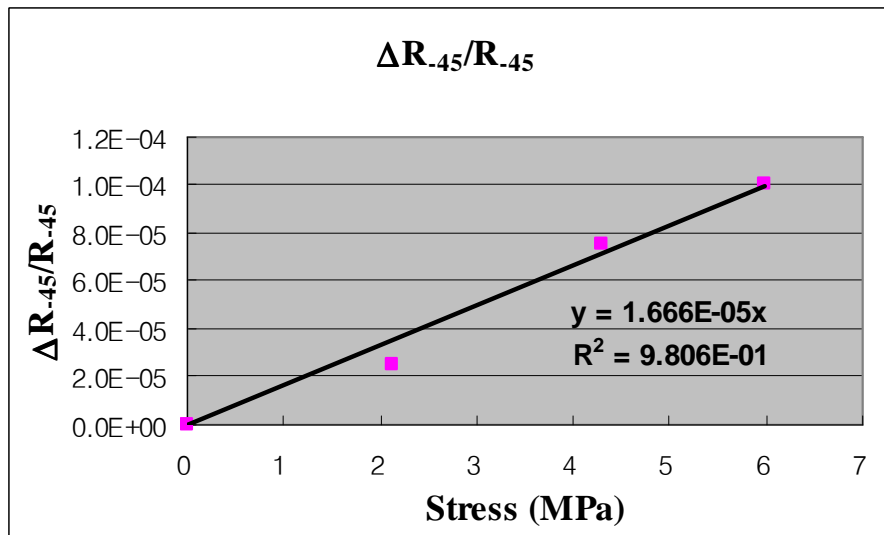
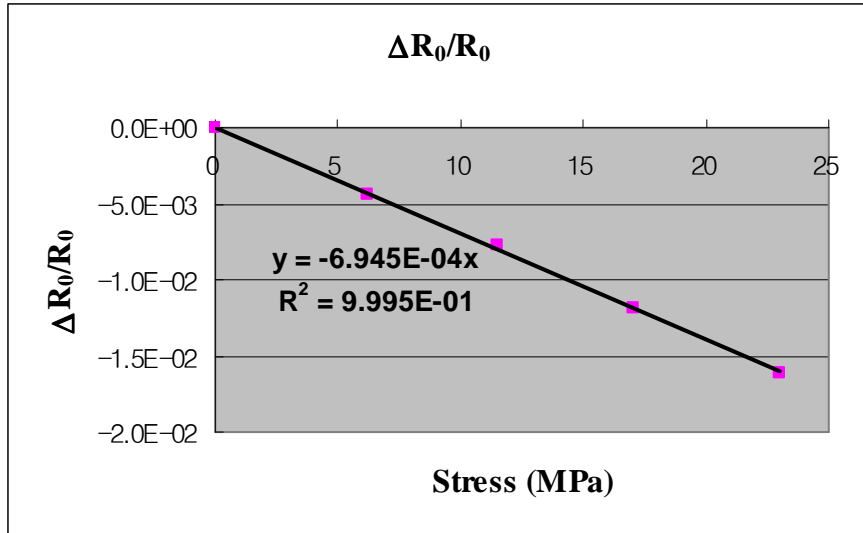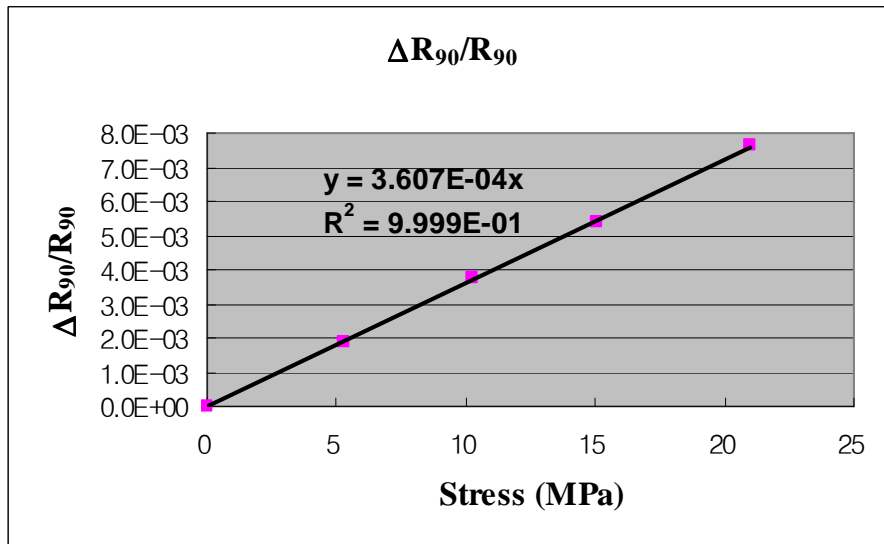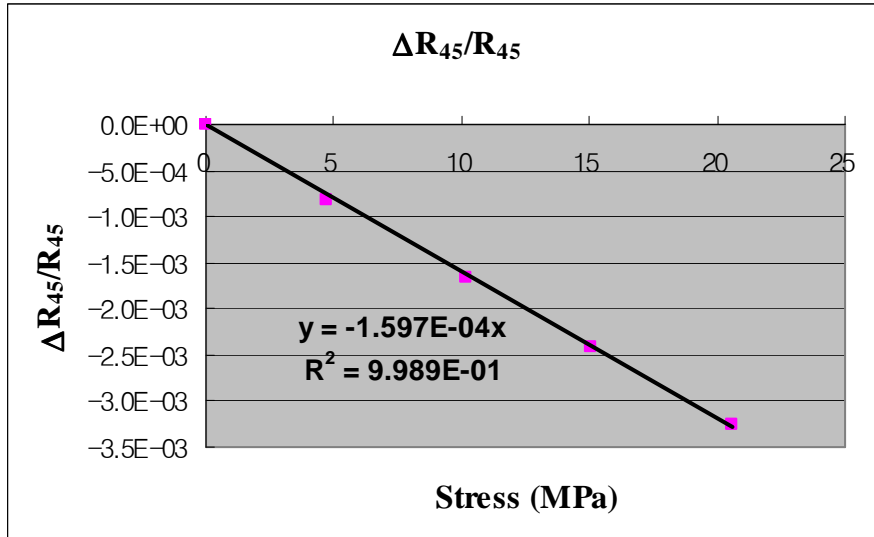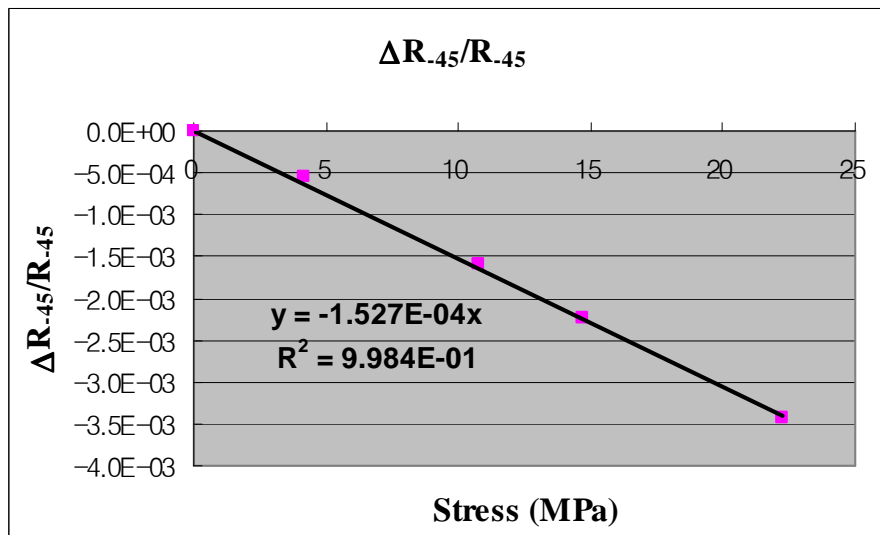Fig. G.4 - Typical stress sensitivity of p-type resistors on the [100] silicon strip (R_{-45})
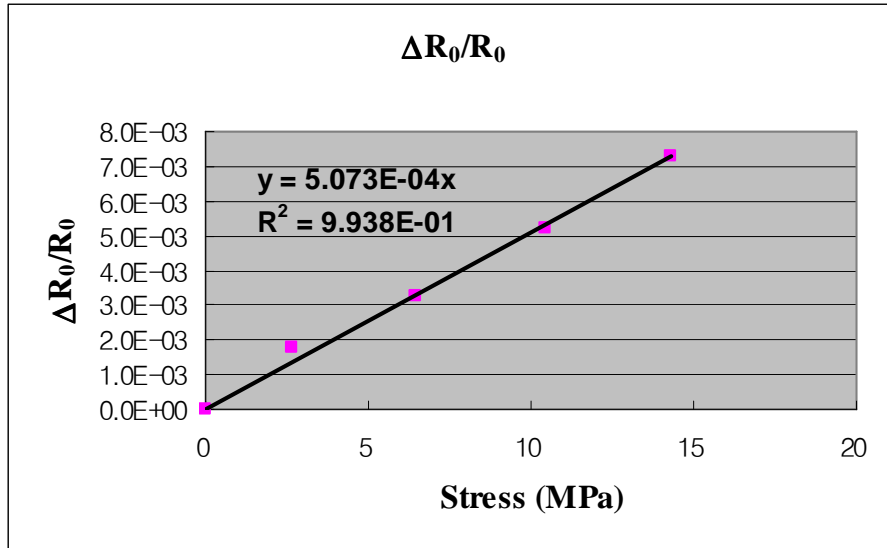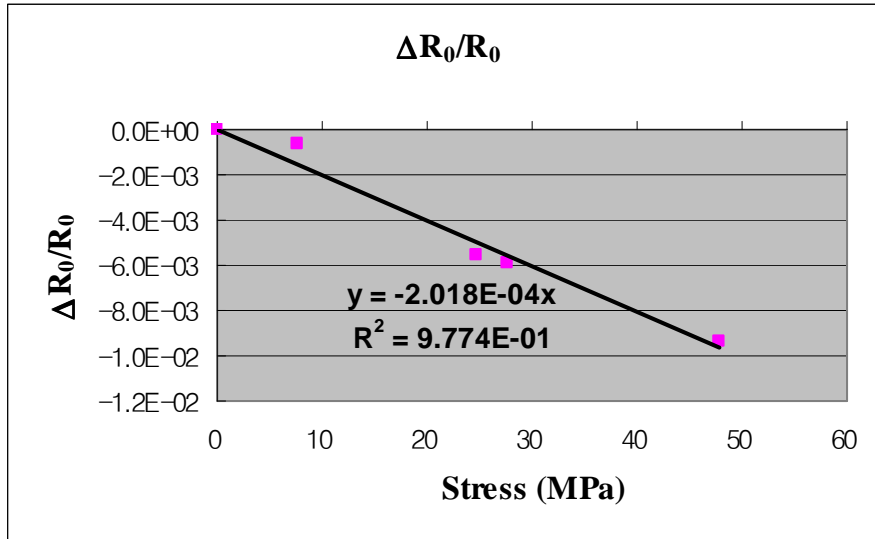
Fig. G.5 - Typical stress sensitivity of p-type resistors on the [110] silicon strip (R_0)
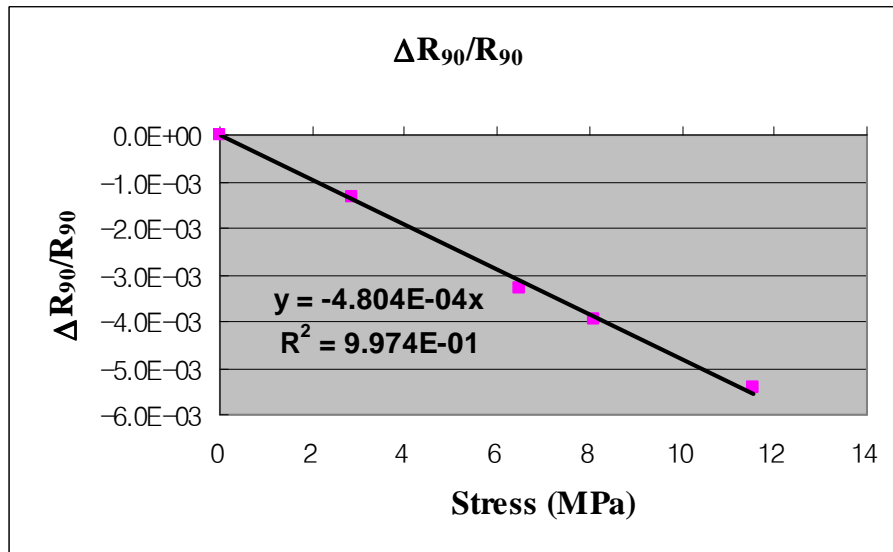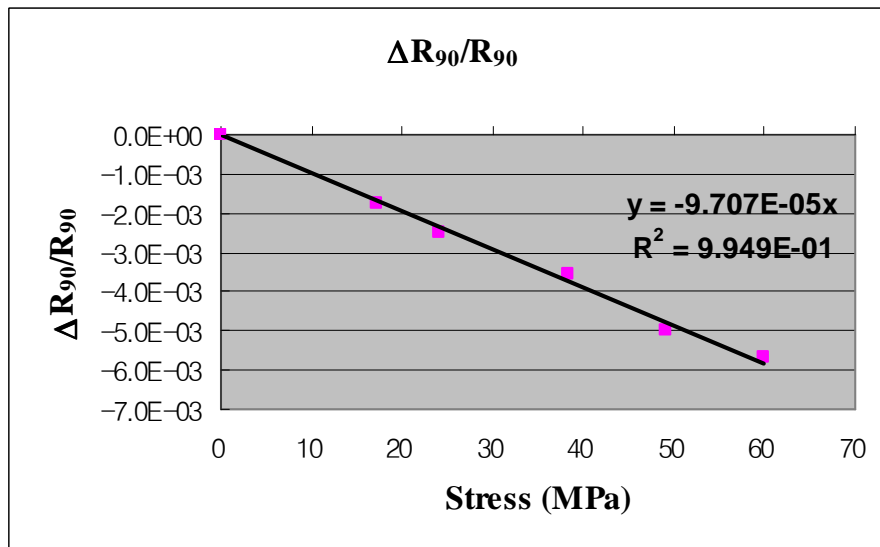

Fig. G.6 - Typical stress sensitivity of p-type resistors on the [110] silicon strip (R_{90})

Fig. G.7 - Typical stress sensitivity of p-type resistors on the [110] silicon strip (R_{45})

Fig. G.8 - Typical stress sensitivity of p-type resistors on the [110] silicon strip (R_{-45})

Fig. G.9 - Typical stress sensitivity of n-type resistors on the [100] silicon strip (R_0)

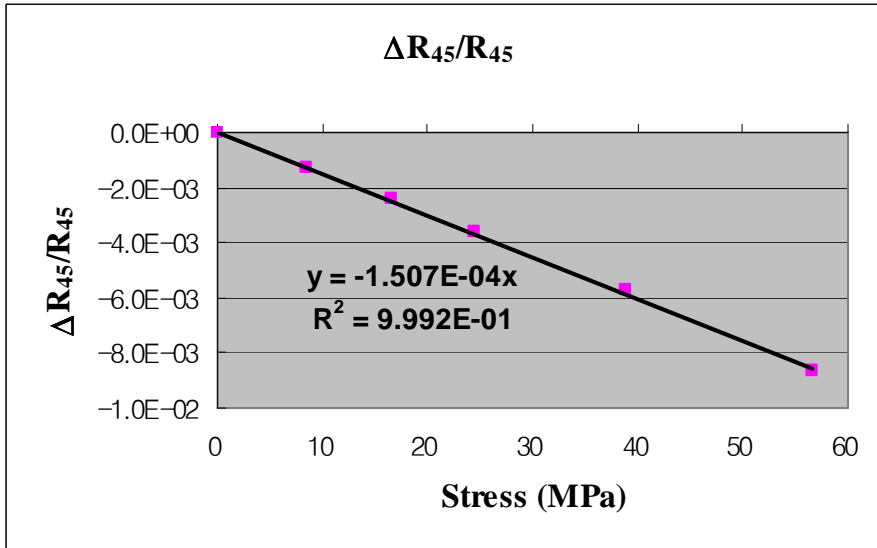Fig. G.10 - Typical stress sensitivity of n-type resistors on the [100] silicon strip (R_{90})

Fig. G.11- Typical stress sensitivity of n-type resistors on the [100] silicon strip (R_{45})

Fig. G.12- Typical stress sensitivity of n-type resistors on the [100] silicon strip (R_{-45})

Fig. G.13- Typical stress sensitivity of n-type resistors on the [110] silicon strip (R_0)

Fig. G.14- Typical stress sensitivity of n-type resistors on the [110] silicon strip (R_{90})

Fig. G.15- Typical stress sensitivity of n-type resistors on the [110] silicon strip (R_{45})
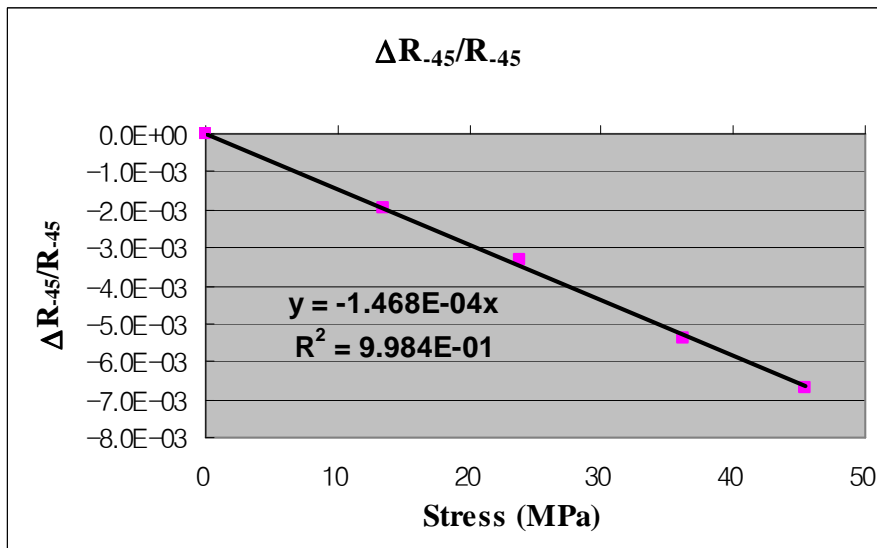

Fig. G.16- Typical stress sensitivity of n-type resistors on the [110] silicon strip (R_{-45})

The comparisons of pi-coefficients between stress test strips and double-sided silicon strip-on-beam are summarized in Tables G.2 through G.5. It may be noted that 5 samples are reflected in the values of strip. Both have an agreement in sign for all pi-coefficients. For p-type silicon, large spreads in magnitude are observed for π_{11} and π_{12} (and then π_s) because the coefficients are small. For n-type silicon, the smallest pi-coefficient π_{44} shows a relatively large spreads in values. On the other hand, the large pi-coefficients π_{11}, π_{12}, and π_s are close for both cases.

- [100]

Table G.2 - Comparisons of pi-coefficients for p-type [100] silicon (Unit: TPa^{-1})				
p-type	π_{11}	π_{12}	π_s (0, 90)	π_s (+45, -45)
strip	36.1	-7.9	28.2	30.2
strip-on-beam	29.4	-6.2	23.2	20.4

Table G.3 - Comparisons of pi-coefficients for n-type [100] silicon (Unit: TPa^{-1})				
n-type	π_{11}	π_{12}	π_s (0, 90)	π_s (+45, -45)
strip	-673	361	-312	-324
strip-on-beam	-691	390	-301	-302

- [110]

Table G.4 - Comparisons of pi-coefficients for p-type [110] silicon (Unit: TPa^{-1})			
p-type	π_{44}	π_s (0, 90)	π_s (+45, -45)
strip	965	26.6	27.3
strip-on-beam	898	12.2	26.6

Table G.5 - Comparisons of pi-coefficients for n-type [110] silicon (Unit: TPa^{-1})			
n-type	π_{44}	π_s (0, 90)	π_s (+45, -45)
strip	-105	-295	-302
strip-on-beam	-73.9	-290	-277

APPENDIX H

DETERMINATION OF THE STIFFNESS COEFFICIENT MATRIX FOR THE

UNPRIMED/PRIMED COORDINATE SYSTEM

In Chapter 6, the transformation relations for the reduced index stress and strain components were discussed as repeated below:

$$\sigma_\alpha = [T_{\alpha\beta}]^{-1}\sigma_\beta^{'}$$

<div align="right">Eq. (G.1)</div>

$$\varepsilon_\alpha = [T_{\alpha\beta}^t]\varepsilon_\beta^{'}$$

<div align="right">Eq. (G.2)</div>

Inverting Eq. (G.2) leads to

$$\varepsilon^{'} = [T^t]^{-1}\varepsilon$$

<div align="right">Eq. (G.3)</div>

Through the use of $\varepsilon_{ij} = S_{ijkl}\sigma_{kl}$

$$\varepsilon^{'} = [T^t]^{-1}[S]\sigma$$

<div align="right">Eq. (G.4)</div>

Finally, substitution of Eq. (G.1) into Eq. (G.4) yields the relations between stress and strain in a rotated primed coordinate system as follows:

$$\varepsilon^{'} = [T^t]^{-1}[S][T]^{-1}\sigma^{'}$$

<div align="right">Eq. (G.5)</div>

If an unprimed coordinate system is assumed, $[T^t]^{-1}$ and $[T]^{-1}$ in Eq. (G.5) simplify to unit matrices.

$$[S^{'}] = [T^t]^{-1}[S][T]^{-1}$$

<div align="right">Eq. (G.6)</div>

By $[S^{'}] = [C^{'}]^{-1}$, Eq. (G.6) becomes

$$[C^{'}]^{-1} = [T^t]^{-1}[S][T]^{-1}$$

<div align="right">Eq. (G.7)</div>

Inverting Eq. (G.7) gives

$$[C'] = [T][C][T^t] \qquad \text{Eq. (G.8)}$$

Many calculations may be solved with matrix algebra.

- With respect to the unprimed coordinate system

$$[c_{\alpha\beta}] = \begin{bmatrix} c_{11} & c_{12} & c_{12} & 0 & 0 & 0 \\ c_{12} & c_{11} & c_{12} & 0 & 0 & 0 \\ c_{12} & c_{12} & c_{11} & 0 & 0 & 0 \\ 0 & 0 & 0 & c_{44} & 0 & 0 \\ 0 & 0 & 0 & 0 & c_{44} & 0 \\ 0 & 0 & 0 & 0 & 0 & c_{44} \end{bmatrix} \qquad \text{Eq. (G.9)}$$

- With respect to the primed coordinate system

$$[C'] = \begin{bmatrix} \dfrac{C_{11}+C_{12}}{2}+C_{44} & \dfrac{C_{11}+C_{12}}{2}+C_{44} & C_{12} & 0 & 0 & 0 \\[2ex] \dfrac{C_{11}+C_{12}}{2}-C_{44} & \dfrac{C_{11}+C_{12}}{2}+C_{44} & C_{12} & 0 & 0 & 0 \\[2ex] C_{12} & C_{12} & C_{11} & 0 & 0 & 0 \\[1ex] 0 & 0 & 0 & C_{44} & 0 & 0 \\[1ex] 0 & 0 & 0 & 0 & C_{44} & 0 \\[1ex] 0 & 0 & 0 & 0 & 0 & \dfrac{C_{11}-C_{12}}{2} \end{bmatrix}$$

$$\text{Eq. (G.10)}$$

where $C_{11}=165.7$ GPa, $C_{12}=63.9$ GPa, and $C_{44}=79.6$ GPa [90].

APPENDIX I

THE PROFILES OF CARRIER CONCENTRATION VERSUS DEPTH IN SILICON

The profiles of carrier concentration vs. depth in silicon are provided using Spreading Resistance Analysis (SRA) as presented in the following figures. For the p- and n-type samples prepared for this research, the impurity concentration at the wafer surface (N_0) is $2.0 \times 10^{18}/cm^3$ and $4.0 \times 10^{18}/cm^3$, respectively. The metallurgical junction depth at which the impurity profile intersects the background concentration is approximately 1.7 μm for p-type sensors and 1.2 μm for n-type sensors.

Fig. I.1 - The profiles of carrier concentration vs. depth in n-type silicon (sample #1)

Fig. I.2 - The profiles of carrier concentration vs. depth in n-type silicon (sample #2)
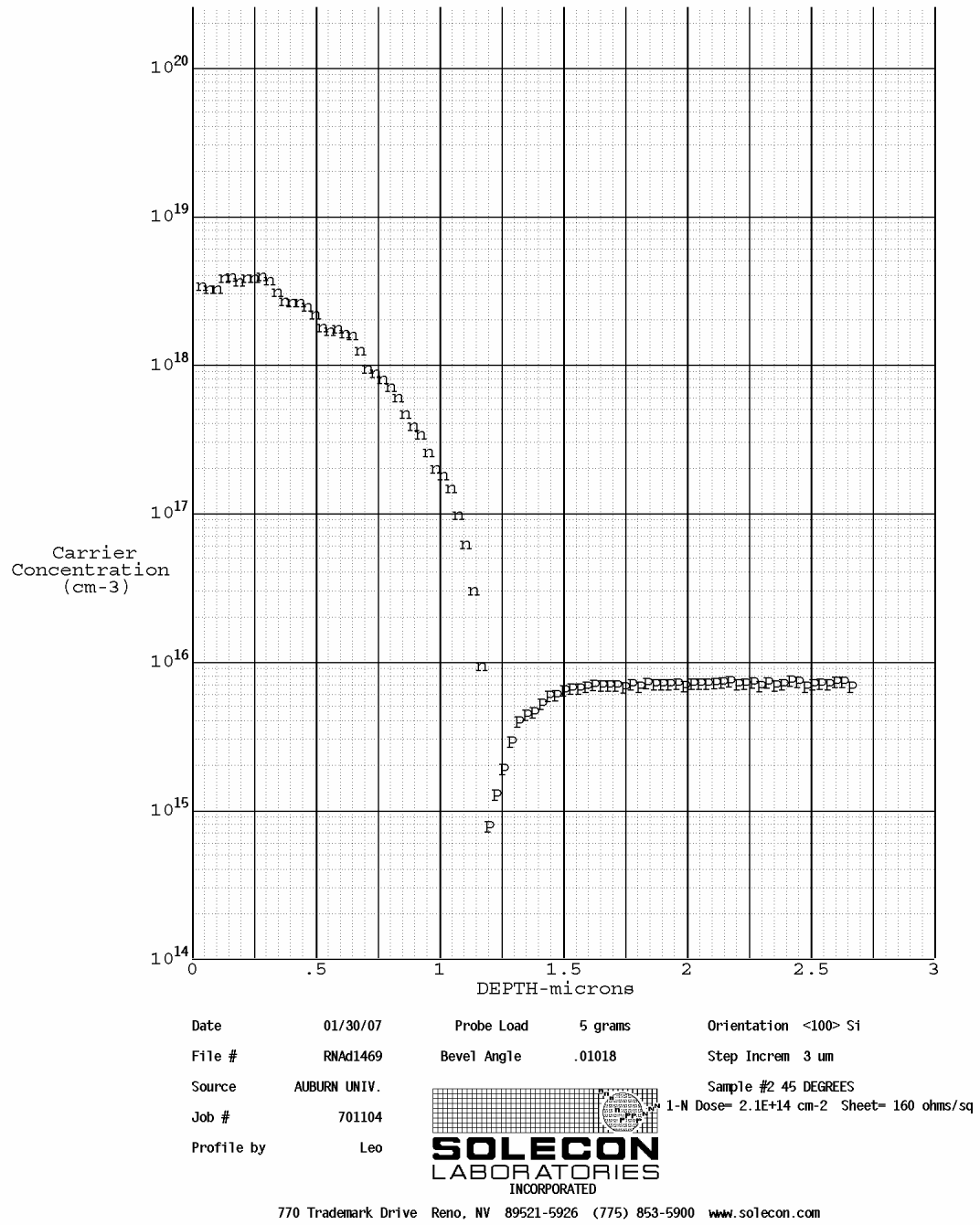
Fig. I.3 - The profiles of carrier concentration vs. depth in p-type silicon (sample #1)
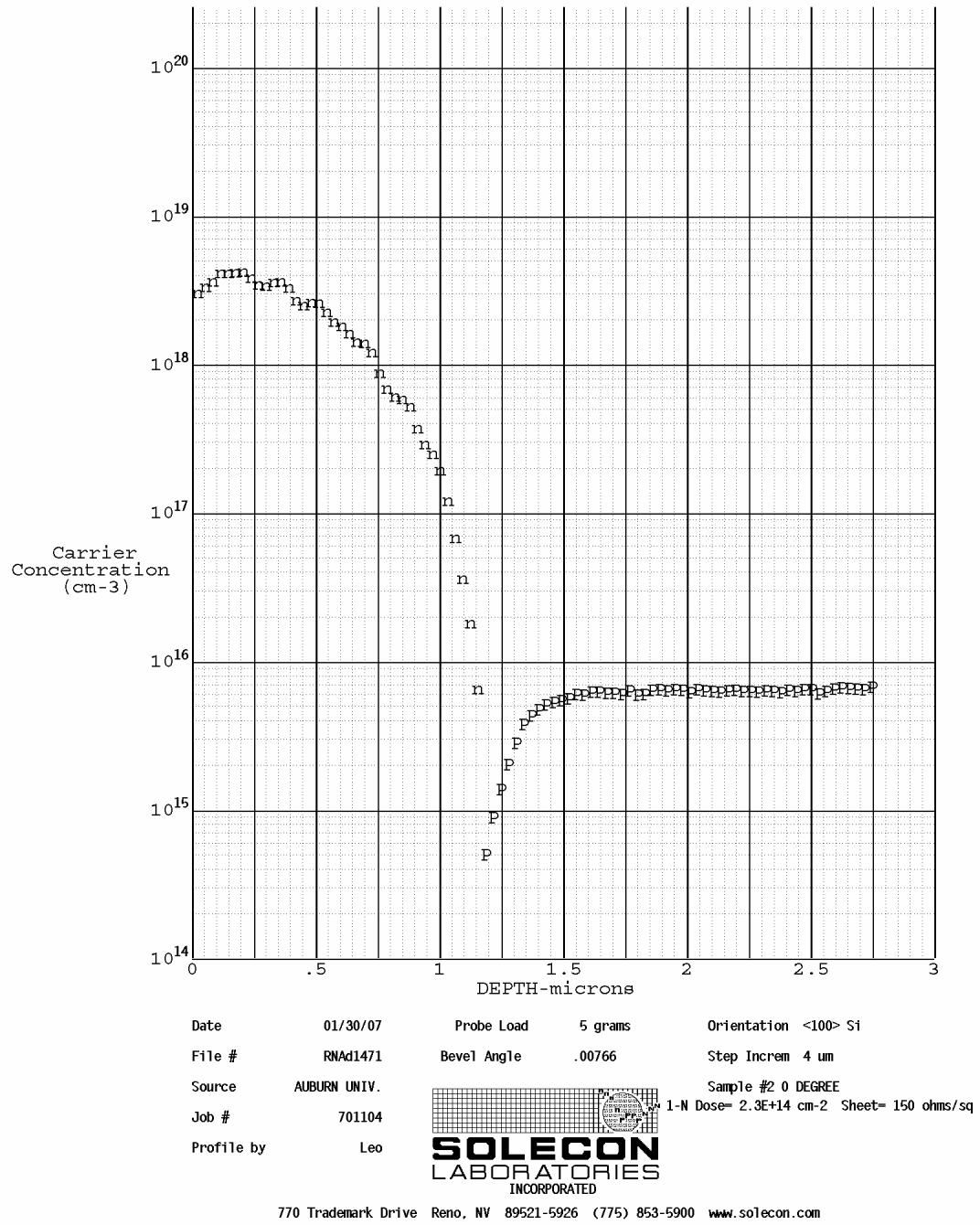
Fig. I.4 - The profiles of carrier concentration vs. depth in p-type silicon (sample #2)